Master's thesis

NTNU
Norwegian University of Science and Technology
Faculty of Engineering
Department of Civil and Environmental Engineering

Hallvard Skrede

CPTU-detection of thin clay layers in sand

Results from calibration chamber testing

Master's thesis in Geotechnical Engineering
Supervisor: Steinar Nordal
Co-supervisor: Hallvard Berner Hammer
July 2021

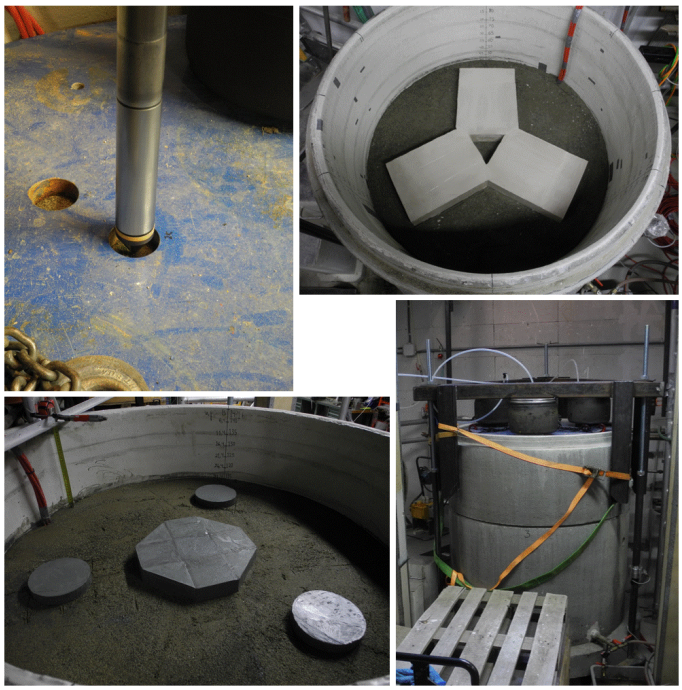

NTNU
Norwegian University of
Science and Technology

Hallvard Skrede

CPTU-detection of thin clay layers in sand

Results from calibration chamber testing

Master's thesis in Geotechnical Engineering
Supervisor: Steinar Nordal
Co-supervisor: Hallvard Berner Hammer
July 2021

Norwegian University of Science and Technology
Faculty of Engineering
Department of Civil and Environmental Engineering

NTNU
Norwegian University of
Science and Technology

Abstract

Landslides along the coastal areas of Norway pose a threat to communities and infrastructure. Analyses of past landslides have shown that thin clay layers in sandy shoreline deposits often act as a glide plane, also called a weak layer, for these landslides. Unfortunately, the detection of such thin layers (i.e. < 20 cm) is challenging for all the conventional geotechnical field investigations techniques, including high quality CPTU tests.

During the last two years, a research program with a large-scale model testing facility has been carried out in the geotechnical laboratory at NTNU in Trondheim. The work aims to identify possibilities and limitations in detection of thin layers of clay in sand; and determination of the soil properties of the thin clay layers using the CPTU-tool. In this master's thesis the main focus has been to improve an existing test setup; design and perform a test program, and consider CPTU-interpretation for the thin layer problem.

Tests were run in a pressurized chamber (diameter: 1,2 m, height: 1,5 m) that allowed regulation of the ground water table. In four experiments, different combinations of thin, horizontal clay layers of 2-12 cm of respectively pottery clay and natural quick clay were built into medium dense sand. The CPTU-soundings were conducted by utilizing both a standard piezocone penetrometer (10 cm^2) and a mini-piezocone penetrometer (5 cm^2), recording tip resistance, shaft friction and penetration pore-pressure.

The results show that the CPTU-response in thin clay layers is influenced by the surrounding sand, and that 8-12 cm thick clay layers can be identified using the conventional CPTU-tool normally used in practice. The tip resistance in the thin layers do not reach the material's characteristic tip resistance (as defined by a significantly larger thickness of the same material), since the failure mechanism around the tip will involve both materials. In practice this implies that the shear strength of thin layers is overestimated. Regarding sample preparation, the experiment conducted on quick clay proved that it actually is possible to build easily disturbed quick clay specimens cut from field block samples into the chamber. Only a very moderate disturbance of the quick clay properties could be detected. The lab results illustrates that the regular classification charts cannot be used for detecting thin weak layers, as they only regard measurements at specific depths or time instances. It is apparent that during transitions the relative changes of the measured parameters must be taken into account.

This study suggests that tip resistance is the most prominent parameter in detection of thin clay layers in sand, while pore pressure readings provide a good support for the findings. Three elements have been identified to influence the thin layering effect the most, these are: the CPTU probe diameter; the intermediate layer's thickness; and the contrast in soil strength, or more specifically, the contrast in the materials' characteristic tip resistance. Regarding quick clay it is confirmed that such sensitive clays require considerable awareness, precision, and careful execution when thin layers are built from clay sampled by a block sampler at depths in the field.

Sammendrag

Skred langs kystområdene i Norge forekommer og utgjør stadig en risiko for samfunnet og generell infrastruktur. Studier av tidligere skred har vist at mellomliggende tynne leirelag i breelv- og elveavsetninger ofte fungerer som glideplan, også kalt svake lag, for disse skredene. Dessverre er påvisning av slike tynne lag (dvs. <20 cm) utfordrende med alle konvensjonelle geotekniske feltundersøkelsesmetoder. Dette gjelder også trykksonderinger som generelt er ansett som både pålitelig og presis.

De siste to årene har det pågått et forskningsprogram i det geotekniske laboratoriet ved NTNU i Trondheim. Hensikten ved arbeidet er å identifisere muligheter og begrensninger i påvisning av tynne leirelag avsatt i sand, og bestemmelse av de tynne lagenes egenskaper ut fra trykksondering. I denne masteroppgaven har hovedfokuset vært å videreutvikle de fysiske modelltestene, gjennomføre et omfattende forsøksprogram og å samle inn data for påfølgende tolkning.

Testene ble gjennomført i en betong-kum (diameter: 1,2 m, høyde: 1,5 m) med mulighet for regulering av vertikal påsatt last og regulerbart grunnvannsspeil. Gjennom fire eksperimenter har horisontale leirelag blitt bygget inn i middels tett sand, hvor ulike kombinasjoner av lagtykkelser (2-12 cm) og leiremateriale er blitt benyttet, henholdsvis keramikkleire og kvikkleire. Trykksonderingene ble utført ved å benytte både en standard piezocone-penetrometer (10 cm^2) og en mini-piezocone-penetrometer (5 cm^2), som registrerte spissmotstand, sidefriksjon og poretrykk.

Resultatene viser at CPTU-responsen i tynne leirelag er påvirket av den omkringliggende sanden, og at 8-12 cm tykke leirelag kan identifiseres ved hjelp av det konvensjonelle CPTU-verktøyet som normalt brukes i bransjen. Den målte spissmotstanden i tynne leirelag gir høyere verdier enn materialets karakteristiske spissmotstand, grunnet at bruddmekanismen rundt spissen av sonden påvirkes av nærliggende sterkere lag. Dette innebærer at estimeringer av skjærstyrken basert på CPTU-data vil overvurdere styrken til svake tynne lag.

Hva angår den lagvise oppbyggingen i kummen viste forsøket på kvikkleire at det er mulig å bygge kumprøver med prøvestykker av kvikkleire inn i sand. Det ble imidlertid målt noe prøveforstyrrelse i kvikkleiren, som dermed hadde endret egenskapene sine noe under forsøket. Prøveforstyrrelsene var imidlertid mindre enn ventet. Laboratorieresultatene viser at de vanlige klassifiseringsdiagrammene ikke fungerer særlig godt for å identifisere tynne lag. For overganger og tynne lag må man betrakte relativ endring av målte parametere.

Denne studien antyder at spissmotstand er den mest fremtredende parameteren i påvisning av tynne leirelag i sand, mens poretrykkavlesninger vil kunne støtte opp om tolkningene. Det er identifisert tre elementer som påvirker tynnlagseffekten i størst grad: geometrien på konusen og sonden; tykkelsen av det mellomliggende laget; og kontrasten i styrke, eller mer spesifikt, kontrasten i materialenes karakteristiske spissmotstander. Når det gjelder de fysiske modelltestene, var det tydelig at kvikkleire er svært sårbart for påvirkning. Bruken av kvikkleire krever derfor god planlegging, forsiktighet og nøye utførelse.

Forewords

This master's thesis in geotechnical engineering, TBA4900, includes documentation on physical large-scale model testing aimed at simulating ground conditions found in the field. More specifically, soundings in thin layers of clay embedded in sand deposits have been emulated in the pursuit of the research question: How to identify thin layers of clay embedded in sand deposits, and furthermore assess soil properties based on readings in said deposits. The workload for experiments 0, 1a, 2 and 3, has been respectively around 55, 130, 140 and 275 hours, with an additional 60-90 hours for experiment 0 in project thesis. Moreover, administrative work, the succeeding data treatment, literature review and writing constituted ca. 520 hours. All hours are excluding breaks.

The experiments have been performed at the Norwegian University of Technology and Science, NTNU, and is a continuation of previous work by Hallvard Berner Hammer (2020). The advisor of this master's thesis has been Steinar Nordal, professor in geotechnics at NTNU, and the co-advisor was Hallvard Berner Hammer, former student and research assistant at NTNU, now working at Dr.techn. Olav Olsen.

The research program has involved several people which all deserve acknowledgement for their contributions. Espen Andersen and Karl-Ivar Kvisvik have been some of the closest assistants in the physical works, and have assisted with practical work, such as setting up the experimental system, adjusting the model chamber, perform soundings, provide materials and equipment, and extracting natural clay. The staff engineers Frank Støhli and Tage Westrum have also been very helpful and made specially customized equipment for the physical model facility with an amazing precision and skilled craftmanship. Senior engineer Per Asbjørn Østensen have made all the programs related to the actuator and the pressure reading devices and has furthermore developed the calibration equipment. I want to thank research assistants Maja Morawska and John Lau for helping med out with some lab procedures and for generally encouraging my work. Further, I would like to thank Jean-Sébastien L'Heureux for allocating time to counsel in group meetings and showing general interest in the project. The head of service group at Geomil, Jody Jansen deserves many thanks for lending equipment for the research program and for all the technical aid. I want to thank my girlfriend Johanne Eggum for keeping me with company in the otherwise solitude at the lab, and for aiding me in general, improving my written works, help me with some difficult lab procedures and generally supporting me. I also want to thank my advisor Steinar Nordal for always being enthusiastic, full of ideas and very understanding in all of his counselling. I am very grateful for the extensive efforts done by previous participant Hallvard B.H. for his sacrificed spare time which he has spent teaching me about the project and collaborating with me inside and outside the lab. His genuine interest in the project has been very encouraging.

Trondheim, 02.07.2021

Signature

Hallvard Skrede 

As this thesis in TBA4900 (constituting 30 ECTS) builds on the project thesis (TBA4510, constituting 7,5 ECTS), it is of importance for the institute that the content which is in part, or completely self-plagiarism, is clarified, as to make the sensor aware. With this regard, some paragraphs are partially self-plagiarism in this thesis, but mostly the previous work is edited and developed. Some of the perhaps least edited chapters are:

Ch. 2.1

Ch. 2.1.2

Ch. 2.3

Ch. 2.3.1.3

Ch. 2.3.2

Ch. 2.3.3

Spread fractions of chapter 4

Table of contents

Symbol list

α	Non-directional inclination	σ_h	Horizontal total stress
β	Plastification angle	σ'_h	Horizontal effective stress
β_1 and β_2	Bi-directional inclinations	$\sigma'_{h,0}$	In-situ horizontal effective stress
γ	Unit weight of sample	σ_m	Mean stress
γ'	Effective unit weight of soil	σ_v	Overburden total stress
γ_d	Dry unit weight	$\sigma'_{v,\infty}$	Asymptotic level of overburden effective stress
γ_i	Unit weight of material i	σ'_v	Vertical effective stress
γ_w	Unit weight of water	$\sigma'_{v,0}$	In-situ vertical effective stress
Δ	Volume change parameter	σ_w	Horizontal normal stress acting on the wall
δ'	Mobilized interface friction angle between wall and fill material	$\overline{\sigma_v}$	Average vertical total stress
ε	Strain	$\overline{\sigma'_v}$	Average vertical effective stress
ε_V, $\varepsilon_{V,\mathrm{III}}$	Volumetric strain, in zone III	$\sigma_{v,0}$	In-situ total stress, Overburden stress
η	Cone resistance ratio	$\sigma'_{v,0}$	Effective overburden stress
η_{thin}	Characteristic cone resistance ratio (relative to the surrounding layer)	$\Delta\sigma'_v$	Change of effective overburden stress
μ'	Friction coefficient	τ	Shear stresses
ν	Poisson's ratio	τ_c	Shear strength of the soil
ρ	Density	τ_f	Maximum allowed shear stress
ρ_b	Bulk density	τ_w	Shear stresses acting along wall interface
ρ_d	Dry density	ϕ'	Friction angle
ρ_s	Grain density	a	Attraction
σ_{atm}	Atmospheric pressure, ≈ 100 kPa	a	Unequal area ratio
σ_i	Measured total stress on pressure cell i	A_c	Cross section area of the cone
σ'	Effective stress	$A_{f_{sleeve}} = A_f$	Cross section area of the friction sleeve
σ'_i	Measured effective stress on pressure cell i	$A_{sleeve} = A_s$	Surface area of friction sleeve
σ'_1, σ'_2, σ'_3	Principal effective stresses	B	Foundation width

B_q	Pore pressure ratio	g	Gravitational acceleration
c	Cohesion	h	Height
C_c	Compression index	$h_c + h_e$	Cone height including cylindrical part
d_c	Cross section diameter of the cone	h_w	Height of ground water in chamber
$d_{f_{sleeve}}$	Cross section diameter of the friction sleeve	Δh	Final height of sand layer
$d_{filter} = d_{u_i}$	Cross section diameter of filter at position i	Δh_c	Settlements resulted by vibration
d_{10}	10 % of grains have a diameter lower than this value	Δh_f	Layer height of a newly filled sand layer
d_{50}	50 % of grains have a diameter lower than this value.	$\Delta h_{s,1}$	Settlements resulted by saturation
d_{60}	60 % of grains have a diameter lower than this value	$\Delta h_{s,2}$	Settlements resulted by discharge of water
D	Diameter	H	Interbedded layer's thickness
D_c	Chamber-/silo diameter	H_i	Interbedded sub sample layer's thickness
D_h	Hydraulic diameter	H_c	Chamber inner height
D_r	Relative density	$H_{c,\mathrm{I}}$	Chamber base inner height
e	Void ratio	$H_{c,\mathrm{II}}$	Chamber extension inner height
e_{max}	Maximum void ratio	H_D	Developing depth
e_{min}	Minimum void ratio	H_I	Influence depth
E	Young's modulus or elastic modulus	H_s	Sensing depth
$E_{oed} = M$	Oedometer modulus	i or i_i	Gradient of the ground water (in segment *i*)
E_u	Elasticity modulus under undrained conditions	i	Average cone penetration, falling cone
E_{50}	Elasticity modulus based on cutting the ε, σ-curve at 50 % of interpreted failure load, as a function of stress	I_c	Soil behaviour type index
f_s	Side friction	I_L	Liquidity index
$f_{s,red}$	Reduction of side friction due to rate effects	I_P	Plasticity index
$F_r = R_{fn}$	The normalized friction ratio or net friction ratio	K'	Coefficient of lateral earth pressure
F_s	Total forces acting on the frictions sleeve	K'_a	Rankine's active earth pressure coefficient

K'_w	Wall pressure coefficient	N_σ	Cavity expansion factor
$K_{L,}$	Soil viscosity coefficient	OCR	Overconsolidation ratio
$K_{L,i}$	Soil viscosity coefficient for material *i* (pc=pottery clay, qc=quick clay)	p_a	Reference pressure
K_H	Thin layer correction factor	p'_c	Effective preconsolidation stress
K'_0	Coefficient of earth pressure at rest	$q = q_{load} = \Delta\sigma'_{v,1}$	Applied load on chamber sample
l'	Decay length	$q_b = q_{ult}$	Unit end bearing resistance
l_s	Length of the friction sleeve	q_c	Cone resistance
m	Deformation modulus	q_e	Effective cone resistance
m	Cone mass, falling cone	q_{cd}	Measured tip resistance
n	Effective stress exponent	q_{dev}	Deviatoric stress
n	Porosity	$q_n = q_{net}$	Net cone resistance
n_{max}	Maximum porosity	q_t	Corrected total cone resistance, simplified to cone resistance after its introduction
n_{min}	Minimum porosity	q_t^{char}	Characteristic tip resistance
N_c	Undrained bearing capacity factor	$q_{t,i}^{char}$	Characteristic tip resistance of material i
N_c^*	Undrained bearing capacity factor without any factors imbedded/incorporated.	$q_{t,thin,peak}$	Maximal measured cone resistance in thin layer
$N_{k,i}$	In-situ cone factor	q_{ult}	Ultimate bearing stress
N_{ke}	Conus factor based on corrected tip resistance and water pressure	Q_c	Total force acting on the cone
N_{kt}	Conus factor based on net tip resistance	Q_t, Q_{tn}	Normalized tip resistance
N_m	Cone resistance number	r	Ratio of shear stresses transferred between the wall and the soil
N_q	Drained bearing capacity factor	R_{fn}= F_r	Normalized friction ratio or net friction ratio
N_u	Theoretical bearing capacity factor	s_c	Bearing capacity shape factor
$N_{\Delta u}$	Conus factor based on excess water pressure	S_r	Saturation

S_t	Sensitivity	w_L	Liquid limit
$S_{u,i}$	Undrained shear strength measured by method *i*	$w_{L,i}$	Liquid limit for material *i* (pc=pottery clay, qc=quick clay)
$S_{u,r,i}$	Remoulded undrained shear strength measured by method *i*	w_P	Plastic limit
$\overline{S_u}$	Average undrained shear strength working along failure surface	$w_{P,i}$	Plastic limit for material *i* (pc=pottery clay, qc=quick clay)
u_i	Measured pore pressure at sensor position *i*	w_S	Shrinkage limit
u_0	Static pore pressure, Initial pore pressure, Ground water pressure	z	Depth from surface in sample or in field
Δu, Δu_2	Excess pore pressure	z_c	Critical depth
U	Chamber-/silo perimeter	z_L	Depth in sample from upper rim of current chamber
v	Penetration rate or velocity	z_{q_t}	Depth of data point associated q_t
v_{A_c}	Penetration rate of probe with cross section area A_c	z_{f_s}	Depth of data point associated q_{f_s}
v_s	Lowest utilized penetration rate	z_{u_2}	Depth of data point associated q_{u_2}
w	Water content	z_w	Depth to water table
w_i	Water content for material *i* (pc=pottery clay, qc=quick clay)	$z_{w,i}$	Depth of change of gradient

1 Introduction

1.1 Background

Analyses of past landslides along the coast of Norway have shown that thin clay layers in sandy shoreline deposits often act as a glide plane (L'Heureux et al. 2010, p.1). The thicknesses (i.e., < 20 cm) may be so thin that the layers may not manifest themselves for conventional geotechnical field investigations. Even for high quality survey techniques alike the CPTU-test struggle to detect such layers and the issue consequently remains a topic of research. An example of a recent landslide that caused fatalities with these characteristics, is the Finneidfjord landslide, which occurred in 1996 (Longva et al. 2003).

In the northern hemisphere there are many historic estuary deposits located above the modern sea level. They originate from the previous glacial period and the succeeding glacial retreat, and have since then been subjected to post-glacial rebound. The geomorphological processes which have taken place in these estuaries are mainly of glacio-marine and glacio-fluvial character. The sediments in such deposition environments consist of all soil separates, interbedded in inclined sheets. Among the deposited layers saline marine clay layers may build-up, which when subjected to leaching will increase its sensitivity and may over time transform into a quick clay. Such layers are characterized as soft and brittle, and pose a serious safety hazard, especially for areas subjected to anthropogenic activities, which might incite landslides (L'Herueux et al. 2012). In an article published in 2010, L'Heureux et al. presented some back-analyses of slope failures in the bay of Trondheim, see *Figure 1.1*. They used a limit equilibrium slope stability model to validate the interpretation of the assumed failure mechanism, and their results implied that the hypothesis was conforming, yet the causes and the development of landslides remained a topic of discussion. On the basis of the presented information, the detection of such clay layers is consequently of high importance.

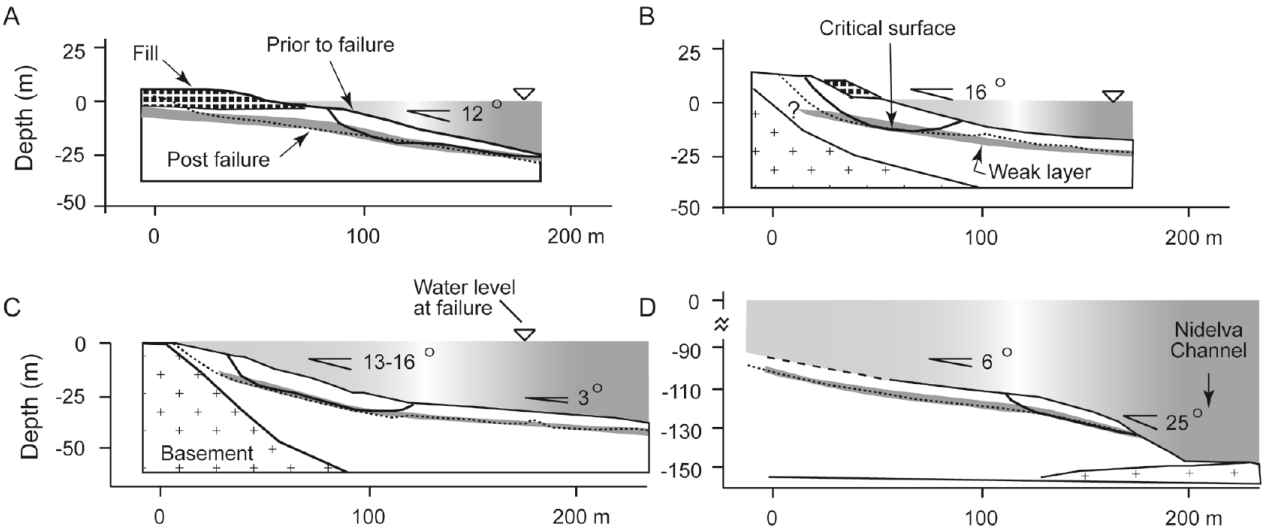

Figure 1.1. Back-analyses of slope failures in the Bay of Trondheim, based on a limit equilibrium slope stability model. Solid lines show previous boundaries, while the thin dotted lines show landslide scars.

In geotechnical field investigations, the use of CPTU is essential in the determination of soil layering profile and of the soil properties associated the layers. A brief and concise summary on the application of the CPTU was provided by Mayne (2005):

> *In-situ and laboratory testing provide complementary data for the site characterization of geomaterials. Reference values are provided by the lab measurements, but require high-quality sampling and are obtained only at discrete points at high cost. The in-situ data are collected quickly and continuously, but need calibration for interpretation.* – Mayne (2005)

Obviously/Naturally, the CPTU is an important tool for geotechnical designers. However, upon sounding through layer transitions, CPTU-readings are obscured, neither reflecting the soil properties of the upper- nor lower laying layers. The obscurity aggravates for thin interbedded layers, where the characteristic values of the interbedded layer may never be approached.

This is the background of the ongoing research program at NTNU, where a large-scale model testing facility has been set up to investigate the possibilities and limitations of the CPTU-method related detection of thin layers of clay in sand deposits, and associated determination of soil properties. The testing chamber of ca. 1,5 meter height consist of manhole rings og 1,2 meter in diameter. It can be defined as a semi-calibration chamber, as the chamber sample can be pressurized vertically from the top of the sample.

The master's thesis work has involved further development of the testing facility, and data acquisition by conducting experiments. The latest advancement of the research program involved replacement of the pottery clay by natural sensitive clay samples from the research site at Tiller-Flotten. Tiller-Flotten is one of five Norwegian Geo-Test Sites (NGTS) and a acts a benchmark for quick-clay deposits, rendering it possible to compare and correlate data from the lab-experiment and already acquired high-quality data.

1.2 Objectives

The objectives associated to the master's thesis were as follows:

1) Refine chamber sample construction with respect to sample quality and workload.
2) Produce data which can be further used in assessment of the thin layering effect.
3) Attempt to use quick clay in a chamber sample, as to progress the research program towards emulating as realistic conditions as possible.

a) Assess soundings and supplementary laboratory test results with respect to reference site.

4) Utilize different combinations of chamber sample settings, as to investigate the opportunities associated the current experiments. This includes testing chamber samples with variations of stress levels and preparing chamber samples with various material arrangements, that being differently compacted sands, pottery- and natural clay and using different clay layer thicknesses.
5) Utilize another sized piezocone penetrometer, to assess the scaling effect or "the scale ratio factor".
6) Look upon assumptions and limitations associated the chamber experiments:
    i) Assess stress situation in chamber with respect to the silo effect.
    ii) Identify possibilities and limitations in detection of thin clay layers in sand and determination of the layers' associated soil properties using the CPTU-tool.

1.3 Structure of thesis

The literature in this thesis is partly divided in two. Firstly, the theoretical framework regarding the nature of the experiments is presented in ch. 2. The following chapter, ch. 3, gives a description of the natural clay utilized in the experiments.

The theoretical frameworks review the sounding method and its application, weighting the possible parametrizations used in CPTU-assessment. Furthermore, some elements which may influence the experimental CPTU-readings are looked upon. The second part of the literature contains a general summarize of the conditions at the sample extraction site with associated data acquisition. In addition, this chapter will to some extent regard the implicit effects of using quick clay samples in the model chamber.

As the majority of this thesis revolves around laboratory works and further development of the experiments, the methodology regarding the experiments is quite comprehensive and shown in entirety in the main text, see ch. 4. The experimental results are also shown in its entirety in the main text as these results namely were the main part of the thesis, see ch. 5. The results are discussed in ch. 6. Some conclusions and recommendations for further work are given in the last chapter, ch. 7. In the Appendices some complementary information is presented, which might give a further insight in the works or the results.

Regarding the structure of citation, a Reference list is included, while no bibliography is included. Secondary sources are specified, and not included in the reference list. If secondary sources are of interest, it is referred to the reference list of the primary source. None of the figures include references in the text, not as to discredit any creators, but rather to enhance readability. Instead, references are given in the Figure list found at the end of the thesis. The same applies for some of the presented tables, see Table list.

1.4 Definition of terms

To be concise, the sample elements have been quite descriptively labelled, and a reference system for the chamber is presented in ch. 4.2.1.

The term *the research program at NTNU* describes all of the work related to the masters' theses on the large scale model testing. I.e., inclusive literature studies, interpretation works and development or refinement of new data treatment methodologies. In lack of a better phrasing, the term *the encompassing experiments at NTNU*, or simply, *the encompassing experiments*, is used to describe the collection of experiments: from Hammer's thesis work (2020); the project- and master's thesis work this academic year (2020-2021); and possibly, future experiments on the subject.

The experiment from the project thesis is labelled as "experiment 0", as to differentiate from the experiments in the master's thesis, which are labelled "experiment 1a, 2 and 3". All of these four experiments are labelled *the current experiments*. The specific notation "1a" will be explained in ch. 4.2.3.2.2. Hammer (2020) labelled his experiments as case A and B. In this

thesis, these letters will be replaced by numbers, to be more concise. Typically, the notation in the graphs will have an initial index for the reviewed experiments, abbreviated to: E0, E1a, E2 and E3; and HBH1 and HBH2. For future experiments, it is recommended that the notations of the current experiments are changed to HS0, etc. The samples built into the chamber will be labelled as *chamber samples*.

Whenever a "primary" parameter is followed by a parenthesis in the text, it means that it is a function of what is inside the parenthesis. The mentioned secondary parameters may be an excerpt, or all secondary parameters are included. An example is $\gamma(\rho_s, n)$, which mean that γ relies on both ρ_s and n. If a parameter is related to another, by unknown or not mentioned expressions, the notation is typically $p_{prim} \sim p_{sec}$, not to be mistaken as "proportional to", as used in some literature.

1.5 The current experiments

The current experiments are divided in four:

- The first experiment, experiment 0, was meant to give familiarity with the study and the experiment procedures. Moreover, the experiment was meant to replicate the last experiment by Hammer, as to check the conformity between the new set-up in the new laboratory with the old set-up.
    - This experiment was followed by a load-test with the load application framework.
    - Excavation was first commenced after the project thesis was delivered.
- The succeeding experiment, 1a, included soundings respectively in sand exclusively, and in a very thick layer of clay. The motivation was two-folded: To test a new build-in procedure for sand, and to describe each of the materials separately, as to obtain a better reference for comparisons in data treatment.
    - In this test the imposed load was higher during soundings.
- In experiment 2, different stress levels were tested for equal layering profiles, with primary and secondary soundings performed in a combination which enabled better assessment of secondary soundings. New and old layer thicknesses were utilized.
- In experiment 3, the pottery clay was replaced by quick clay extracted from the Flotten research site. Moreover, the imposed load on the chamber sample was high. The three previous experiments can be regarded as preliminary to experiment 3.
    - This experiment gave the project a new dimension: Enabling comparison between experimental results up against various field- and laboratory results associated the sample material.
    - A new probe was utilized.
        - Layer thicknesses sounded by this probe were normalized with respect to its diameter.

1.6 Limitations

The limitations regarding the nature of the experiments are elaborated in ch. 4.4. A summarize of the most important limitations, both methodological and conceptual ones are listed below:

- The chamber samples utilized to describe the thin layering phenomenon do not reflect the structure of natural deposits.
    - The transitions are very sharp, and each layer are relatively homogeneous compared to natural deposits, considering grain size distribution and other soil properties.
    - The sensitivity of the pottery clay is extremely low as compared to most Norwegian natural clays.
- The desired sample structure is not obtained perfectly:
    - The desired chamber sample should consist of homogeneous sand, this is not the case.
    - There remain some uncertainties regarding the natural clay samples' properties during soundings.
- Regarding stress level in the chamber:
    - Due to sensitivity drifting of the pressure cell readings, the presented stress states for each chamber sample cannot be stated as certain.
    - The horizontal stresses working on the chamber walls remains generally uncertain, as the vertical pressure cell drifted excessively.
- There are multiple factors affecting the soundings, yet these are never corrected:
    - The soundings are performed in proximity of each other.
    - They are affected by the chamber boundary conditions.
    - They are performed with reduced penetration rate as compared to branch practice. (Marginal effect)

Generally, it has been attempted to present a complete examination of the laboratory experiments and results, but due to the disproportionality associated with the labour disposition, the are some shortcomings to the written master's thesis:

- E.g., there are a lot of details from the methodology that are not described (however, many of these may be excessive to most readers).
- Only an excerpt of the most important results is shown, and some desired treated data results regarding the thin layering assessment is lacking.
    - I.e., some details may be missing, and the results could have been further processed, in the pursuit of more and possibly new knowledge about the phenomenon.
- The background data from Flotten used in the assessment of both sample quality and CPTU-parametrizations, are not presented in entirety. And the assessment or comparison is rather coarse.

The disproportionality stem from:

- The laboursome experiments with their meticulous progressions (in the pursuit of as good results as possible).
    - Finalized 11th of May.
- The large effort laid in the parametrization of CPTU-results, also demanding interpretation work on the data from Flotten.
- Lastly, excessive literature study (which was driven by the pursuit of better understanding of elements associated with the experiments, and the pursuit of higher academic integrity of the thesis).

Despite the shortcomings, the outcome of the thesis laboratory work is fortunately good. The work has been performed thoroughly, with emphasizes on making it verifiable and systematized, so it should be easier for e.g., succeeding participants of the research program to gain further output from the results.

2 Theoretical framework

The work in this master's thesis is primarily consisting of building chamber samples, performing soundings, and treating the produced data. It is therefore of interest to present in detail which formulas and relations that have been utilized, as to make the work more verifiable. This may appear excessive, but it describes the level of detail at which the computations have been made, and thus, how accurate the presented treated data results are. A well elaborated theory may also be of interest to future master students continuing the project associated with the current experiments at NTNU.

2.1 The sounding equipment

This chapter is presenting some preliminary theory of cone penetration testing, concerning terminology and relations, which moreover is the foundation for the data treatment of lab results.

The *cone penetration test*, CPT, is designed to find layering profile, identify soil types and estimate associated mechanical properties in the different soil layers. It is among the most reliable field investigation methods in use, and may be the most accurate method of sounding, as measurements are made at the probe and data is not disturbed by side friction acting on the rods (NTNU Geoteknikk, IBM, 2017). There exist many versions of the sounding method, the most basic edition has a probe consisting of a friction sleeve and a solid coned tip. The probe is referred to as a *cone penetrometer* and sometimes the test itself, CPT, is referred to as a *cone penetrometer test*. The cone penetrometer is placed at the end of a series of rods which are pressed into the soil at a constant speed of 20 ± 5mm/s according to standards (CEN, 2012). Measurements are made of *stresses acting on the cone*, q_t, and *stresses acting on the frictions sleeve*, f_s, at the probe, with pressure cells. The test has been refined since it was first developed, and many variants of the test have later been invented with supplementary tools that measure e.g., pore pressure, inclination of probe, seismic waves (compression and shear waves), resistivity/conductivity, temperature and many other supplementary measurement methods which are less common ('Cone penetration test', 2020).

Cone penetration testing with pore pressure measurements have different kinds of abbreviations and associated denotations, but they all represent the very same equipment and method. E.g., CPTu is short for *cone penetration test with pore pressure measurement* (Lunne et al., 1997, p. 1), where the u denotes the *pore pressure* that is measured, CPTU is short for *cone penetration test undrained* (Solberg, 2019), or PCPT which is short for *piezocone penetration test* (Lunne et al., 1997, p. 1). A probe with a pore pressure sensor installed is called *piezocone penetrometer*. The pore pressure sensor can be placed at 3 standard locations where *the measured pore pressure*, u_i, at each location has its own notation: at the cone tip, u_1, behind the cone, u_2, or behind the friction sleeve, u_3, see *Figure 2.1.* Multiple locations are also possible, but this would be for rather niche purposes. The recommendation of placement of the filter according to international standard (CEN, 2012) is behind the cone u_2. The most

broadly used composition of tools as of today is CPTU with pore pressure filter at u_2, inclinometer and potentially a temperature sensor.

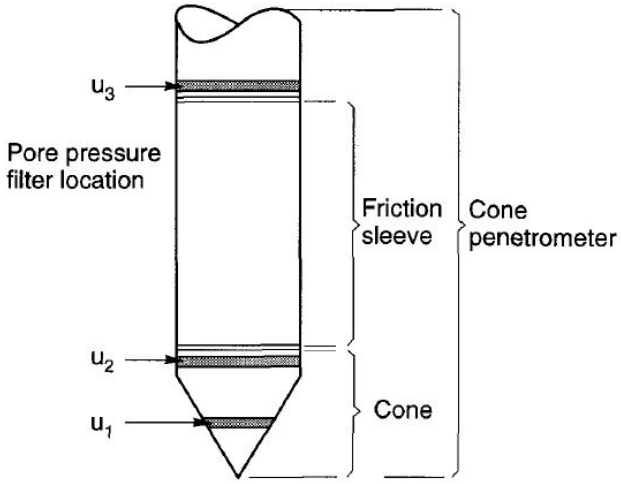

Figure 2.1. Sketch of piezocone penetrometer with different possible locations of pore pressure sensors/-filters.

Today there exist probes which transmits data made with either acoustic or electrical signals (through interior cable). For the wireless solution, audio signals are sent through the rods and are recorded at the drilling rig where the results are recorded by a microphone, and stored on a PC. Another alternative is to record and save readings on a back-up logger if it is installed. The logger stores the raw data, meanwhile data transmitted to the computer at the rig typically is treated before it is saved. This point is quite essential for the experiments performed in this research project, as some data-treatment algorithms interpolate points in a manner which may misrepresent the results to some extent. Thus, for the topic of the thin layering effect this aspect is of importance, reference is made to ch. 4.3.

2.1.1 Equipment geometry

In accordance with international standard (CEN, 2012) the 1000 mm² piezocone penetrometer components shall have dimensions according to following rules:

Cross-section diameter of:	
Cone	$\boldsymbol{d_c} = 35{,}7 \pm 0{,}4$ mm
Friction sleeve	$\boldsymbol{d_{f_{sleeve}}} = d_c$, with a tolerance of 0 to +0,35 mm
Filter at position u_2	$d_{f_{sleeve}} - 0{,}2 \leq \boldsymbol{d_{filter}} = \boldsymbol{d_{u_2}} \leq d_{f_{sleeve}}$, simultaneously as $d_c \leq \boldsymbol{d_{u_2}} \leq d_c + 0{,}2$
Pushing rods	$\boldsymbol{d_{rods}} = d_c$, for the at least 400 mm measured from the base of the cone

Cross-section area of:	
Cone	$\boldsymbol{A_c} = 1000$ mm²
Friction sleeve	$A_c \leq \boldsymbol{A_{f_{sleeve}}} \leq A_c + 21$ mm²

Length or height of:	
Friction sleeve	$132{,}5 \leq \boldsymbol{l_s} \leq 135$ mm
Cylindrical part of cone	$24 + 0$ mm $\leq \boldsymbol{h_c} + \boldsymbol{h_e} \leq 31{,}2 + 5$ mm

Outer surface area of:	
Friction sleeve	$\boldsymbol{A_{sleeve}} = \boldsymbol{A_s} = 15000$ mm²

The cone angles shall be 60°.
Dimensions of the cone and the friction sleeve are shown in *Figure 2.2* as illustrated in the standard, where 1 and 2 denotes limitations of cone geometry respectively for worn cones and fabric new cones.

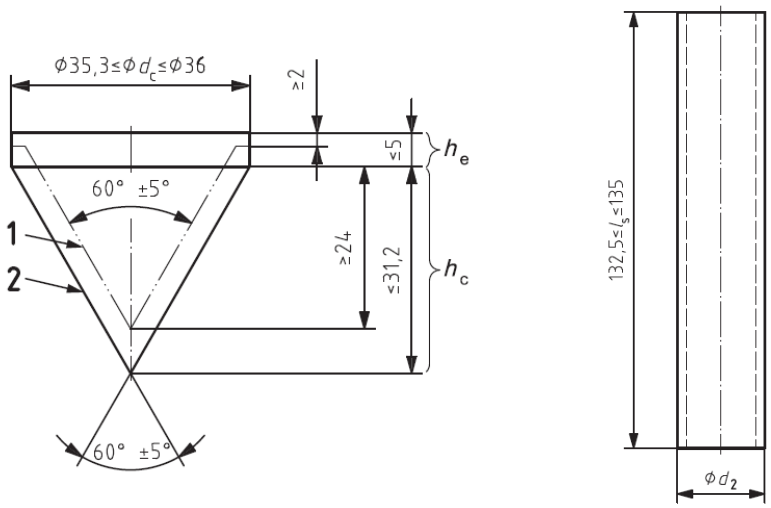

Figure 2.2. Geometry of cone (left) and friction sleeve (right).

Regarding other versions of probes, $A_c \neq 1000\ \text{mm}^2$, the geometry of the cone should be adjusted proportionally to the diameter. For other parts, as e.g., push rods and friction sleeve, the adjustment should preferably have the same proportionality, with some varying requirements of maximum allowed deviation (CEN, 2012). It is emphasized that the usage of cones with $A_c \neq 1000\ \text{mm}^2$ should always be stated.

2.1.1.1 Other specifications

According to the standard the penetration rate, v, shall be set to $20\text{mm/s} \pm 5\ \text{mm/s}$. Changes in speed gives different reference levels for the S_u, as this parameter depends on the strain rate. The topic of rate effects is elaborated in sub-ch. 2.2.

2.1.1.2 Uncertainties

The standard (CEN, 2012) mentions several sources of error or uncertainty: Temperature effects, poor or lacking saturation, zero-/sensitivity shift, deviation of geometry, etc. Lunne et al. (1997, p. 124) could tell that, in general, different probe sizes had little effect on measured stresses, as long as they are corrected, as will be explained in the following sub-chapter.

2.1.2 Formulas and physical relations

The formulas and physical relations regarding CPTU-parameters are presented in this sub-chapter. *The side friction*, f_s, is the product of *the total force acting on the friction sleeve*, F_s, divided by *the surface area of the friction sleeve*, A_s, *eq. {2.1}*. *The cone resistance*, q_c, is a result of *the total force acting on the cone*, Q_c, divided by *the cross-section area at the base of the cone*, A_c, eq. {2.2} *1.* Something that should be reckoned is that the measurements are done over some vertical length for each component, thus the results are the average of forces acting on the components' lengths. This may not be a drawback regarding sounding in thick layers of homogenous soil, but for transitions between materials this influences the results. Sounding readings provide f_s, q_c, and u_i directly, still, nonetheless, eq. {2.1} and {2.2} were included as they tell something about the principles of the sounding method.

$$f_s = \frac{F_s}{A_s} \qquad \{2.1\} \qquad\qquad q_c = \frac{Q_c}{A_c} \qquad \{2.2\}$$

The parameters f_s and q_c can be furthermore refined, where factors which affect the measurements and give "untrue" results are considered. E.g., to find the total stresses that the soil acts on the cone, the water pressure that acts on the cone on its backside, specifically in the gap between the cone and friction sleeve, must be subtracted. This is done in eq. {2.3}, where a denotes *the unequal area ratio* and q_t is *the corrected total cone resistance*. Henceforth the term q_t is for simplification denoted *cone resistance*, as this is the parameter of interest instead of q_c. It should be noted that the mentioned "a" only is used in eq. {2.3}, and any other expressions containing a, is regarding *attraction*. The mentioned effect is typically little for small-to-mediate pore pressures. To correct the side friction in an equivalent manner a second

1 - The resulting force includes the subtracting factor of water pressure behind the cone as elaborated related q_t.

pore pressure sensor must be installed behind the friction sleeve at position u_3. The advantage of having corrected measurements is obviously that the values are of correct magnitude, but another important fact is that the results now should be quite similar independent of what cone penetrometer is used (Lunne et al., 1997, ch. 3). A further note is that the side friction is often regarded as less reliable because of the sleeve's geometry with its implicit averaging effect, its dependency on placement, and lastly, its dependency on the geometry of the cone and the filter ahead of it (NTNU Geoteknikk, IBM, 2017; Lunne et. al. 1997). Thus, as the tip resistance is the most reliable and descriptive parameter, the standards recommendation to use u_2 becomes obvious, as this provides the opportunity to correct q_c, which in addition gives comparable results. A downside of using u_2 which Lunne et al. (1997, ch. 5.1.4) mentioned, was that transitions from one layer to another was less clear if the pore pressure sensor was placed behind the cone, u_2, as compared to at the tip, u_1.

$$q_t = q_c + (1 - a) \cdot u_2 \qquad \{2.3\}$$

2.1.2.1 Stress situation

The stress situation in the soil is pertinent upon assessing CPTU-soundings. The force needed to push the probe becomes greater with greater stress level in the soil. To achieve a more coherent reference level upon assessing soil characterisation, the cone resistance can be normalized with respect to *the total overburden stress*, σ_v, giving *the net cone resistance*, q_n or q_{net}, see eq. {2.6}. The estimation of σ_v in eq. {2.4} is based on *the unit weight,* γ, which typically is averaged for either sections or the entirety of depth profiles. In this thesis some simplifications are made, e.g., the weight contribution from the clay and the sand is assumed equal. γ_{sand} is for each test based on eq. {2.5}, where *the saturation,* S_r, is assumed 100% regardless of groundwater table, as it is typically close to the surface during the tests. The comprising parameters *the dry unit weight,* γ_d, and *the porosity*, n, is found during each excavation.

$$\sigma_v = \gamma \cdot z \qquad \{2.4\} \qquad \gamma = \gamma_d + n \cdot \gamma_w \cdot S_r \qquad \{2.5\}$$

$$q_n = q_t - \sigma_{v,0} \qquad \{2.6\}$$

Further, for depths greater than the groundwater table, $z > z_w$, the effective stresses, σ_i', are of interest. σ_i' are independent of stress plane evaluated and are given by eq. {2.7}. The ground water pore pressure, u_0, is for hydrostatical conditions given by eq. {2.8}. At some locations there may also be a difference in energy potential in the groundwater, i.e., the water has a gradient, i. This condition is typically found in for example uneven terrain. If there is a gradient, it can be approximately constant with depth, or otherwise varying. For gradients that are constant with depth, the first line of equation in {2.9} describe u_0. Meanwhile, for i varying with depth, the formulation is expanded to include the succeeding lines of equations for each time the gradient, i_i, changes. The notation z_w equals the water table, meanwhile consecutive $z_{w,i}$ denotes depth of change for gradient. The concept is visualized in *Figure 2.3*. The assessment of field soundings in the appendix is based upon u_0 from eq. {2.5}.

$$\sigma_i' = \sigma_i - u_0 \qquad \{2.7\} \qquad u_0 = \gamma_w \cdot (z - z_w) \qquad \{2.8\}$$

$$u_0(z) = \begin{cases} \gamma_w \cdot (1 \pm i_1)(z - z_w), & z \geq z_w \\ \gamma_w \cdot \Big((1 \pm i_2)(z - z_{w,2}) + (1 \pm i_1)(z_{w,2} - z_w)\Big), & z \geq z_{w,2} \\ \dots, & z \geq z_{w,3} \end{cases} \quad \{2.9\}$$

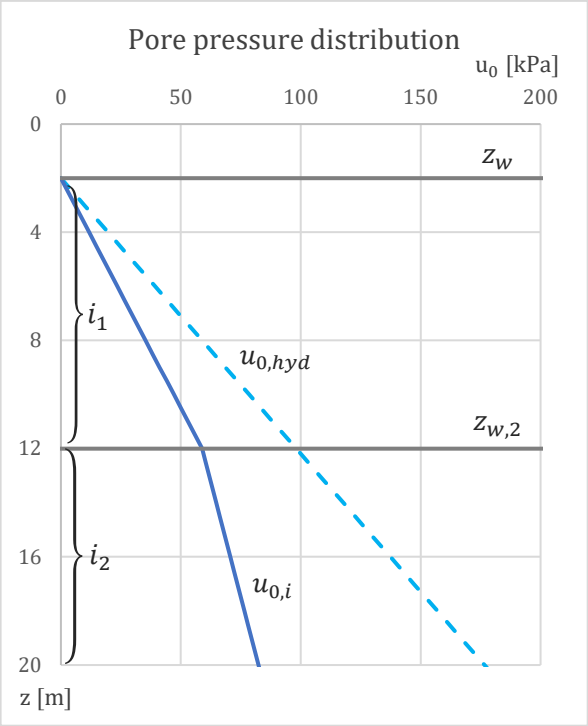

Figure 2.3. Visualizing an arbitrary pore pressure distribution.

The last parameter describing the stress situation is *the effective lateral stress*, σ_h', which is typically expressed proportional to the vertical stress, σ_v', where the ratio between them is defined by the earth pressure coefficient, K', eq. {2.10}. This ratio is depending mainly on stress history, and chemical- and structural composition (Lindgård & Ofstad, 2017, p. 34, Lefebvre et al. 1991, p.1). The ratio can be approximately constant with depth for normally consolidated soils, meanwhile it is typically varying with depth for overconsolidated soils. The natural clay utilized in this thesis work, originating from Tiller-Flotten, possess the latter property, as illustrated in the extensive site characterization made by L'Heureux et al. (2019). The lateral earth pressure coefficient will be further reviewed in ch. 2.4.1.4.

$$\sigma_h' = K' \cdot \sigma_v' = K' \cdot \gamma' \cdot z \quad \{2.10\}$$

A remark regarding the stress situation is that calculations are based on horizontal layers of homogenous masses and an even terrain surface. The overburden solutions presented are thereby neglecting any stress dissipation with depth due to frictional interaction with e.g., bedrock, different inclined soils, walls or otherwise imposed stress anisotropy etc. Both the sub-chapter 2.4.1 and sub-ch. 6.2.

2.1.2.2 Water pressure

The penetration process may increase the pressure in the water that surrounds the probe depending on the permeability of the medium that is sounded. This increase in pressure is denoted as *the excess pore pressure,* Δu_2, and it is estimated by eq. {2.11} which in turn is based on eq. {2.8}. For highly permeable soils as for example loose sand, the medium will act drained and no or little, extra pressure is induced in the water. Pore pressure measurements, u_i, in such mediums give the actual ground water pressure, u_0 (with associated equipment accuracy). On the other hand, for low-permeable soils such as silts, clays and dense sands, the water pressure increases significantly as the water cannot dissipate through the pores fast enough to escape its host-medium before it is penetrated. These soils are described as undrained, and how "undrained" these materials acts are depending on their permeability and the rate at which deformation is imposed. For intermediate permeable soils such as silts and dense sands the response in water pressure induced by sounding is dependent on the choice of penetration speed (Lunne et al. 1997, ch. 5.8.3). For dilating silt, the pore pressure may be reduced beyond u_0 during penetration, i.e., $\Delta u_2 < 0$. For idealized fully undrained materials, no volume change is undergone upon applied stress, due to the incompressibility of water (Nordal, 2020, p. 84). In *Figure 2.4* some of the presented relations are illustrated, note that Δu_2 is written as Δu_T and u_2 as u_T.

$$\Delta u = \Delta u_2 = u_2 - u_0 = \Delta u_{excess} \qquad \{2.11\}$$

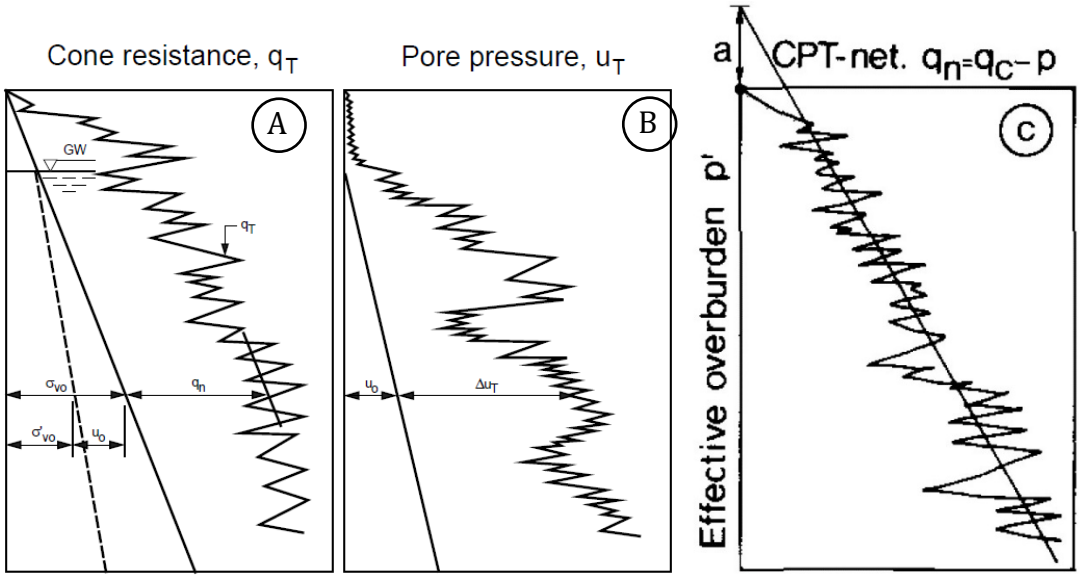

Figure 2.4. CPTU-profile with associated parameters and relations, including interpretation of attraction ©.

2.1.2.3 Other normalized relations

Several dimensionless measures have been suggested to characterize the soil stratigraphy with CPTU-parameters. Such measures are *the pore pressure ratio,* B_q, *the normalized tip resistance,* Q_t, and *the normalized friction ratio,* F_r, which all are shown with their formulas in eq. {2.12}, {2.13} and {2.14}. The latter is also sometimes referred to as *the net friction ratio,* R_{fn}. The measures are normalized, which means they are intended to eliminate the effect of

the in-situ stress level on the measured parameters. Consequently, these operations require acquisition of supplementary field data, e.g., measurements of u_0 with piezometer and estimation of the vertical stress by weighting soil samples. These parameters can also be approximated using experience data from other sites or tables found in literature, though this would only give approximate results. With the normalized parameters calculated, it only remains to insert them in charts which are supposed to automatically, and roughly, identify soil type and behaviour, e.g., Robertson diagrams (1990), see *Figure 2.5*.

$$F_r = \frac{f_s}{q_t - \sigma_{v,0}} \cdot 100\% = \frac{f_s}{q_n} \cdot 100\% = R_{fn} \qquad \{2.12\}$$

$$B_q = \frac{u_2 - u_0}{q_t - \sigma_{v,0}} = \frac{\Delta u_2}{q_n} \qquad \{2.13\}$$

$$Q_t = \frac{q_t - \sigma_{v,0}}{\sigma'_{v,0}} = \frac{q_n}{\sigma'_{v,0}} \qquad \{2.14\}$$

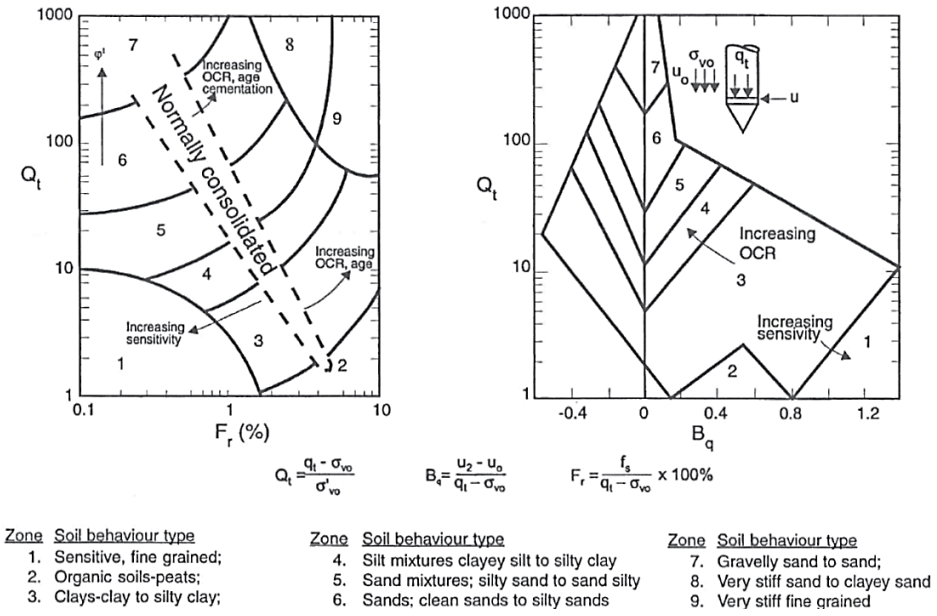

Zone	Soil behaviour type
1.	Sensitive, fine grained;
2.	Organic soils-peats;
3.	Clays-clay to silty clay;
4.	Silt mixtures clayey silt to silty clay
5.	Sand mixtures; silty sand to sand silty
6.	Sands; clean sands to silty sands
7.	Gravelly sand to sand;
8.	Very stiff sand to clayey sand
9.	Very stiff fine grained

Figure 2.5. Robertson-diagrams with associated categories of materials.

Considering that during a sounding, the soil is pushed sideways around the tip, and in addition, there is a confining pressure working on the friction sleeve, it would be of natural interest to include the horizontal stress in the normalization assessment. However, $\sigma'_{h,0}$ is per now not considered, due to the technical difficulties in obtaining this information (Lunne et al. 1997). The latter assertion should still be up to date, 24 years later, with reference to the thesis of Lindgård & Ofstad (2017) in which the topic of $K'/\sigma'_{h,0}$ were thoroughly investigated. They acquired both field- and laboratory data from the research site Flotten (see ch. 3.1), but experienced large scattering, also when applying correlation methods.

Houlsby & Hitchman (1988) found that for CPT-tests in calibration chambers filled with sand, "the tip resistance is substantially dependent on density and horizontal stress". They also implied that q_t was independent of the vertical stress, not taking into consideration that σ'_h was different in each test they performed. Even though this claim possibly is a bit faulty, an important reflection can be drawn; q_t is more depending on the horizontal stress and the density, than σ'_v. Thus, obtaining information on σ'_h and implementing it into the normalization assessment would be of great interest.

Robertson & Wride (1998) could tell that the normalized tip resistance, Q_t, can be corrected further, for more precise classification if the terms *the effective stress exponent*, n, and *the reference pressure*, p_a, are added as in eq. {2.15}. The regular Q_t, from eq. {2.14}, is accordingly based on a linear stress exponent, i.e., $n = 1$. For characterization of sandy soils, $n = 0{,}5$ is recommended, while for clayey soils $n = 1$. Further instructions are given in the article, where n is adjusted according to *the soil behaviour type index*, I_c, in an iterative procedure (Robertson & Wride, 1998, p.8/449). If the penetration depth is low, i.e., the stress level is low (50-150 kPa), then the choice of stress exponent is rather insignificant.

$$Q_{tn} = \left(\frac{q_n}{p_a}\right)\left(\frac{p_a}{\sigma'_{v,0}}\right)^n \qquad \{2.15\}$$

The Robertson-diagrams (Robertson, 1990) presented on the previous page gives guidance about which layering the sounding profile may have, but they are not flawless, as they do not account for the patterns related to the pertinent parameters, specifically transitions between two or more layers. Last year, Hammer (2020) included a diagram with input from his experiment, which is shown in *Figure 2.6*. As can be seen in the plot, the transition from one material to another is not shown as a sharp turn of values giving the correct materials, instead the parameters climb steadily towards the characteristic value of the thin-layered material. As can be expected, for a specific material, the datapoints move nearer the characteristic one, proportionate to the layer thickness. For thick layers of homogenous soils, the charts should be quite accurate. In addition, every survey area is more or less unique, with respect to materials, packing, mineralogy etc., so empirical correlations should always be reviewed with a certain scepticism. It
should be kept in mind that the different parameters are measured at different positions on the probe. Thereby, to acquire the most accurate representation of the sounding profiles,

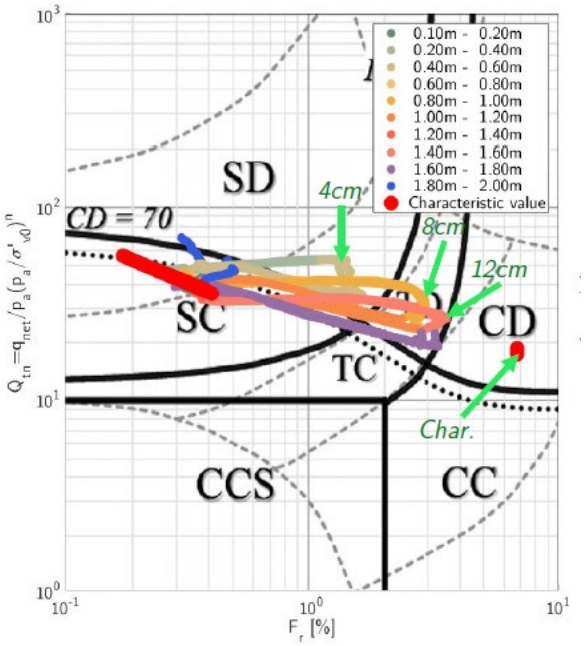

Figure 2.6. Robertson classification chart (2016-version) with F_r & Q_t, with input from experiment done by Hammer (2020) which is sorted colour-wise based on depth.

the pore pressure and the side friction should be corrected vertically in the graphs, according to their relative position compared to the cone. To clarify, while the pore pressure is geometrically corrected for each data point, the pore pressure reading used for correcting the tip resistance should be time-wise nearest to the tip resistance-reading, not geometrically.

2.1.2.4 The NGI-99 approach

The expected tip resistance in sand is reliant on relative density, among other parameters. The stress state is of importance, and as mentioned, many have correlated q_t in sand to the vertical effective stress, but many researchers have pointed out that indeed, the horizontal- or mean effective stress would be more correct ((Al-Awkati & Vesić, 1972, Vesić, 1973, Al-Awkati, 1975; as cited in Vesić, 1977, ch.3), Houlsby & Hitchman, 1988, Lunne et al. 1997, p. 83). However, as already mentioned, the horizontal stress is typically difficult to obtain (Lindgård & Ofstad, 2017), so Clausen et al. (2005) proposed an empirical correlation between q_t and D_r based on $\sigma'_{v,0}$ given by eq. {2.16}, named the *NGI-99 approach*. This expression does in a large degree resemble the equation of Baldi et al. (1986, as cited in Lunne et al. 1997), except that the different soil constants were altered and atmospheric pressure, $\sigma_{atm} = 100$ kPa, was added in the equation. In the displayed results in ch. 5.1, the constant of 22 in the denominator is typically replaced by some other value to conform better with the conducted density samples. From now on, this empirical constant is denoted k_{2,D_r}, meanwhile the constant of 0,4 may be denoted k_{1,D_r} even though this is never changed. The reason to alter the expression below, is due to e.g., the boundary effects of the chamber, the particular stress distribution in chamber and influence of other performed soundings in the vicinity.

$$D_r = 0{,}4 \cdot \ln \frac{q_t}{22 \cdot \sqrt{(\sigma'_{v,0} \cdot \sigma_{atm})}} \qquad \{2.16\}$$

In addition to previous mentioned effects, Robertson & Campanella (1983b, as cited in Lunne et al. 1997) pointed out that in addition to q_t's dependence on relative density and effective stress, the compressibility of the sand altered q_t too, showing that different sands yielded different q_t-values given the same $\sigma'_{v,0}$ and relative densities. Furthermore, Lunne et al. (1997, p. 85) emphasized that q_t may not reach its full value within a thin layer of sand, and by such, correlations revolving q_t should be revised with care.

2.2 Rate effects

Due to the encompassing experiments' nature, it is of interest to obtain the largest possible numbers of readings per meter penetrated. Considering that the reading frequency of the equipment cannot be altered, the penetration rate has been set to 15 mm/s, equal to the lower limit of the standardized range of 15-25 mm/s (CEN, 2012). According to Lunne et al. (1997) readings laying in the standardized range were deviating little. However, as most representative results are of interest, the impact of the choice was investigated further.

Meca (2004) could tell that Casagrande & Willson (1951, as cited in Meca, 2004) suggested a hypothesis for the cause of the rate effect on S_u, linking it with the excess pore pressure, Δu, generated under undrained loading. He reported that several other researchers had acquired data which supported this hypothesis (Bjerrum et al. 1958, Crawford, 1959, O'Neill, 1962, as cited in Meca, 2004). Lunne et al. (1997, p. 47) could tell that in addition to the dominant effect of pore pressure on rate effects, occurrence of particle crushing, and creep effects alter the rate effect too.

Lunne et al. (1997, ch. 5.8.3) could further specify that rate effects experienced in clay was linked with mainly two factors, "dissipation" or "drainage effects", and viscosity. For low penetration velocities, v, the failure mechanism would be of a more drained nature. As v is increased, the water is trapped, i.e., it dissipates slower than the load is imposed, and the condition can be described as *undrained*. Due to the water's incompressibility, the imposed pressure will be transmitted to the water, reducing the effective stresses between the grains (NTNU Geoteknikk, IBM, 2018, p.78). This will decrease the medium's strength, reducing q_t. Upon further increase of v, q_t is more and more dominated by viscous forces, exceeding the reduction of strength experienced by the soil, due to loss of effective stresses. The path of q_t is shown in *Figure 2.7*.

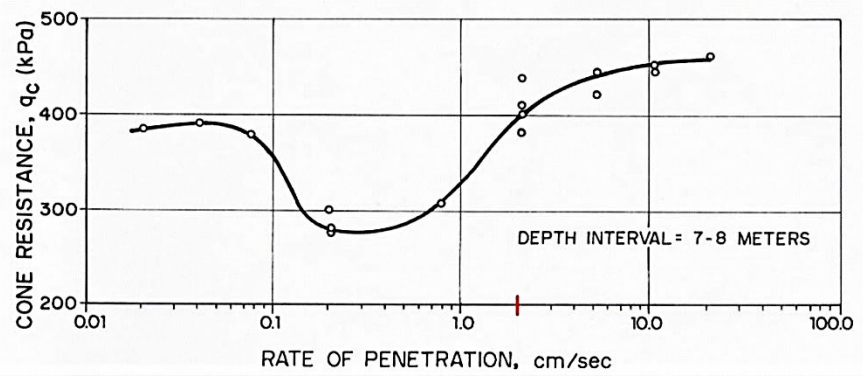

Figure 2.7. Rate effect on q_t for a lightly overconsolidated varved clay (Bemben and Myers, 1974, as cited in Lunne et al. 1997). Penetration rate 2 cm/s is marked with red.

In the 70-ties Dayal & Allen (1975) conducted an experimental model test with a CPT (modern standard 10 cm^2-probe), to assess the penetration rates' effect on measurements of q_c and f_s. They filled a barrel with one material type for each test: This included loose- and dense silica-sand, and remoulded pottery clay with different stiffnesses based on water content. The clay had following consistency properties: $w_P = 21\%$, $w_L = 37\% \Rightarrow I_P = 16\%$. Their materials were thus quite similar to those utilized in this thesis work, and the magnitude of influence caused by penetration rate is expected to correlate well for the experiments associated this thesis.

The two found that the measured q_c in the pottery clay was proportional to the logarithmic penetration rate with a proportionality constant they defined as K_L - the soil viscosity coefficient. This coefficient was depending on the soils' strength, $S_u = S_{u,r}$ (which again was depending on the water content), and it was increasing for decreasing shear strength. Their interpretation was based on measurements at depths greater than the critical depth, which they defined as $z_c > 4d_c$ (Sanglerat, 1972, as cited in Dayal & Allen, 1975). More information

on the critical depth is presented in the ch. 2.3.3. They formulated an expression, which related an "arbitrary" penetration velocity rate v, with some specific reference value, being the lowest utilized v, denoted v_s. The measured tip resistance q_{cd} at rate v would then relate to q_c (reference measurement at v_s), with K_L as shown in eq. {2.17}. The same applied for sleeve friction, but with K_L of other magnitudes. Some empirical values of K_L obtained in their experiment is shown in *Table 2.1*. They considered their results as valid for 0,13 cm/s up to 550 cm/s for q_c, meanwhile the upper validity limit for f_s was 13,9 cm/s as f_s suddenly increased after this, exceeding the logarithmic proportionality found for lower velocities.

$$\frac{q_{cd} - q_c}{q_c} = K_L \cdot \log_{10}\left(\frac{v}{v_s}\right) \qquad \{2.17\}$$

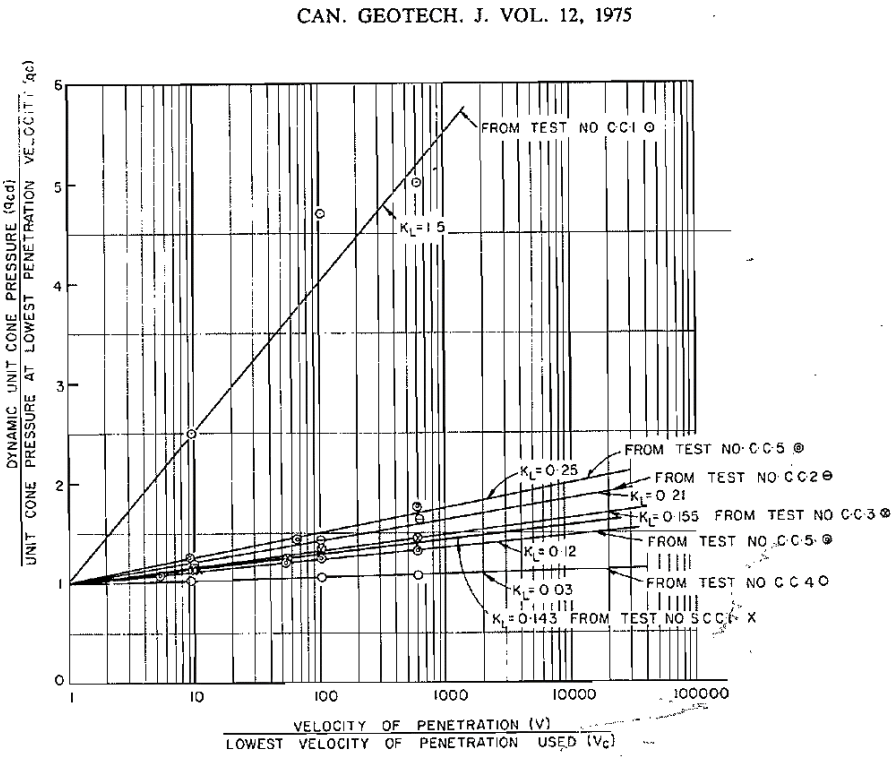

Figure 2.8. Relation between "remoulded undrained shear strength" or "viscosity", and penetration rate.

Table 2.1. Segment of results presented by Dayal & Allen (1975).

S_u [kPa]	$K_L(q_c)$	$K_L(f_s)$
9,5	0,25	$0{,}31 < K_L < 0{,}38$
46	0,21	0,31
51	0,155	0,24
64,8	0,12	$0{,}17 < K_L < 0{,}24$

2.2.1 Impact on the current experiments

2.2.1.1 Rate effects in clay

The weakest sample tested by Dayal & Allen (1975) had $w = 43{,}5\% > w_L = 37\%$ and $S_{u,r} = 3{,}4$ kPa, with a much higher $K_L = 1{,}5$. They reasoned that this sample acted "more like a viscous medium rather than a plastic medium", hence q_t had a greater dependence on the rate effect (Dayal & Allen, 1975). To repeat, the clay samples they used were already remoulded, such that S_u for each sample technically was $S_{u,r}$. Knowing all of this, a rough estimate for rate effects of v can be made for the clays utilized in this thesis experiment, with pottery clay ($w_{pc} = 25\%, w_{P,pc} \approx 20\%, w_{L,pc} \approx 30\%$) and quick clay ($w_{qc} \approx$ 40-50%, $w_{P,qc} \approx 20\%$, $w_{L,qc} \approx$ 30-40%):

For the pottery clay with $S_{u,FC} \approx 35$ kPa, $S_{u,r,FC} \approx 20$ kPa, $K_{L,pc}$ would be ca. 0,225. The rate effect for (v, v_s)=(15-,20 mm/s), would then give a reduction of $q_{c,\mathrm{red}} \approx 2{,}7\%$.

Meanwhile, the quick clay has a much greater span for its shear strength, $S_{u,FC} \approx$ 25-50 kPa and $S_{u,r,FC} < 0{,}5$ kPa, not making it entirely clear what $K_{L,qc}$ is. As the sounding may disturb the material in in front of the probe the experienced tip resistance may become low. Thus, an interval of rate effect is most pertinent to present. In the most conservative case $K_{L,qc}$ would be 1,5, meanwhile it would be quite close to 0,2 if little disturbance in advance was experienced. This would give a range of rate effect on q_t, giving a reduction in the range ca. 2,5%-15,7%, probably nearest 2,5%. So, rate effects are negligible for the pottery clay, while it may have a small impact on the quick clay. The reduction due to rate effects on the side friction would be in the scale of $f_{s,\mathrm{red}} \approx 4\%$ for both clays.

2.2.1.2 Rate effects in sand and silts

From both the literature of Lunne et al. (1997) and the experiment by Dayal & Allen (1975) it was concluded that for sand, there is practically no expected rate effect for quite large differences of v. This is linked with sand being a drained material. The result is that the rate effect graph for sand is basically linear for all speeds assessed in *Figure 2.7*. Silts on the other hand, are regarded as partly drained, something intermediate sand and clay, and thereby probably have a non-linear rate effect profile for the assessed velocities, but this topic have not been investigated further in this thesis.

2.2.1.3 Other

The bearing capacity factors (see ch. 2.3.1) are depending on the determined S_u, which from certain lab tests, e.g., triaxial tests, is obtained by imposing a much slower rate of strain as compared to the strain rate imposed by CPTU-soundings. This gives correlations through the bearing capacity factors some uncertainty. Moreover, using probes with other diameters than 10 cm², v should according to Lunne et al. (1997) ideally be adjusted to account for differences in time to failure. For the "current experiments" this was not done as the ISO-standard (CEN, 2012), specified v to be 20 ± 5 mm/s, not commenting on the use of other probes. As $v_{A_c=10\mathrm{cm}^2}$ from previous experiments was already as low as the standard specified, $v_{A_c=5\mathrm{cm}^2}$ was consequently set to the same.

2.3 Flow mechanisms

The flow mechanism ahead of the cone is depending on the geometrical design of the probe, and the materials which are sounded. The second element is explained in ch. 2.3.4, but in short it mainly concerns the shear strength and stiffness of the soil. The geometrical design of the probe can be imagined through a thought experiment, if the probe is thinner, then the area of soil influenced around the advancing cone becomes smaller. If the cone geometry is more acute, then the probe is in a larger degree dividing the soil instead of pushing it ahead. Thus, a nearly infinite-small probe would not be influenced, in advance, by changes of sounding medium, as the lower layers would not be disturbed by the advancing probe. Hence sharp transitions would be measured according to the resistances of the layers, see ch. 2.3.1.3 and *Figure 2.21* for more information. The effect of the cone geometry on the transition distance, called critical depth (see ch. 2.3.3) is referred to as *the scaling effect*, it has been researched by De Beer (1963) and the relevant theory presented in this, and ch. 2.3.3, is mostly from the retellings of De Beer's research, done by Nottingham (1975).

There have been different approaches as of how to theoretically interpret tip-resistance of CPT-soundings, two main theories are based on different flow mechanisms and are presented in the two following sub-chapters. Sub-chapter 2.3.1 present theory is about bearing capacity which is based on either drained or undrained strength, while 2.3.2 present theory on expanding cavity, based on elastic and plastic response. Combinations of the two may also be utilized. The sketch below, *Figure 2.9* show different approaches of both theories.

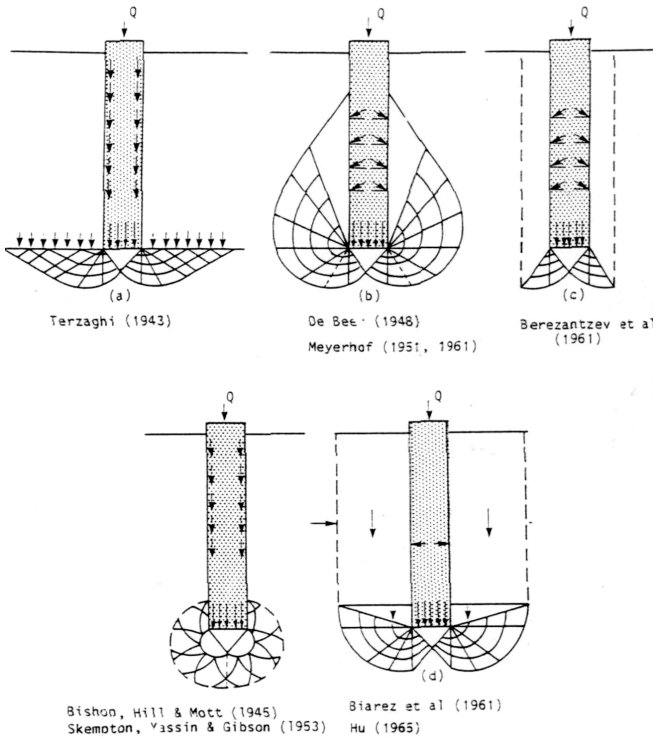

Figure 2.9. Different theoretical frameworks of interpretation, showing concepts of bearing capacity and expanding cavity.

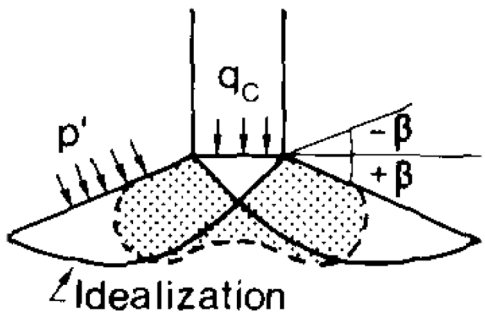

Figure 2.10. Bearing capacity with drained conditions, according NTH-method .

2.3.1 Bearing capacity

When the penetrometer is pressed into soil, a continuous passive failure in the ground is created in front of it. An analogy to a static bearing capacity problem can be made, by dividing this process into several time-frames, see

*Figure 2.*11 and *Figure 2.12*. For undrained loading conditions q_t would be equal to *the ultimate bearing stress* q_{ult}, expressed in eq. {2.18}. $\overline{S_u}$ is here *the average undrained shear strength working along the failure surface*, while N_c is *the undrained bearing capacity factor*. N_c is depending on r which is described as the ratio of *shear stresses transferred between the wall and the soil*, τ, relative to the *shear strength of the soil*, $\tau_c = S_u$. For zero shear interaction (theoretical), $r = 0$, meanwhile for $\tau = S_u \Rightarrow r = \pm 1$ depending on the direction. For a strip foundation on the surface, the plane-strain bearing capacity factor for completely vertical load, becomes $N_c = 2 + \pi = 5{,}14$, with $r = 0$, full explanation is presented in compendium (NTNU Geoteknikk, IBM, 2016, Ch. 7.2).

$$q_{ult} = N_c \cdot \overline{S_u} \qquad \{2.18\}$$

Further, N_c also depends on the horizontal shape, and the term *the bearing capacity shape factor*, s_c, can be introduced as to formulate N_c as a function of the shape: $N_c = N_c^* \cdot s_c$. In most literature, the factor is already incorporated in N_c. For footings, that are circular or squared, N_c becomes approximately 6,14 (Mayne, P.W., 2007, p.51).

So far, only foundations on the surface have been considered, upon pushing the foundation further down, the pushing of soil up on each side is to some extent counteracted by the weight of the side-laying soil. The magnitude of this counteraction is depending on the degree of transition and is illustrated in *Figure 2.12*. This can also be described by a new factor, *the bearing capacity depth factor* d_c, giving $N_c = N_c^* \cdot s_c \cdot d_c$. This factor tells how far a pile or foundation is pushed down, relative to its own diameter, D, and how it impacts the bearing capacity.

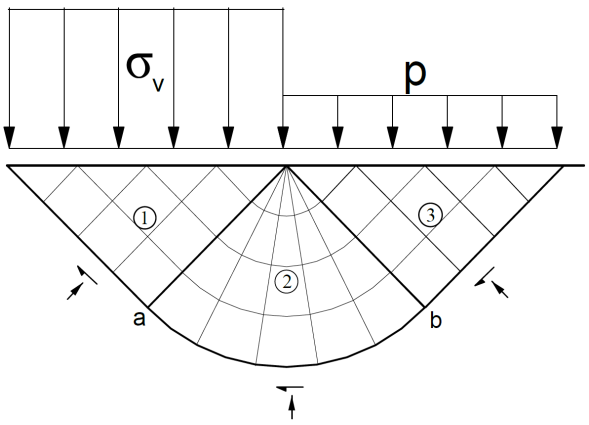

Figure 2.11. The classical bearing capacity case, including the reference pressure, p, that typically is zero at ground level.

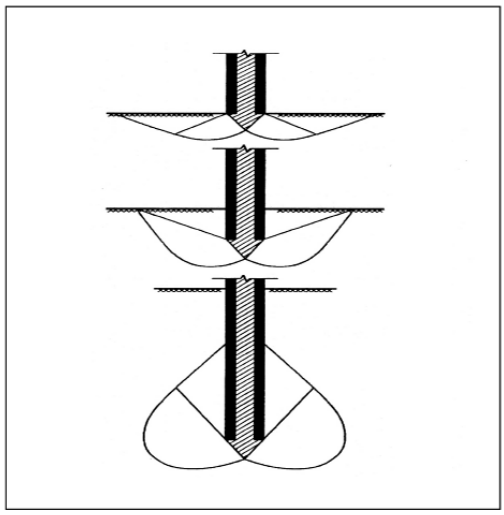

Figure 2.12. Transition from shallow to deep penetration or -foundation.

In the ISO-standard 19905-1 (CEN, 2016, p.148) shallow foundations are thoroughly evaluated for shallow- and partly shallow failure mechanisms, where they assessed d_c, or *the width, B*, in their case, with the formula $B = 1 + 0{,}2(z/D) \leq 1{,}5$. As can be seen, z have in this particular case an upper limit of $2{,}5B$, probably because they reckoned beyond this depth penetrations are transitioning from inducing shallow failure mechanisms to a deep failure mechanism. As will be elaborated in ch. 2.3.3 when the critical depth is reached, the failure mechanism around the pile will become "constant" as the pile is pushed further down. For deep foundations or -piles, values of N_c can be calculated based on cavity expansion (e.g., Vesić 1977) or limit plasticity. The ultimate bearing stress can then be denoted as *unit end bearing resistance*, $q_b = q_{ult}$. The limit plasticity solution is given by eq. {2.19} and for deep circular or square footings $N_c = 9{,}33$ (Mayne, 2007, p.58).

$$q_b = N_c \cdot \overline{S_u} \qquad \{2.19\}$$

In addition of basing N_c on s_c, d_C, r and $\overline{S_u}$, it is also possible to regard the vertical shape of the foundation or pile that is pushed in the soil. For conical footings, the normal stresses will be inclined, and in practice τ/r will change. Houlsby & Martin (2003) wrote a paper on N_c specifically for conical footings on clay, for depths shallower than $2{,}5B$, enabling comparison between CPTU-data and theoretical-/numerical bearing capacity solutions, but only for this limited range (deviance is expected between the theoretical/numerical and empirical data).

For this chapter, it should be emphasized that the regarded $\overline{S_u}$ is the average undrained shear strength working along the failure surface under the foundation, or pile end. Another remark is that the bearing capacity approach involves some simplifications in general. E.g., there will be induced an elastic response outside of the plastified area, which is not accounted for that may contribute to the ultimate bearing resistance or tip resistance (Houlsby & Hitchman, 1988, p.3). This extra resistance may instead be embedded in the undrained strength that is measured or predeterminable approximated. As previously mentioned, the cone geometry/-size and the material properties are the two elements that govern the flow mechanism around the probe. This have been illustrated in *Figure 2.13* which shows a log-spiral flow-mechanism of a drained bearing capacity problem with increasing flow-size according to the strength of the soil, and it is moreover shown with the scale factor which will be explained in ch. 2.3.3.

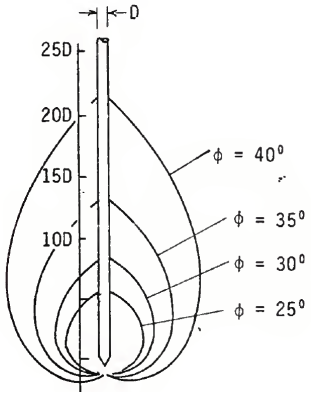

Figure 2.13. Flow mechanism considering log-spiral based bearing capacity for materials with different friction angles. The scale factor is used as depth reference.

2.3.1.1 Drained conditions (NTH-method)

In the mid-80s, Senneset & Janbu (1985) synthesized a theoretical plane-strain solution of the bearing capacity for drained conditions. They further back-calculated values of *the drained bearing capacity factor*, N_q, on the basis of pile- and plate load tests, to show the correlation between empirical data and their theory. As drained conditions are considered, the Mohr-Coulomb criterion govern the maximum allowed shear stress, which is denoted τ_f on effective stress basis. τ_f depends on the stress level σ', or maybe better, the deviatoric stress, $q_{dev} = \sigma_1' - \sigma_3'$, the attraction, a, and the friction tan (ϕ') or the friction angle, ϕ'. The Mohr-Coulomb criterion as written by Senneset et al. (1989) is written in {2.20}.

$$\tau_f = (\sigma' + a) \cdot \tan(\phi') \qquad \{2.20\}$$

They formulated the expression in {2.21}, for the tip resistance, or for "the failure load under the cone", denoted q_t. This formula is based on the previous mentioned criterions and does in addition regard the idealized plastification angle, β, which describes the area of plastification around the cone, as seen illustrated in the upper left corner of *Figure 2.14*. β can be assumed based on experience data, shown in

Table 2.2 and in *Figure 2.14*. Further, N_q, which is a function of $\phi'$and β are theoretically given by eq. {2.22}, and {2.23},. As ϕ' typically is of interest, the previous formulas are used to back-calculate $\phi'(N_q, \beta)$ by utilizing the CPTU-data combined with in-situ stress estimations, see eq. {2.24}. With estimations of N_q and β, ϕ' can be found by using the graph in *Figure 2.14*. Typical intervals of the friction angle for the different soil types are accompanied along the x-axis. Remark the marked "confidence band" in the graph, this represents experience data from sands and silts, meanwhile the interval over clays is extrapolated. The band goes from $\beta < 0$ for dense hard sediments, to $\beta > 0$ for fine, soft soils. (Senneset & Janbu, 1985)

$$q_t + a = N_q\left(\sigma'_{v,0} + a\right) \qquad \{2.21\},$$

$$N_q = N_f e^{(\pi - 2\cdot\beta)} \tan(\phi') \qquad \{2.22\},$$

$$N_f = \tan^2\left(45 + \frac{\phi'}{2}\right) \qquad \{2.23\},$$

$$N_q = \frac{q_t + a}{\sigma'_{v,0} + a} \qquad \{2.24\}$$

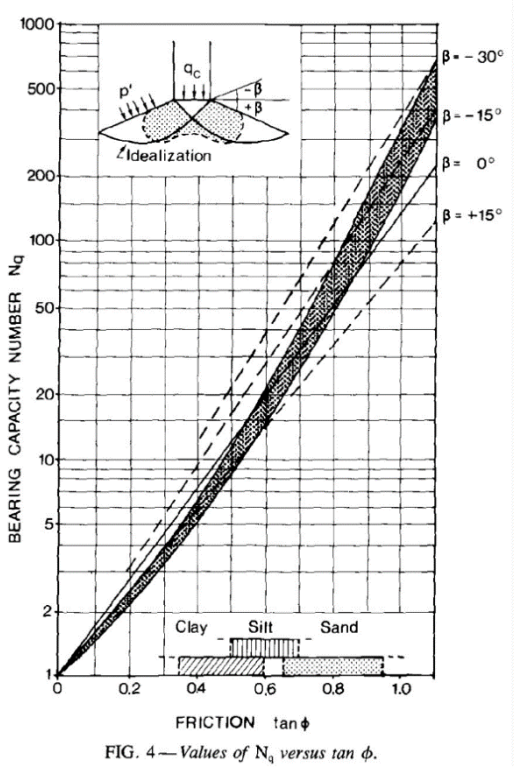

FIG. 4—*Values of* N_q *versus tan* ϕ.

Figure 2.14. Plane strain drained bearing capacity solution, accounting for plastification angle β.

2.3.1.2 Undrained conditions (NTH-method)

For undrained conditions, the ultimate bearing capacity is decreased as a result of the excess pore pressure, Δu_2. Senneset & Janbu (1985) formulated eq. {2.25} to account for this excess pore pressure. Here the denotation of q_n and B_q are equal to prior, (eq. {2.6} & {2.13}), and $\sigma'_{v,0}$ is indexed with 0 as to underline "reference pressure in-situ". $N_q(\phi', \beta)$ is the same as before, see eq. {2.22}, and {2.24}. Two new terms are added, first is *the cone resistance number*, N_m, seen in eq. {2.26}, which together with the relation of B_q, can substitute terms in {2.25} creating the new, shorter formula {2.27}. The second introduced term is *the theoretical bearing capacity factor*, N_u, which is approximated by equation {2.28}. A theoretical solution of N_u has been developed based on base roughness, r, and ϕ' (Kirkebø, 1986, as cited in Senneset et al., 1989). Yet, the approximation of N_u fits well in the range $\phi' = 17\text{-}35°$, covering the typical ranges of clay and silts, which namely is most pertinent for undrained situations. Note that N_m in {2.29} (and {2.26}) is quite similar to Q_t, eq. {2.14}, the difference being that attraction is also regarded. Some typical values of N_m and B_q are presented in *Table 2.3*.

$$q_n = (N_q - 1)(\sigma'_{v,0} + a) - N_u \Delta u_2 \qquad \{2.25\}$$

$$N_m = \frac{N_q - 1}{1 + N_u B_q} \qquad \{2.26\}$$

$$q_n = N_m(\sigma'_{v,0} + a) \qquad \{2.27\}$$

$$N_u \approx 6\tan(\phi')\,(1 + \tan(\phi')) \qquad \{2.28\}$$

By combining eq. {2.26} and {2.27}, eq. {2.29} is obtained, which enable determination of ϕ', based on estimations of $\sigma'_{v,0}$, u_0, a, β, q_t, u_2. The two first can be obtained through field investigations, q_t, $u_2$are read from CPTU-data, β may be found using experience data shown in

Table 2.2, and lastly, the attraction may be found using different methods, as explained on the next page.

$$\frac{q_n}{\sigma'_{v,0} + a} = \frac{N_q - 1}{1 + N_u B_q} = N_m(\phi', \beta) \qquad \{2.29\}$$

Table 2.2. Chart of tentative values of β for different soil types.

Soil type	Tentative values of β, [°]
Dense sand, overconsolidated silts, high plastic clays, low-compressible overconsolidated clays	-20 to -10
Medium sands and silts, sensitive clays, high-compressible clays	-5 to +5
Loose silts, clayey silts	+10 to +20

Table 2.3. Soil characteristics chart with typical values of a, ϕ', N_m and B_q.

	Shear Strength Parameters				
	a (kPa)	tan ϕ'	ϕ'	N_m	B_q
Clay					
Soft	5–10	0.35–0.45	19–24	1–3	0.8–1.0
Medium	10–20	0.40–0.55	19–29	3–5	0.6–0.8
Stiff	20–50	0.50–0.60	27–31	5–8	0.3–0.6
Silt					
Soft	0–5	0.50–0.60	27–31		
Medium	5–15	0.55–0.65	29–33	5–30	0–0.4
Stiff	15–30	0.60–0.70	31–35		
Sand					
Loose	0	0.55–0.65	29–33		
Medium	10–20	0.60–0.75	31–37	30–100	<0.1
Dense	20–50	0.70–0.90	35–42		
Hard, stiff soil, OC, cemented	>50	0.8–1.0	38–45	100	<0

The attraction can be found by conducting triaxial tests, this may be assumed based on knowledge of the soil and the use of charts, e.g., *Table 2.3*, or a last solution is to calculate it following the method described in the section "Determination of In-Situ Attraction" in the article of Senneset & Janbu (1985). For the latter method, the obtained apparent attraction is typically much larger than those typically found by laboratory testing. They stated this possibly was caused by both the suction in the pore water, and the speed which induces a continuous failure mechanism. This method is less accurate for inhomogeneous soils and is further obscured by large fluctuations in q_t, but they underlined that it should be correct in theory. A simplification of the concept is shown in the rightmost profile in *Figure 2.4*. *Table 2.*2 and *Table 2.3* are both based on correlations between laboratory work and CPTU-interpretations done at NTH (Prior name of NTNU). (Senneset & Janbu, 1985, Senneset el al. 1989)

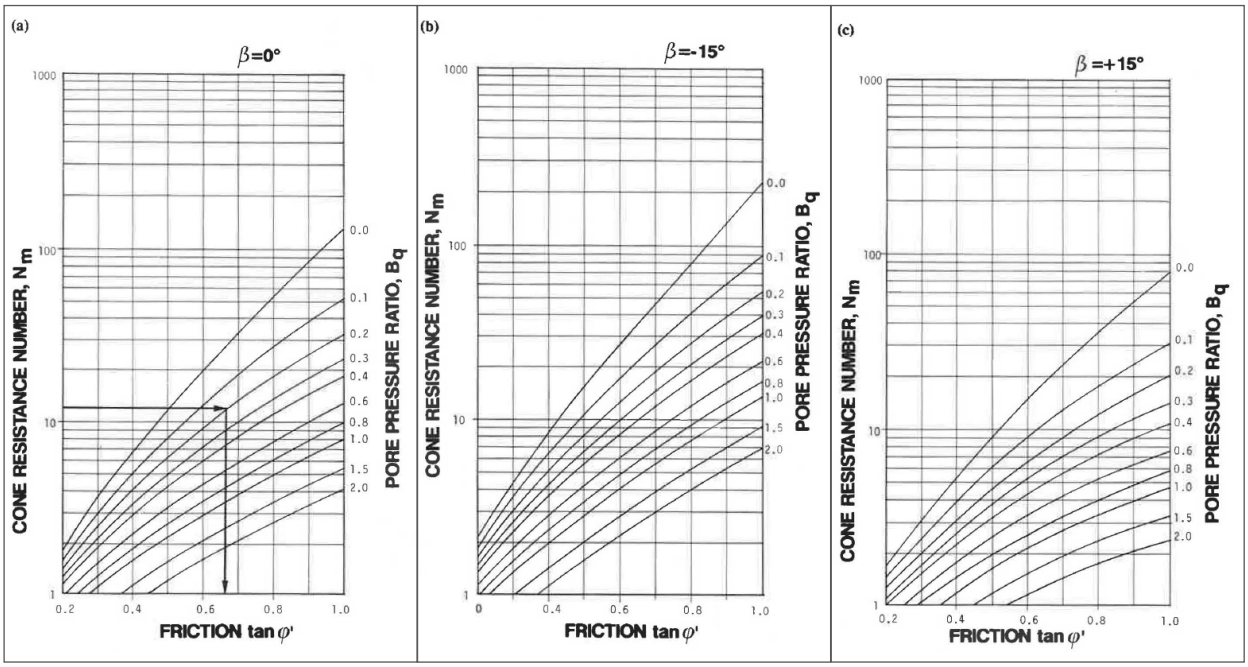

Figure 2.15. Interpretation diagrams for different β.

To summarize the method, the left-hand term in {2.29} is calculated, estimating N_m. Subsequently, expected/assumed β is chosen, based on *Table 2.2* or *Figure 2.14*. ϕ' can then be read of the interpretation charts in *Figure 2.16* using these values.

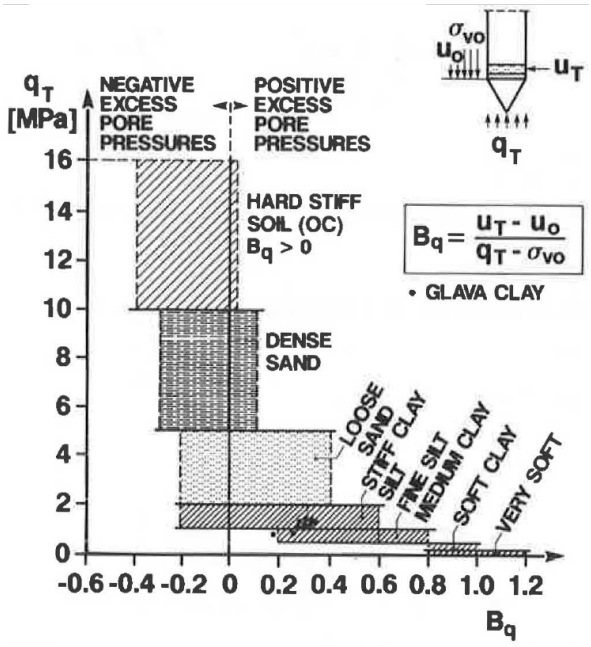

Figure 2.16. Soil classification chart based on q_t and B_q.

Senneset et al. (1989) presented a classification chart based on q_t and B_q, see the figure above. For the particular case where $\beta = 0°$, the classical bearing capacity case apply. Mayne wrote about the NTH-method in (Mayne, 2005, p.14), and presented a chart for ϕ' based on zero attraction, where he correlated ϕ' with B_q the pore pressure ratio and N_m the cone resistance number, which for $a = 0$ is equal to Q_t, the normalized tip resistance. Using $\beta = 0°$ and $a = 0$, $20° < \phi' < 45°$, with a lower limit of $B_q > 0{,}1$, and, ϕ' could be estimated as below. (Mayne, 2005)

$$\phi' = 29{,}5° \cdot B_q^{0{,}121}\left[0{,}256 + 0{,}336 \cdot B_q + \log(Q_t)\right] \qquad \{2.30\}$$

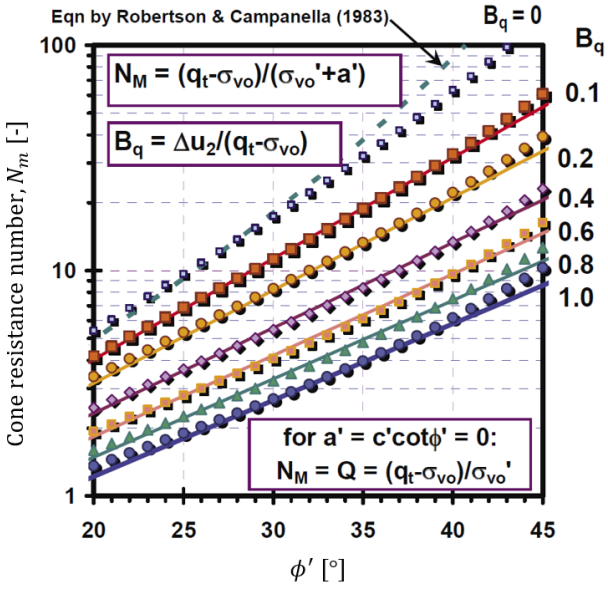

Figure 2.17. Effective ϕ' from B_q and N_m using the NTH-method, attraction is set to zero ⇒ $N_m = Q_t$.

2.3.1.3 In-situ cone bearing factors

Instead of using analytical bearing capacity factors as those presented in the previous sub-chapters, it has also been broadly practiced to use an empirical *in-situ cone factor*, $N_{k,i}$, with different subscripts based on parameter-basis. By simply substituting the analytical N_c, with the *cone factor based on* q_{net}, N_{kt}, estimates of S_u can be correlated with CPTU-soundings, see eq. {2.31}. Due to a large scatter of experienced N_{kt}-values, the factor has to be calibrated for each site. Senneset et al. (1989) attributed different factors to this uncertainty, e.g., the obtained S_u which is used for calibration depends on the test method with its associated strain rate, reference level of S_u (I.e., is the consolidation level equal preconsolidation level or in-situ stress?), and is further not a unique measure of soil strength. Lunne et al. (1997) supplemented that sample disturbance and fissures in the soil influenced N_{kt} in addition. Senneset et al. (1985, 1989) could tell that N_{kt} is generally larger than N_c and typically ranges from 15 to 20 for stiff dilatant OC-clays, 10-15 for NC-clays and 6-10 for soft contractant clay, e.g., quick clay, or other soils that are generally of brittle character.

$$q_t = N_{kt} \cdot S_u + \sigma_{v,0} \Rightarrow S_{u,kt} = \frac{q_n}{N_{kt}} \qquad \{2.31\}$$

Another cone factor, N_{ke}, was proposed by Senneset et al. in 1982 (as cited in Lunne et al., 1997) and is based on the "effective cone resistance" q_e where u_2 is subtracted from q_t, see eq. {2.32}. Lunne et al. (1997, p.67) pointed out that u_2 typically is quite similar to q_t in soft NC-clays: about 90 %, which makes $N_{ke}(q_e)$ a measure quite sensitive to errors of u_2- and q_t-readings. A last theoretical cone factor presented herein is $N_{\Delta u}$, which is based on cavity expansion theory, see eq. {2.33}. This cone factor is derived for clays which have experienced light- or no overconsolidation, and has little conformity for sounding intervals with low or negative Δu_2. From eq. {2.32} and {2.33}, the ratio in eq. {2.34} can be deduced.

$$S_{u,ke} = \frac{q_t - u_2}{N_{ke}} = \frac{q_e}{N_{ke}} \qquad \{2.32\} \qquad S_{u,\Delta u} = \frac{u_2 - u_0}{N_{\Delta u}} = \frac{\Delta u_2}{N_{\Delta u}} \qquad \{2.33\}$$

$$B_q = \frac{\Delta u_2}{q_n} = \frac{N_{\Delta u}}{N_{kt}} = \frac{S_{u,kt} \cdot \Delta u_2}{S_{u,\Delta u} \cdot q_n} \qquad \{2.34\}$$

In the article by Karlsrud et al. (1997) the cone factors were correlated with different index-properties of block-samples at various research sites, mainly being *the plasticity index* I_P, *the sensitivity*, S_t, and *the overconsolidation ratio* OCR. These properties are further elaborated in ch. 3.3. They mentioned that the plasticity's significance was to some degree depending on the sensitivity of the clay, especially for $S_t < 15$, but underlined that the presented relations were not universal. They provided the empirical relations given in equations {2.35}-{2.40}, where the unit of I_P is given as percent. Among the three cone factors Karlsrud et al. (1997) implied that $N_{\Delta u}$ had the best conformity between CPTU-readings and measured S_u, and consequently should be weighted the most upon evaluation of S_u based on the cone factors. As can be understood from the presented relations, to find S_u, the cone factor must be known, and vice versa for the cone factor. This self-reference requires either calibration for every site, or relying on the approximate empirical relations given by Karlsrud et al. (1997).

A last note in this chapter is that Lunne et al. (1997) could tell that a recognized approximation of *remoulded shear strength* S_{ur} was f_s. This means that the sensitivity for a clay could be approximated directly by the use of CPTU-readings, if S_u is estimated, -or approximated using a cone factor.

$$N_{kt}(S_t < 15) = 7{,}8 + 2{,}5 \cdot \log(OCR) + 0{,}082 \cdot I_P \quad \{2.35\}$$

$$N_{kt}(S_t > 15) = 8{,}5 + 2{,}5 \cdot log(OCR) \quad \{2.36\}$$

$$N_{ke}(S_t < 15) = 11{,}5 - 9{,}05 \cdot B_q \geq 2 \quad \{2.37\}$$

$$N_{ke}(S_t > 15) = 12{,}5 - 11{,}0 \cdot B_q \geq 2 \quad \{2.38\}$$

$$N_{\Delta u}(S_t < 15) = 6{,}9 - 4{,}0 \cdot \log(OCR) + 0{,}07 \cdot I_P \quad \{2.39\}$$

$$N_{\Delta u}(S_t > 15) = 9{,}8 - 4{,}5 \cdot log(OCR) \quad \{2.40\}$$

2.3.2 Expanding cavity theory

So far, all theory on bearing capacity has been based on limit plasticity solutions, where the elastic domain is not accounted for. Meanwhile, in expanding cavity theory, the deformation prior to failure is also included in the calculations, by separating the area around the cone into plastic and elastic zones, having an elasto-plastic interface. The pile or probe is then said to displace the soil radially, and the geometry of this influence zone is depending on the cone geometry and on the medium that is sounded. The measured tip resistance becomes a combination of soil strength and the stiffness of the underlying and radial layers. (Zhao et al. 2018, Vesić & Jones, 1977)

In the theory one assumes that the normal stresses along the interface between the plastic- and the elastic zones are equal to the pressure needed to expand a spherical cavity in an infinite soil mass. The mass which is moved is typically assumed to behave ideal elastic-plastic and is characterized by the deformation parameters: *the Young's modulus, E*, and *the Poisson's ratio*, ν; the strength parameters: *cohesion*, c, and *the friction angle* ϕ'; and a *volume change parameter*, Δ, alternatively the *volumetric strain in zone III,* ε_V. In the particular case composed by Vesić & Jones (1977, p. 75), the failure pattern is shown equal to that in *Figure 2.18*. Here the volumetric strain in the plastic zone, $\varepsilon_{V,\mathrm{III}}$, is equal to zero upon undrained loading. The complete calculations are intermediately comprehensive and complicated, so they are not included here, instead the very basic formula eq. {2.41} which shows the ultimate capacity of the pile load is presented. Numerical values of N_σ and N_c can be found in the text of Vesić & Jones (1977, pp. 76-77). Additionally, eq. {2.42} is included as to underline that theory by Vesić and Jones is based on *mean normal stresses,* σ_m, in the ground, as they argued that tip resistance is governed by the mean normal stress and not the vertical. The latter is in accordance with the previously mentioned statement of Houlsby & Hitchman (1988). (Vesić & Jones, 1977)

$$q_{ult} = q_0 = c \cdot N_c + \sigma_m \cdot N_\sigma \quad \{2.41\}$$

$$\sigma_m = \frac{1 + 2K_0}{3}\sigma_{v0} \quad \{2.42\}$$

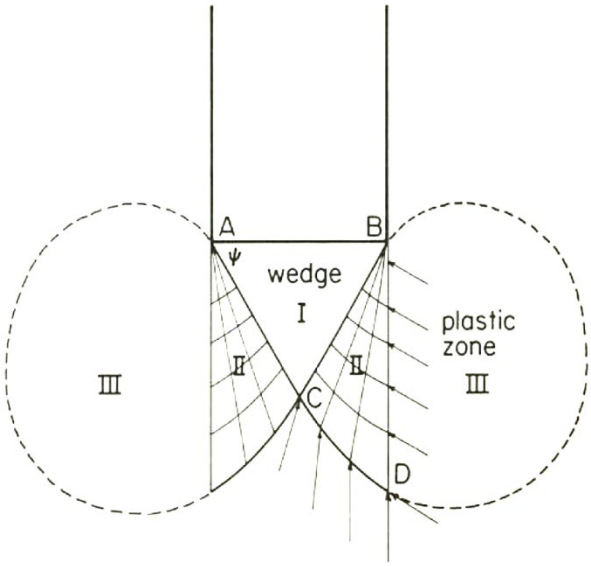

Figure 2.18. Cavity expansion failure pattern in the theory of Vesić & Jones.

Other conceptual approaches of the expanding cavity theory exist, below in *Figure 2.19* and *Figure 2.20* another flow mechanism is assumed as compared to that in *Figure 2.18. Figure 2.20* show initial expansion (dashed circles) and expansion at the same depth upon deeper penetration. Another possible way to interpret the figure is that the illustration shows two different sections at different stages of deformation in the same point in time.

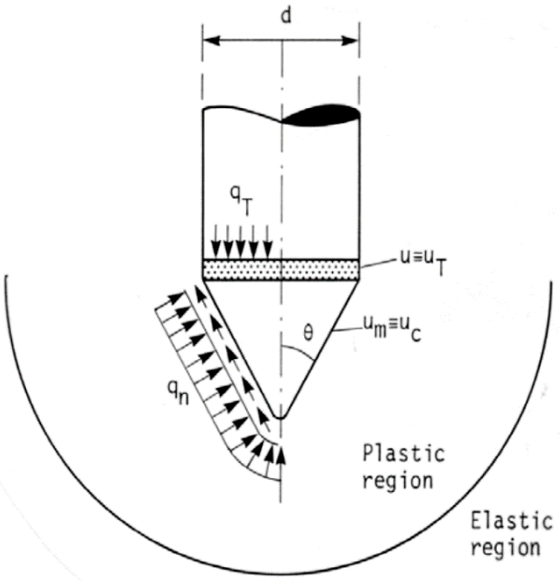

Figure 2.19. Illustration of induced cavity expansion by CPTU.

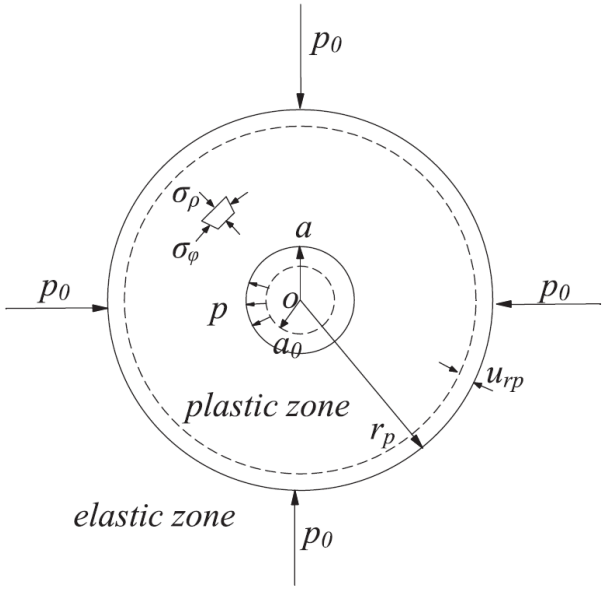

Figure 2.20. Sketch with cavity expansion with in-plane perspective.

2.3.3 Critical depth and the scaling effect

The strength of sand is to a large degree proportional to the stress level, consequently q_t is lower at shallower depths. Upon sounding, the cone resistance increases quite rapidly until it reaches a certain depth, called the critical depth, where the cone resistance is no longer influenced by the free surface. I.e., after reaching a certain depth, the penetration generates a quite constant failure flow mechanism around the probe, and the concept can be compared to that of a deep foundation, see sub-chapter 2.3.1. An important remark regarding the phenomenon is that the critical depth is proportional to the diameter of the pile or probe that is pushed down, and this is the beforementioned *scaling effect* (Nottingham, 1975). After the critical depth is surpassed, the tip resistance should approach a level which is common disregarding the penetrometer size. The critical depth is denoted z_c in the text of Hammer, and will for continuity-reasons be denoted equally in this text, meanwhile in the literature of De Beer (1963) and Nottingham (1975) it is denoted D_c as can e.g., be seen in *Figure 2.21*.

According to De Beer, during the transition between a shallow and deep penetration of a pile, the tip resistance increases rapidly in a linear fashion, until the deep penetration mode is reached whereupon the tip resistance is increasing only slowly and is entirely reflecting the resistance of the soil. It has surpassed the critical depth. This is sketched as route ABED in *Figure 2.21*. For an infinite-small pile or -penetrometer, this would yield resistances according to the route ABCD. While there exists no such penetrometer, the standardized penetrometer comes relatively close to the idealized infinite-small in this sketch, and is shown following route ABC'D. According to the scaling effect, z_c is a function of the cone diameter, d_c, hence it would be more advantageous to use the ratio $\left({}^{z_c}/_{d_c}\right)$ to describe the critical depth. This ratio can also be denoted *the scale factor*. In sands this ratio is a function of e.g., the relative density, D_r, and is typically ranging from 5 in loose sand to 15-25 in dense sands. Accordingly, for a standard penetrometer the respective critical depths would be expected to be $z_c \approx 20$ cm in loose sand and $z_c \approx 50 - 90$ cm in dense sand. (Nottingham, 1975)

The concept of critical depth apply not only to the transition between surface to deep penetration, it can also be transferred to transitions between an above laying weaker layer onto a lower laying strong layer as in the illustrations *Figure 2.21* and *Figure 2.22* from Nottingham's Ph.D. thesis (1975). In the latter figure the above-laying weaker layer has been set equal to zero strength, equal atmosphere pressure as to only illustrate an idea. If the above-laying layer exercised any resistance, the flow mechanism would be changed depending on the properties of the above-laying layer, and would be unique. Instead, an extreme has been shown as to illustrate one side of the scale. The other side, or extreme, of that same scale would be to replace the layers with each other, giving a piercing concept instead of a penetration concept. In reality the transition between two layers will be a thing in between. If the two layers were equal, then the penetration would follow the mechanism of steady-state flow around the probe.

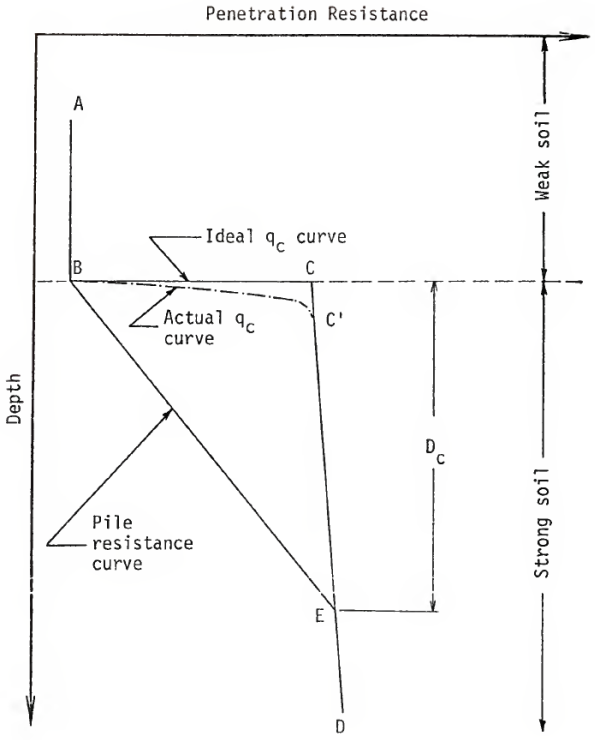

Figure 2.21. Tip Resistance, including a pile foundation, an idealized curve, and an actual curve of penetrometer.

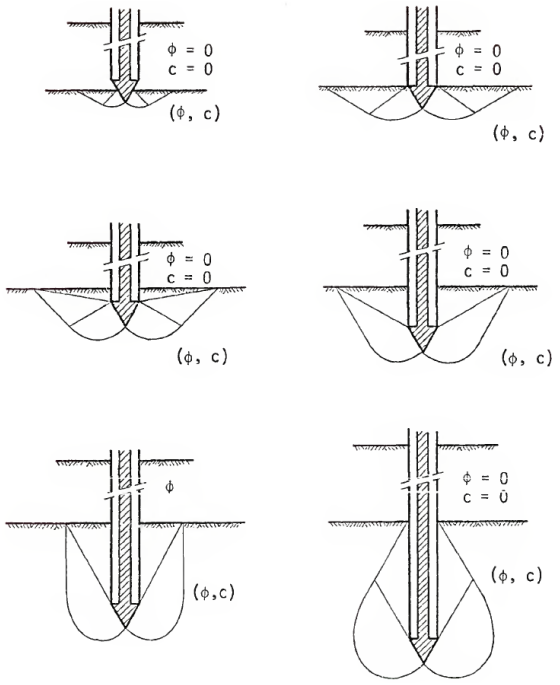

Figure 2.22. Two different sketches of transition from a weak-layer (atmospehere in this case) to a strong one.

In this experiment, the critical depth in the samples were reduced by both imposing a higher stress level on the top, and to some degree physically restraining the penetration from inducing a shallow failure mechanism near the surface.

2.3.4 Transitions

To explain the thin layering effect some prerequisite information must be presented. Much of the theory presented in this chapter is based on the work previously done by Hammer (2020). As explained in the previous sub-chapter, after some penetration depth, the tip resistance, q_t, will be quite constant or slowly roughly linearly increasing. It can be stated that *the characteristic cone resistance,* $q_{t,i}^{char}$, of the material, i, is reached. This value mainly depends on the material's stiffness and shear strength.

Now, considering a two-layered profile with materials a in the upper layer and b in the lower layer. When sounding through a, steadily following $q_{t,a}^{char}$, almost has pierced the layer, then upon closing in on layer b, q_t will deviate from $q_{t,a}^{char}$ and start its approach towards $q_{t,b}^{char}$. The distance from the layer interface a-b to the starting point of this change in tip resistance is called *the sensing depth*, denoted H_s. Upon piercing the interface, q_t will be somewhere between $q_{t,a}^{char}$ and $q_{t,b}^{char}$. The overlying layer will continue to influence q_t after the interface is pierced, with a decreasing magnitude until $q_{t,b}^{char}$ is reached, i.e., the developing distance, H_D, has been surpassed. The concept is shown in *Figure 2.23*. It is quite similar to the critical depth explained in the previous chapter, except that for two materials, some volume of material a will dragged into b, and the failure mechanism will no longer be shallow. Instead, a complex failure mechanism will create a slip surface through both materials which is irregular and is moreover depending on the materials' stiffnesses, shear strengths, tendency of dilatancy, and to which degree they act drained or undrained (as this also decide whether the material can be compacted or not). The sum of H_S and H_D constitute a complete transition, which is defined as *the influence depth* or *-distance*, denoted H_I, where-upon surpassed, q_t will be equal $q_{t,b}^{char}$.

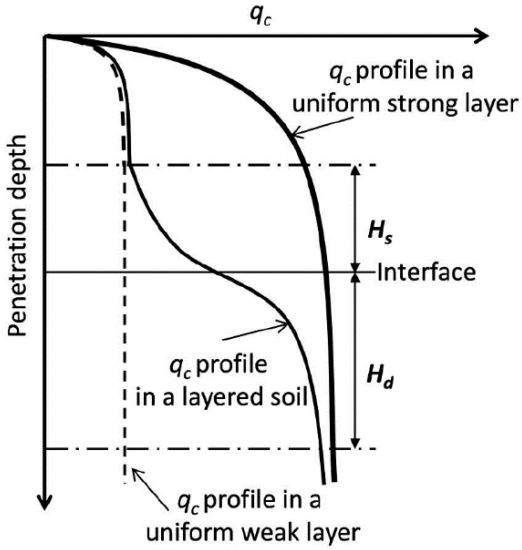

Figure 2.23. Measured and characteristic tip resistance profiles, including notation of H_s & H_D.

If *Figure 2.21* is reviewed again with the new introduced phenomena in mind, it is prominent that the sensing depth in the above laying layer is missing. This stem from the author's focus on the critical depth for penetrations, who thereby defined the upper layer as the atmosphere.

In the work by Vreugdenhil et al. (1994) it was suggested that q_t senses a nearby layer elastically, although the stiffness is not the only parameter which influence the tip resistance, and furthermore, most soils are not perfectly linear-elastic. Anyhow, it can still be viewed as quite correct outside the plastified area. Thus, as the cone approaches the interface, q_t will mobilize the soil in the second layer, which depending on its stiffness will yield another resistance per strain (σ/ε). Consequently, as the transition starts, the obtained q_t start descending or ascending, depending on the new layer's stiffness. But the new layer will also probably yield at a different

stress state, making things more complex. Hammer (2020) proposed in order to simplify the evaluation of transitions, $q_{t,i}^{char}$ in each layer could be used to describe the phenomena, by looking at the shape of transition for $q_t(z)$ and the contrast between $q_{t,a}^{char}$ and $q_{t,b}^{char}$.

When the cone base is at the same level as the interface, $q_{t,b}^{char}$ is still not reached, because of two effects. Firstly, some of the upper layer has been dragged beyond the original interface level, pushing away material from the lower layer down and sideways, replacing it. And secondly, some of the material in the lower layer is pushed up, counteracted by resistance from the upper layer. These effects are in a very large degree depending on the difference in stiffness and strength between the two, and will consequently determine the developing distance. Vreugdenhil et al. (1994) acknowledged that the response after the interface is also depending on the material properties from the upper layer, even though they focused solely on the elastic behaviour of the materials in their numerical- and experimental study, meaning that they added an elastic contribution on q_t from the layer above.

2.3.4.1 Deformation pattern

Thus far, the flow mechanism has only been described for homogenous mediums (ch. 2.3.1), and only briefly for different mediums, pointing out the factors of influence, mainly being shear strength and stiffness. Thereby, it is natural to look upon some observed trends. Mo et al. (2017) conducted centrifuge tests in an axisymmetric half-cylindrical container, where they specifically investigated the transitions between loose and dense sands using *particle image velocimetry* (PIV). On the left-hand side of *Figure 2.24* a sketch is shown of the deformation mechanisms attributed transitions from soft to stiff sand. The downward displacement of sand from the upper layer into the lower layer is restrained, and most soil are pushed sideways due to less resistance.

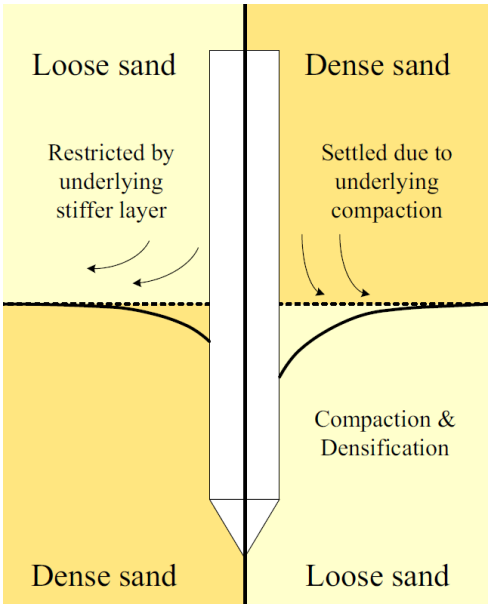

Figure 2.24. Illustration of transition in sands. Left: loose-dense, right: dense-loose.

In the opposite case, upon transition from a stiff to a soft sand layer, the boundary is pushed further down along with the penetrometer, and for an extended distance horizontally, due to the rigid behaviour of the upper medium and the compaction experienced by the lower layer.

Another PIV-centrifuge study was conducted by Wang (2019), investigating the flow mechanism in transitions between very soft and medium stiff clay, respectively with S_u equal to 7,5 and 29,1 kPa, estimated based on a q_{net} and $N_{kt} = 10{,}5$, a procedure which is explained in ch. 2.3.1.3. For a transition from soft to stiffer clay, as in *Figure 2.25*, similarities to the soft-stiff sand transition can be seen, with deformations in the upper softer layer vertically restrained along the interface boundary. For the stiff- to soft clay transition seen in *Figure 2.26* (c) the failure mechanism near the intersect resembles a punch-through, where the stiffer soil is pushed in front of the cone and into the lower softer layer.

To specify, the mechanism of punch-through is in ISO 19905 (CEN, 2016, p. 18) defined as "rapid uncontrolled movement due to soil failure in strong soil overlying weak soil", and may not be entirely directly transferable to a static cone penetration test transitioning from a stiff to softer layer. Moreover, due to the cone geometry, the stiff soil plug that is to be pushed ahead will quickly be split, thus less of the softer layer will be replaced compared to that of a typical punch-through failure. The topic is thoroughly reviewed in ISO 19905, where different ground condition cases have been illustrated as in *Figure 2.27.*

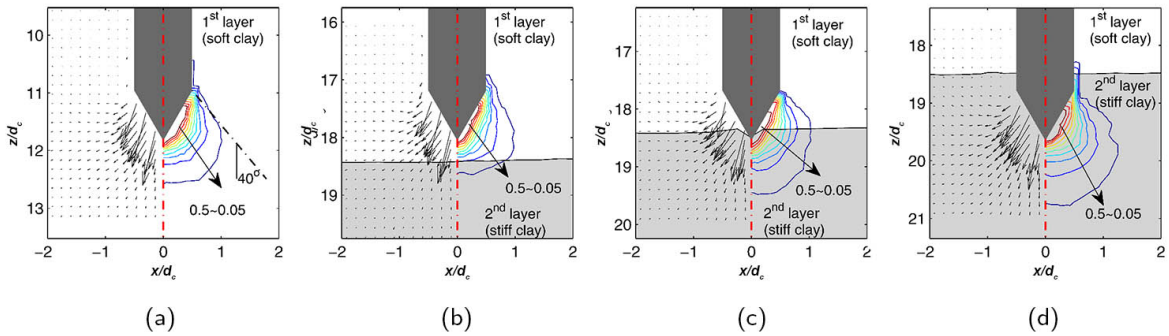

Figure 2.25. Time-frames of transition from a soft clay to a stiff clay.

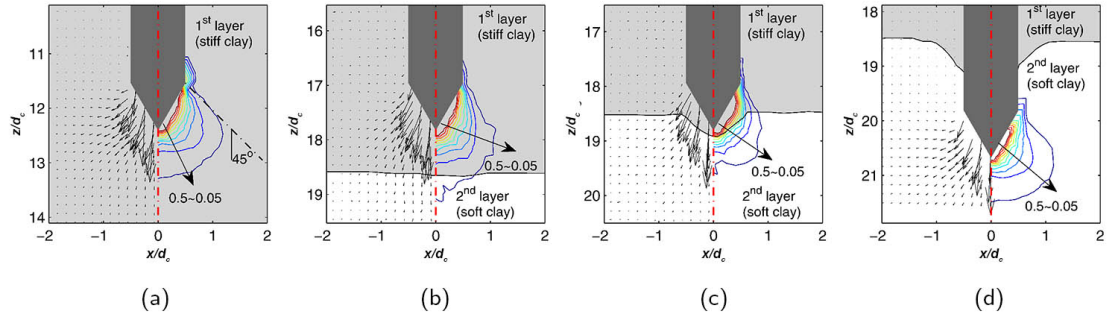

Figure 2.26. Time-frames of transition from a stiff clay to a soft clay.

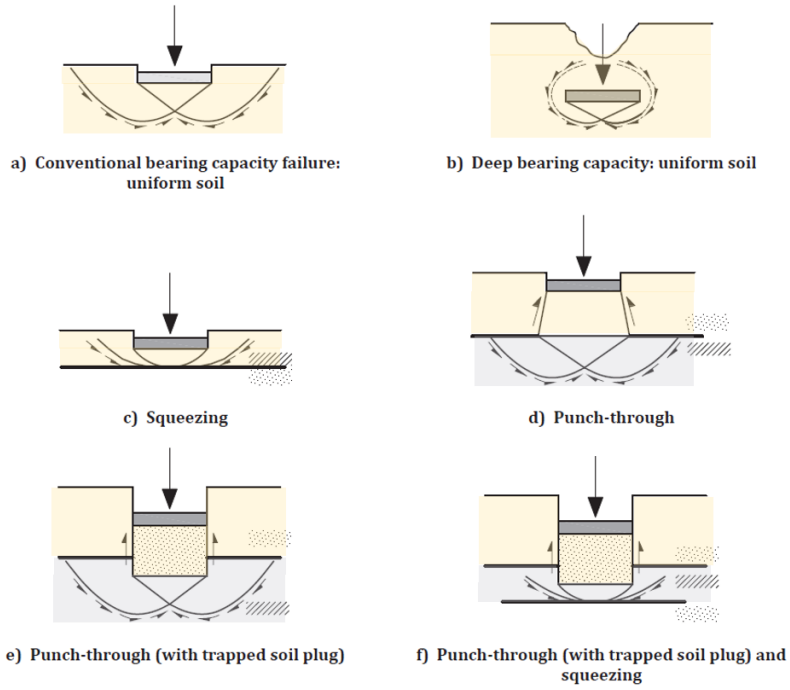

Figure 2.27. Bearing failure mechanisms of a flat foundation (simulated spud-can), with different sub-surface conditions.

As a summary one can say that the deformation mechanism always follows the direction of least resistance, implying that the relative strength and stiffness difference between the penetrated mediums play an important role for the deformation pattern. To underline, the topic is of importance upon assessing layering effects, as it describes to some degree describe the behaviour of q_t and also which medium may be expected to surround the pore pressure filter at a certain position.

2.3.4.2 Tip resistance profiles

The q_t-profile at transitions depend not only on the relative strength and stiffness ratio between the materials, but in addition some intrinsic material properties. Tehrani et al. (2017) conducted a similar experiment to that of Mo et al. (2017), with digital image correction (DIC), also using a half-cylindrical test-chamber. In these experiments a 50 kPa load was imposed on top of each sample. Sand with different relative densities were tested, labelled as loose, medium dense and dense, with respective relative densities $D_r \approx 45, 65$ & 85. In *Figure 2.28* two tests are shown including loose and dense sands. As reference, they conducted tests for homogenous sands first, marked in 2 shades of grey, giving $q_{t,i}^{char}$. They indicated both sensing- and developing depths relative to d_c, with respective magnitudes indicated in the graphs. These depths are subjectively interpreted visually from either the graph or list of q_t-values. The deviance between q_t and $q_{t,i}^{char}$ in the intervals where they are excepted to be matching, is due to the difficulties associated in preparing homogenous sand samples. Hammer (2020) reflected that $q_{t,i}^{char}$ "merely is an estimation of the cone resistance uninfluenced by layering effects". Both H_S and H_D seem to be greater in the denser layers as compared to the looser ones.

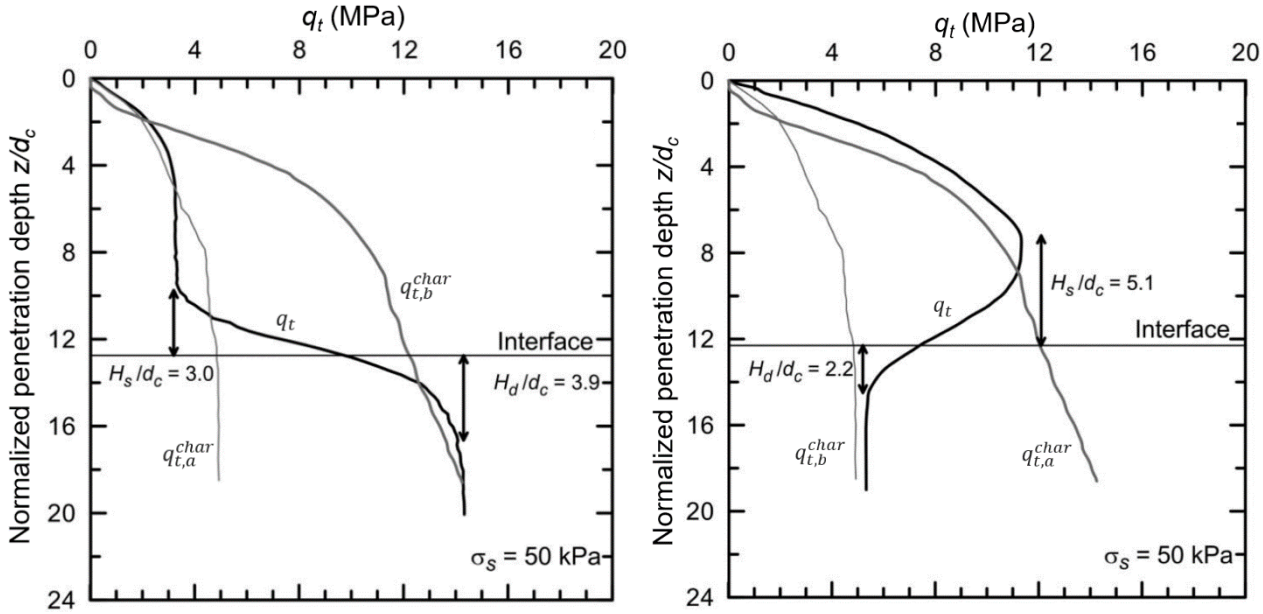

Figure 2.28. Tip resistance versus normalized penetration depth in two-layered profile, including characteristic q_t-profiles for each material. Sand *a* is above and *b* is below, Left: Loose over dense sand. Right: Dense over loose sand.

The q_t-patterns seen in sand are not directly transferable to transitions between soft and stiff clay. In the earlier mentioned study by Wang (2019) the tip resistance profiles followed the patterns seen in *Figure 2.29*, where H_S can be seen to be almost non-existing for both soft and stiff clay. The developing depth in the soft layer profile (red), was ca. $H_D/d_c = 4{,}3$, and in the stiff layer equal to $H_D/d_c = 2{,}1$ (black). Comparing the sand-cases with each other with respect to H_D, and doing the same for the clay-cases, it seems to be a opposite correlation between change in H_D and the sequence of a relative weak and strong layer. A summary is that the transition from one material is not entirely dependent on the relative strength and stiffness of each layer, but also some intrinsic soil properties associated grain-size.

Notice that for the clays, z_c is significantly smaller relative to the cone diameter, as compared to those in the sands. This is associated with the strong relation between stress level and strength in sand. Something that should also be reminded is that the sand samples were imposed with a 50 kPa surcharge, illustrating that even with counteractions, the critical depth is large in sands.

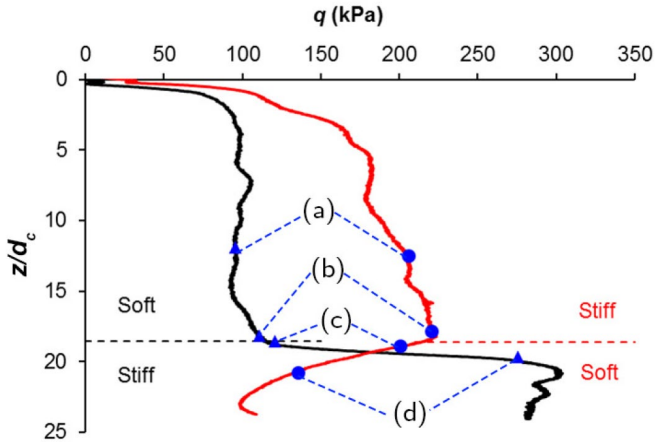

Figure 2.29. Tip resistance versus normalized penetration depth in two-layered profile. Black curve: soft over stiff clay. Red curve: stiff over soft clay.

2.3.4.3 Smoothening effect

In ch. 2.1.2 and 2.1.2.3 it was mentioned that the parameters q_t and f_s were averages of the stresses working on each device component. This is not an issue in homogenous mediums, but the influence becomes apparent for layer transitions. Considering larger sized components, the failure zones in front of the probe will expand. The transition starts earlier, where q_t become some intermediate value of the characteristic tip resistances from both materials over the entire influence distance. One can say that an increase of probe size would have *an averaging effect,* or *smoothening effect,* on q_t, not meaning a true average, but as function of: the transition progression, and the influence of each material. Due to the smoothening effect increasing with larger probe sizes, smaller probes are expected in a greater extent to measure actual extremal values. However, since real materials are not ideal homogenous and scale-independent, the relation between averaging effect and cone size will not be perfectly linear, but also depending on the grain size compared to the cone size.

It has been shown experimentally that the grain size may influence q_t when the ratio of d_c and *the mean grain size*, d_{50}, are less than 28 (Bolton et al. 1999, as cited in Meisina et al. 2021). The sand utilized in the encompassing experiments has a d_{50} of 0,492 mm, and con-sequently, q_t would be influenced by grain size for cones with $A_c < 1{,}5$ cm^2, $d_c < 1{,}4$ cm.

2.3.4.4 Thin layer effect

To conceptualize the thin layering effect, the previous idea of a two layered transition can be transferred to a profile consisting of three layers, majorly consisting of material a, interbedded by a thin layer b with thickness H. When a sounding advances in the first layer a, it will maintain q_t equal to $q_{t,a}^{char}$ until it is the distance H_s from the interface, whereupon it changes towards $q_{t,b}^{char}$. Then, after the sounding has penetrated the interface, it continues through b but do not reach $q_{t,b}^{char}$ before it is influenced by the third layer, again consisting of material a. The influence depth of the first interface was never surpassed, before layer b was completely pierced, and thus no $q_{t,b}^{char}$ was ever measured. The extremal value within b is then denoted $q_{t,thin,peak}$ as illustrated in *Figure 2.31*.

In this aspect lies one of the main essences of the current experiments: It can be difficult to detect a thin layer of clay if $q_{t,thin,peak}$ is deviating little from the general trend of q_t. If a thin clay layer first is identified, then it will be difficult to determine its properties with a satisfactory certainty, as q_t^{char} and H remains unknown. There are two factors which ultimately describe the thin layering effect. First is the scaling factor: the ratio of the cone geometry versus the thickness of the clay layer. I.e., the thinner the clay the layer, the smaller the probe must be to measure the transition completely. Secondly, comes the difference between the different characteristic tip resistances. The contrast between $q_{t,a}^{char}$ and $q_{t,b}^{char}$ creates a change of both the sensing- and developing depth for both the first and the second interface *a*-*b* & *b*-*a*. As previously mentioned, $q_{t,sand}^{char}$ is depending mostly on the sand's stress level, its density, and its compressibility. Meanwhile, $q_{t,clay}^{char}$ is typically associated the clay's stiffness and has lesser reliance on the stress level. Thus, for greater depths, with greater stress levels, the contrast is expected to be higher. The shape of the q_t-profile is as mentioned also depending on other intrinsic properties of the materials.

2.3.4.4.1 Inverse spatial filtering

All of the mentioned effects will together determine the curvature and magnitude of the q_t-profile. It is then possible to simulate the q_t-profile by performing inverse spatial filtering, as presented by e.g., Boulanger & DeJong (2018) and Hammer (2020, appendix B). This requires in-put of parameters such as $q_{t,i}^{char}$ and the layer thickness H, including some weight function which accounts for the influence on q_t of the material both behind and in front of the cone for every data point with depth. Obviously, most of these parameters would be unknown if soundings in thin layers were to be assessed, but by making an educated guess of the

parameters (potentially in the future with reference to empirical tables), a q_t-profile will be generated which can be compared the field q_t-profile. The parameters should then be incrementally changed to approach the profile of the field sounding. Such a method could imply that many, or infinite combinations of parameters may generate the same q_t-profile. But as the shape of the field profile is unique, with a specific curvature depending on the materials, this problem is reduced. And furthermore, the results can be backed up by f_s and u_2 measurements. An example from Hammers' work (2020, ch. 5.3) of a simulated q_t-profile by the means of inverse spatial filtering is shown in *Figure 2.30*. The methodology shows great potential; however, it requires calibration; potentially not only for the generic soil types, but perhaps for unique soils as well.

In addition to the mentioned analytical influences of the theoretical q_t-profile comes the accuracy associated the reading-frequency of the probe, which complicate the CPTU-assessment further. This will be elaborated in ch. 4.3 and ch. 6.3.

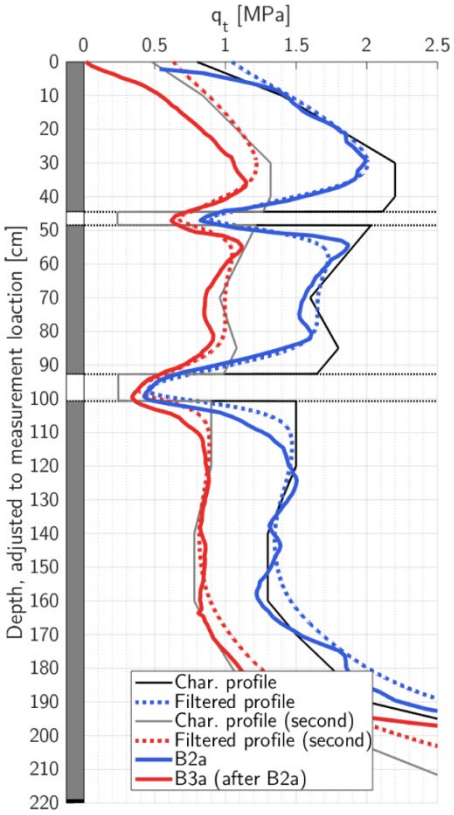

Figure 2.30. Two q_t-profiles from chamber tests (red & blue), with assumed characteristic profiles (black & grey), with simulated q_t-profiles (dotted lines).

2.3.4.4.2 Thin layer correction

The characteristic cone resistance, $q_{t,i}^{char}$ of a layer can be compared with either the measured cone resistance, q_t, or with the characteristic cone resistance in the other layer. The first ratio is denoted η and is called *the cone resistance ratio* as first defined by Robertson & Fear (1995). Its formulation is shown in eq. {2.43}. The second ratio is *the characteristic cone resistance ratio*, which is describing the tip resistance in the thin layer relative to the surrounding layer, denoted η_{thin}, given by eq. {2.44}. If $\eta_{thin} < 1$ then the surrounding soil is strongest, and vice versa for $\eta_{thin} > 1$.

$$\eta = \frac{q_t}{q_{t,thin}^{char}} = \frac{q_t}{q_{t,b}^{char}} \qquad \{2.43\} \qquad \eta_{thin} = \frac{q_{t,thin}^{char}}{q_{t,surrounding}^{char}} = \frac{q_{t,b}^{char}}{q_{t,a}^{char}} \qquad \{2.44\}$$

Soundings in relatively weaker intermediate layers:

$$q_{t,b}^{char} \le q_t \le q_{t,a}^{char}, \quad \text{which gives} \quad {}^{1}/_{\eta_{thin}} \le \eta \le 1 (q_t = q_{t,b}^{char}).$$

Soundings in relatively stronger intermediate layers:

$$q_{t,a}^{char} \le q_t \le q_{t,b}^{char}, \quad \text{Which gives} \quad 1 \le \eta \le {}^{1}/_{\eta_{thin}}.$$

In *Figure 2.31* the thin layer effect is coarsely sketched, e.g., H_S in the first layer is typically not symmetric with H_D in the third layer. The sketch introduces a new relation, written in *eq.* {2.45}, where K_H is *the thin layer correction factor*. This factor is multiplied with the extremal value of q_t; being the greatest reading in strong layers and vice versa in weak layers. The correction is quite basic, considering that only layer thickness and the cone resistance ratio is evaluated. This implies that in order to enable this correction method, K_H has to be calibrated for different thicknesses per material (while also being dependent on surrounding materials). Combining the previous equation with eq. {2.43} gives that the correction factor is equal to the inverse of the cone resistance ratio at the $q_t = q_{t,thin,peak}$, see eq. {2.46}. The correlation K_H is necessarily less than 1 for relatively weaker intermediate layers, and greater than 1 for relatively stronger intermediate layers.

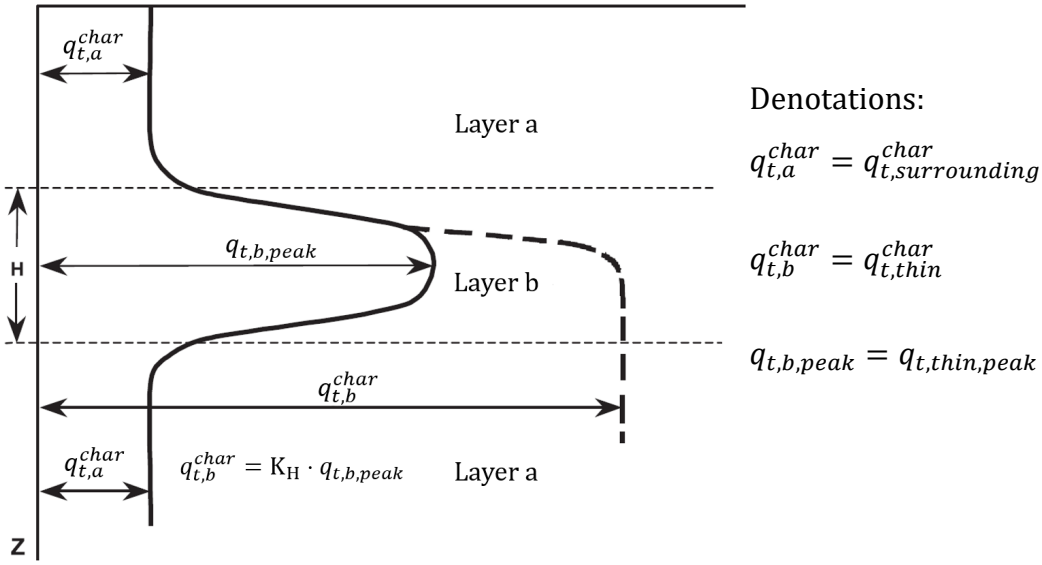

Figure 2.31. The thin layering effect for a stronger intermediate thin layer.

$$q_{t,b}^{char} = K_H \cdot q_{t,b,peak} \qquad \{2.45\} \qquad q_t = q_{t,b,peak} \Leftrightarrow K_H = \frac{1}{\eta} \qquad \{2.46\}$$

So far, liquefaction potential in sands has in a large degree been pushing the research interest of layering effects (eg., Robertson & Fear 1995, Ahmadi & Robertson, 2005, Boulanger & DeJong, 2018). Liquefiable sands are loose sands, which naturally yields smaller q_t than dense sands, but are relatively stronger than most silts and clays. Thus, most K_H-charts found in literature focused on assessing liquefaction potential in deposits with sand interbedded layer of smaller fractions. Consequently, only K_H greater than 1 has been of interest. By correcting soundings in liquefaction-prone areas, either liquefiable layers may be detected, or false positives of truly dense sand layers may be avoided. Robertson & Fear (1995) are possibly the first who proposed the procedure with the correction chart *Figure 2.33*, being included in the book by Lunne et al. (1997, p.47). Since then, the chart has been refined, e.g., in the more recent study by Boulanger & DeJong (2018), see *Figure 2.32*. The curves are all asymptotical, which reflects that a large distance must be covered in order to reach $q_{t,i}^{char}$. Thin layering effects have been shown to alter q_t-readings for layers thicker than $40d_c$ (Ahmadi & Robertson, 2005).

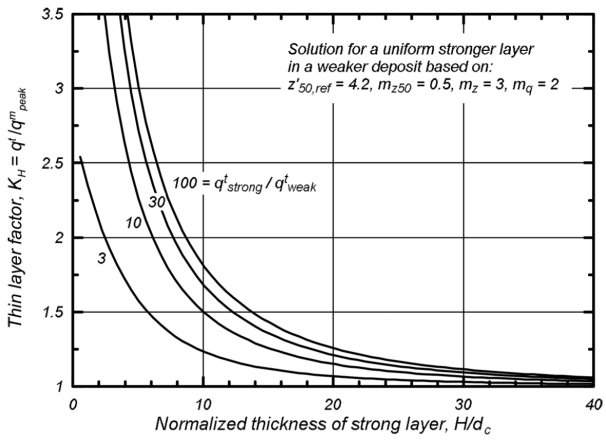

Figure 2.32. K_H computed for strong layers surrounded by two uniform weaker layers. $q^t_{strong} = q^{char}_{t,thin}$ and $q^t_{weak} = q^{char}_{t,surrounding}$, with ratio equal to η_{thin}.

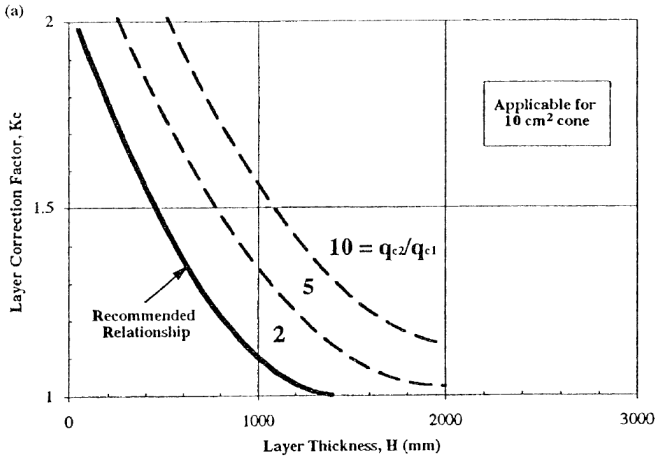

Figure 2.33. Original correction chart. $q_{c2} = q_{t,thin,peak}$ and $q_{c1} = q^{char}_{t,surrounding}$.

In the left figure, the tip resistance q_t is corrected with respect to the ratio between the characteristic tip resistances $q^{char}_{t,strong}$ and $q^{char}_{t,weak}$. Meanwhile, in the figure on the right hand side, q_t is corrected with respect to the ratio between measurement in the thin layer $q_{t,thin,peak}$ compared to the characteristic tip resistance in the relatively stronger surrounding layers $q_{t,strong} = q_{t,surrounding}$. Something which is important to remark regarding thin layer corrections is that the method relies on material a having the same characteristic tip resistance in both the upper and lower level. In practice, the lack of information of q^{char}_t and H associated the layers, render the thin layering effect difficult to evaluate, with an accompanying high related inaccuracy. Thus, one is back at square one.

Regarding thin layering correction for weaker interbedded layers, Hammer (2020) did in his thesis begin to construct a diagram similar to those above (*Figure 2.32* and *Figure 2.33*). Based upon the chamber test results he obtained from his experiments, he measured the thin layer correction factor K_H for different layer thicknesses, and associated these with interpreted characteristic cone resistance ratios, η_{thin}. The resulting chart he provided is presented in *Figure 2.34*. The respective η_{thin}-valkues to each data point is labelled besides.

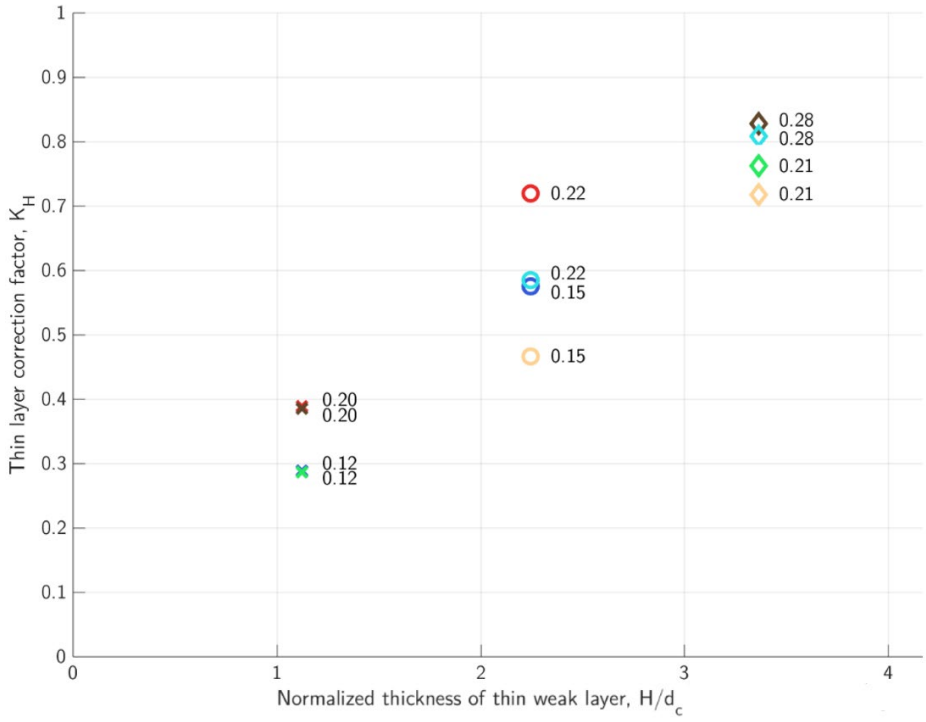

Figure 2.34. Diagram with the thin layering correction factor, K_H, plotted against normalized clay layer thickness. The diagram does more over include the ratio η_{thin}, based on the interpreted $q_{t,clay}^{char}$ and $q_{t,sand}^{char}$.

As to summarize the last chapter: The thin layering effect is a phenomenon which occurs, when the thickness of a layer relative to the cone diameter is too thin for the characteristic cone resistance to be reached. I.e., the influence depth is never surpassed. The thin layering effect show dependence on mainly the ratio between the interbedded layer thickness and the cone diameter, and furthermore on the contrast of characteristic tip resistances yielded by each layer. In addition, there are some other influences on the curvature of the q_t-profiles upon transitions which are caused by other intrinsic materials properties, such as the stiffness and possibly other properties as well.

2.4 Chamber testing

The purpose of testing samples in the chamber is to simulate field soundings, but due to the boundary effects, both the stress level in the fill material is reduced and measured q_t from soundings is reduced. These effects will be elaborated in this subchapter.

2.4.1 The silo effect

The model test is performed in a circular concrete chamber, where the wall gives the sample rigid boundaries conditions. There are frictional forces working along the interface between the wall and the sand in the chamber, where parts of the overburden load, or the vertical load acting through the sand is transferred into the wall. This transfer of forces decreases the stress level within the sample. The phenomenon is called the *silo effect* or eventually the more general term *arching* as named by Janssen who first identified the effect (1895). Terzaghi (1943, p. 66) defined the phenomenon of arching as: "Transfer of pressure from a yielding mass of soil onto adjoining stationary parts", i.e., further displacement, or *strain*, is prevented by a transition of normal stresses to shear stresses that are absorbed by a confining body of e.g., soil or a more rigid structure. This effect only occurs to fill-material, or what is by Schulze (2017a) defined as a *bulk solid*. Bulk solids can transfer shear stresses when the material is in a state of rest, as opposed to for example a Newtonian liquid as (e.g., water & air) where shear stresses are only occurring when a shear rate is applied, i.e., there is movement/flow displacement.

The loss of vertical stresses or the degree of the silo effect is depending on a number of parameters:

1) the diameter of the chamber or "silo", D_c,
2) the depth considered, z,
3) the interface friction, or the shear stresses at the wall, τ or τ_w. That further depend on:
    a. Mobilized interface friction angle, $\delta'_{mob} = \delta'$, between fill material and the wall. Otherwise, described by the friction coefficient, μ, i.e., $\mu' = \tan(\delta')$.
    b. The horizontal stress, σ_h, or "the stress working normally on the wall", σ_w, which is based on:
        i. The earth pressure coefficient, K', which is in some literature called wall pressure coefficient, K'_w (Sun et al. 2018). It depends mainly on:
            1. chemical compound,
            2. stress history, and
            3. deposition mode
        ii. The vertical stress level, σ_v, which again is based on surcharge, q, and bulk density, ρ_b:
            1. The bulk weight depends on level of compaction, i.e., porosity, n, and grain density, ρ_s. The level of compaction can be caused by either:
                a. overlying masses,
                b. applied surcharge load, or
                c. preconsolidation, i.e., the soil has previously been loaded beyond current stress level.

There is a circular reference in the scheme on the previous page: point 3-b), as the stress level alter the silo-effect, and the silo-effect alter the stress level, there becomes an asymptotical approach of some stress situation (for both σ_v and σ_h) with increasing depth. Hence, a ratio that is important to describe is the "height to diameter". As can be intuitively imagined, if the diameter is several times proportional to the height, then the only volume affected by the silo effect will be that close to the wall. The combined effect by K' (giving σ_h) and δ' gives larger transfer/transmission of vertical forces to shear forces working along the wall, decreasing vertical stresses within the fill material, increasing the rate at which the stress level reaches its asymptotical stress state ($\sigma_{v,\infty}$, $\sigma_{h,\infty}$ and $\tau_{w,\infty}$).

2.4.1.1 Janssen's method of differential slices

The average vertical stress, $\overline{\sigma_v}(z)$ working over the cross-section area can be deduced by setting up an equilibrium equation, with contributions accumulated over increments of slices as first set up by Janssen (1895). The method is also known as "the method of differential slices" or "the shear plane method" (Widisinghe & Sivakugan, 2012). A more perhaps refined and comprehensibly walkthrough has been compiled by Schulze (2017a), focusing on dry materials without surcharge. Some important reflections mentioned in his article will therefore naturally also be presented/repeated here. As the effect of surcharge was seldom included in literature, and since most literature revolved around dry materials (except of the preceding thesis by Hammer (2020)), it felt natural to present the theory utilized in this thesis a bit more in-depth. Hence, a deduction is included in Appendix A, while the solutions and uncertainties are presented in the following sub-chapters. An assumption that is used in the deduction is that the solutions given for total stresses are equally valid for effective stresses. This will be further elaborated in 2.4.1.5. Thereby, the notation in the equations will be given by effective stress state.

2.4.1.1.1 Stress state solution

An illustration with an infinitesimal vertical increment, with thickness dz, is shown below as background to the deduction of $\overline{\sigma_v'}(z)$. In the figure, g is the gravitational acceleration, and φ_x is the wall-soil interface friction angle, denoted δ' in this thesis. To repeat, the deduction is in Appendix A, and it is in addition followed up by a short note on Terzaghi's arching theory.

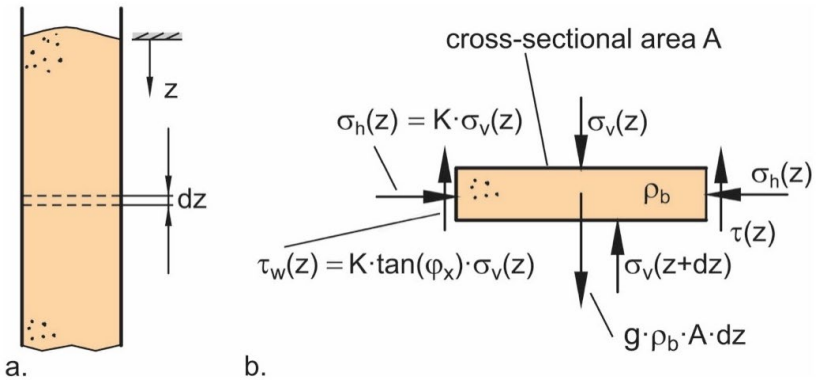

Figure 2.35. Incremental slice element (b.) of cylinder (a.), with associated forces acting on slice notated.

By introducing the term, *the decay length, l'*, many of the equations in the deduction can be simplified, see eq. {2.47}. Moreover, this measure describes the level of the asymptotical reached, and how quickly it is reached. Schulze (2017a) pointed out that the silo effect is depending on the cross-section area, A, relative to perimeter, U, i.e., the hydraulic diameter, D_h.

$$l' = \frac{D_h}{4 \cdot K' \cdot \tan(\delta')} \quad \{2.47\}$$

The solution for $\overline{\sigma_v'}$ become equal to eq. {2.48} for the case without surcharge, meanwhile when q is included the equation become equal to {2.49}.

$$\overline{\sigma_v'}(z) = \gamma' l' \left(1 - e^{-\frac{z}{l'}}\right) \quad \{2.48\}$$

$$\overline{\sigma_v'}(z) = \sigma_v' = q e^{-\frac{z}{l'}} + \gamma' l' \left(1 - e^{-\frac{z}{l'}}\right) = \gamma' l' + e^{-\frac{z}{l'}}(q - \gamma' l') \quad \{2.49\}$$

It should be emphasized that all solutions presented are based on some assumptions as e.g., the δ', γ' and K' are all constant with depth. The vertical stress in every slice is an average over the whole cross-section area, giving us a $\overline{\sigma_v'}$ (see ch. 2.4.1.5). The horizontal force that is accounted for, through K', is working along the wall, meaning that the horizontal stress elsewhere in the fill material does not necessarily have the same proportionally with σ_v', this can be imagined by looking at *Figure 2.35*. The estimation of K' will be discussed in 2.4.1.4.

2.4.1.2 Special cases

If there is a surcharge acting on top of the bulk solid, and the water table is placed at some depth, z_w, underneath the top/surface, the effective vertical stress, $\overline{\boldsymbol{\sigma_{v,2}'}}$ can be calculated as:

$$\sigma_{v,2}'(z > z_w) = \gamma' l' + e^{\left(-\frac{z - z_w}{l'}\right)} \cdot \left(\sigma_{v,w}'(z_w, q, \gamma) - \gamma' l'\right) \quad \{2.50\}$$

As previously mentioned, δ' and K' influence how quickly the asymptotic stress state ($\sigma_{v,\infty}'$, $\sigma_{h,\infty}'$, τ_∞) is "reached". The stress state, which is asymptotically approached when, $z \to \infty$, $z/l \to 0$, is shown in equations {2.51} and {2.52}.

$$\sigma_{v,\infty}'(z = \infty) = \gamma' l' \quad \{2.51\}$$

$$\tau_{w,\infty} = \sigma_{h,\infty}' \cdot \tan(\delta') = \sigma_{v,\infty}' \cdot K' \cdot \tan(\delta') = \gamma' \cdot \frac{D_h}{4} = \gamma' \cdot \frac{4 \cdot A}{U} \quad \{2.52\}$$

2.4.1.3 Interface friction angle

The interface friction angle can either be estimated by back-calculation, based on stress situation at the top and the bottom of the silo (σ_v', σ_h'), or by measuring it by performing direct box shear tests. An assumption widely used in geotechnics is that the internal friction angle is approximately proportionate to the interface friction angle, with a ratio of ca. $\omega = \delta'/\phi' = 2/3$ (Bowles, 1996, CGS, 2006, as cited by Li et al. 2012). Shear box tests performed by Li et al. (2012) associated their silo model test, demonstrated that this assumption works fairly well, obtaining a factor of $\omega = 0{,}6$ (δ' measured to 25,5° for their sand-steel interface, while ϕ' of the sand was determined to be 42,9°). For a specific fill material, this ratio will vary depending on the wall material, and δ' should therefore preferably be investigated instead of using the empirical approximation, even though it may provide a quick, rough solution.

2.4.1.4 Lateral earth pressure

Different estimations have been suggested as of how to obtain the coefficient of lateral earth pressure, K', for fill material that is either partly or completely confined by some rigid structure, e.g., silos (Yang et al. 2018, Sun et al. 2018, Li et al. 2012, Tien H.-S. 1996, ch. 3.3.4). The focus in literature is typically laid on either K' along the vertical centreline of the silo, or maybe more frequently on the stresses acting on the wall, with the coefficient sometimes referred to as the wall pressure coefficient K_w'. The most frequent mentioned estimations of K' will be presented here, and are all based on normally consolidated soils.

K' in silos is according to Yang et al. (2018), Sun et al. (2018) and Li et al. (2012) expected to lay somewhere in between Rankine's active earth pressure coefficient, K_a', presented in eq. {2.53} and the "coefficient of earth pressure at rest", K_0 (Jáky, 1948 as cited in Li et al. 2012), as presented in eq. {2.54}. All favoured K' to be close to K_a', near the silo wall. Li et al. also cited Marston (1930) telling that the approximation showed an adequate empirical correlation. Elsehow, for a more *ideal* fill material, being both linear-elastic and isotropic, K' can be deduced using Hooke's law and the Poisson's ratio, ν, see eq. {2.55}.

$$K' = K'_a = \tan^2\left(45° - \frac{\phi'}{2}\right) \quad \{2.53\}$$

$$K' = K'_0 = 1 - \sin(\phi') \quad \{2.54\}$$

$$K' = \frac{\nu}{1-\nu} \quad \{2.55\}$$

An in-depth article on the specific topic, by Sun et al. (2018), proposed 4 more coefficients based on invariants of the stress deviator tensor and one based on modified Coulomb theory, presented below, all of them were dedicated silo conditions.

$$K'_{MC} = \frac{\cos^2(\phi')}{1 + \sqrt{\sin(\phi' + \delta')/\cos(\delta')}} \quad \{2.56\}$$

As previously mentioned, the height to diameter ratio is important, so it is expected that σ_h' is proportional to σ_v' with another $K' \neq K_w'$ closer to the centre, that is dependent on the D_c/H-ratio. Considering that Jáky's formula regards a natural soil deposit in-situ, i.e., not affected by the boundary, it is reasonable to state that K' goes from K_a' along the wall, toward K_0' in the centre.

2.4.1.5 Sources of errors / Drawbacks of the method of differential slices

Some sources of errors mentioned in literature will be presented here. More will be discussed in the ch. 6.2.2.

2.4.1.5.1 Lateral earth pressure

There are many assumptions related the correlations for K' in silos leading to a high degree of uncertainty, 1) both implicit in the formulations and 2) going back and forth between analytical and experimental data, meaning both numerical- and practical data acquisition. For the first, K_a' is only valid for friction-less interaction, meanwhile the investigated phenomenon arching occurs exactly when there is friction at work, as reflected by Tien (1996, p. 55). Consequently, K_a' underestimate the real K', even for silo walls that yield (Jakobsen, 1958, as cited in Tien 1996, p. 59). Secondly, how σ_v' and σ_h' relates to each other are influenced by many factors, where Lindgård & Ofstad (2017) mentioned e.g., stress history, chemical composition, and mode of deposition to be of importance. For normally consolidated soils, the linear proportionality of K' is valid, meanwhile for soils that have experiences stress relief, the previous linear proportionality between σ_h' and σ_v' is no longer correct, as illustrated in *Figure 2.36*.

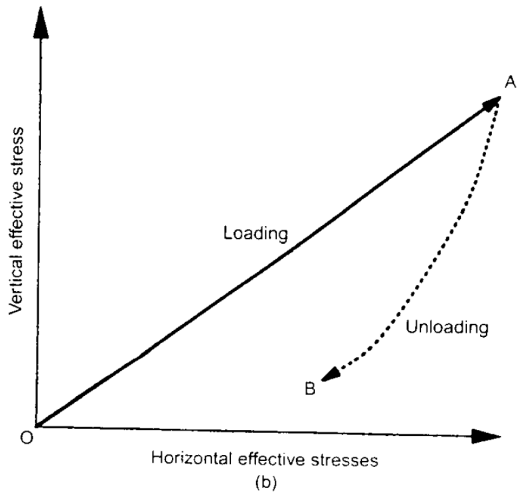

Figure 2.36. Proportionality between σ_h' and σ_v' during loading and unloading.

2.4.1.5.2 Stress distribution

It is unlikely that the real stress-distribution is symmetric and follow the idealized pattern which the calculations are based upon. The internal structure of the fill material and the interaction with the wall come both into play. Even with a completely homogenous fill, the silo

wall could still have imperfections as either points on the wall, or extensions/narrows along the whole perimeter. The effects are equal for both small imperfections, and those acting along the complete perimeter: For sections with increased cross-section area, there is a reduction of stresses that are transferred to the walls along the overhanging inclination, meanwhile more stresses are transferred at the up-faced inclination. The sum of forces further down on the wall may or may not be the same as prior, depending on geometry. For narrowed cross-sections, there is a peak followed by a drop in stress transfer. Figure 2.37 illustrate the stress distribution along such impurities. (Schulze, 2017b)

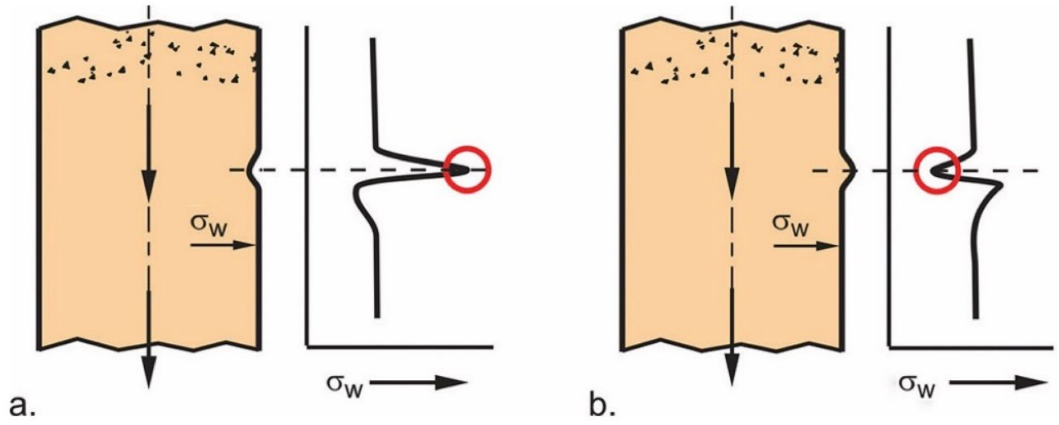

Figure 2.37. The effect of irregularities in the silo wall, inducing local increase, or decrease, of σ_h (denoted σ_w in figure).

There are other boundary conditions which also is neglected in the differential slices solution. E.g., the assumption of a completely linear increase in lateral stresses acting on the wall may be faulty, by not taking the lower boundary condition into account. Experience shows that, depending on surface roughness on the wall and on the bottom, there is a lateral stress relief as compared to what we assume theoretically, as shown in *Figure 2.38* (NTNU Geoteknikk, IBM, 2017, p. 321).

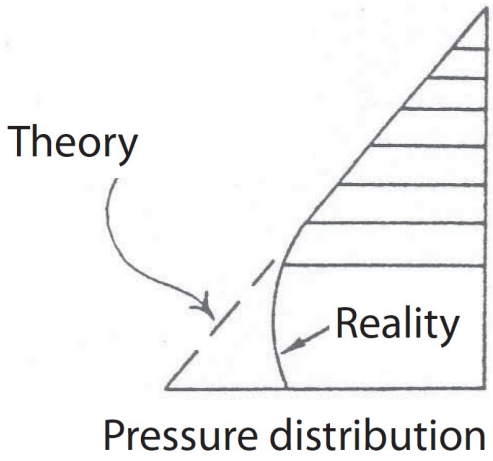

Figure 2.38. Illustration of lateral stress distribution on a wall inside a small model sand box ($55 \times 55 \times 50\ cm^3$) mounted with pressure cells.

Tien (1996, pp. 55-59) could in his literature study tell that the assumption of uniformly distributed vertical normal stress used in Janssen's model was incorrect and referenced to Jakobsen (1958, as cited by Tien) for a more correct solution. He did however tell that the equations based on Janssen's work were appropriate for some situations. Levesque et al.

(2017) conducted a numerical study, using a plane strain-model to estimate the stress distribution in a backfilled mine stope, with no surcharge, and a homogenous fill. Their result of σ_v- distribution can be seen in *Figure 2.39*, and can be said to confirm the previous statement. The distribution of σ_v, was highest along the centreline and decreased gradually towards the wall, giving an upward arrow-pattern of the vertical stress. Similarly, as $\sigma_v' \rightarrow \sigma_{v,\infty}'$, regardless of q' being smaller or larger than $\sigma_{v,\infty}'$ at the top, the arrow shape would point the opposite direction for $q' > \sigma_{v,\infty}'$. For the particular case where $q' = \sigma_{v,\infty}'$ the distribution will be according to the idealized slice-solution and completely uniform for the complete sample.

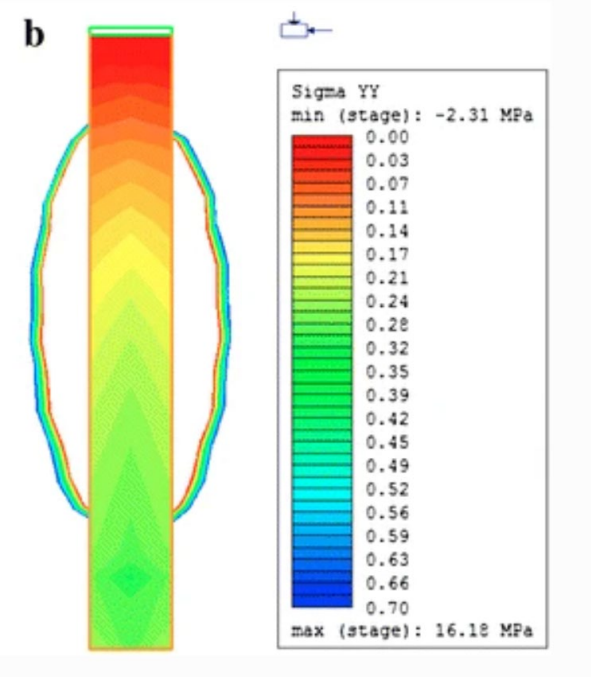

Figure 2.39. Simulated arching in a backfill of a mining stope, with contours of σ_v, red being zero stress and green being maximum stress.

2.4.2 Expected field values

The chamber boundaries do not only affect the stress situation in the test sample, they do also influence the measured tip resistance, which is reduced relative to what would be expected in the field. Different corrections have been suggested to simulate a "true value" which would be expected in the field. One example is from Mayne & Kulhawy (1991, as cited in Hammer, 2020, p.50), shown in eq. {2.57}, which was calibrated for tests in sand with larger stress levels (σ_v' around 140 kPa) relative to the current experiments performed at NTNU. Hammer (2020, p. 51) referred to different studies which tell that lower stress states within chamber samples yield larger differences between expected field values of q_t relative to measurements in chambers. Similarly, it was mentioned that the deviance increases with increased relative density in the samples.

$$q_{t,\infty} = q_t \cdot \left(\frac{D_c/d_c - 1}{70}\right)^{-D_r[\%]/200} \quad \{2.57\}$$

The study by Mayne & Kulhawy was concerning soundings performed in the middle of the chamber. For sounding closer to the boundaries, the influence on q_t will be even larger. As with the silo effect, if the ratio D_c/d_c is increased, the influence of the boundaries is reduced. However, this solution is rather impractical. Furthermore, even though the intention of the lab experiments is to simulate conditions in the field, no corrections have been utilized in the data treatment as this would require further research.

3 Natural clay samples

In the last experiment mini-blocks of both low- and high sensitive clay have been extracted and utilized in the large scale model testing. Accordingly, a brief description of the extraction site and of the sampling method is presented. The soil properties are reviewed based on site characterization made by L'Heureux et al. (2019), with reference to classification charts presented in the field and lab-compendium (NTNU Geoteknikk, IBM, 2017). The last sub-chapter is a review of sample disturbance and the accompanying influence on the soil properties. The motivation for presenting all this information is to support the link between the data found in this experiment with the reference of the NGTS-research.

3.1 NGTS-research site

The natural clay utilized in the current experiments have been extracted from the Tiller-Flotten geo-test site, south in Trondheim municipality, see *Figure 3.1*. Tiller-Flotten is one of five sites in the research- and developing program "NGTS – Norwegian Geo-Test Sites". These five sites are dedicated as reference areas which enables a solid foundation for comparison of different field methods, comparison between field and laboratory data, and for other similar purposes.

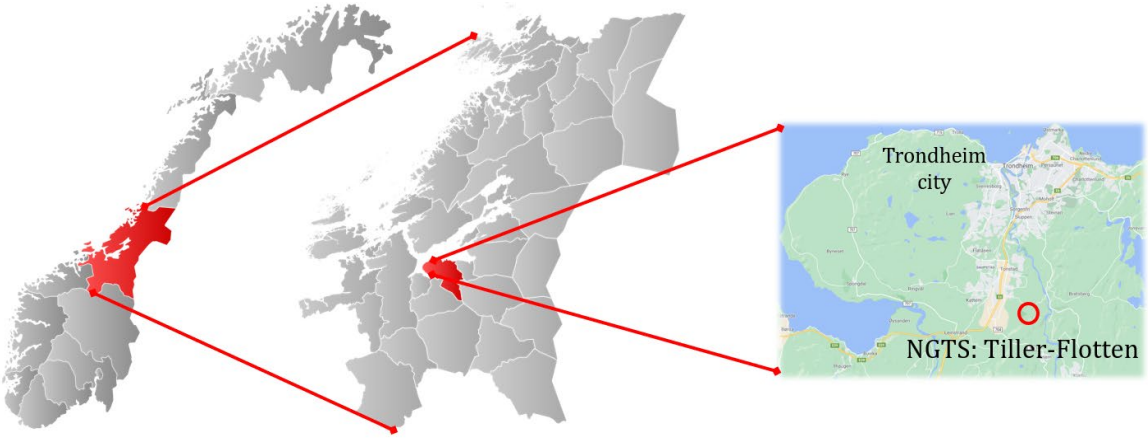

Figure 3.1. Tiller-Flotten research site, located south-east in Trondheim municipality, Trøndelag county.

The Flotten-site is well documented, with open-content information such as field test output data, and a comprehensive report on field characterization by L'Heureux et al. (2019), hereafter referred to as *the site report*. In the site report field- and laboratory data are presented, based on both high quality investigations and standard ones. In addition, much of the data are accompanied by interpretations. The deposits in the area originate from the seabed which has emerged since the last glacial period, and mainly consist of marine and glaciomarine sediments. The surface altitude is at 125 m.a.s.l., well below the local marine limit of ca. 170 m.a.s.l. The sedimentary composition in the area is shown in detail on the left in *Figure 3.2*. The map on the right, is retrieved from the open-content site DataMap, developed by Geocalcs (Doherty et al. 2018), and shows the extent of geotechnical surveys executed on the site.

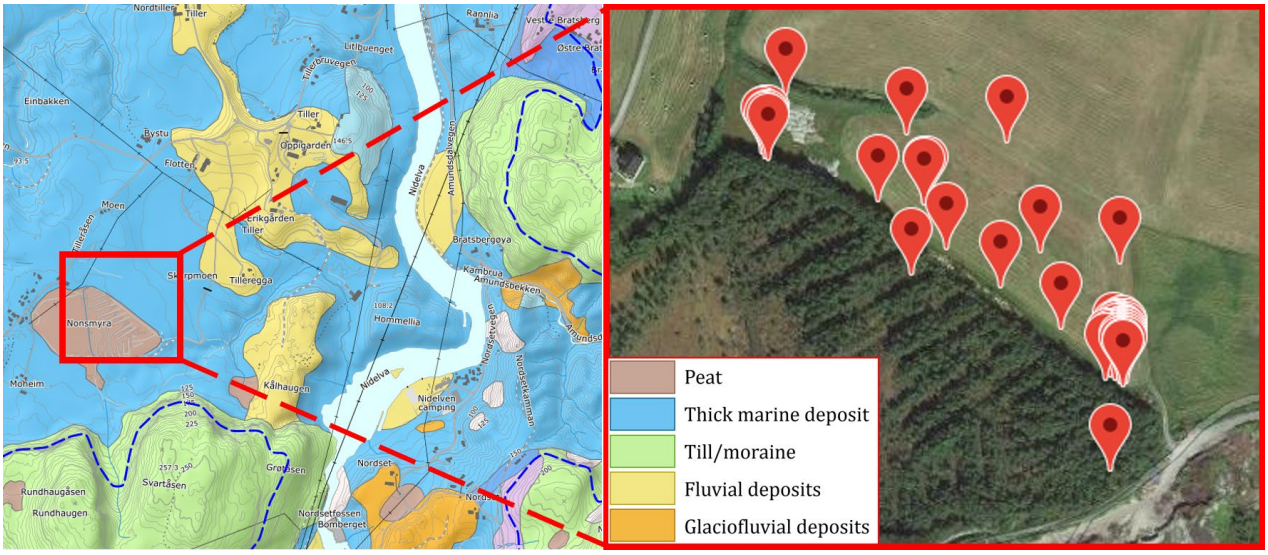

Figure 3.2. Left: Quaternary geology map of the site, mainly based on superficial deposits. The blue dashed line marks marine limits. Right: Map with the positions of field tests subjected the NGTS-project at Flotten.

The basic soil stratigraphy is in the site report divided into 3 intervals, I, IIa and IIb, with depths of 0-2 meter, 2-7,5 meter and 7,5-20 meters, respectively characterized as dry crust, low to medium sensitive clay, and very sensitive quick clay. The deposits extend further down, more than 50 meters below surface but these are not regarded in the report, and are neither relevant for the sampling done at 6-10,5 meters depth.

The position of the sampling hole, *A1*, is included in this chapter as it appeared most practical to have the map alongside the other maps of the extraction site. In *Figure 3.3* the position of the sampling hole is highlighted in yellow, with marked CPTU-soundings nearby, located south-east of the site. Other surveys have been filtered out of the map, due to tidiness. There are some piezometers installed along the woodside between the soundings and *A1*. The specific coordinate is found in the figure list and more information about the samples is given in ch. 3.3.

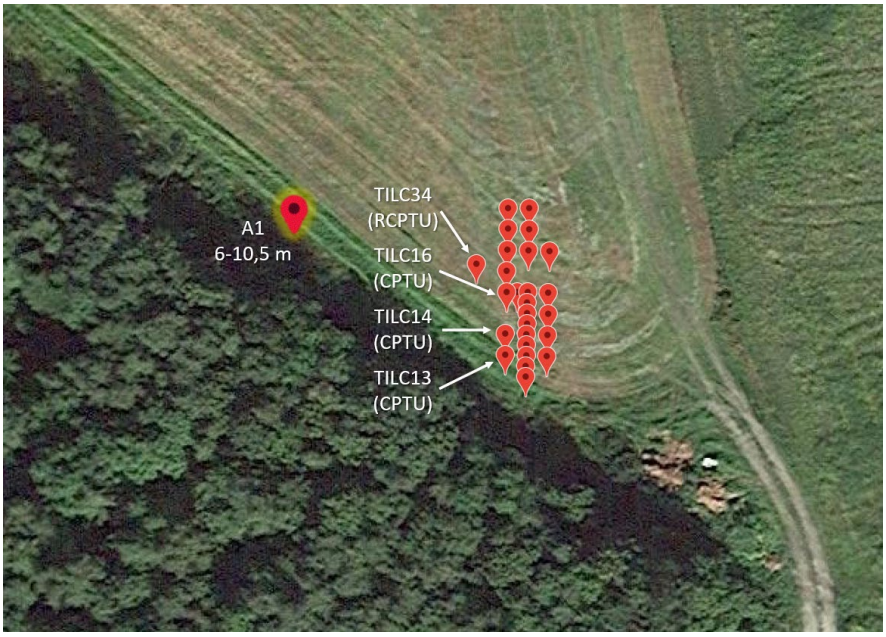

Figure 3.3. Sampling hole position, with filtered CPTU-soundings.

3.2 The mini-block sampler

As mentioned, the newly developed mini-block sampler at NTNU has been utilized in the extraction of clay samples for the model test. It is illustrated in *Figure 3.4*. High quality samples were desired for the experiment, leaving the options to either use the original Sherbrooke sampler by Lefebvre and Poulin (1979) or the mini-block sampler, which essentially is a scaled down Sherbrooke sampler (Emdal, et al. 2016). The influence of boundary effects is naturally larger for the smaller blocks, but due to practical reasons the latter was chosen. The method is more practical in the sense that it allows for easier rigging, preparation and is less labour intensive, giving an over-all increased efficiency and lesser cost. The size makes storage and transport easier, while it also eases the handling in the laboratory. Another expected implication of using smaller samples, apart from boundary conditions, is that the quality would deteriorate. The topic was researched in the master's thesis by Rognlien (2017), which stated that most properties remained equivalent for both methods, but deviances were seen in certain tests.

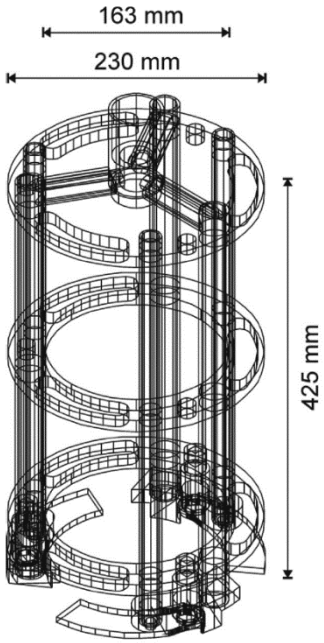

Figure 3.4. Technical drawing of the mini-block sampler.

3.3 Sample properties

To assess how representative the clay specimens in the test chamber were, some index tests have been performed before and after the chamber soundings. Some data from the Flotten site report will be presented in this chapter, including some classification tables and definitions. In addition, a short review of sample disturbance is included. For further details regarding properties of the sample material it is referred to the site report (L'Heureux, 2019).

3.3.1 Soil properties

In the site report, the trends are showing quite homogenous soil properties within the different defined strata. Some plots from the report will be included in this chapter, e.g., *Figure 3.5* which shows some index properties, and *Figure 3.6* which shows different field- and lab measurements of undrained shear resistance, including the shear strength normalized with respect to vertical effective stress. Both include basic stratigraphy, segmented into zone I, IIa and IIb.

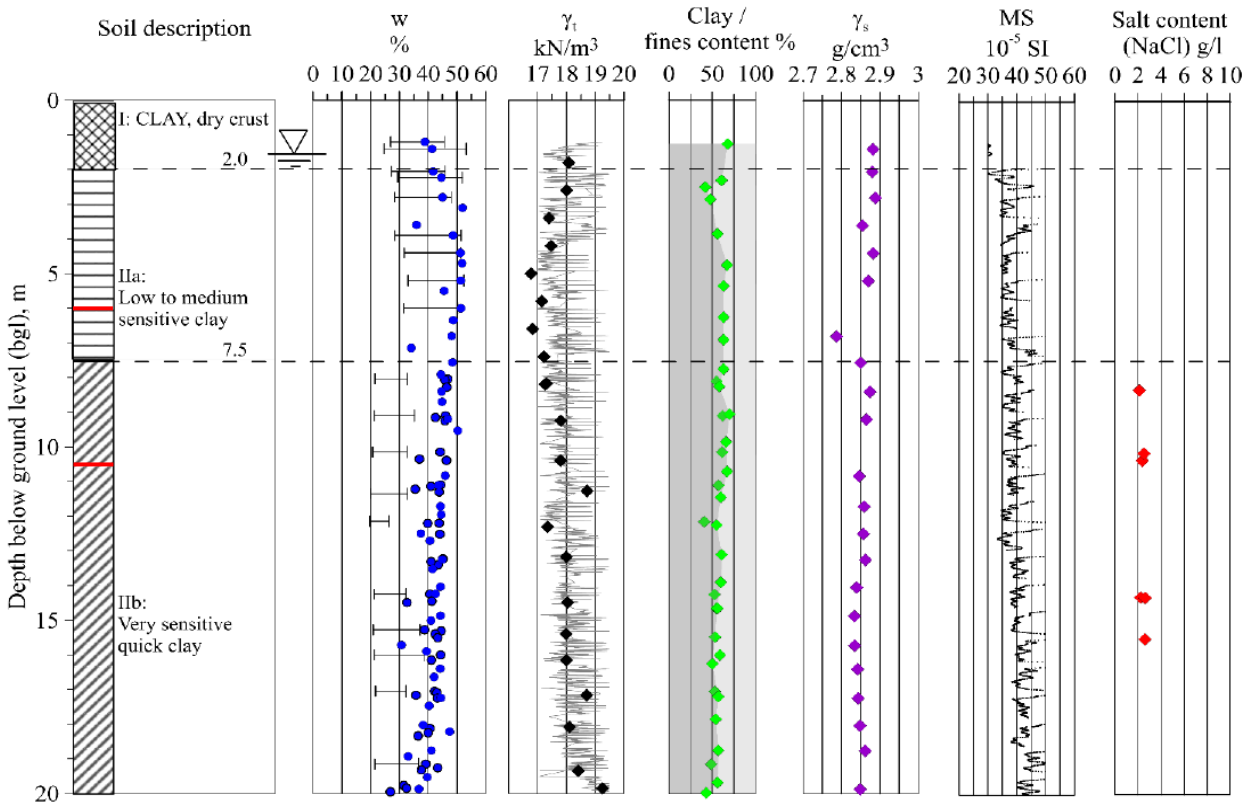

Figure 3.5. Basic soil stratigraphy with index properties. *MS* = magnetic susceptibility.

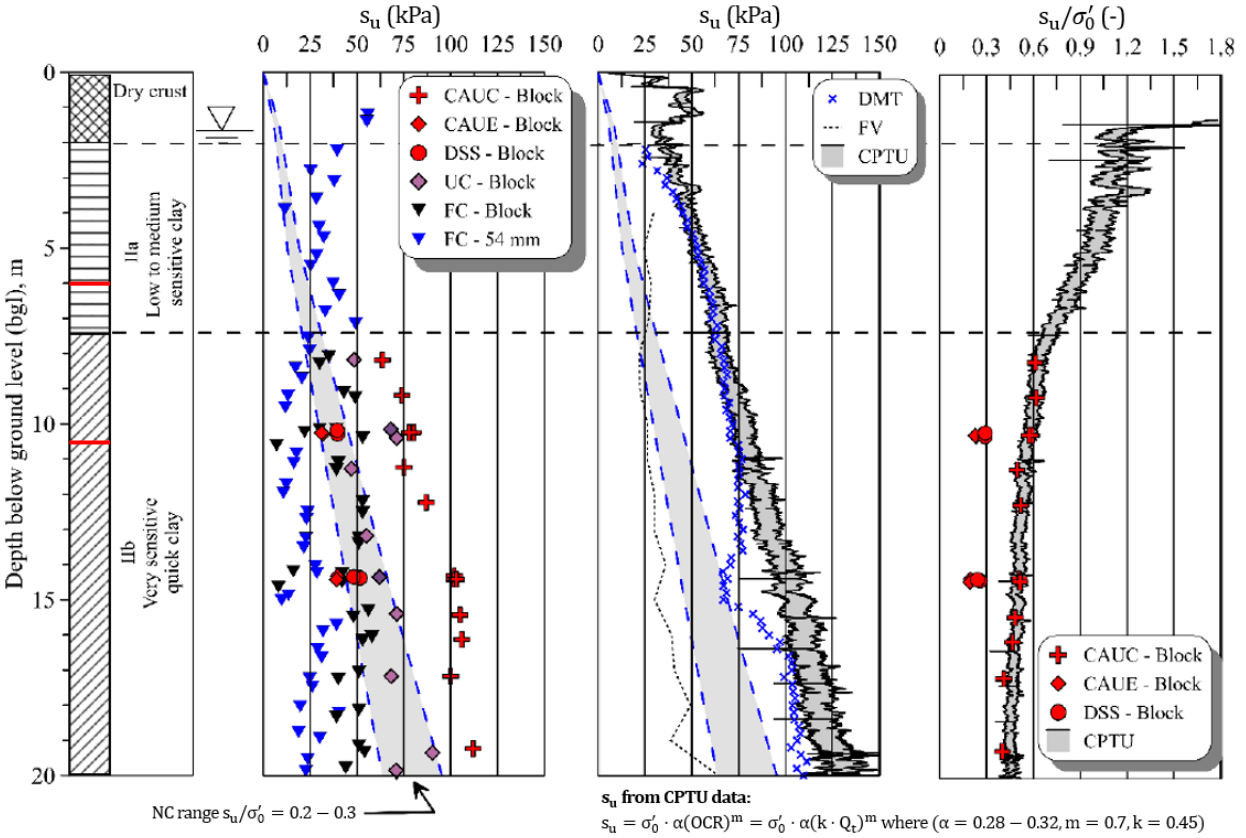

Figure 3.6. Different field (mid) and laboratory measurements (left) of undrained shear strength, accompanied by shear strength ratio (right).

The undrained shear strength shown in the previous figure varies a lot according to which tests have been performed, which underlines the statement that S_u is not a uniquely defined parameter. It varies according to imposed strain rate and also the stress state, which involve consolidation and anisotropy (confining stress). Moreover, the different methods; yield different accuracies; depend on the practice and sample treatment by the practician; and may be calibrated for certain soil types or conditions. A sample's shear strength is also influenced by disturbances, as will be explained in the next sub-chapter. If the sample is completely disturbed, i.e., remoulded, the denotation is $S_{u,r}$, which can be determined by the use of falling cone (denoted FC in *Figure 3.6*). The ratio between undisturbed and remoulded shear strength is defined as *the sensitivity* S_t, eq. {3.1}. Both $S_{u,r}$ and S_t is plotted in *Figure 3.7.* According to compendium in TBA4110 clay can be classified based on shear strength and sensitivity according to *Table 3.1* and *Table 3.2* (NTNU Geoteknikk, IBM, 2017). An alternative soil classification to that presented in *Table 3.1* is the classification chart given in ISO 14688-2 (CEN, 2017, p.9), but as the one presented below has been created with reference level to Norwegian soils, it seemed more appropriate.

$$S_t = S_u / S_{u,r} \qquad \{3.1\}$$

Table 3.1. Classification of soil strength.

Classification of soil type	Classification of shear strength	S_u [kPa]
Very soft	Very low	<12,5
Soft	Low	12,5-25
Medium stiff	Medium high	25-50
Stiff	High	50-100
Very stiff	Very high	>100

Table 3.2. Classification of sensitivity.

Classification of soil type	Classification of sensitivity	S_t [-]
Low sensitive	Low	<8
Medium sensitive	Medium	8-30
Very sensitive	High	>30

Some extra definitions have been provided in the study on "detection of brittle materials" as a 6th subject of the joint venture "the NIFS-project" (Sandven et al. NIFS, 2015, p.9):

- Brittle materials have per definition both $S_t < 15$ and $S_{u,r} < 2{,}0$ kPa;
- Quick clay has per definition $S_{u,r} < 0{,}5$ kPa.

In the lowest interval, IIb, the clay is very sensitive, with sensitivities reaching up as high as 350, while the remoulded shear strength is below 0,5 kPa. Thereby, the complete interval can be defined as a very sensitive quick clay. The measured S_u is higher for the block samples as compared to the 54 mm samples, which is linked to the sample quality and furthermore explains the difference in sensitivity. The clay in section IIa is low to medium. All these trends are highly visible in *Figure 3.7*.

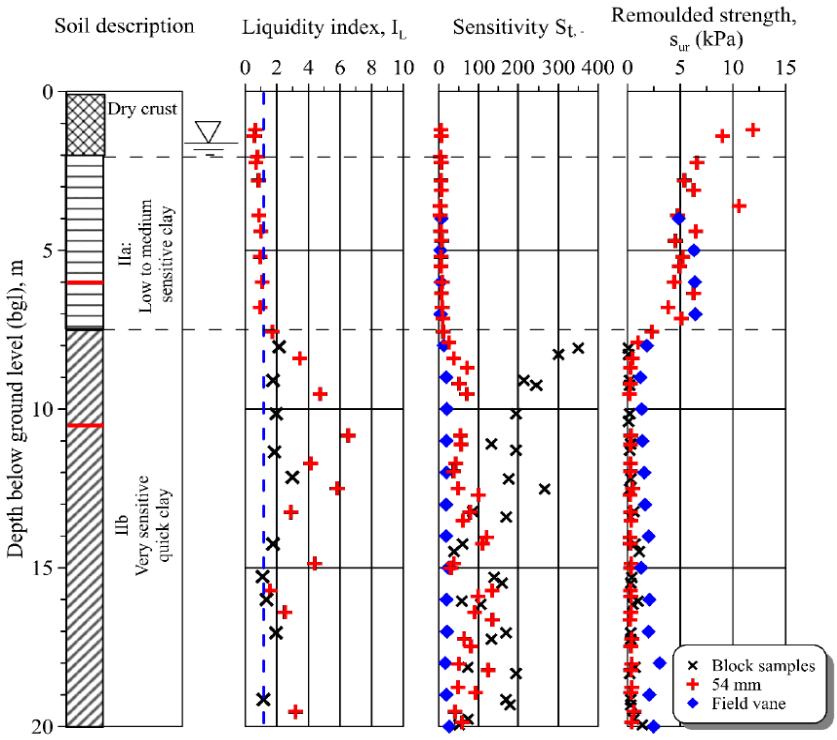

Figure 3.7. Depth profile with liquidity index, sensitivity, and remoulded strength.

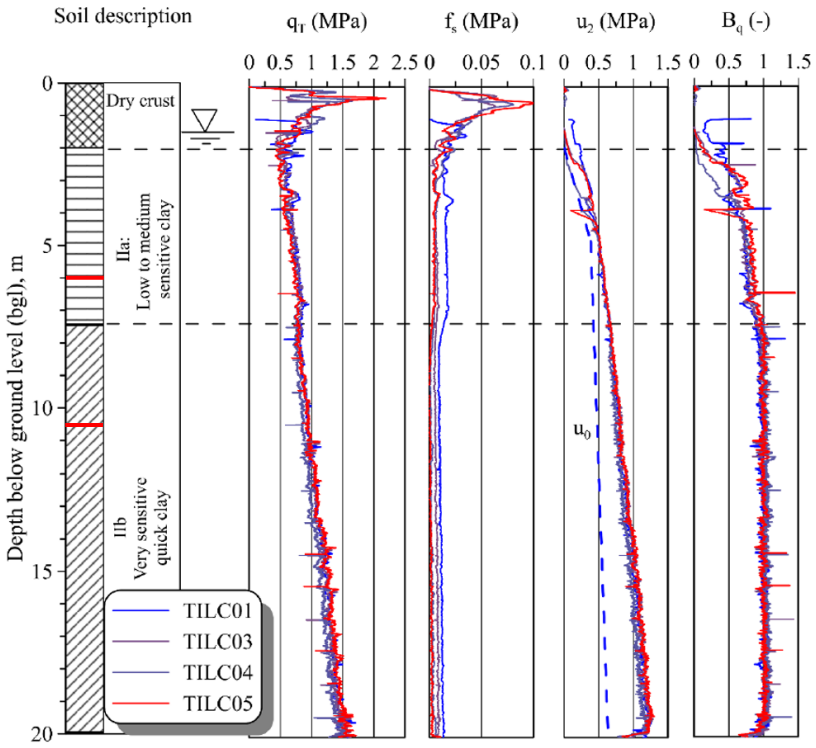

Figure 3.8. CPTU-profile of basic parameters, including the pore pressure ratio, B_q.

A collection of CPTU-profiles from the site is shown in *Figure 3.8*. L'Heureux et al. (2019) reflected that while the parameters q_t and u_2 deviated little between section II and IIb, the side friction dropped. This can be linked with the clay's high sensitivity. As mentioned in ch. 2.3.1.3 Lunne et al. (1997) pointed out that the measured side friction from CPTU-soundings is approximately equal the remoulded shear strength, implying that the sensitivity has a large impact on f_s. L'Heureux et al. (2019) referred to Sandven & Want (1995 as cited in L'Heureux, 2019) correlating quick clay with pore pressure ratios equal to, or greater than one. Hence, B_q is included in *Figure 3.8*, conforming with this statement.

Some further connections between the plots are possible to make, but first some more explanation will be given to *Figure 3.5*. Some of the consistency limits are here shown together with the natural water content. These limits describe the state of the clay based on water content, divided into four states: 1) Hard and dry, 2) Firm or crumbling, 3) Plastic or 4) Liquid. The transitions are defined by *the shrinkage limit*, w_S, *the plastic limit*, w_P and *the liquid limit*, w_L, whereas the interval between the two latter is defined as the plasticity index, I_P, eq. {3.2}. In the field and lab compendium at NTNU, based on plasticity, the material can be classified according to *Table 3.3*. The clay at Flotten, is ranging around 20 % in the interval IIa, while it is ranging between 8-15 % in interval IIb. Respectively defined as medium plastic and low plastic.

The state of the soil can be expressed by *the liquidity index*, I_L, eq. {3.3}. A liquidity index equal to either zero or one implies respectively $w = w_P$, and $w = w_L$. Values above one may indicate quick clay behaviour (NTNU Geoteknikk, IBM, 2017). Leroueil et al. (1983, as cited in L'Heureux et al. 2019) suggested an empirical correlation between the remoulded undrained shear strength and the liquid limit when $w > w_L$, as seen in eq. {3.4}. This correlation implies that $I_L > 1{,}6$ indicate quick clay. Thus, making the link between the graphs in *Figure 3.7* more evident. For the connection between undrained shear strength, the plasticity and sensitivity, made by Karlsrud et al. (1997), it is referred to ch. 2.3.1.3.

$$I_P = w_L - w_P \ [\%] \qquad \{3.2\}$$

$$I_L = \frac{w - w_P}{w_L - w_P} \qquad \{3.3\}$$

$$S_{u,r} = \frac{1}{(I_L - 0{,}21)^2}, \qquad I_L > 1 \qquad \{3.4\}$$

Table 3.3. Classification based on plasticity.

Classification of material	Classification of plasticity	I_P
Low plastic	Low plasticity	< 10
Medium plastic	Medium plasticity	$10 - 20$
Highly plastic	High plasticity	> 20

Other pertain information is that the preconsolidation stress, p_c' is about 250 kPa at 7,5 meters depth, increasing quite linear towards 450-500 kPa at 20 meters depth, roughly parallel to the in-situ stress $\sigma_{v,0}'$ with a difference of ca. 150 kPa. This indicates a probable stress relief on the site, but as stated in the site report, other effects on p_c' exist, e.g., aging and change in groundwater conditions, so it is referred to the report for more details. The OCR goes from ca. 5 close to the surface down to 1,5 in the bottom of the assessed depth profile, reinforcing the previous speculation.

In *Figure 3.6* the CPTU data (e.g., *Figure 3.8*) has been related to the S_u by two relations as will be explained. Firstly, by following the SHANSEP concept developed by Ladd & Foott (19,74, as cited in L'Heureux, 2019), the undrained shear strength is related with the stress history (OCR) and furthermore normalized with respect to $\sigma_{v,0}'$, see eq. {3.5}. By using the relation proposed by Mayne (1986, as cited in L'Heureux, 2019) in eq. {3.6}, the OCR can be found. Both expressions are empirical and must be calibrated with curve fitting parameters, α, m, and k. Respectively, these were found to be $0{,}28 - 0{,}32$, 0,7 and 0,45.

$$\frac{S_u}{\sigma_{v,0}'} = \alpha \cdot OCR^m \qquad \{3.5\} \qquad\qquad OCR = Q_t \cdot k \qquad \{3.6\}$$

Another relevant strength characteristic from the site report is the friction angle. From triaxial tests, the friction angle ϕ' has been interpreted to be in the range $29 - 32°$ with an associated *cohesion*, c, of ca. 5 kPa. The last relevant property is the grain size distribution. The report investigation shows that the clay content ranges from 45-70%. This falls within the clay-classification (>30%) according to the classification to to Norwegian Geotechnical Society (2011, p.14).

3.3.2 Sample disturbance

Extracted samples are prone to disturbances during all stages from extraction to the final testing in the laboratory. Hvorslev (1949) were among the first to extensively investigate and describe the causes and effects of sample disturbance. He classified disturbance of samples into five categories:

A) Changes in stress condition,

B) changes in water content and void ratio,

C) disturbance of the soil structure,

D) chemical changes and mixing, and

E) segregation of soil constituents.

He emphasized that different soils have different susceptibility of disturbance regardless of treatment. Due to the uniqueness of different soils, no universal measurement of disturbance was developed at that time, however, some trends were described for each of the classes listed above. Today, the topic has been further researched, and some objective measurements have been suggested for some specific soils. E.g., some different quality criterions have been suggested for triaxial testing on specific clays by Lunne et al. (1997, as cited in Rognlien, 2017) and Andresen & Kolstad (1979, as cited in Rognlien, 2017), respectively based on void ratio

and volumetric strain, both of which focus on the re-consolidation phase. Likewise, there exist quality criterions for odeometer tests too, e.g., the one suggested by Karlsrud & Hernandez-Martinez (2013, as cited in Rognlien, 2017). All of these criterions are quite specific, in contrast, the supplementary tests conducted in the last experiment are rough and have little objective criterions to be compared with. Thus, it is a bit difficult to assess the impact made by the deviances between the field- and lab data, in a qualitative way. I.e., comparing data from the Flotten site report with the lab results from the last experiment.

Most literature is in-depth analysing sampling methods based on more advanced testing, and look at the detailed changes of design parameters such as the oedometer modulus, M, p_c', and S_u. For such studies designated the mini-block sampler it is referred to the articles by Emdal et al. (2016), Amundsen et al. (2016) and the master's thesis by Rognlien (2017). The latter is focusing most on the performance of the mini-block sampler relative to the standard Sherbrooke sampler, but include more information on simple lab properties, such as the water content, unit weight and S_u based on falling cone.

The literature perhaps most pertinent to this thesis is the review on sample disturbance: report nr. 68 (L'Heureux & Kim et al. NIFS, 2014), which mainly focuses on storage time, and associated deterioration. The report summarizes that the most important mechanical effect of storage is the decrease in the parameters M, S_u (peak), p_c', $S_{u,r}$, S_t and *the compression index* C_c. The alternations are mainly attributed changes in the pore water, being chemical changes (e.g., oxidation, which moreover alter pH), drying and loss of moisture, and internal migration of pore water. In addition, changes in temperature and biological activity are mentioned.

The report states that a general trend for Scandinavian clays is increased w_L during storage, leading to a reduced I_L, which according to eq. {3.4} would explain the apparent trend of decreased sensitivity with time, especially if S_u is decreased too. Regarding the last, it is referred to a study on quick clay by Bjerrum (1973, as cited in L'Heureux & Kim et al. NIFS, 2014, p. 17) where triaxial tests were performed on samples directly after extraction on site and on some samples 2-3 days afterwards. They observed a relative reduction of peak S_u of 13,5 %. This was mainly linked with swelling due to stress relief. For other types of soil, the storage effects on S_u are varying. Bjerrum & Rosenqvist (1956, as cited in L'Heureux & Kim et al. NIFS, 2014, p. 27) observed an increase of both w_P and w_L, with an increased difference between the two, i.e., $\Delta I_P > 0$. This was linked with weathering of the clay minerals, detected by changes in the pore water chemistry.

It is stated in report nr. 68 (L'Heureux & Kim et al. NIFS, 2014), that storage of more than 10 days will entail changes in soil properties, especially for, but not limited to, piston samples. A proposal repeated several times in the report is to measure the pH upon sample extraction or upon arrival at the laboratory, and then once more upon sample preparation. The reason is that the pore water pH is sensitive to oxidation, and thereby provide a good indication of sample alternation. The report also underlined that the sources of sample disturbance is difficult to separate.

In addition to all the mentioned disturbances, it is obvious that mechanical impacts, vibrations and similar will weaken the material as well.

4 Method

This chapter is divided into methodology associated literature study; the set-up and methodology in the laboratory; the sounding equipment; the pressure cells; and lastly, a list of the limitations associated the experiments.

4.1 Literature

The literature review was originally quite systematically logged in a self-made excel-sheet, with the intention of providing a bibliography which could complement the reference list. However, this turned out to be laborious and tedious, so it was discarded mid-way through most of the literature review. A bibliography would probably anyhow contain less relevant literature and thereby be excessive. Most of the literature work was done after the last experiment, which ended 11th of May. In the following sub-chapters, the most relevant literature is presented and briefly reviewed.

4.1.1 Silo effect

In a literature study by Tien, H.-J., (1996), much of the foundations of arching theory is presented, including works by Terzaghi (1936, 1943), Marston (1930) and Janssen (1895). Further, Schulze (2017a) presented an in-depth practicable and concise walk-through of the silo effect for dry materials, based on the theoretical framework by Janssen (1895). To take the surcharge into consideration, a complete equation was available from Hammer's thesis (2020). However, since the literature on arching effects rarely took surcharge into consideration, it felt natural to present the theory behind. It was not until later in the thesis work, other literature including surcharge was found, e.g., the work by Terzaghi (1943, p. 88), which was also presented in the work by Tien (1996, p. 46). Moreover, almost all found literature on the silo effect was focusing on dry granular fill material, so some assumptions were adopted from Hammer's work (2020). It was not until later that the series of articles made by Li and Aubertin (2008, 2009a, 2009b, 2009c, 2010 as cited in Li et al. 2012) on the silo effect including wet fill material was found. Because of insufficient time, I was not able to proofread and compare assumptions in the silo chapter with those presented in their work. By skimming through some of it, many similarities concerning assumptions were found.

4.1.2 Lateral earth pressure coefficient

The drift of the vertical earth pressure cell during tests was high, making it of interest to see how well the produced readings are correlated with both empirical and analytical results found in literature. For K' in the specific case of rigid boundaries, literature was quite consistent, with experimental data from Li et al. (2012, 2014), Widisinghe & Sivakugan (2012), and numerical data from Levesque et al. (2017), Yang et al. (2018), Sun et al. (2018). For K' in the more general terms only "factors of influence" were of interest, where the master's thesis of Lindgård & Ofstad (2017) was found the be the most relevant.

4.1.3 CPTU-correlations

Due to recommendations, the topic of cone factors was studied. The topic combines analytical geotechnics with the empirical nature of CPTU, and can thereby be used in assessment of soil properties and soil classification. Typically, the suggested relations work well for homogeneous soils, however for transitions their associated assumptions are no longer met, and consequently the theory is no longer valid. The readings include: the literature for limit plasticity theory included in the educational compendium (NTNU Geoteknikk, IBM 2016), the work by Senneset & Janbu (1985), Senneset et al. (1989), Mayne (2005, 2007), CEN (2016); for cavity expansion theory Vesić & Jones, (1977) and Zhao et al. (2018); for cone factors in general Karlsrud et al. (1997); for soil classification Robertson (1990, 1998, 2016); and for all listed topics Lunne et al. (1997).

4.1.4 Thin layering effect

This topic was of main interest subjected this thesis, but due to extensive laboratory work, the literature was investigated relatively briefly. Hammer (2020) provided an abundant amount of literature on the topic, so those articles which appeared most pertinent were read, and referred to here. These were Boulanger and Dejong (2018) which had a combined report on experimental results and inverse filtering, and furthermore Mo et al. (2017), Tehrani (2017) and Wang (2019) which in detail investigated the transition between clays, and between sands, by the use of DIC and PVI. Moreover, the scale effect should be regarded as of great relevance, not only because of different sizes of cones were utilized, but also regarding transitions from the surface and between materials. Nottingham (1975) presented this topic as part of his Ph.D. Thesis, and the information was considered adequate for the purpose. The articles of Van der Linden (2017, as cited in Hammer, 2020) has also been stated as important within the topic but has not been read.

4.1.5 Use of natural clays

Sample quality or sample disturbance, is of high importance for experiments involving samples of natural clay. Such samples are susceptible for changes in properties in every stage from extraction to the very sounding of a chamber sample. Literature on sample quality is abundant on the internet, yet typically the literature is too specific with respect to materials and testing methods. The report by L'Heureux & Kim et al. (NIFS, 2014) was relevant on a general basis, and is thereby a good starting point for preliminary planning of sample preparation with natural materials. It may provide a more conscious approach regarding preventative measures, and it provide some recommendations on relevant tests to assess sample quality as well. In addition, the quality criterions by Lunne et al. (1997, as cited in Rognlien, 2017) and Andresen & Kolstad (1979, as cited in Rognlien, 2017) could be utilized in quality assessment of samples prior to, and after a chamber experiment. The study by Hvorslev (1949) is very comprehensive, and is mainly focusing on sampling methods and

associated disturbances, therefore, only chapter 6 is regarded as pertinent to the experiments. For disturbance regarding sampling methodology, it is referred to Emdal et al. (2016) and Amundsen et al. (2016). No little literature was found on the usage of field samples in construction of large-scale model tests. Thereby, it may be a research interest to develop some assessment criteria regarding the representativeness of such experiments, with comparison to what is simulated.

4.1.6 General literature

In general, the book "Cone penetration testing" by Lunne, Robertson and Powell (1997) is extensively investigating many topics related CPTU and included many useful references. The thesis by Hammer (2020) was the initiation of the research program at NTNU and naturally provide much information about the complete nature of the encompassing experiments. Secondly, researchers, consulting firms and institutions who have published their research and publish data free of charge, deserve some appreciation, e.g., Mayne, Robertson and contributors to the open-content service DataMap (e.g., NGI in the NGTS-project). An effort has been laid down in presenting links to as much literature as possible, to secure quick access for the readers.

4.2 The laboratory equipment, set-up, and methodology

4.2.1 The structure of the experiments

To be concise, some specific notations have been given the different elements involved in the experiments:

- Firstly, *the chamber sample* is the assembly of clay and sand that fills up the test chamber, which later is sounded.
- Secondly, the arrangement of the clay blocks utilized in the experiments has been given specific notations:
    - The term *block* is used for single packaged blocks of pottery clay, or for extracted natural mini-block samples. The extraction profile of the mini-blocks has been numerated with roman letters, see. ch. Appendix C.
    - The blocks are cut into several *specimens*.
    - The specimens that are placed in the chamber, either stand alone, or are placed adjacent to other specimens in a collection, supposed to act as "one". Both of these options are denoted as *units*.
    - Several units at the same base level makes up a *layer*, labelled with Greek letters chronologically from the bottom and upwards, e.g., α, β, and γ.
    - A *sub-sample* constitute the layering profile which is sounded, within one *section*. I.e., different sections with equal layering profiles are differentiated. Sections are described in the paragraph under.

To describe further arrangements, the horizontal cross-section reference system will first be explained, as illustrated in *Figure 4.1*: The chamber is conceptually partitioned in three 120°-*sectors*: AB, BC, and CA. The intermediate dividing radiuses, and the chamber centre are respectively denoted as; *section* a, b, and c; and *section* S. As there is a metal disc on top of the sample, the soundings positions are restricted to the pre-cut holes in the disc. These holes are partitioned along the sections a, b, and c, including one in the centre, S. The holes are then numerated with reference to the centre, i.e., the centre is numbered 1, the second tier of holes from the centre are numbered 2, etc. Thereby, the soundings are assigned a number according to the disc hole, followed by a letter for the sounded section.

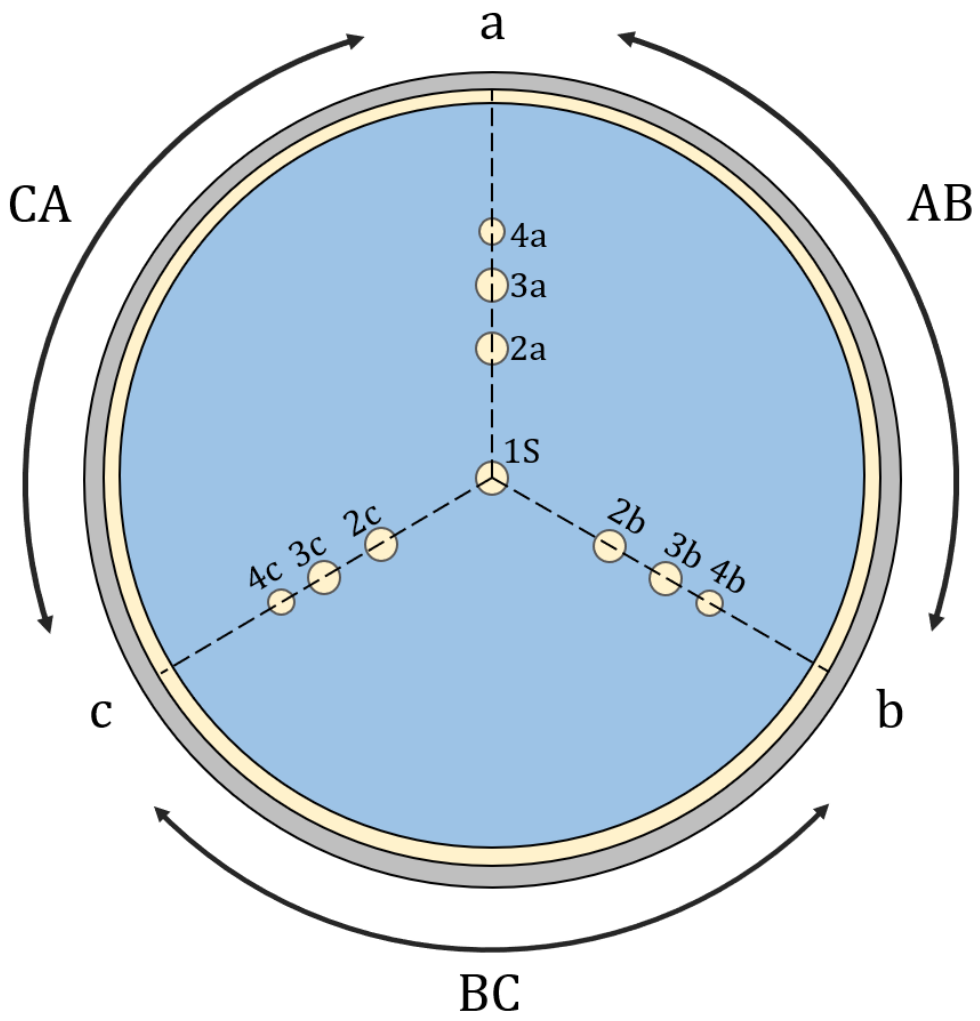

Figure 4.1. Chamber partition, with marked: sectors; sections; and sounding holes in the metal disc.

4.2.2 Equipment and materials

The large-scale model experiments have a comprehensive list of equipment and materials. A compressed list of the most basic equipment is listed in the Appendix D, while the most important components and materials will be explained in detail in the following subchapters, including elaboration of the construction of the chamber samples. The natural clay is only in part described in sub-chapter ch. 4.2.2.4, while its properties and origin are described in ch. 3.

4.2.2.1 The chamber

The chambers samples in the current experiments were built inside a chamber consisting of a manhole base and a ring (denoted chamber extension), both made of reinforced concrete. This provides rigid boundary conditions for the samples. The same chamber was used in the experiments of Hammer, reaching a height of 2,3 meters. The magnitude of the silo effect experienced in his experiments was great, with an approximate constant effective stress level throughout the chamber sample. Tall samples are more influenced by the silo effect, so in posteriority of his experiments the height of 2,3 meter was considered excessive, as it would only give the sample construction more complexity and work-effort. In addition, the experiments were allocated to another location, which constrained the heigh of the model size. Consequently, the chamber was downscaled to ca. 1,5 meters height. The interior dimensions of the chamber elements were 1,20 meter in diameter, D_c, with an inner height of 95 cm for the chamber base, $H_{c,\mathrm{I}}$ and 51,4 cm for the chamber extension, $H_{c,\mathrm{II}}$, making up an inner height of 146,4 cm, H_c. Upon lowering the chamber extension on the base, a rubber gasket was placed in-between to prevent leakage. In the bottom of the chamber there was a water in-/outlet with valves, the water set-up is described in ch. 4.2.3.3.

Figure 4.2. Chamber base, with some guiding height lines.

Figure 4.3. The chamber extension, note the rubber gasket on the rim of the chamber base.

4.2.2.1.1 Treatment of interior walls

The inner surface of the chamber was quite rough, with scattered cavities and some protrusions. Thus, to minimize the friction along the wall, thereby decreasing the silo effect, Hammer (2020) covered the interior of the chamber with a plastic film in his experiments. The walls have since been through different treatments: Prior to experiment 0, the interior wall was painted with epoxy-paint to decrease the wall-friction. In the preparation stages of the experiments 1a-3, the chamber wall was cleaned and plastered with spackle, followed by sanding and painting a thick layer of epoxy-paint. This made the surface very smooth relative to the original one. There were some hitches associated this treatment, which required tentative repairs, as will be discussed in ch. 6.1.1. The magnitude of the silo effect will be presented in the graphs in chapter 5.3.3 and is furthermore discussed in ch. 6.2.

4.2.2.2 Sand

The same sand has been utilized for all of the current experiments at NTNU. It is extracted from *Stokke Grustak* in Kvål, Melhus municipality, and is labelled type 0/2, which means that grain size should be less or equal to 2 mm. The sand from Stokke contained 0,2 mass-percent of larger grain size than 2 mm, meanwhile 1,2 mass-percent of the grains had less than 0,06 mm diameter (Hammer, 2020). As reference, the grain size of sand is defined to be within 0,06-2 mm (NTNU Geoteknikk, IBM, 2018). The sands properties were determined by Hammer in his thesis and are listed in *Table 4.1*. They were found through sieve analysis, pycnometer test, porosity procedures by DEGEBO (Deutsche Gesellschaft für Bodenmechanik) and undrained triaxial tests performed on reconstituted sand samples. Prior to sample construction, water content samples in the sandbags have been made from ca. 10-20 cm into the sand. Hammer's sand had $w \approx 6\%$, the water content has generally been $3 - 4\%$ in the later experiments, yet some bags have been very dry with respectively 4‰ and 1%.

Table 4.1. Sand properties determined by Hammer (2020).

Property	Mean	Unit
d_{10}	0,175	mm
d_{50}	0,492	mm
d_{60}	0,742	mm
$C_u = \frac{d_{10}}{d_{60}}$	4,24	-
ρ_s	2,73	g/cm³
e_{max}	0,873	-
e_{min}	0,502	-
n_{max}	46,6	%
n_{min}	33,4	%
$\rho_{d,max}$	1,83	g/cm³
$\rho_{d,min}$	1,45	g/cm³
$\rho_{max}(S_r = 100\%)$	2,15	g/cm³
$\rho_{min}(S_r = 100\%)$	1,94	g/cm³
$E_{50}(p' = 35\ \text{kPa}, \text{e} = 0{,}65)$	18	MPa
$E_{50}(p' = 35\ \text{kPa}, \text{e} = 0{,}86)$	4	MPa

Figure 4.4. Sand from Kvål.

4.2.2.3 Pottery clay

In the early phase of the current experiments, Hammer and his advisors evaluated different solutions of preparing the clay material. They landed on acquiring a pallet with blocks of pottery clay as it required less preparation, both with respect to time consumption and complexity. The pottery clay has been utilized in all experiments except from the very last, experiment 3, where natural clay was used. The clay is produced by *Sibelco*, is named *K148* and consists of kaolin clay. The clay was delivered in plastic wrapped "12x13x31 cm³"-cuboids which weighted ca. 10 kg each. Consequently, the density of the clay was approximately $\rho = 2$ g/cm^3. The clay was homogenous with close to no impurities. A new batch of clay blocks was bought after Hammer's experiments. These were stored in a cold storage room. Some tests have been performed in order to determine the properties of the clay, both in the latest experiments and by Hammer in 2020. The tests performed solely by Hammer are undrained triaxial compression tests (CAUc and CIUc) and oedometer test. Both have performed tests on the consistency limits, water content, and on the undisturbed and remoulded shear strength by falling cone test. All the new test results (under Mean$_{E0\text{-}2}$ in *Table 4.2*) are from sounded specimens, with the exception of the water content, which is from newly opened blocks. The results from Hammer (2020) are listed under Mean$_{HBH}$, where the measurement of S_u is based on triaxial tests (CAUC, CIUC), and are thereby regarded as accurate. A picture of a packed block and a cut block is seen in *Figure 4.5*.

Table 4.2. Clay properties of K148 determined by Hammer (2020).

Property	Mean$_{HBH}$	Mean$_{E0\text{-}2}$	Unit
w	23,8	24,6	%
w_L	30,5	34,9	%
w_P	18,5	19,1	%
I_P	12,0	15,8	%
I_L	0,44	0,35	-
$S_{u,CAUC}$	27,5	-	kPa
$S_{u,FC}$	-	41	kPa
S_t	~1	2,3	-
E_u	3	-	MPa
G	1	-	MPa
E_{oed}	4	-	MPa
m	27	-	-
p'_c	100	-	kPa

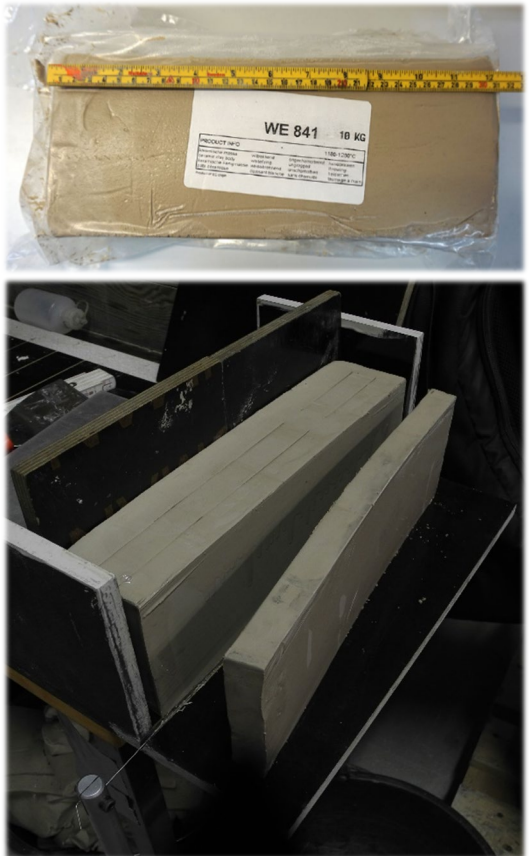

Figure 4.5. Above: Wrapped pottery clay block. Below: cut block.

4.2.2.4 Natural clay

The blocks of natural clay were extracted 16th and 17th of march at borehole A1 at Flotten, with UTM-32-coordinates 7023917., 571088., 123. EUREF89. Due to uncertainty regarding the feasibility of using quick clay as a sample material, some of the extracted clay was taken from the depth of low to medium sensitive clay ($z < 7{,}5$ m). The blocks were extracted with the mini-block sampler, giving maximum dimensions of 35 cm in height and ca. 16 cm in diameter. The blocks were taken from 6-10,5 meters depth. The sampling above the quick clay was more challenging, and thus some blocks before and close to the layer transition had smaller dimensions. The sampling profile is partitioned into continuous intervals, and subsequently, the blocks are numerated according to position within these intervals, as listed in *Table 4.3*. A preliminary test was done on block III-II before easter holidays, with an 8 cm specimen (8,55-8,63), the rest of the block was wrapped thorough and placed back into the storage room. It was checked whether if the specimen would survive build-in, considering that the surrounding layer of sand is compacted with a heavy plate vibrator. Visually, there were no noticeable changes after the excavation, see *Figure 4.6*. Moreover, the specimen was tested with a field inspection pocket vane prior to, and after build-in, and in addition tested with the falling cone test. The specimen survived well and had values coinciding well with those seen at Flotten, ch. 3.3. See ch. *Figure 5.23*, 5.2.1 for the results. Unfortunately, among the blocks of quick clay, III-1,5 was not discovered standing in the storage room until the experiment was already done, thus it was never used.

Table 4.3. Block extraction depth profile.

Block name	Top	Bottom	Day extracted	Day taken out of storage
I-I	6,15	6,45	16.03.2021	Not used
I-II	6,45	6,8	16.03.2021	16.04.2021
II-I	7,15	7,416	16.03.2021	09.04.2021
III-I	7,87	8,2	17.03.2021	12.04.2021
III-1,5	8,20	8,55	17.03.2021	Not used
III-II	8,55	8,9	17.03.2021	23.03.21 (rewrapped), 14.04.21
III-III	8,9	9,25	17.03.2021	13.04.2021
III-IV	9,25	9,6	17.03.2021	10.04.2021
III-V	9,60	9,95	17.03.2021	16.04.2021
III-VI	9,95	10,3	17.03.2021	19.04.2021

Figure 4.6. Pocket vane test prior to (left), and after (middle), build-in. Excavated intact specimen (right).

4.2.3 Set-up

4.2.3.1 Clay layer set-up

The layering of the finished chamber samples ended up as listed in *Table 4.4,* with clay layer thickness, H, for each sub-sample listed in *Table 4.5.* As may be understood from the first presented table below, layers did not necessarily end up at the exact intentioned heights, as these typically had round numbers. A vertical cross-section of experiment 0 is shown in *Figure 4.7*, with a somewhat misleading horizontal dimension of the clay samples. The true geometry will be clearer after the next sub-chapters.

Table 4.4. Layering of the sample as of finalization, with height, H_c, and the depth, z, given in cm.

	Experiment 0		Experiment 1a		Experiment 2		Experiment 3	
Distance	H_c	z	H_c	z	H_c	z	H_c	z
Sand, top level	138,4	0	90,3	0	141,1	0	141,1	0
Clay, base of level 3	-	-	-	-	109,6	31,5	114,7	26,4
Clay, base of level 2	99,5	38,9	-	-	79,1	62,0	81,3	59,8
Clay, base of level 1	47,7	90,7	37,5	52,8	46,2	94,9	47	94,1
Earth pressure cells	22,5	115,9	21	69,3	21	120,1	21	120,1
Gravel, top	10	128,4	10	79,3	10	131,1	10	131,1
Bottom	0	138,4	0	90,3	0	141,1	0	141,1

Table 4.5. Clay layer thickness, *H*, with unit given in cm.

	Experiment 0			E1a	E2	E3	
Zone	a	b	c	b	a-c	S	a-c
H, level 3	-	-	-	-	2	4	2,8
H, level 2	4	4	8	-	4	8	5,7
H, level 1	8	12	12	36	8	12	8,5

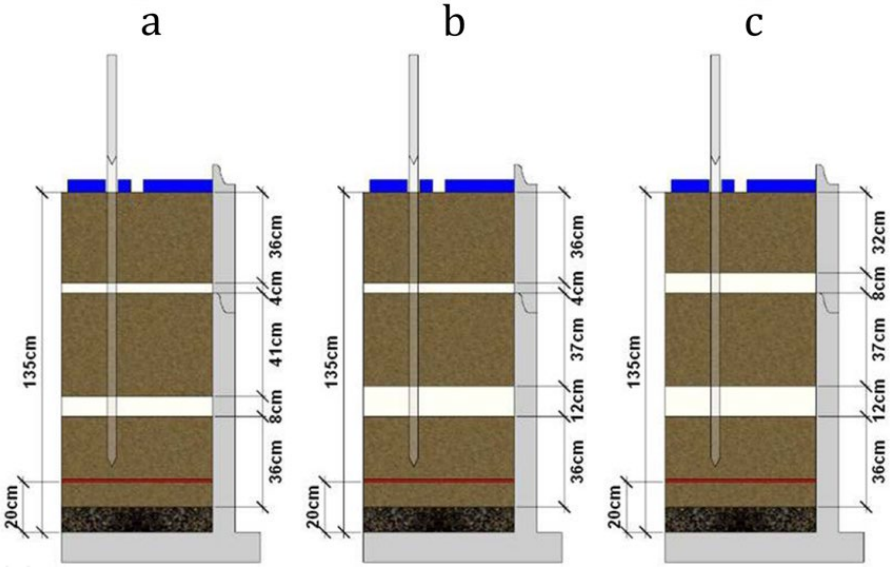

Figure 4.7. Intentioned layering in experiment 0, the horizontal width of each clay layer is misleading.

4.2.3.2 Preparation of test specimen

At the bottom of the chamber a 10 cm layer of gravel was placed. This was then covered by a couple of filter cloths, to prevent washing of the deposits from the chamber. These were overlapping each other with 20 cm and the endings were sealed by pushing and stubbing sand on the folds in a suitable manner. The elements are illustrated in the figures below.

Figure 4.8. Utilized gravel.

Figure 4.9. The first 10 cm of the chamber was filled with gravel.

Figure 4.10. Filter cloth.

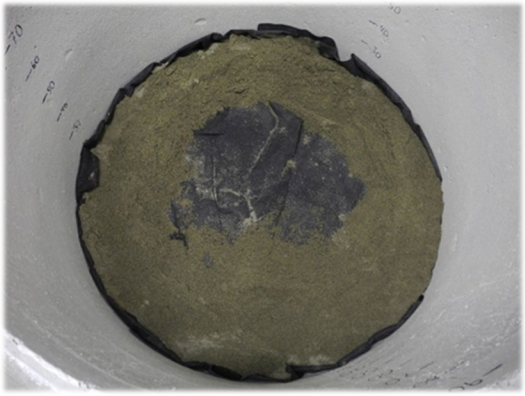

Figure 4.11. The cloth was squeezed to the wall by pushing and stubbing the sand.

The first sand layer was laid above the filter cloth. Throughout the course of the year, the procedures of creating sand layers have varied. The methods were intended on creating homogeneous, medium densely packed sand ($D_r \sim 40 - 60\%$) that could resemble a natural sand deposit. The procedures are explained in the following sub-chapters.

4.2.3.2.1 Sand preparation procedure 1

In experiment 0, the repeatable 4 stage method for adding sand developed by Hammer was used. The first out of four stages consist of adding sand by an approach similar to dry-pluviation, except that moist sand is utilized ($w \approx 4 - 6\%$). The sand is furthermore placed directly on the sieve, seen in *Figure 4.12*. The metal sieve was composed by two layers of expanded metal mesh, wired together with steel wire, giving equal to or less than 15x15 mm openings. The sieve was placed at fixed heights, hanging in chains from four steel brackets placed on the rim of the chamber. The diameter was 1,15 meters, which allowed for sideways movement in the chamber. When the sand was placed on the sieve, it was then rained through the sieve down on the sample by shaking the sieve. The height of a new loose sand layer has been denoted Δh_f in this text. This part of the procedure could also rather be called a raining procedure.

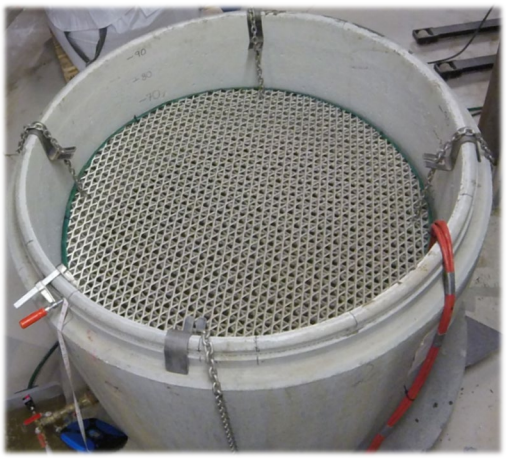

Figure 4.12. Metal sieve hanging from brackets.

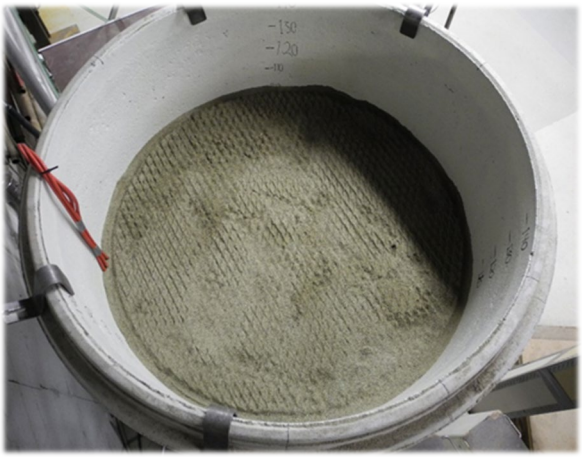

Figure 4.13. 1st phase, newly rained sand.

In Hammers' experiment the raining procedure gave a very loose state of the sand. Hammer observed porosities of the rained moist sand ranging up to around $e = 1{,}25$, which is above the determined $e_{max} = 0{,}873$. This is explained through the standardized procedure of DEGEBO on how to determine e_{max}, which is based on an approximation of finding the loosest state which occurs naturally, not artificially. The sand that was rained in the current experiments was partially saturated which gave the sand cohesive properties and a looser state was achievable.

In the second phase, the sand was fully saturated with water which gave settlements, denoted $\Delta h_{s,1}$. This was done by filling the chamber through the inlet at the bottom, with an appropriately low water flow, preventing fines from being transported and sorted within the sample. It further prevented the development of interior channels within the sand as well. The 10 cm of gravel was meant to distribute the waterflow evenly along the horizontal cross-section of the chamber. In the third stage the water was discharged again and typically a low additional settlement was observed, commonly ranging one sixth of the settlement in the prior stage. This settlement has been denoted $\Delta h_{s,2}$.

Figure 4.14. 2nd phase, fully saturated sample, excess water on top.

Figure 4.15. After 4th phase, water discharge, followed by vibration.

In the fourth and last stage a stiff circular wooden plate of 1,14 meter diameter was laid on the sand to distribute the impact of the plate vibrator over the whole surface, see *Figure 4.16*. For every new layer that was vibrated, the lower layers got additional vibration. To prevent this, undercompaction was performed, i.e., the vibration cycles were incrementally longer for each new layer, to approximately achieve a final homogenous packing of the entire sample. After the settlements caused by the vibration, Δh_c, the final height of the new layer, Δh, was reached.

Special care was necessary for sand layers surrounding clay units, with different raining heights for the sieve. The lowest placement was intended as "max overlay height" for the thinnest clay units, and was rained on the whole cross-section. This was followed by a second height intended for the thickest clay unit, where the whole cross-section except parts over the lower clay unit was filled, and finally, a max level where the sand was rained everywhere except over the clay units. This was done as clay do not get compacted by the vibration, and thus the sand above the clay would absorb much of the vibration and get more compacted than the sand elsewhere.

Figure 4.16. 4th phase, plate vibrator on wooden plate.

Figure 4.17. Sand layer thicknesses adjusted the clay units' heights.

A picture of sand over clay before saturation is shown in *Figure 4.17*. The full sand procedure for experiment 0 is sketched in *Figure 4.18*.

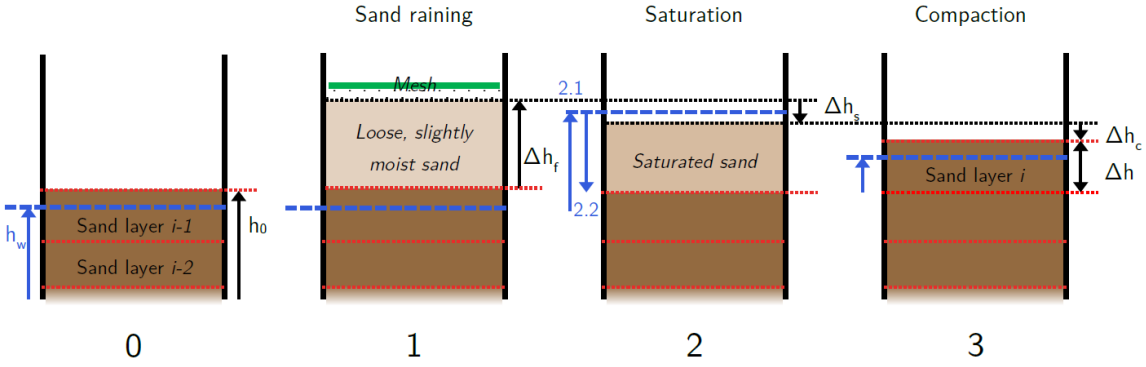

Figure 4.18. Schematic construction of sand layers.

4.2.3.2.2 Sand preparation procedure 2

The sand of the first procedure yielded less tip resistance than desired, and was deemed too loose. Therefore, some new procedures were evaluated, where the original idea was to build a series of chamber samples consisting of solely sand, termed 1 followed by a letter: e.g., 1a. These would provide a good foundation for comparing build-in methods based on time consumption and compaction, and would moreover provide critical depth, z_c, associated each build-in method. As the time was restricted, it was determined that only the chamber base would be used, giving 90 cm samples. Only one such sample was built due to the time consumption, where further sand tests would have restrained the number of future tests with clay. Moreover, the test 1a yielded useful results, and thus new sand tests were cancelled.

Different stress levels were considered for the different sand tests, but as to have a solid foundation, additionally accounting for the homogeneity, two of the inner soundings had to be equal. It was then considered more valuable to use the third sounding hole to some other purpose. The very first chamber test by Hammer (2020, p. 152, case A) intended to determine the characteristic tip resistances in loose sand and clay, consisted of very loose sand ($D_r \approx$ 10%) and consequently the clay block attached the probe mid-way, getting dragged between

0-3 cm down. The readings were thereby not optimal, and the new experiment 1a provided thereby an excellent opportunity to create a more consistent reference profile for q_t^{char} of the pottery clay.

The procedure was simpler and faster: In the first phase sand was shovelled directly into the chamber, circumventing the raining part. Phase 2 and 3 remained the same, while in the 4th phase, the plate vibrator was put directly into the chamber without the use of the wooden plate. The latter method required a shorter vibration time due to the increased magnitude of compaction per area. Thereby, the plate vibrator was only turned rapidly on and off, where the compaction by vibration still commenced while the plate vibrator settled/calmed. A systematic "flower" pattern was followed, as to distribute the compaction as homogeneous as possible, performed in two rounds, covering the complete layer surface. Due to the rapid nature of this methodology, undercompaction was not performed. The vibration method also allowed for construction of a high clay sample simultaneously as the adjacent sand could be compacted without the need of new, special cut distribution plate.

Some disadvantages regarding the method were: anticipated less homogeneity within the sand, and secondly, construction-wise, some of the "saved time due to simplicity" lead to less even layer surfaces. To flatten the surfaces, large spatulas of 20 and 40 cm were used, respectively in the end of phase 1 and phase 2. This increased the workload again, yet in total, this procedure was faster. The sand was gently spread with the spatulas, while it was attempted to not compact the sand in the areas with excess sand. The layers were checked with a spirit level. Due to this control, a previous unclear perception was confirmed, the chamber rim, which was actively used as a reference level, was not completely even (a few millimetres). The soundings of experiment 1a yielded large thrust forces through the probe and the rods, close to the capacity of the actuator, so it was decided that the sand-building procedure would be renewed a second time.

4.2.3.2.3 Sand preparation procedure 3

The third, and last sand procedure that was utilized was quite equal to the previous one, where phase 4 was reverted to the first methodology. I.e., the wooden plate was again used to distribute the vibration compaction, which again allowed for undercompaction. This refined procedure was deemed successful with a relative density of ca. 40%, and was therefore used in experiment 2 and 3.

4.2.3.2.4 Sand procedures in general

In all the procedures, a height measurement was made after every phase. This was done using a self-made height measurement device made up of a L-beam, with a steel measuring tape fastened with a F-clamp, see *Figure 4.20*. Under the construction of the sample, the distances were measured with reference to the current rim of the chamber, which was denoted z_L. The logging was made with an approximate millimetre precision, with specific reference points in the chamber. Yet, due to the extent of the sample surface, this precision must be considered a bit obscured.

Figure 4.21. Broken silt-/clay lump.

Figure 4.19. Collection of impurities, mainly soft lumps, and a little gravel.

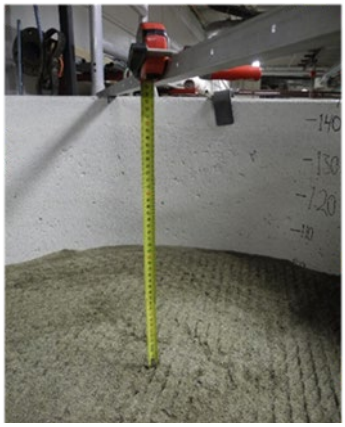

Figure 4.20. Height measurement device. Measurements were made after every phase.

During construction, any observed impurities, such as clay-lumps and seldom some rocks, were removed and discarded, see *Figure 4.21* and *Figure 4.19*. The risk of including such impurities was small in sand preparation procedure 1 due to the sieve. Meanwhile, for the other procedures, the risk was much higher. Yet, if one is observant during the filling operation in these latter procedures, one may avoid a majority of these impurities anyhow.

The plate vibrator was very heavy to lift all alone into and out of the chamber, especially due to the momentum of stretching the arms over the rim, into the chamber. Some different solutions were utilized throughout the experiments: Sometimes the lab technicians or some friends helped lifting it in and out. Mostly it was done alone by hand, but equipment such as a hand hydraulic stacker and a chain hoist was used as well. The latter was first available for experiment 3, and was then hung in the rack above the chamber, as shown in *Figure 4.22*. It turned out to be very helpful and much safer.

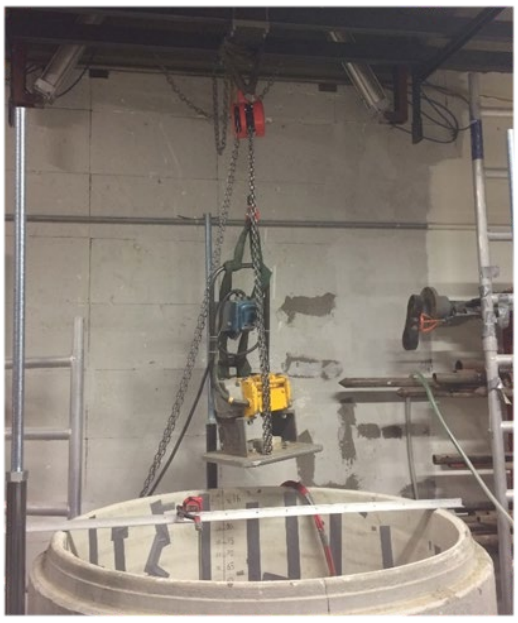

Figure 4.22. A chain hoist provided a good solution for the plate vibrator handling.

4.2.3.2.5 Pressure cells

Some circular Geokon Model 3500-3 earth pressure cells were placed close to the bottom of the chamber, to log the pressure from both the sample's self-weight and the artificial load. This has been of importance, as the stress level affect the material properties of sand in a large degree, while it is also of interest in the CPTU-assessment. Furthermore, it is known that chamber fills are subjected to silo effects, as elaborated in ch. 2.4.1.

The arrangement of the pressure cells is as illustrated in *Figure 4.23*, with an upright pressure cell, "number 5", which was added after experiment 1a. I.e., it was only included in experiment 2 and 3. The cells were 23 cm in diameter and ca. 1 cm thick, and placed horizontally with a surface level of 22,5 cm and 21 cm respectively for experiment 0 and 1a-3. The upright cell 5 was placed with vertical centre point at height $h = 24{,}5$ cm with the top and bottom reaching heights respectively of 36 and 13 cm. The cell was supported by pushing moist sand ($w \approx 4\%$) against the plate.

For the best performance of the pressure cells, the cells were installed according to the instruction manual (Geokon, 2019). "Preferably the cells should be surrounded by soil equal the fill material it is to be installed within". I.e., in the chamber, the cells should be placed some distance from the gravel, as to obtain equal stiffness above and below the cell. Furthermore, the sand should be homogeneously compacted around the cells, in order to reduce potential arching in the surrounding soil.

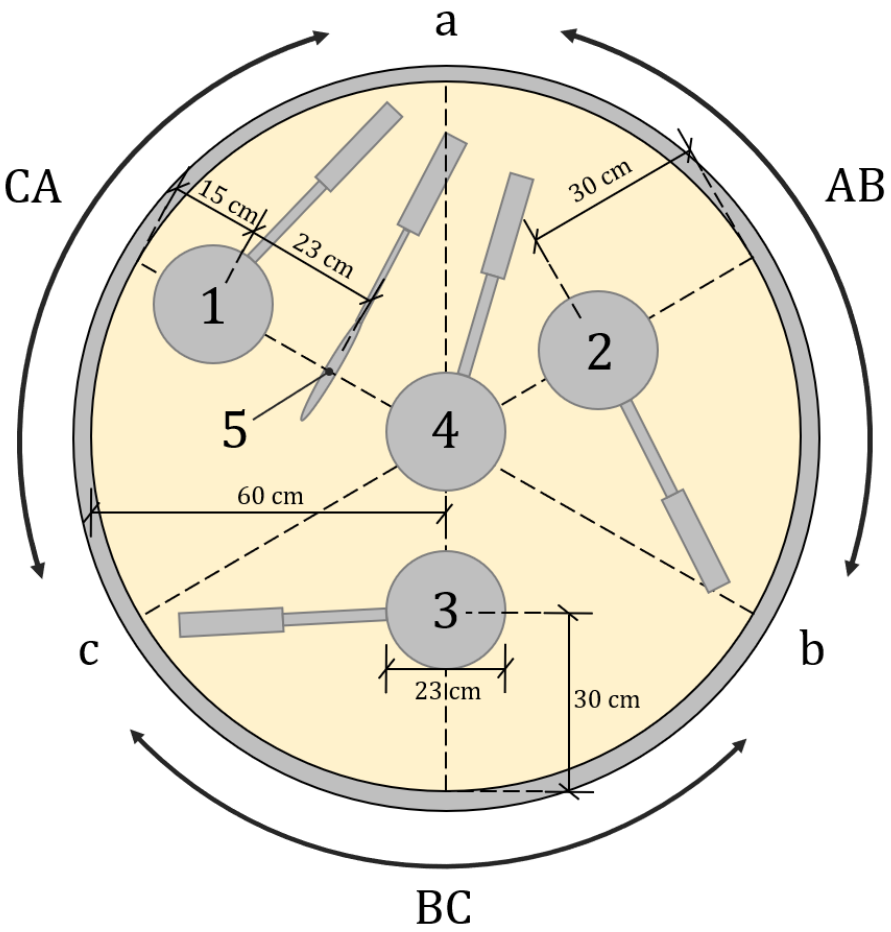

Figure 4.23. Arrangement of pressure cells, with numeration and sector denotation.

Practically, the pressure cell cables were bundled together at the end of the transducer housings of cells 1, 4 and 5, and were further lead along the wall, over the rim. The cables were thereafter connected to a DAQ-box (Data acquisition box) connected to the computer. Upon adding a chamber extension, the cables had to be lifted into the chamber during the installation, (typically together with the DAQ-box to save time). Afterwards, the equipment was reconnected to the computer. Obviously, the operation gives a break to the pressure logging and should hence be done in one continuous operation, as to keep track on both the water level, and on the potential change in readings from cell 1-5 (see end of this chapter).

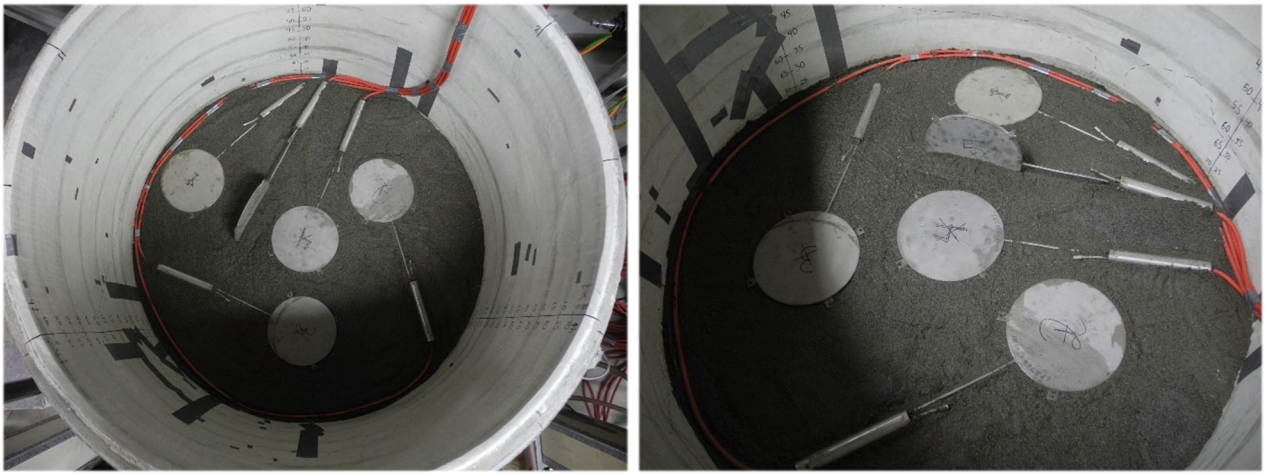

Figure 4.24. The pressure cell set-up in experiment 2 and 3, from different angles.

The cells were taken out of the chamber and re-calibrated between experiment 0, 1a and 2, while they remained untouched for the last transition. When test 1a was done, a short process of testing and comparing available cells was commenced. This was provoked by the deviating logging from cell 2. Thus, in order to get more conforming results, cell 2 was changed, and in addition, cell 5 was added. The sand layer underneath the cells was only recreated once, between experiment 0 and 1a, as the cells had no downward displacement between the other experiments, i.e., the stiffness of the entire sand layer below the cells was equal between these experiments. The vertical pressure cell 5 stayed at rest throughout experiment 2, but was slightly inclined after experiment 3 as can be seen in *Figure 4.25*.

Figure 4.25. Slightly inclined pressure cell. It appears more inclined in the picture due to camera angel.

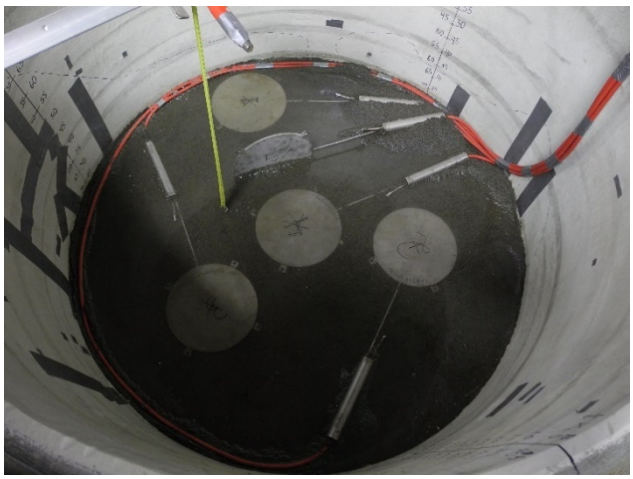

Figure 4.26. Zero-calibration procedure, with cells submerged under a 5 mm water film.

The Geokon Model 3500 pressure cells utilize hydraulic oil to measure the pressure imposed on the plates. Due to the measuring method's nature, the readings are prone to changes in ambient conditions. This was experienced throughout all experiments, and consequently some preventive measurements were attempted, e.g., all added groundwater was roughly room-tempered (which was difficult to achieve with current settings). Moreover, the zero-calibration was done after a day's period of submerging the cells under a 5 mm water film, with ca. 18,5°C, with hope of maintaining that temperature for the rest of the experiment. Cell 5, was naturally not completely submerged during this procedure.

The cells had a pressure range of 100 kPa. A special casing was developed for calibrating the earth pressure cells as shown in *Figure 4.27*. A pressure calibrator, model *Fluke719Pro*, was used to measure the pressure in the casing while air was pumped into the casing. It was considered using water as surrounding medium to the cells as to attain certain temperatures within the cell more quickly and with higher certainty. However, the available equipment would not allow for high water pressures (only static water columns within generic containers), and thereby the associated accuracy would be low for higher stress states. The use of a water pump on the casing would not be viable either, as the calibrator required dry air as the pressure medium.

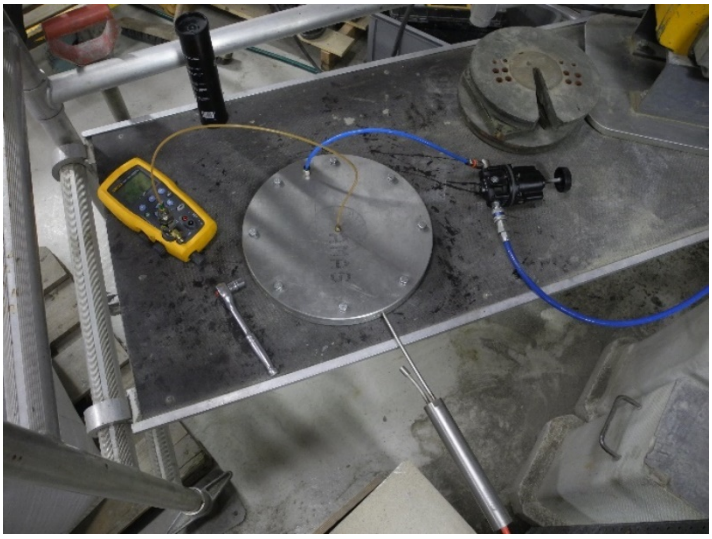

Figure 4.27. Calibration set-up.

4.2.3.2.6 Preparation of clay specimens

In advance of every experiment, the dimensions of the clay units were carefully planned, both with respect to the experiment purpose and to the consumption of blocks. The practical preparation of clay specimen was a time-consuming operation:

The clay blocks were measured meticulously with a folding meterstick or when applicable pre-cut boards were use, which improved the efficiency considerably. The specimens were cut with a thread saw, and to ease the general procedure silicone lubricant was added on the working surfaces. For the pottery clay, and the less sensitive Flotten clay, the material was typically difficult to handle, as it provided more resistance and was stickier than the quick clay. Consequently, lubricant was sometimes added in the cutting procedure as to separate

cut parts from each other. On the other side, the quick clay was sensitive to physical impacts or handling in general, requiring more care and resulting in a roughly equal time consumption per specimen. While handling the clay, it was attempted to keep the contact surface as large as possible, e.g., plates were used on flat surfaces. Clay that was not handled, was watered and covered with plastic foil to sustain the water content.

A layer of pottery clay typically required 9-15 hours, so the clay blocks were laid in the chamber continuously, where they were watered and covered (except from the underside which was partly saturated in advance). The layers of natural clay consisted of specimens from several blocks, thereby requiring more time for cutting. Consequently, these specimens were completely confined with plastic foil and set aside until the layers were to be built. Upon assemblance of a unit consisting of several specimens, the blocks were clamped together with F-clamps after being sprayed with a film of water in between. The intention was to make the units act as one. When possible, water content samples were cut from the specimens, always attempting to include the clay closest the block centre as to have as representative samples as possible. Considering the measurement accuracy upon determination of w, the samples should preferably have been smaller with centroid further into the clay. The pottery clay showed little deviance in w, and was therefore tested on a fraction of the specimens.

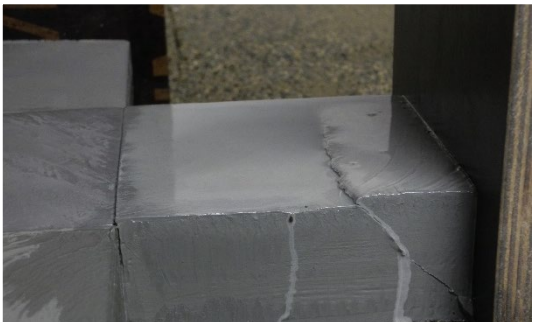

Figure 4.28. Passive failure in a quick clay specimen, upon clamping of a unit.

The vertical layout of the different sub-sample is given in ch. 4.2.3.1, the horizontal cross-sections are shown in *Figure 4.29* to *Figure 4.32*. The clay did not cover the entire cross-sections because of two reasons: Firstly, the clay would create an "impermeable" layer due to its very low permeability, making the construction procedures unfeasible. Secondly, the flow mechanism caused by a sounding is quite local in clay with an influence zone of ca. 2-3 d_c, so the required horizontal extent is quite short. In the sand however, horizontal influence may be large, closer to $\approx 20d_c$, and thereby, in experiment 1a, the clay was trimmed a bit on the side closest the sand-soundings, see *Figure 4.30*. For experiment 3, other set-ups were considered, as shown in the Appendix B.

Prior to experiment 3, it was tested whether if the quick clay would survive sample build-in. It was also checked if it was possible to create units, as with the pottery clay. This proved to be feasible, but the specimens could get a more sudden failure upon clamping them together, as seen in *Figure 4.28*. Thereby, the units had to build even more carefully than those of pottery clay. Furthermore, a mini-probe was used utilized in the third experiment, where the sub-samples consisted of cylindrical specimens. The thicknesses of the centre sub-samples and the cylinders were normalized with respect to the cone diameter, see *Table 4.5*. The disposition of specimens was thoroughly investigated, with some criterions: Firstly, the sum of specimens had to be within the block intervals and not cut by each block's extents, proving to be a solid "solitaire". With this in mind, it was attempted to have the sounded specimens as close to each other as possible, and thereafter the adjacent centre specimens too. The layers were placed

according to in-situ stress level, i.e., the deepest specimens from the extraction profile were placed at the top where the most stresses were achieved. Anyhow, the effective stress level within the sample was lower than the in-situ one ($\sigma'_v = 80 - 65$ kPa versus $\sigma'_{v,0} \approx 100 - 140$ for the "sounded specimen"-depth $z = 8 - 10{,}5$ metres).

Unfortunately, the soundings from experiment 3 yielded rather unexpected results, and upon excavation, it was evident that indeed, the layers were laid erroneous. The error was systematic, with cylinder perimeters placed at the planned centre. The solution was to re-build the sector again and cut new holes (tier 4) in the disc on top, so that the sub-samples still could come to use. The actual sounded layout is seen in *Figure 4.32*.

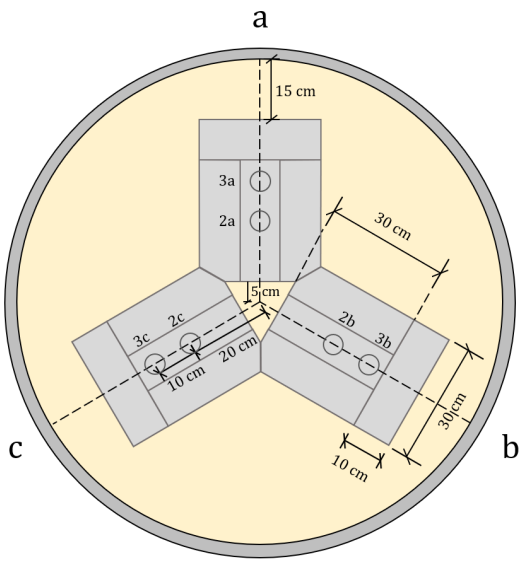

Figure 4.29. The layer design in experiment 0 and 2.

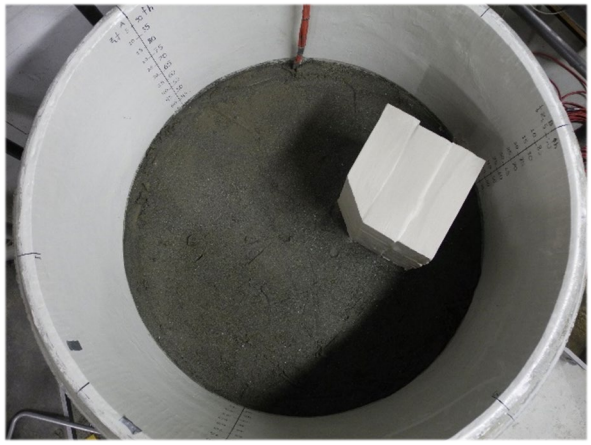

Figure 4.30. Layout for sample 1a.

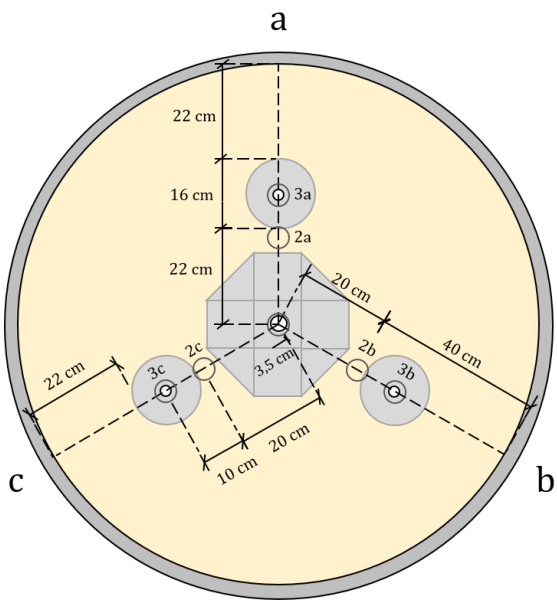

Figure 4.31. Intended design for experiment 3.

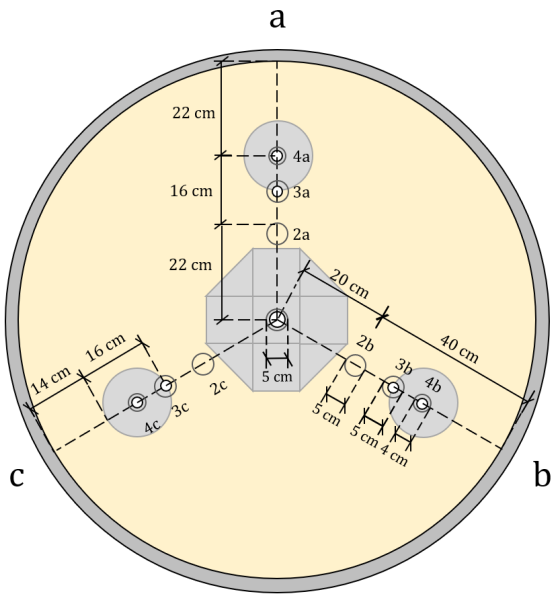

Figure 4.32. Actual layer layout for experiment 3.

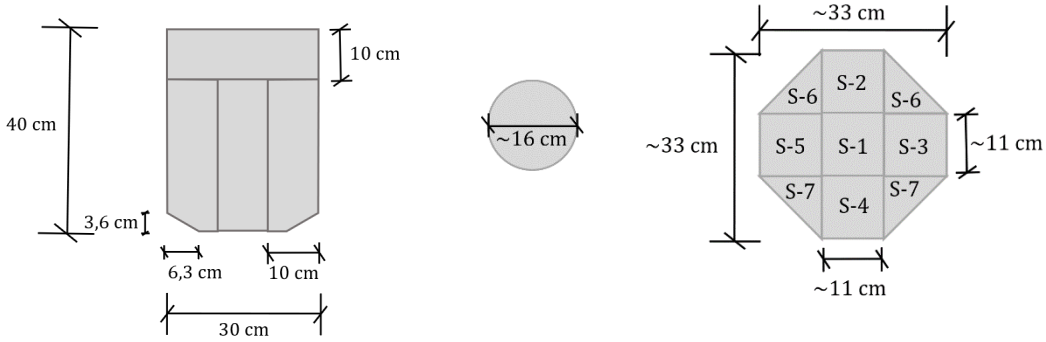

Figure 4.33. Unit dimensions for E0 and E2 (left) and E3 (middle and right). Specimens were numerated according to that shown in the octagon.

The blocks were labelled according to intervals of continuous sampling, followed by order within interval, chronologically from the surface and downwards e.g., III-IV. A list is included in the Appendix C, *Table C.1*.

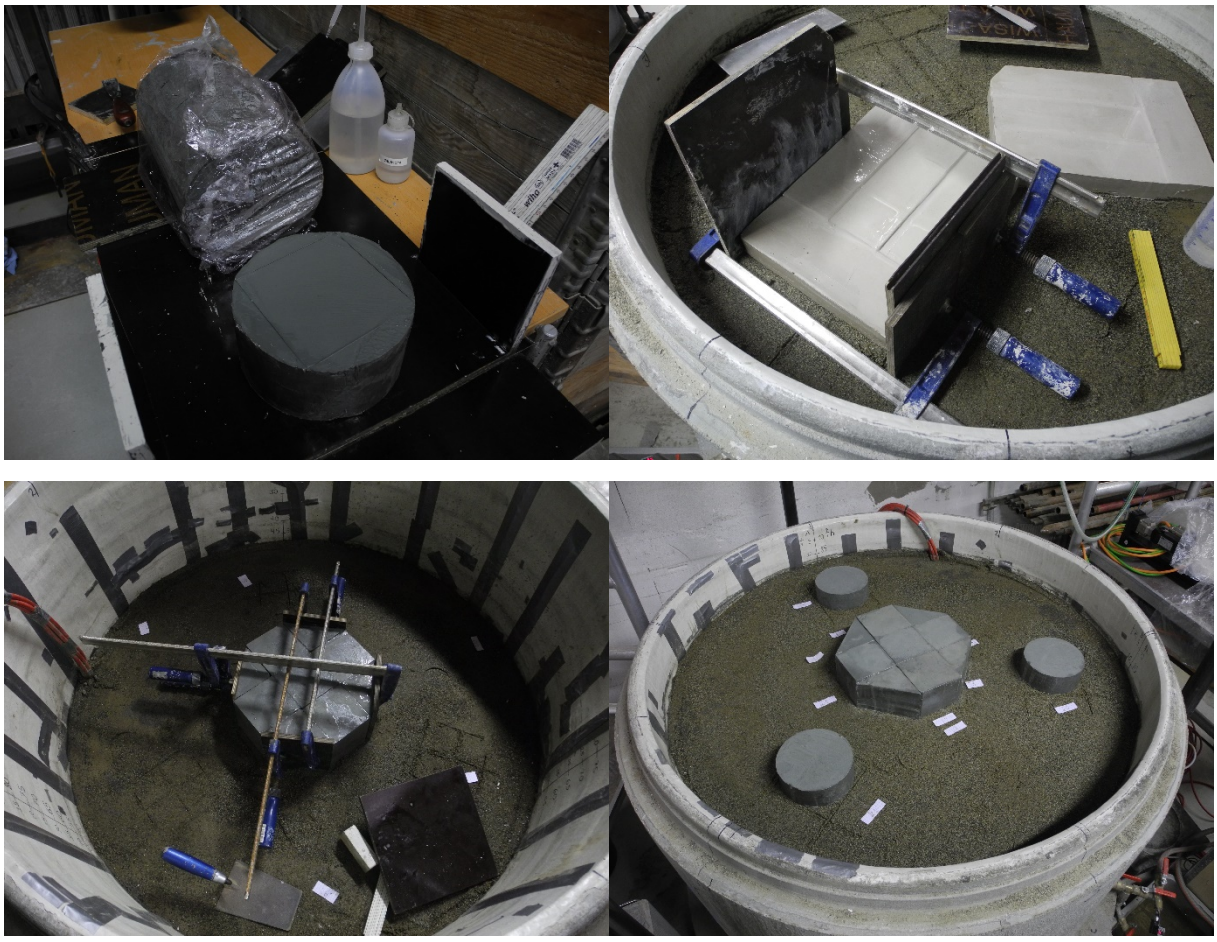

Figure 4.34. Excerpt of clay layer preparations.

4.2.3.3 Water/hydraulic set-up

The hydraulic system was consisting of a 20-litre water container, a small crate which exerted as a sedimentation basin, four hoses, a pore pressure sensor and four valves, whereof two were strictly necessary and two were supplementary. The system is illustrated in *Figure 4.35*. The water container was mobile and was installed with a spillway for excess water, an outlet to the chamber and an inlet for the water filled from the faucet. The necessary valves were number 1 and 2. Valve 1 could be opened to discharge the chamber and also potentially the water container, meanwhile valve 2 controlled the water in and out of the water container which could be moved. The 3rd and 4th valves were already mounted and were not strictly necessary, though they did allow some supplementary flow routes if desired. To control the height of the ground water in the chamber, h_w, the water container was simply elevated or lowered to the preferred height. A small crate was placed under the outlet, and was meant to prevent flow of potential outgoing fractions into the drains. The filter cloth primarily prevented this, but it was considered as a back-up for the filter cloth both with respect to poor installation and potential rupture of the cloth.

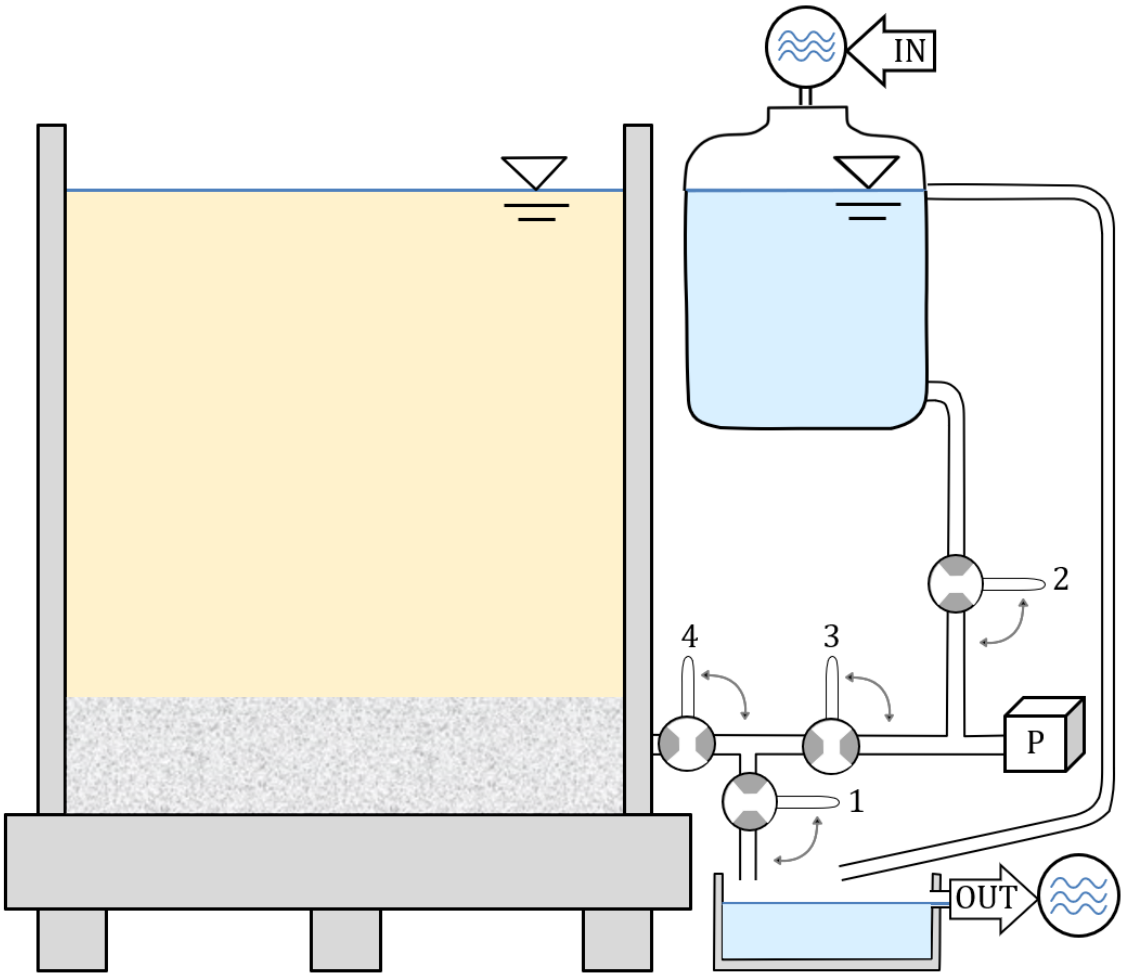

Figure 4.35. The hydraulic system for the model.

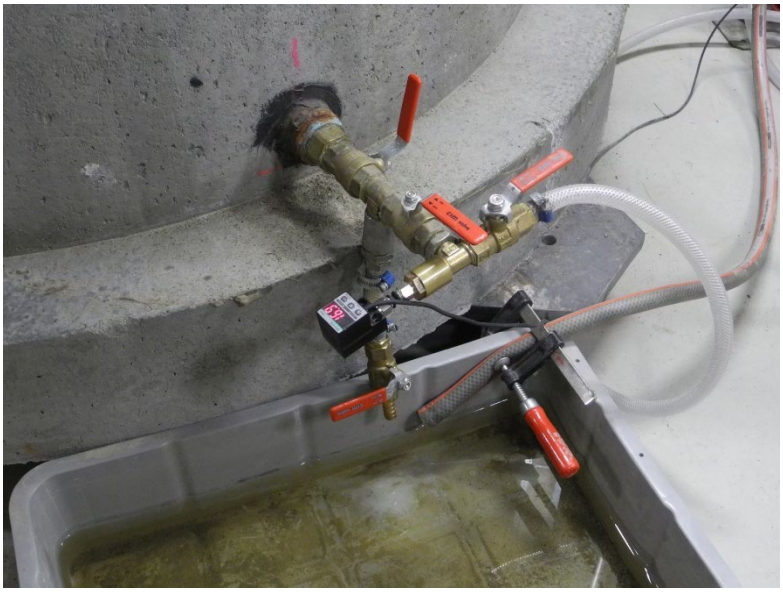

Figure 4.36. Actual footage of the in-/outlet-system.

4.2.3.4 Artificial overburden load

An artificial overburden load is imposed on the chamber samples to simulate stress states at larger depths, and to limit the effect of critical depth from the surface. A framework has been built in order to induce vertical pressure on the sample. The frame consisted of four main parts: a circular metal disc, three air bellows, a steel frame and three metal rods.

The dimensions of the metal disc are shown in Figure 4.38, with a diameter of approximately 1,15 meter and 10 holes arranged in 3 radial sections, including the centre. It was 7 holes prior to experiment 3. The disc, including the parts of the metal frame weighted ca. 3 kN and had a contact surface to the sand very close to 1 m^2. The top of the test chamber was accessible through a hatch between the lab and the (next) floor (upstairs). From there the disc was lowered unto the sample with a crane, see *Figure 4.37*.

Figure 4.37. Metal disc and loading framework lowered unto the sample.

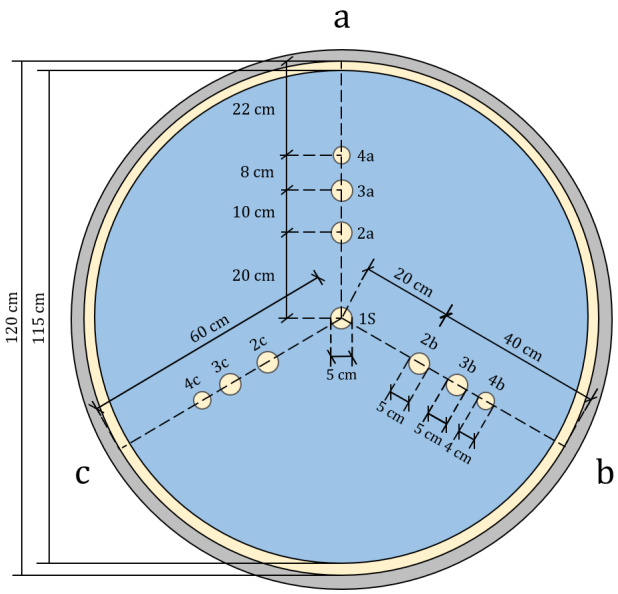

Figure 4.38. Metal disc dimensions and section partitioning.

In the experiment by Hammer (2020), the imposed load was equal to 11,4 kPa. As the intention of experiment 0 was to replicate his experiment at a new laboratory with a new set-up, the applied load, q, was adapted the new sample height, predetermined to be 13,5 kPa. After Hammer's experiments, the load was imposed by using a more flexible designed with a triangular steel framework with air bellows instead of using weight plates. To apply more load on the disc through the bellows, a counterforce was needed. A triangular steel frame was placed one top of the bellows, and holes were drilled at the corners of this frame to enable fastening some threaded steel rods to the frame with nuts. These rods were also fastened to a frame in the bottom of the chamber, which was built in to create some fastening points for the rods and also give easier transportation of the chamber. To measure the pressure imposed on the sample, a tension measurement device was placed on one of the rods and connected to the DAQ-box. In the program used to log the imposed pressure, the dead weight of the steel frame and metal disc was included as initial stress point, and loading of the sample was done reading the stresses in the program. Likewise, it could have been possible to calculate the total force acting on the disc from the bellows by reading of the pressure on the manometer on the air-valve connected to the bellows.

After the first soundings, the pressure system was tested towards its limits, as to check the effect on the sample, and to make sure everything worked before an entirely new sample was built. Due to some faults with the design, the framework was redesigned to be sturdier, with thicker rods, vertical steel supports welded to the frame, ratchet straps were added to prevent any possible torsion and the air bellows were screwed into the disc. The new design was more flexible, allowing construction of chamber samples using only the chamber base. Pictures of the first and second set-up are shown in *Figure 4.39*. The different load settings associated each experiment are listed in the table underneath, *Table 4.*6.

Figure 4.39. Loading framework, initial (left), redesign with chamber base (middle) and extension (right).

Table 4.6. Imposed load in the different experiments.

Experiment	Load
HBH1 & 2	$q = 11{,}4$; $(\sigma'_v = 13{,}5)$
E0	$q = 13{,}5$
E1a	$q = 40$
E2	$q_{2a,2b,3a} = 40$; $q_{2c,3b,3c} = 80$
E3	$q = 80$

Figure 4.40. The framework with bellows and rods.

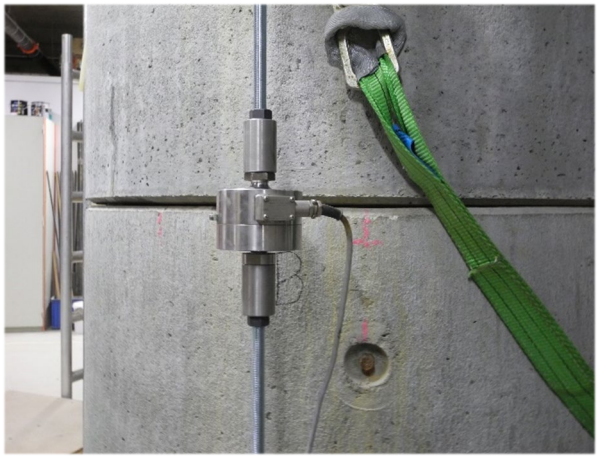

Figure 4.41. The tension sensor installed on a rod.

4.2.3.5 Actuator

The last component of the lab model was the actuator, model ETH050, M05, by Parker equipment. This device was bolted on a steel rack and used to press the penetrometer down into the sample with a constant predetermined speed. The rack allowed for easy handling of the actuator with steel bars that could slide on two horizontally fixed beams, as shown in *Figure 4.42*. While no sideways movement of the actuator was expected upon running the tests, 4 F-clamps were fastened to constrain any possible movement. The actuator was first dedicated its own computer, but later on the actuator program was integrated into the pressure cells' logging program so only one computer would be necessary. With all of these components fixed, the experiments were ready to commence, as shown in *Figure 4.43*.

Due to experience of high thrust forces on the probe and the rods upon the soundings in experiment 1a, the actuator was equipped with a pressure cell. The actuator program would then abort further penetration if the thrust force reached near the capacity load. Considering that the actuator was clamped with several bolts to a steel plate on the rigid steel rack; and that the tip was supported sideways by the fill; the load *case 1* in the catalogue applied (Parker, 2019). However, due to extension rods, the capacity should be considered somehow altered, with longer buckling length, yet larger diameter.

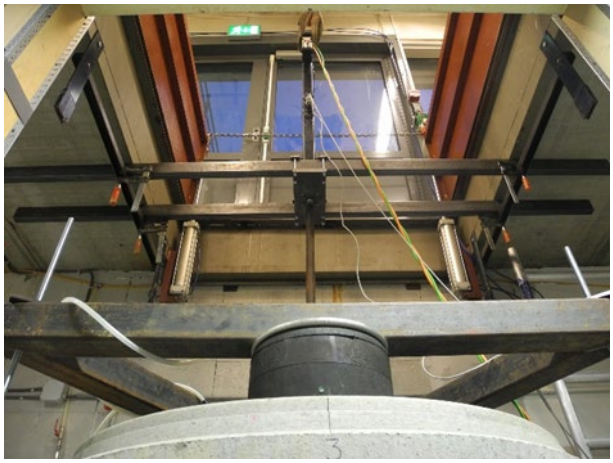

Figure 4.42. Steel frame for actuator, with actuator installed.

The penetration length had to be considered in detail prior to the soundings, with respect to the pressure cells at the bottom and the new pressure cell on the actuator. The target was to log as far as possible, without risking damage to the equipment. Therefore, a couple of centimetres were subtracted as a safety measure.

Figure 4.43. Penetrometer fixed to rod, placed above sub-sample 2a.

Figure 4.44. Crane used for lifting heavy equipment. Here with the actuator placed on the actuator frame.

4.2.4 Excavation

During all excavations, the density of the sand was investigated. Furthermore, there were conducted some basic laboratory tests on the clay.

4.2.4.1.1 Density tests

To measure the density of the sand, two cut steel cylinders were utilized, with dimensions of 5 and 10 cm heights, with diameters of 7,2 cm. The tests were made in the sectors approximately 30 cm from the centre, as to have less disturbance from the soundings. The cylinders were pushed into the sand by pushing a second cylinder on top of the sampling cylinder and then using a plate on top to push the cylinders downwards with an evenly distributed force. The sand adjacent to the cylinder was then dug carefully out, and a masonry trowel was cut underneath to get a flat sample bottom. The top was then trimmed with a thread saw, and the sample put in a bowl. This was then weighted and put in an oven.

Both the diameter and the height used in computation of the volume is subtracted by 2 times $d_{50}/2$ for each boundary as it is expected that sand at the boundaries is forced either in or out of the cylinder. With this information, ρ_d was calculated, eq. {4.1} and by using ρ_s determined by Hammer, both the void ratio and the relative density was calculated, eq. {4.2} and {4.3}.

The latter term, *relative density,* or *density index*, is used to express the degree of compaction of a cohesionless soil relative to the upper and lower bounds, found in laboratory procedures. These procedures are intended on expressing the interval of porosity found in natural deposits, meaning that artificial deposits may drop below $D_r = 0\%$ or surpass $D_r = 100\%$. The associated soil classification based on D_r according to ISO 14688-2 is shown in *Table 4.7* (CEN, 2017, p. 8).

$$\rho_d = \frac{m_s}{V} \qquad \{4.1\}$$

$$e = \frac{\rho_s}{\rho_d} - 1 \qquad \{4.2\}$$

$$D_r = \frac{e_{max} - e}{e_{max} - e_{min}} \qquad \{4.3\}$$

Table 4.7. Soil classification based on relative density.

Classification term	Relative density D_r, I_D [%]
Very loose	0-15
Loose	15-35
Medium dense	35-65
Dense	65-85
Very dense	85-100

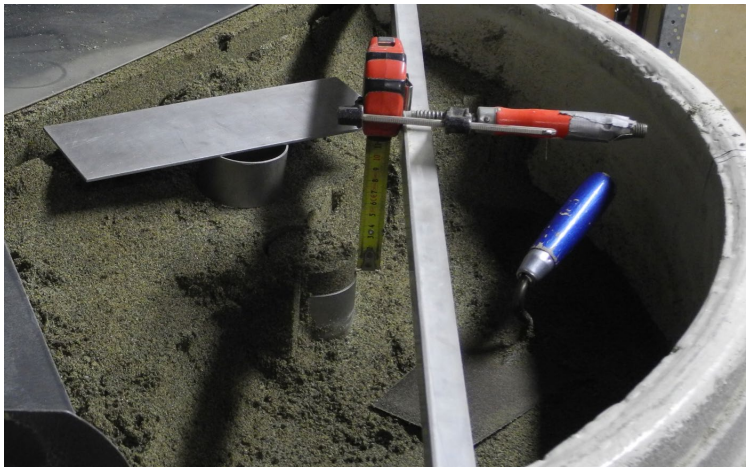

Figure 4.45. Picture from during a density test.

4.2.4.1.2 Laboratory tests on clay samples

The clay samples were tested with a variation of index tests. Water content samples were always taken as part of the excavations with one sample per unit for the very homogeneous pottery clay and 1 sample for each specimen in the quick clay, with exception of some adjacent blocks in the centre units.

Furthermore, some test series were conducted. A *test series* included checking w_L and w_P according to ISO 17892-12:2004 (CEN, 2004), and determining S_u and $S_{u,r}$ according to the standard NS8015 (Standard Norge, 1988) with use of calibration charts provided at the institute. It should be noted these calibration values are with reference to the old standard of falling cone test NS8015 (SN, 1988), which has been superseded by the new NS-EN ISO 17892-6:2017 (SN, 2017). The new standard yields lower values of $S_{u,r}$ for the same penetration. E.g., the limit value of 0,5 kPa for quick clay correspond to 0,33 kPa in the new standard, according to the formula {4.4} (SN, 2017, ch. 6.2.). In the formula, the constant c is associated cone geometry (e.g., for a 60° tip, c=0,27), g is the gravitational acceleration $[m/s^2]$, m is the cone mass $[g]$, and i is the average cone penetration $[mm]$.

$$S_{u,r} = c \cdot g \cdot {}^{m}/_{i^2} \qquad \{4.4\}$$

To emphasize, in this master's thesis, the both laboratory results and the limit value of quick clay (0,5 kPa) is associated the old standard.

Only one test series was conducted for the pottery clay, meanwhile, it was done for the each of the natural clay specimens that were sounded, plus an extra series in the middle (α) and lower (β) centre specimen. In addition, for the natural clay: uniaxial compression tests were conducted on sub-sample *a, b,* and *c* in the lowest layer, α; salinity was checked for 5 different samples according to description in the field- and lab compendium (NTNU Geoteknikk, IBM, 2017); and as previously mentioned, for the very first build-in test of natural clay, a pocket vane was used. Both the Casagrande device and the conductivity-meter were calibrated before use.

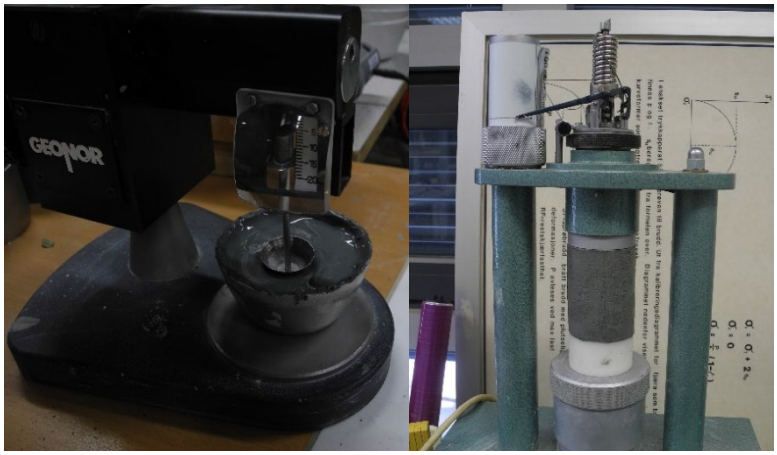

Figure 4.46. Falling cone test and uniaxial test on (possibly disturbed) quick clay.

4.3 The sounding equipment

4.3.1 The standard probe

The standard piezocone penetrometer (10 cm², $d_c = 3{,}57$cm) was of the type *NOVA-sonde*, made by GeoTech. The equipment registers readings with reference to time. This may not be entirely clear for data treated by the regular CPTU-programs, where post-treatment datasets have specific depth intervals of 1 cm for readings, meaning that each parameters' position is rounded off to the nearest cm, see *Figure 4.47*. Moreover, upon deficiency of readings compared to logging intervals, the algorithm will make the parameters inherit values from other steps. This set-up may be intended to ease data treatment with a standardized matrix, or data set, where the values are presented in a quite tidy manner. I.e., the treatment method is intended for better visualization in e.g., excel or similar. This method is however a bit faulty or misrepresentative with respect to the measurement's real positions, and thereby also the different parameter profile curvatures. Neither is the design intended on compressing storage space, concerning that a data-treated CPT-file ≈ 7,8 kB per meter, compared to raw data ≈ 0,85 kB/m.

Consequently, to avoid misrepresentation of readings, the data in this thesis have been based on the readings with time, with associated physical positions based on the data-log from thee rig/actuator which logged sounding length and time. Thereby, the raw data was extracted from the logger, which is placed at the interior of the probe, found at the transition between the probe and the regular rods (GeoTech AB, 2012). The data was later treated in Excel.

The Nova-probe had fixed time stamps with 64 datapoints every 25 seconds. This would give measurements every 7,8 mm with a standard speed of 20 mm/s, or every 5,9 mm with the lowest allowed speed according to the international standards (CEN, 2012). I.e., with 1,5 mm/s there would be relatively 33 % more datapoints for the same length. As the highest possible accuracy for the current experiments was intended, the latter penetration rate was chosen2.

2 - See reference 6.3.4, for discussion of discrete readings as compared to continuous (idealized).

In the raw files, the data points from the NOVA-probe were divided into five categories, with indexes *A*, *B*, *C*, *F* and # in the dataset. Each of these datapoints contain measurements of two parameters, except of # which is a reference time-stamp. E.g., *C* gives tip resistance and tilt angle, while *F* gives side friction and pore pressure, these are the most frequent measurements, see *Figure 4.48*.

```
D=1.020,QC=1.4986,FS=10.4,U=126.8,TA=0.09,O=15.6,B=20,M=0.00,RM=0.000,%1467158
D=1.030,QC=1.4986,FS=12.6,U=128.1,TA=0.09,O=15.6,B=19,M=0.00,RM=0.000,%1467485
D=1.040,QC=1.5156,FS=16.4,U=110.5,TA=0.06,O=15.6,B=20,M=0.00,RM=0.000,%1468250
D=1.050,QC=1.5156,FS=16.4,U=110.5,TA=0.06,O=15.6,B=20,M=0.00,RM=0.000,%1468687
```

Figure 4.47. Line of code from a typical CPTU-data series that has been post-treated in the automatized manner. Note the roundoff of position and inherit of values.

```
#,201201,163810,0,26,4320,390,64,1,0,0,0
C,12464,17919,1
F,12077,12844,2
C,12338,7676,3
F,12077,12845,4
B,262143,262143,5
```

Figure 4.48. Code with un-treated raw data.

This part may seem too detailed, but the automatized processing of the data would not be a satisfactory solution for the current experiment. Explanations are furthermore included as the procedures in the lab have not followed the norms in the branch outright, even though they are still according to standards. E.g., the decrease in speed to 15 mm/s have affected the magnitude of some measured values to some extent, but the general trends should be reasonably in accordance with regular responses as the two materials used in the experiments are pragmatically *fully undrained* and *fully drained*, ref. ch. 2.2.

4.3.2 The mini-probe

In the last experiment a mini-probe (5 cm^2, $d_c = 2{,}52cm$) was utilized. In the data-treating program of this probe, it was possible to assign a register frequency of 1 data point each millimetre. I.e., this probe had also technically readings associated time stamps, which in fact were not as often as one reading per 1 mm (15 Hz), but rather something less. However, due to the much higher reader frequency as compared to the standard probe, it was deemed adequate to use the CPTU-treatment program directly. The data was thereby discretized with respect to depth. The algorithm of inheriting values sustained (this may be different from the Geotech-algorithm), but due to the high reading frequency, the solution was regarded as adequate. The effect of using the program's algorithms will be visible in the graphs from experiment 3 in ch. 5.1.

As part of the preparation works to use the mini probe ($5cm^2$), software was downloaded and the procedures by Geomil equipment (201Xb-d) were followed. It took some time to get familiar with the equipment, and some human error was made upon one of the soundings, as explained in ch. 5.1.1. To measure the depth a linear-wire position sensor was mounted to the actuator as seen in *Figure 4.49*.

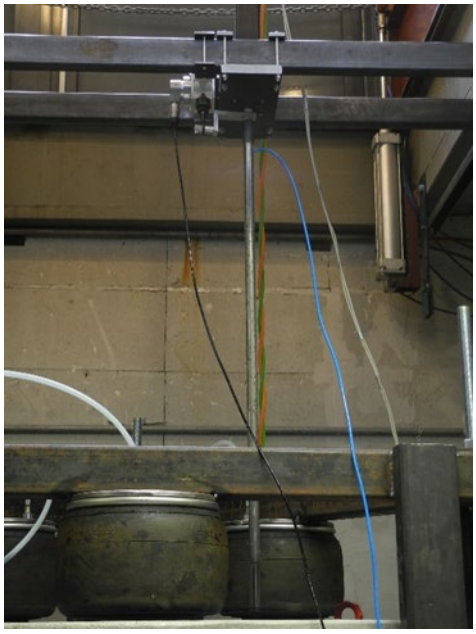

Figure 4.49. The mini-probe was cabled. The depth was measured with a linear-wire position sensor.

Figure 4.50. The two utilized probes besides each other.

4.3.3 Saturation process

The standard piezocone penetrometer had a filter made of bronze. The regular saturation procedure at NTNU is quite basic, and is divided in two: First the filter is saturated with glycerol or "glycerine" many days in advance of any sounding mission. Secondly, shortly prior to a sounding while shortly the filter is placed on the probe and the cavity behind is filled with antifreeze as shown in *Figure 4.52*.

The mini-probe had a plastic filter and is saturated with silicone oil only. The procedure of saturating the mini-probe filters was as described in (Geomil equipment, 201Xa). First, a container was filled with silicone oil and put inside a vacuum desiccator. Then the vacuum machine was turned on for more than 24 hours. Another container was filled with silicone oil and vacuum pumped for 1 hour. The probe was then mounted into the saturation chamber, and the latter container was emptied into it. The filter was mounted, and the saturation chamber was vacuum pumped for at least 10 minutes, see *Figure 4.51*. A rubber membrane was placed on the probe, and it was ready for testing. It is regular practice in field investigations to let the membrane stay on, and be torn off the first 1-2 m by the soil. However, as this was considered too risky for such a small sounding depth, the membrane was taken off before the cone was adjusted the surface, and the sounding was started.

When the plastic filters of the 5 cm^2-probe were saturated, they floated on top of the silicone oil. Intuitively, one may thereby expect that they did not become completely saturated. On the other side, the filters laid in the oil being pumped by the vacuum desiccator for more than 24 hours, according to supplier's standardized procedure, so they probably were completely saturated anyhow.

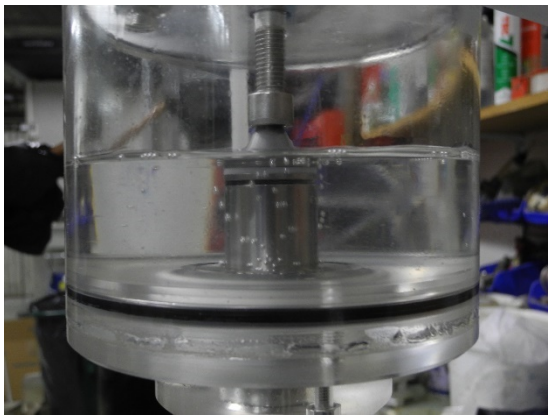

Figure 4.51. Mini-probe (5 cm²) saturation chamber.

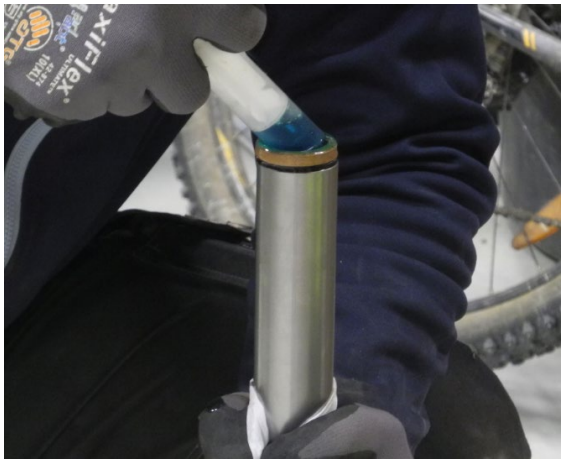

Figure 4.52. Saturation of standard probe (10 cm²).

As a general note, some key points mentioned by Lunne et al. (1997) is summarized: To sustain complete saturation behind and within a pore filter, the saturation liquid should not have a too low viscosity, considering that it may escape the cavities, before or during a sounding. At the same time, more viscous liquids are typically less responsive, lowering the performance of the equipment.

4.3.4 Data treatment

All of the CPTU-data have been corrected with respect to the sensors' positions on the probe. I.e., q_t is the basis for the depth-reference, with depth denoted as z_{q_t}, meanwhile u_2 and f_s have been superposed, with depths denoted z_{u_2} and z_{f_s}. For the latter, it was chosen to only superpose readings to the very front of the friction sleeve, see ch. 6.3.3 for reasoning. Upon deriving CPTU-parameters, the superposed positions were used for each parameter (e.g., Q_t and B_q). Furthermore, each CPTU-derived parameter was calculated with reference to z_{q_t}, meaning that the values of u_2 and f_s were interpolated. This latter point is quite important, as this implies that extremal values of f_s and u_2 are missing. In future works on data assessment, a secondary line of derived parameters based on either f_s and u_2 should be made with interpolations of q_t, as to include the extremal values of these parameters too. The two datasets could then be combined. To be clear: for best assessment of derived CPTU-parameters, the data should first be interpolated with respect to one parameter, and then the others, finalized by combining these data. All data presented from this thesis is only reference to z_{q_t}.

Inclination of the probe has not been accounted for in the soundings performed in lab, as the impact of this parameter is very low. E.g., with a sounding inclined 4° for the whole depth the effect on 1,1 m would be just under 0,3 cm. In reality the inclination of rods during sounding is imposed gradually with depth, so this error becomes even less. For the interpreted soundings from the field, presented in the Appendix E, the inclination was considered, using formula {4.5}. The notation is β_1 and β_2 for bi-directional inclinometers, and α for non-directional inclinometers.

$$z = \int_0^l \cos(\alpha)\, dl = \int_0^l \frac{1}{\sqrt{1 + \tan^2(\beta_1) + \tan^2(\beta_2)}} dl \qquad \{4.5\}$$

4.4 Limitations of the experiment

In this chapter limitations of the experiment are looked upon, with references to an ideal set-up with no concern of time- or resource demand. Some pertinent sources of error will also be mentioned, and all comments are based on the framework of the experiment with its underlying assumptions.

4.4.1 The sample and model chamber

4.4.1.1 Sample sand

Idealized, the sand would be totally homogenous for the analytical review, meanwhile, in the field, the sand is expected to be layered with different fractions in potentially inclined sheets with thicknesses depending on the cycles of the rivers transporting the sediments and the sediment source. This would give different properties at different depths, with a much more frequent alteration of properties than those achieved in this experiment. Artificially made sand layers do have some variability of properties, but these do not reflect natural variabilities. The preparation of the sand layers would ideally be equal for every layer, with equal effects of every building stage, and equal effect of vibration for every layer, see ch. 6.1.2.1. The thin-layering effect is much affected by the tip resistance exercised by surrounding layers, thus homogenous sand in the sample would have been preferred.

4.4.1.1.1 Density samples

The methodology of sampling density samples has some conceptual associated inaccuracy regarding boundary conditions. Moreover, the method is susceptible for changes in measurements, e.g., for every gram that is added or subtracted due to practical inaccuracy, the relative density is increased or decreased with 1-3 % for both the small and the larger sampling cylinders.

4.4.1.2 Clay specimens

4.4.1.2.1 Pottery clay

The aspect of using pottery clay was two-sided: Firstly, this artificial clay was easy to obtain and to handle, and it was very uniform. The latter was obviously an advantage related analytical review, with known soil properties, and with small associated deviations. Secondly, on the other hand, the purpose of the research program is to simulate natural conditions, and thereby the chamber samples with natural clay yield best data for final comparison with field data. Anyhow, the use of pottery clay was smart as a reference, and provided a good starting point for developing the research program's experiments further. Considering that the experience related the experiments was little to begin with, the use of natural clay was a cheaper option for training.

4.4.1.2.2 Representativeness of natural clay specimens

The topic of sample disturbance has been of high importance regarding the representativeness of the results as compared to what is simulated. No matter how much effort is laid in preserving the soils properties, the clay will be subjected to disturbance, all the way from sampling to sounding, and possibly in subsequent laboratory testing.

For the last experiment, the lack of experience with quick clay lowered the awareness regarding sample conservation. I.e., the pottery clay was robust against changes due to exposure to air and also to the lowering of groundwater in the chamber samples. A better understanding of the quick clay's extreme susceptibility to exposure would have prevented the lowering of ground water between the first and second round of soundings in experiment 3, and during the following excavation. Thereby, it is unknown to which degree the natural clay specimens may endure an entire experiment, including both build-in, sounding and excavation.

4.4.1.2.3 Clay in general

Ideally, the sub-samples should be wide enough such that the soundings do not deform the clay blocks by any significance, i.e., the sub-sample sides should not be rotated at all. This problem was never encountered, even for the clay samples that was smallest with respect to cone diameter. Anyhow, in an idealized world the clay layers could have been larger in the horizontal direction. Anyhow, with respect to economics, it is expected that sampling with e.g., a regular Sherbrooke sampler would be much more expensive as compared to the research output.

Another practical aspect associated the clay specimens was unifying them by using F-clamps, water, and working them by hand (plates if flat surfaces). This was done to prevent cavities in-between, and required extremely flat surfaces and good measurements upon cutting each specimen. The effect of such cavities is little in the horizontal direction, but for specimens that are stacked upon each other, the fissures allow for pore water dissipation, which yield lower readings of u_2. Thereby, the units no longer can be said to behave as one true unit with respect to pore pressure readings.

4.4.1.3 The silo effect

The measured silo-effect limits the stresses that can be simulated in the chamber. Thereby, the stresses that are at greater depths in the field cannot be imitated, consequently preventing the natural clay samples from reaching their in-situ stress levels. By not accounting for the silo-effect, any calculation involving stress will become very inaccurate. Secondly, if the measurements are not done properly, the associated accuracy is also lowered. For better understanding of the actual stress distribution and the arching effect, additional pressure cells at different heights could provide valuable information.

To diminish the silo effect, the width-height ratio could be increased, and moreover, the friction reduced, or idealistically, removed. The first element would of course not be realistic due to the experiment's nature, meanwhile, the second could be a plausible approach to achieve higher stresses in the chamber.

4.4.2 Measurement devices

Generally, there is some accuracy associated to all measuring devices. This may be negligible or rather decisive. The CPTU-equipment is regarded as very reliable, yet many articles were found stating that q_t typically varies somewhat between different probe designs. The other measurements devices included in the current experiments were the pressure cells, the rod tension cell (used to measure artificial overburden load) and the pore pressure sensor. The pressure cells had a lot of drifting as will be explained in ch. 6.2.1.1.1. The pore pressure sensor was very reliable with minimal amounts of white noise, the third sensor was also regarded as reliable, as the pressure in the air bellow was adjusted by a nozzle with a pressure meter, this was possible to verify.

4.4.2.1 Pressure cells

For an idealized experiment, the pressure cells would experience no drifting. The data would then not need as much effort to interpret, and would have an accuracy that would let estimates of the stress state in the chamber become accurate. Matters are even worse for the vertical pressure cell, typically accurate measurements of K' are very difficult to obtain as explained by Lindgård & Ofstad (2017).

4.4.2.2 Piezocone penetrometer

The standard probe's potential of accuracy is not completely utilized, with readings every 0,39 seconds. Moreover, the readings are of different kinds, making the accuracy of each parameter even lower. In an idealized world the readings would be continuous, only giving geometrical and methodological sources of error. With continuous readings, the speed would no longer influence the accuracy of the method. Thus, the most used speed in the branch of 2 cm/s would be more pertinent to use in the experiment.

The influence of reducing the penetration speed on the tip resistance for relatively drained and undrained materials is as previously mentioned in ch. 2.2 not of a considerable magnitude. Depending on the disturbance of the quick clay in advance of penetration, there may be some rate effect that is barely noticeable, but not of significance.

4.4.3 Chamber soundings

Performing several soundings close to one other affect the measurements, especially in sand, so the distance between the most prioritized soundings should preferably be far from each other and done first. The boundary conditions of the chamber are also affecting the soundings, yet this is difficult to compensate for, and some calibration would require a large amount of work, both regarding to literature study and experimental work.

4.4.4 Working methodology

In hindsight, considering the comprehensive laboratory work, the amount of time spent on literature study and data treatment was probably quite disproportionate. Nevertheless, the presented literature gives a good foundation for assessing the different elements of the large-scale model testing, yet many of the hours spent on this could perhaps been directed towards presenting the data in more detail, with more thought behind what to highlight, and what to discard or "blur" out as less important.

5 Results

The following subchapters will present:

The CPTU-profiles with associated derived parameters; the normalized q_t-profiles for different clay layer thicknesses; the supplementary laboratory results; the sounding profiles from experiment 3 with associated laboratory results; and lastly, the pressure cell data with associated stress profiles for the different chamber-samples.

As a foundation for comparison, some soundings from Flotten have been assessed. These plots are included in Appendix E and have data presented for the depth interval 8-10,5 m where the quick clay specimens are extracted from.

5.1 Soundings

Before presenting the data, some remarks must first be made: The data are acquired and treated in accordance to explanation in ch. 4.3, and further CPTU-assessment is done in accordance to description given in ch. 4.3.4. To underline that the sounding results are discrete, the graphs are shown with sharp curves. Moreover, it should be reminded that the measurement density of these experiments is higher as compared to what is typically used in the industry, with 33 % more readings per meter. All tip resistances are the corrected tip resistance, q_t.

5.1.1 Compilation of experiments

In the profiles, the clay blocks are highlighted, with interfaces as indicated. For clay layers with different thicknesses in the different sub-samples, the units will have a common bottom. The thickness of the different sub-samples will be specified under each data series. For a compilation of the different layer thicknesses and relative depths in the chamber, it is referred to ch. 4.2.3.1.

Emphasizes should be put on the first soundings in each zone, with index number 2, e.g., 2a. These soundings are marked with lighter colours, meanwhile the supplementary soundings in holes 3a-c, are marked with darker corresponding colours. These are acting more as "back-up" soundings as they are somewhat influenced by the sounding in their neighbouring hole, with regard to first a penetration and secondly a withdrawal of the CPTU-probe. The exception is experiment 3, where the order of soundings was 3a, 3b, 3c, and lastly 1S, and then in a second round 4a, 4b, and 4c. Unfortunately, sounding 3a-c was unsuccessful (systematic error, see last paragraph in ch. 4.2.3.2.6). Thereby, the sounding 1S (10 cm^2-probe) is most reliable, followed by 4b-4c. Another unfortunate mishappening in experiment occurred when sounding 4a was performed. As the proximity switch was turned off (supplementary logging equipment), the logging and data treating-program CPTest did not log the sounding. The back-up file is saved together with the associated actuator-file, so it is possible to retrieve the data by reverse engineering the code build-up in the back-up files. Due to time-restrictions, this

has not been performed, but the valuable data-set is available for deciphering. All soundings by the standard probe are treated by this latter method, by using the back-up raw files, so it should be feasible.

The cone resistance number, N_m, accounts for excess pore pressure, however, it is not limited to undrained conditions. Hence, this factor has also been calculated both in the clay and the sand, setting attraction to respectively 8 and 0 kPa. It should be noted however, that these results are based on some assumptions, and may thereby not be very representable even for soundings in "homogeneous mediums", such as those seen in the Appendix E. This is discussed further in ch. 6.3.5. Only one example of using the cone resistance number in the graph will be provided. N_q, could have been calculated for the sand, but this was not done.

The other cone factors are all based on the correlations given in 2.3.1.3 and correlated with field data from Flotten, with interpolated profiles of soil properties. Data was then retrieved with respect to each specimen's depth. For the OCR-value, the p_c' from Flotten was used together with the estimated stress in the chamber. These estimates were based on the pressure cell readings.

For the different interpreted relative density graphs, the constant k_{2,D_r} in the NGI-99 expression was typically changed from 22 to a smaller number. I.e., the chamber soundings from the experiments yield less tip resistance than the expression "expect" (in field), and thereby, by lowering this constant, a larger D_r is returned, more is discussed in ch. 6.1.2.2. It should be reckoned that the D_r-samples were taken after the soundings were performed, and that these moreover were taken from the centre of each sector, and not close to the soundings.

5.1.1.1 Experiment 0

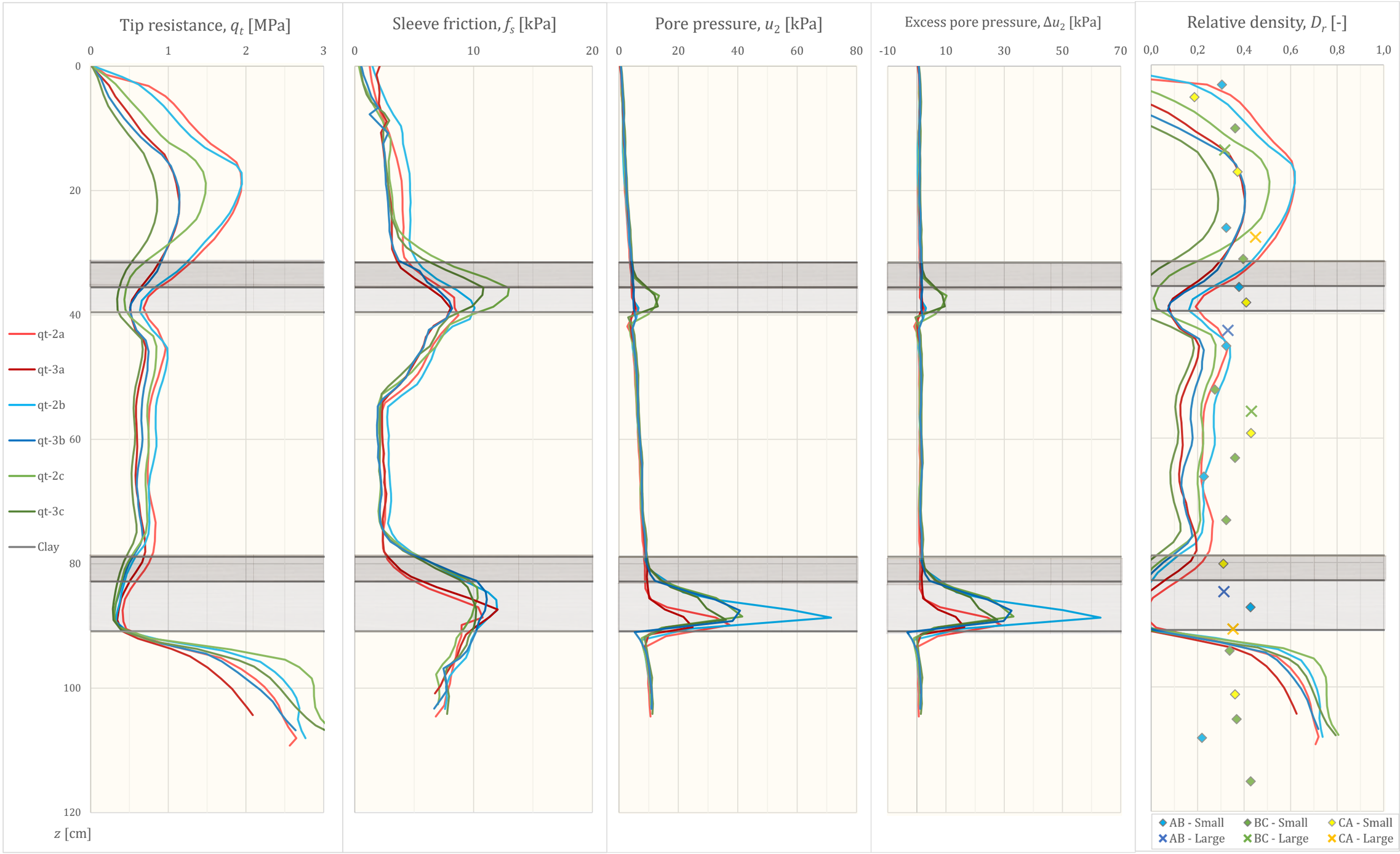

Figure 5.1. Standard parameter profiles: q_t, f_s and u_2, followed by excess pore pressure, Δu_2, and interpreted relative density, D_r.

The clay layer thicknesses in the lower level (α) for the sub-samples **a**, **b**, and **c**, are respectively **8**, **12**, and **12** cm. Likewise, in the upper level, (β) they are respectively **4**, **4**, and **8** cm.
The constant k_{2,D_r} was set equal to 11 for all the soundings. For all of the interpreted relative density curves, the constant k_{2,D_r} has been changed to 11 from 22.

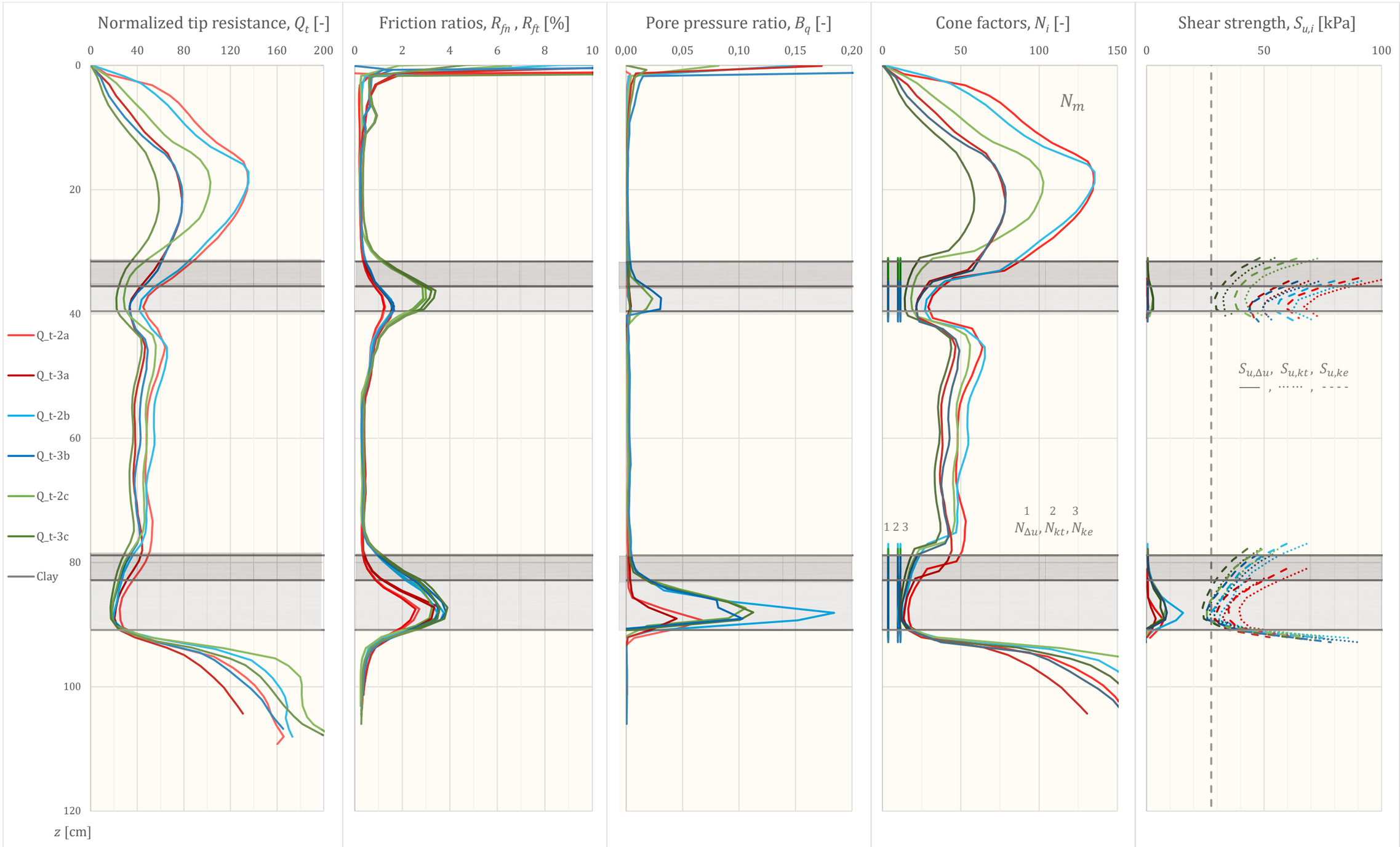

Figure 5.2. Normalized parameters, Q_t, R_{fn}, R_{ft}, B_q; Interpreted cone bearing factors N_m, $N_{\Delta u}$, N_{kt}, N_{ke}; and interpreted undrained shear strength, $S_{u,\Delta u}$, $S_{u,kt}$, $S_{u,ke}$ with reference value.

The cone factors $N_{\Delta u}$, N_{kt}, N_{ke} are all based on the laboratory results and the equations in ch. 2.3.1.3.

Regarding N_m, for the sand and the clay, respectively, the attraction is assumed equal to 0 and 8 kPa, while β is assumed to be -15° and 0°.

5.1.1.2 Experiment 1a

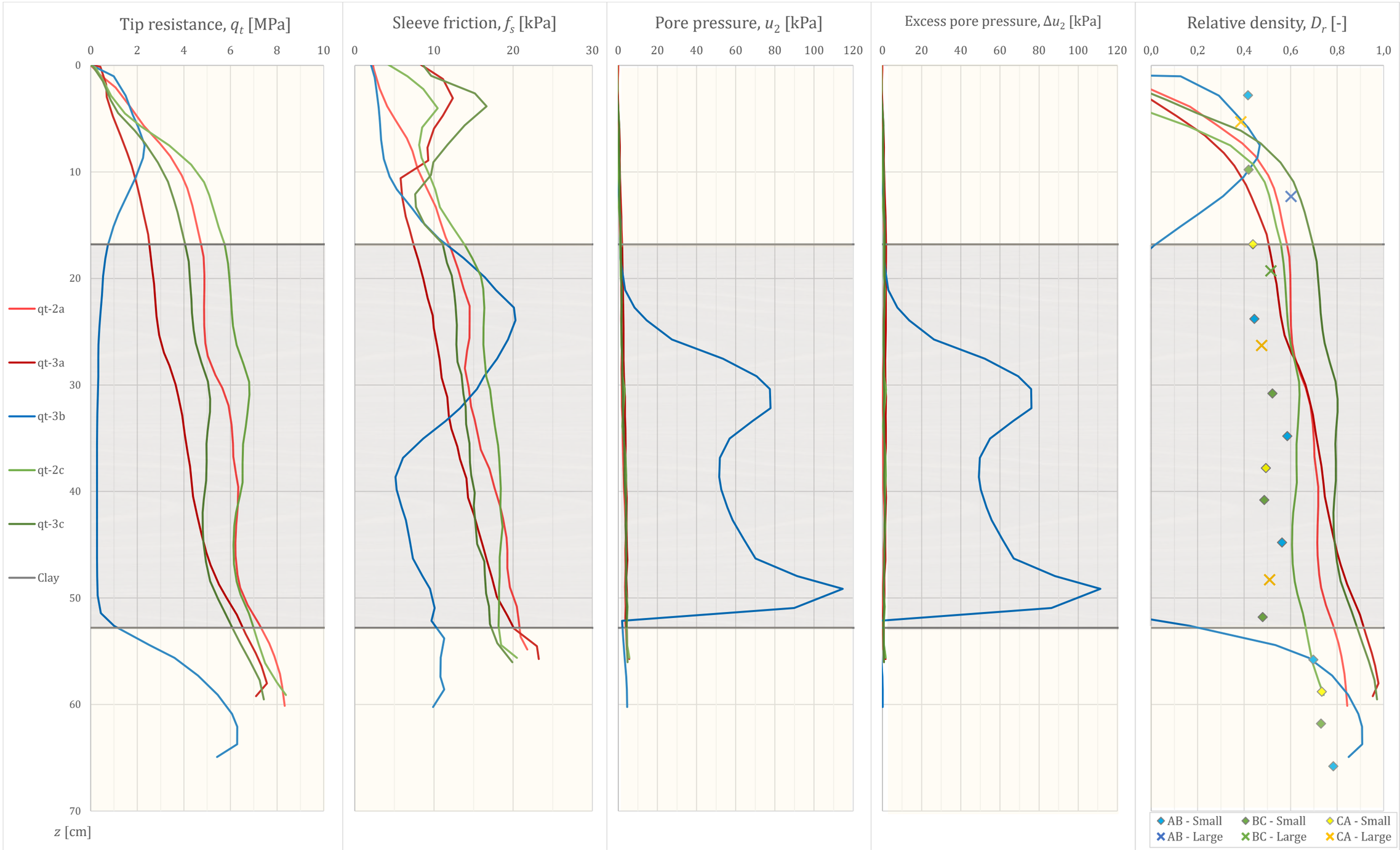

Figure 5.3. Standard parameter profiles: q_t, f_s and u_2, followed by excess pore pressure, Δu_2, and interpreted relative density, D_r.

In this experiment, sounding 3b penetrated a clay block of 36 cm height, the rest were sounded in sand solely. Hole 2b was not sounded at all.
For the interpreted relative density curves, the constant k_{2,D_r} was set to **17**, **22**, 11, 11, and 11 for respectively **2a**, **2c**, 3a, 3b, and 3c.

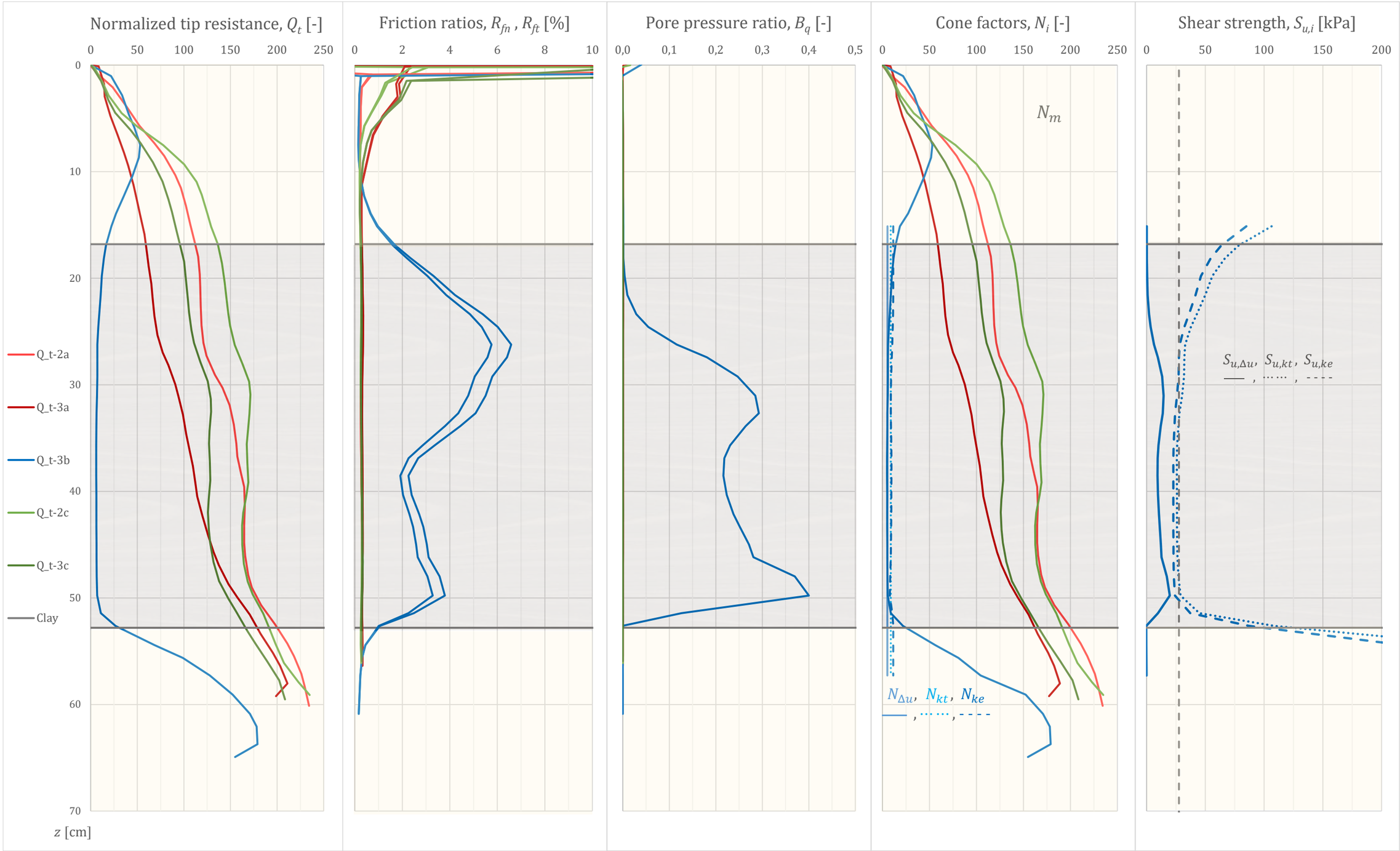

Figure 5.4. Normalized parameters, Q_t, R_{fn}, R_{ft}, B_q; Interpreted cone bearing factors N_m, $N_{\Delta u}$, N_{kt}, N_{ke}; and interpreted undrained shear strength, $S_{u,\Delta u}$, $S_{u,kt}$, $S_{u,ke}$ with reference value.

$N_{\Delta u}$, N_{kt}, N_{ke} are all based on the laboratory results and the equations in ch. 2.3.1.3.

Regarding N_m, for the sand and the clay, respectively, the attraction is assumed equal to 0 and 8 kPa, while β is assumed to be -15° and 0°.

5.1.1.3 Experiment 2

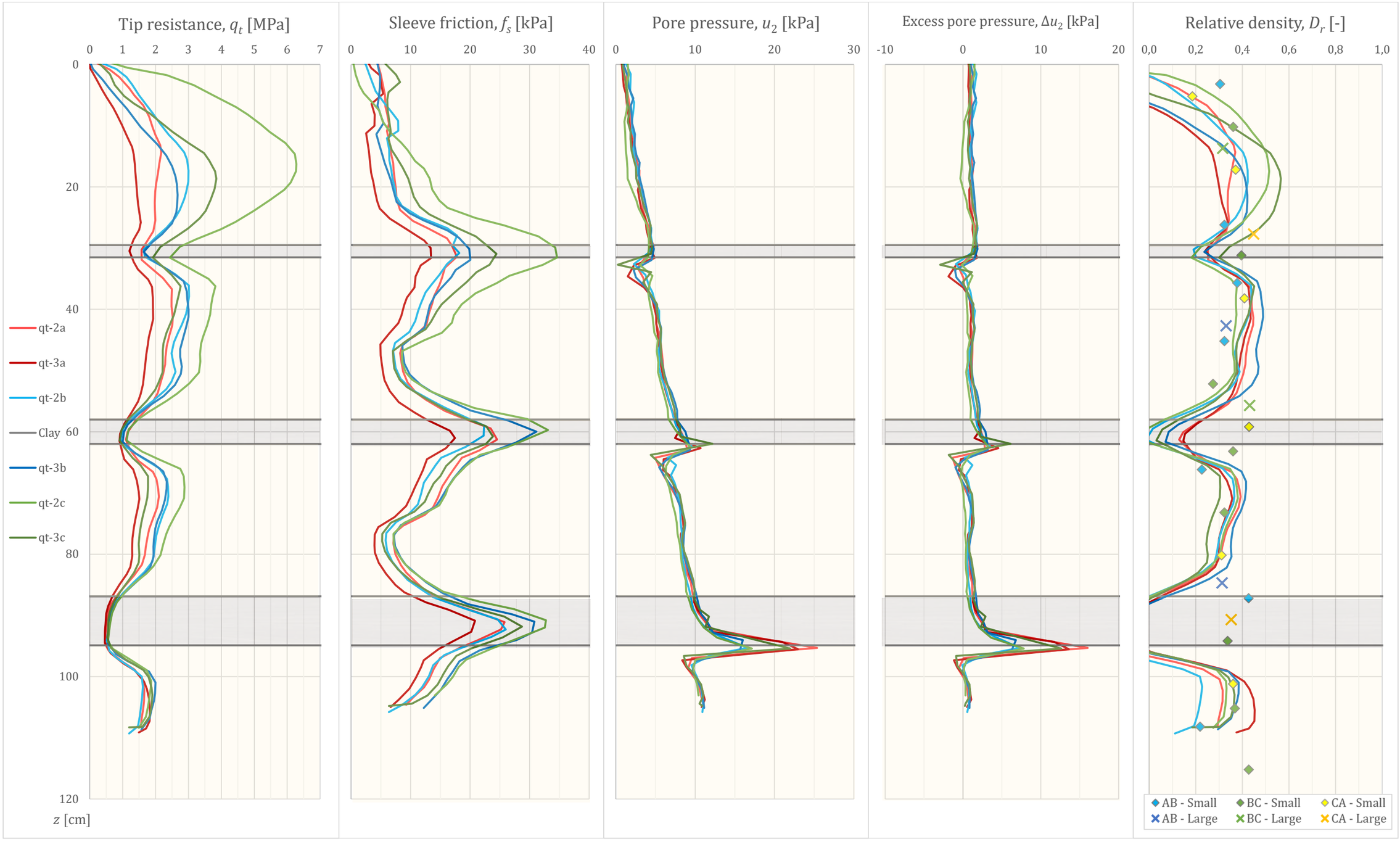

Figure 5.5. Standard parameter profiles: q_t, f_s and u_2, followed by excess pore pressure, Δu_2, and interpreted relative density, D_r.

The clay layer thickness in the lower level (α) is equal to 8 cm for all the sub-samples a, b, and c. Likewise, in the middle level, (β), the thickness is 4 cm; and in the upper level, (γ), it is 2 cm.
For the interpreted relative density curves, the constant k_{2,D_r} was set to **14**, **17**, 11, 11, and 11 for respectively **2a**, **2b**, 3a, 3b, and 3c. For **2c** k_{2,D_r} was set to be linearly decreasing from 22 in the top to 11 in the bottom.

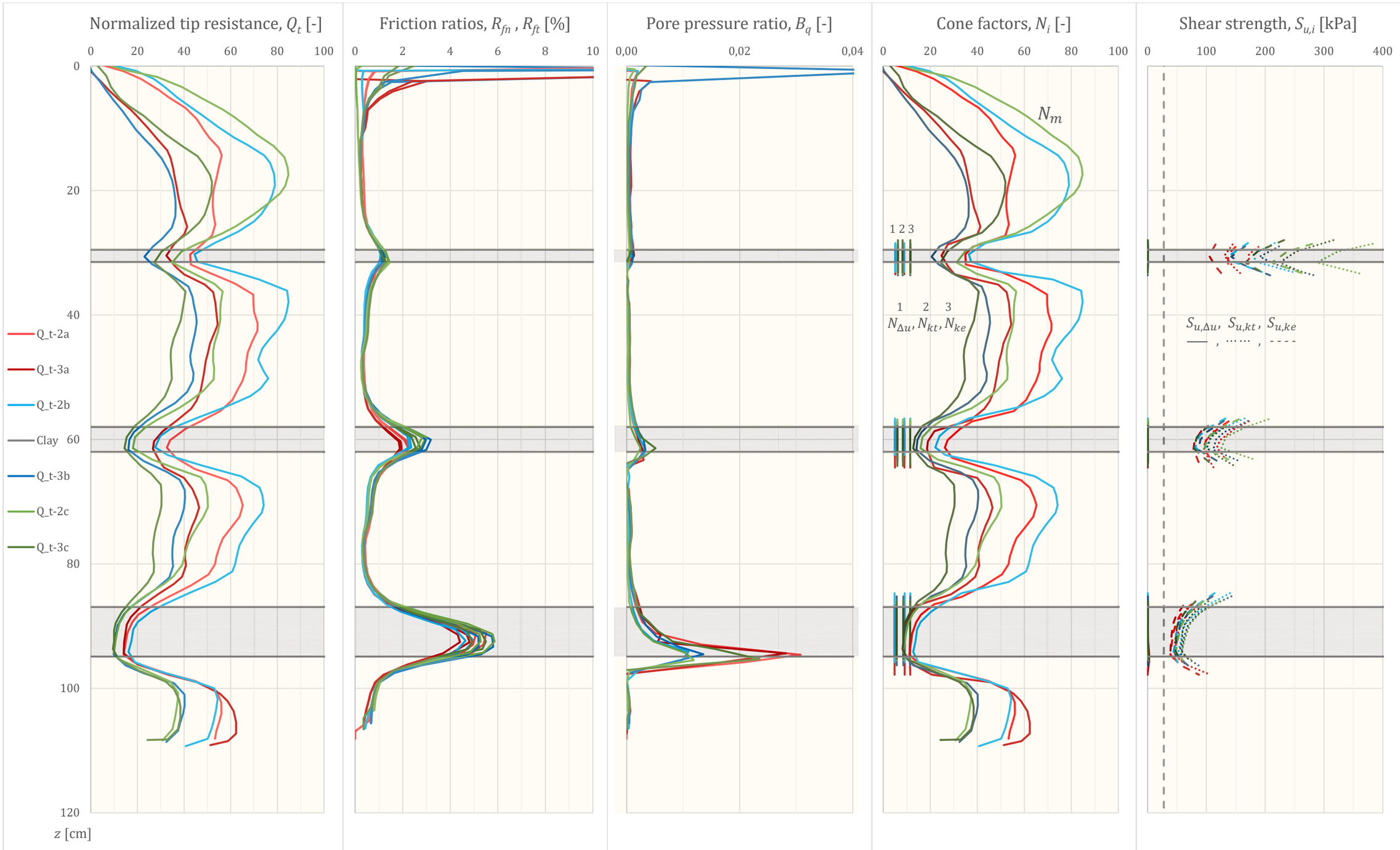

Figure 5.6. Normalized parameters, Q_t, R_{fn}, R_{ft}, B_q; ; Interpreted cone bearing factors N_m, $N_{\Delta u}$, N_{kt}, N_{ke}; and interpreted undrained shear strength, $S_{u,\Delta u}$, $S_{u,kt}$, $S_{u,ke}$ with reference value.

The cone factors $N_{\Delta u}$, N_{kt}, N_{ke} are all based on the laboratory results and the equations in ch. 2.3.1.3.

Regarding N_m, for the sand and the clay, respectively, the attraction is assumed equal to 0 and 8 kPa, while β is assumed to be -15° and 0°.

5.1.1.4 Experiment 3

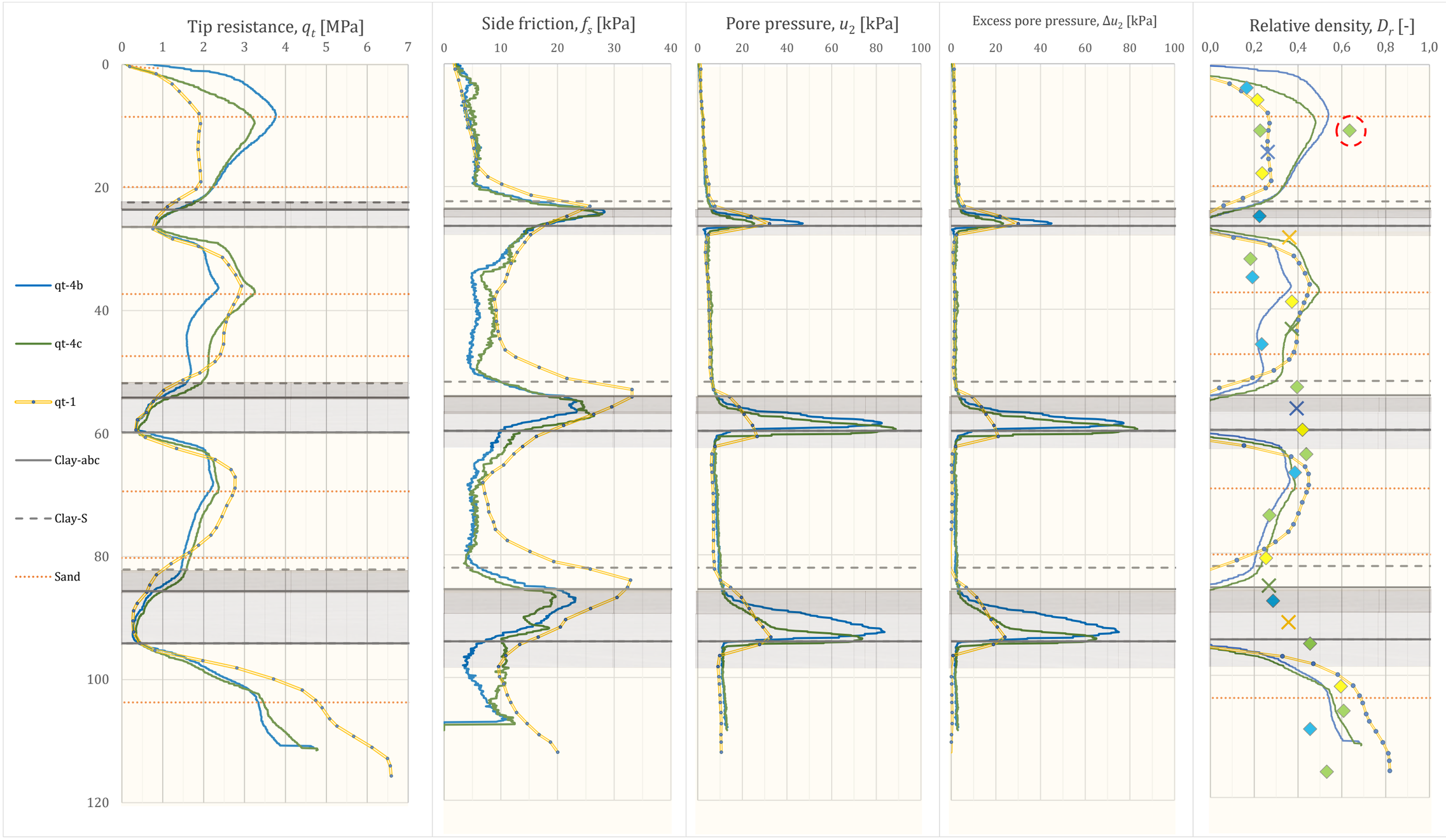

Figure 5.7. Standard parameter profiles: q_t, f_s and u_2, followed by excess pore pressure, Δu_2, and interpreted relative density, D_r.

Thicknesses are as follows: In the lower level (α), $H_{a,b,c} = 8{,}49$ cm and $H_S = 12$ cm ; in the middle layer (β) $H_{a,b,c} = 5{,}66$ cm and $H_S = 8$ cm ; and in the upper level (γ), $H_{a,b,c} = 2{,}83$ cm and $H_S = 4$ cm. For the interpreted relative density curves, the constant k_{2,D_r} was set to 11 in all curves. The marked density sample was for the second sounding round (4a-c) after the rebuild-in, notice that $D_{r,\mathrm{CPTU}}$ is in-between the old and the new D_r due to $\approx 50\%$ influence of old sector and new sector, respectively AB-BC and BC-CA. The top of each sand layer, which were directly vibrated during sample construction, are marked as orange dots in the q_t- and D_r-profiles. To illustrate the effect of reading frequency, sounding S1 is marked as a solid line with dotted data points.

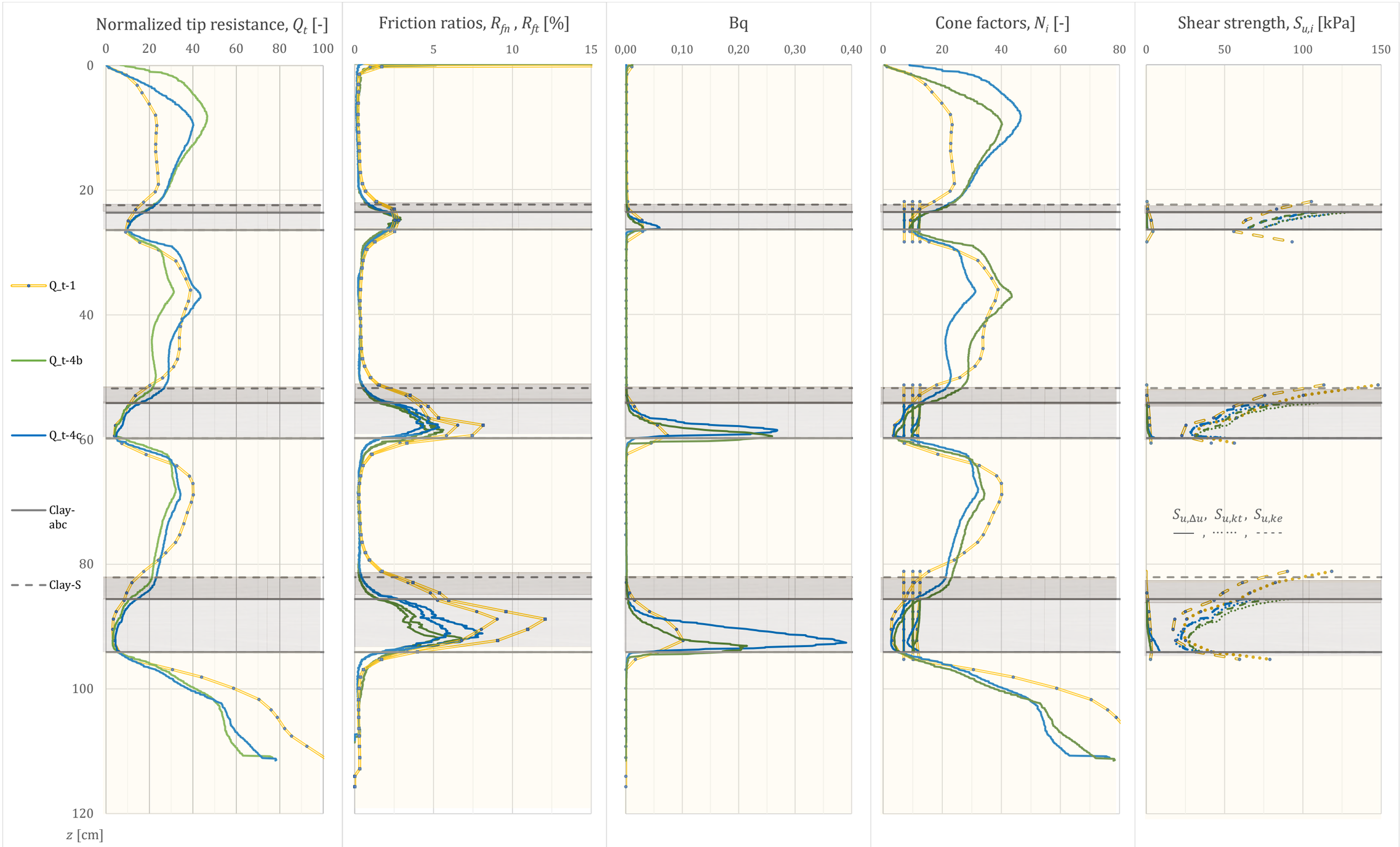

Figure 5.8. Normalized parameters, Q_t, R_{fn}, R_{ft}, B_q; Interpreted cone bearing factors N_m, $N_{\Delta u}$, N_{kt}, N_{ke}; and interpreted undrained shear strength, $S_{u,\Delta u}$, $S_{u,kt}$, $S_{u,ke}$ with reference value.

The cone factors $N_{\Delta u}$, N_{kt}, N_{ke} are all based on the laboratory results and the equations in ch. 2.3.1.3.
Regarding N_m, for the sand and the clay, respectively, the attraction is assumed equal to 0 and 8 kPa, while β is assumed to be -15° and 0°.
Due to the large scatter of data regarding S_u in the Flotten site report, and the unknown effect of disturbance, no reference line is given in the S_u-plot, in contrast to the S_u-plots for pottery clay.

Figure 5.9. Standard parameter profiles: q_t, f_s and u_2, followed by excess pore pressure, Δu_2, and interpreted relative density, D_r.

All soundings are included, even unsuccessful ones (3a-c). Thicknesses are as follows: In the lower level (α), $H_{\mathrm{a,b,c}} = 8{,}49$ cm and $H_{1\mathrm{S}} = 12$ cm; in the middle layer (β) $H_{\mathrm{a,b,c}} = 5{,}66$ cm and $H_{1\mathrm{S}} = 8$ cm; and in the upper level (γ), $H_{\mathrm{a,b,c}} = 2{,}83$ cm and $H_{1\mathrm{S}} = 4$ cm. For the interpreted relative density curves, the constant k_{2,D_r} was set to 11 in all curves.

5.1.2 Classification charts

A few classification charts were tried out for the latest experiment. These examples are shown in *Figure 5.10 – Figure 5.13*. In the figures, the clay layers are marked as blue for the upper and lower level, and red for the middle one. Note that the charts based on sounding 4b is sounded with the mini-probe, while sounding S1 is done with the standard probe. In *Figure 5.11*, the trail of B_q and Q_t goes in cycles following the markup, with the smallest "circle" representing the thinnest and first sounded layer, etc.

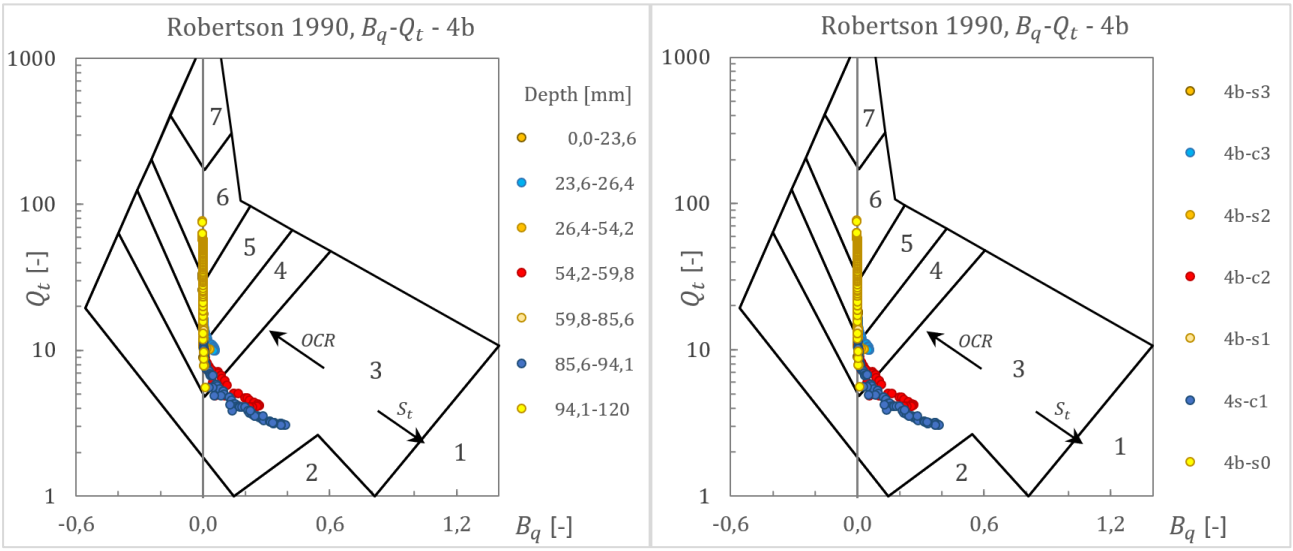

Figure 5.10. Sounding 4b: Robertson diagram for B_q and Q_t. With legend showing depth (left) and labels (right).

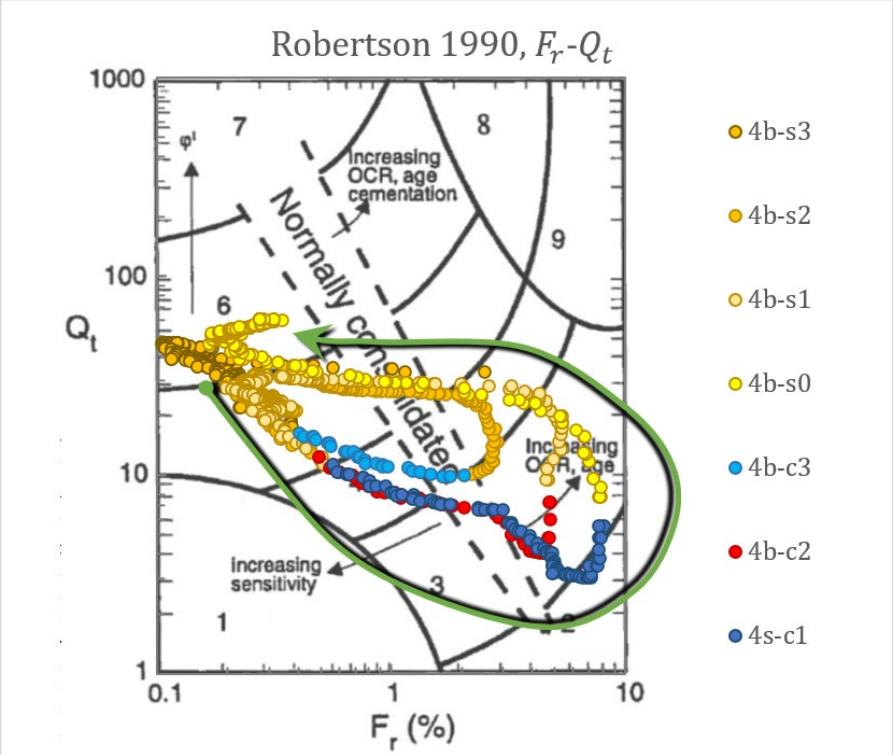

Figure 5.11. Sounding 4b: Robertson diagram for F_r and Q_t. The bottom sand layer is labelled s0, and the top sand layer is labelled s4. Similarly, c1 is the lowest clay layer, meanwhile c3 is the top clay layer.

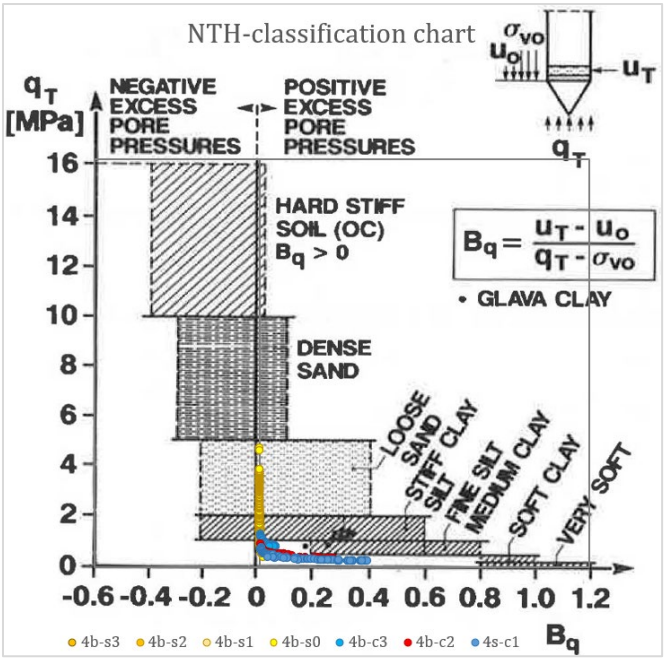

Figure 5.12. Sounding 4b, NTH-classification chart.

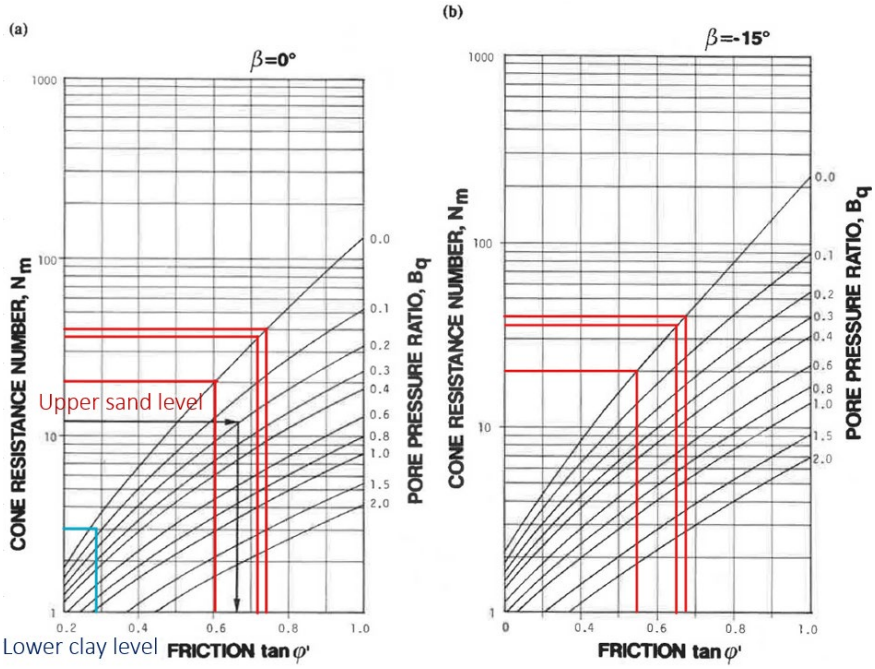

Figure 5.13. Readings of extremal q_t-readings in sand (red) and clay (blue). Sounding 1S.

Figure 5.13 is based on sounding S1, where N_m is read of for the lowest value in the thickest clay layer (blue), and there is one extremal reading for each sand layer (except below the lowest clay layer). The upper sand level has the lowest N_m reading, with the other layers following subsequently with larger values. The interpreted friction angles then become: ϕ'=16,0° for the clay (a=8 kPa, $B_q \approx 0{,}07$); and becomes respectively ϕ'=31,2°, 35,7°, 36,6° in the upper, middle, and lower sand layer, if the plastification angle β of 0° is assumed; and likewise, 28.4°, 33.0°,34.0° for β=−15°. Note the low B_q value of the clay (due to transitioning). Naturally, the interpretation of the thin clay layer and the sand is very unreliable considering that the q_t is affected by both layers. The same assessment method was used in interpretation of the data in the Appendix E. Discussion is found in ch. 6.3.5.

5.1.3 Compilation of normalized tip resistance profiles

In this chapter different segments of each sounding are presented, according to clay layer thickness, with readings normalized with respect to the cone diameter according to the theory in ch. 2.3.3. The plots are labelled with reference to the layer thicknesses sounded by the standard probe. I.e., for a layer thickness penetrated by the standard probe, there may be a corresponding sounding with the mini-probe. Hence, the plots are shown with reference to *equivalent standard layer thickness*, $H_{st.eq.}$.

As a reference for the characteristic value of the pottery clay, sounding 1a is added. The soundings are marked with colours according to the artificial overburden load during the specific sounding, (i.e., not coloured according to stress level in specific unit). Secondary soundings are dashed in all the graphs, as these are considered less reliable. The orange q_t-profiles are from soundings through quick clay units, in experiment 3. The q_t-profiles of the mini-probe are visible altered by the data treatment algorithm and emulate a discrete behaviour. Yet, the reading frequency for these soundings were much higher. The notation in the legend for each sounding through a specimen is as follow:

"Experiment – artificially imposed stress – standard equivalent layer thickness – sounding hole".

5.1.3.1 2 cm layer

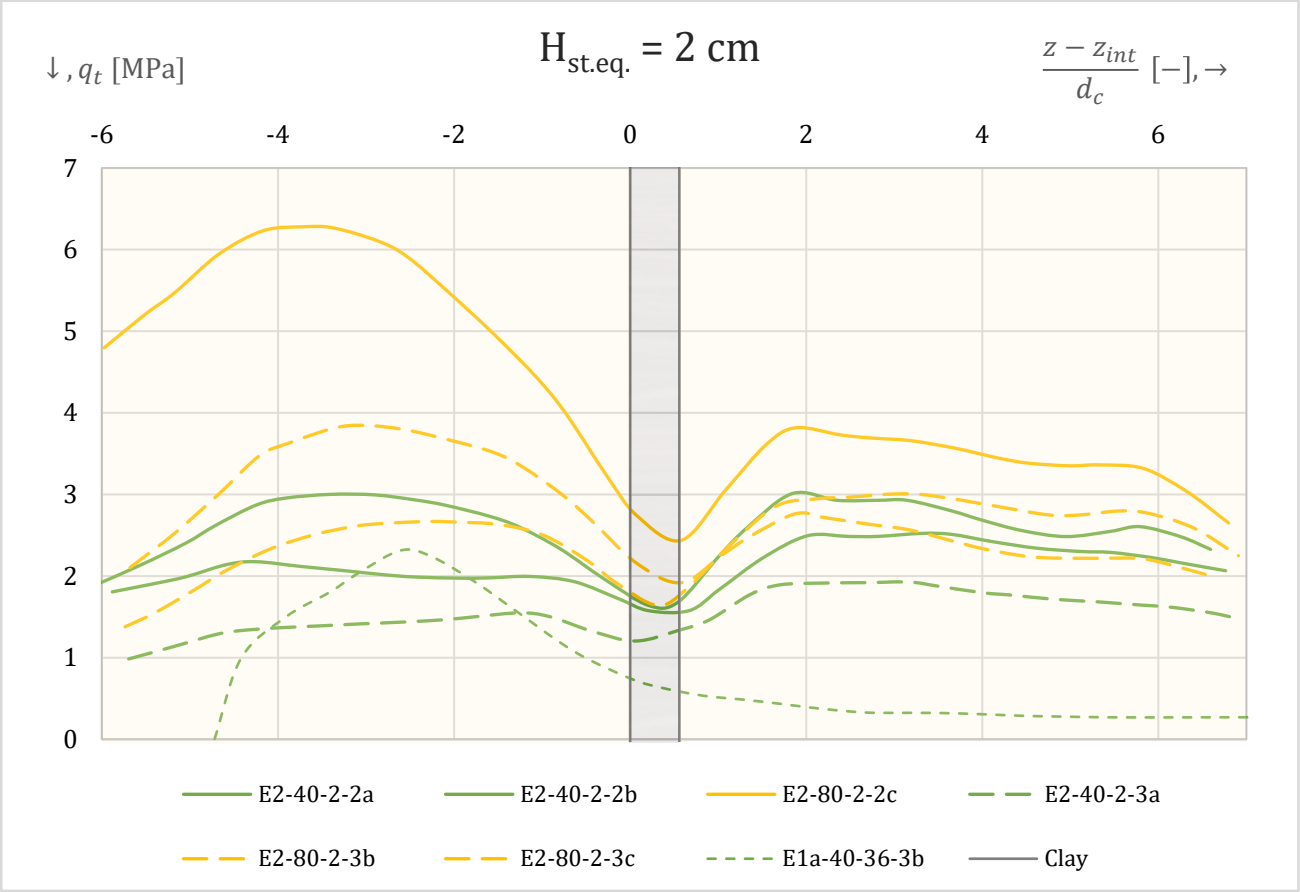

Figure 5.14. $H_{st}.eq. = 2\ cm$: Tip resistance profiles normalized with respect to cone diameter.

5.1.3.2 4 cm layer

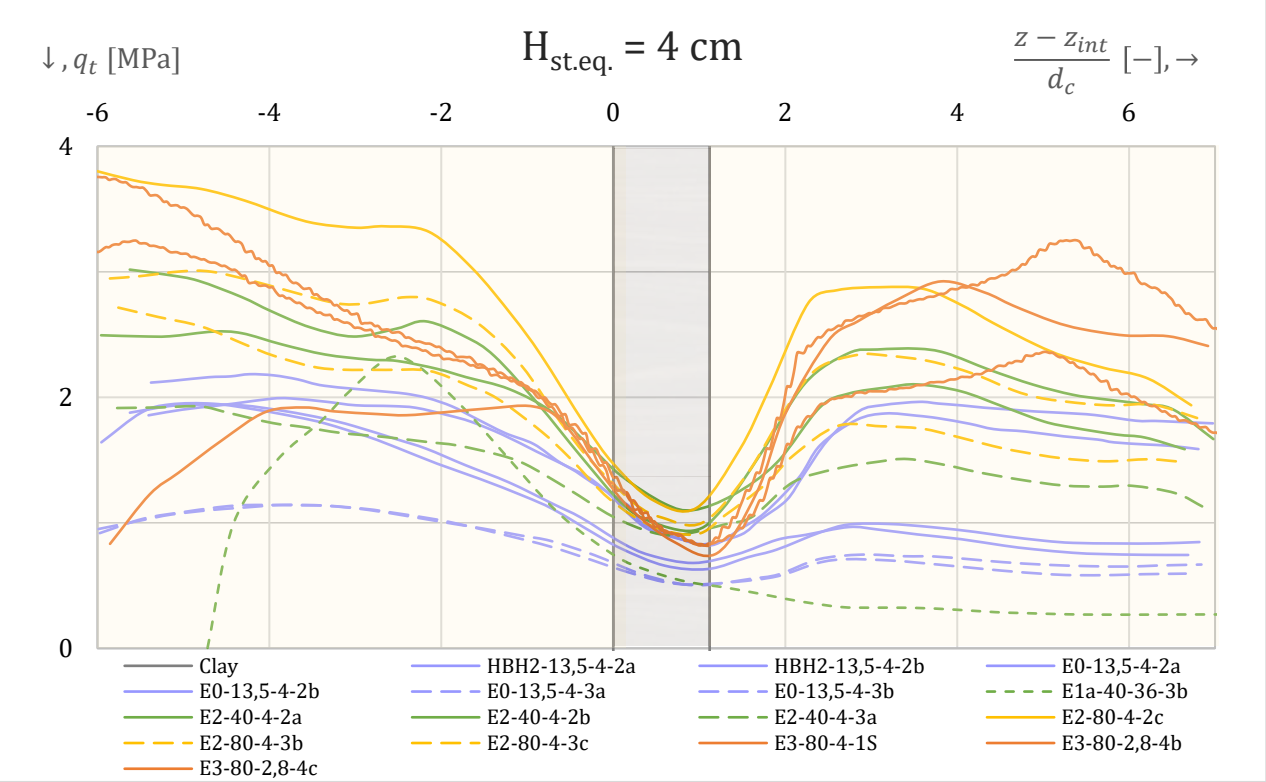

Figure 5.15. $H_{st}.eq. = 4\ cm$: Tip resistance profiles normalized with respect to cone diameter.

5.1.3.3 8 cm layer

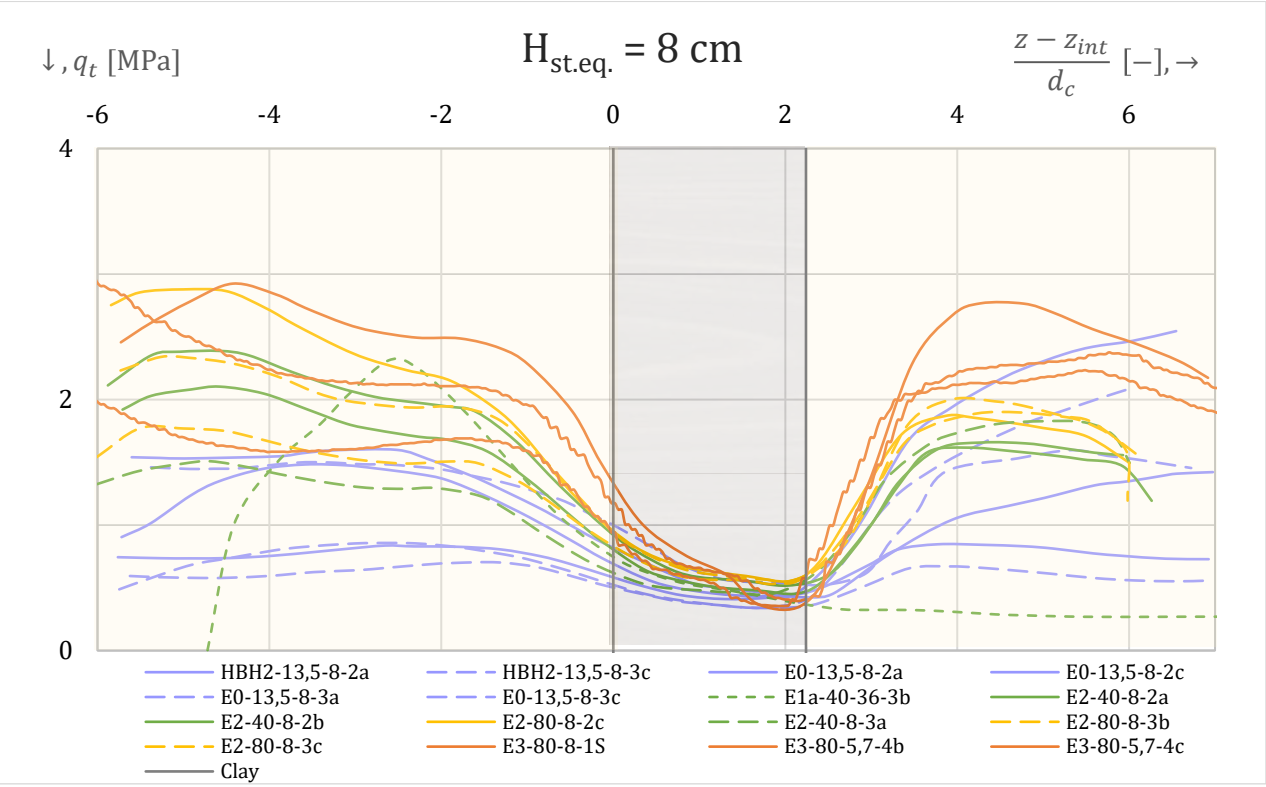

Figure 5.16. $H_{st}.eq. = 8\ cm$: Tip resistance profiles normalized with respect to cone diameter.

5.1.3.4 12 cm layer

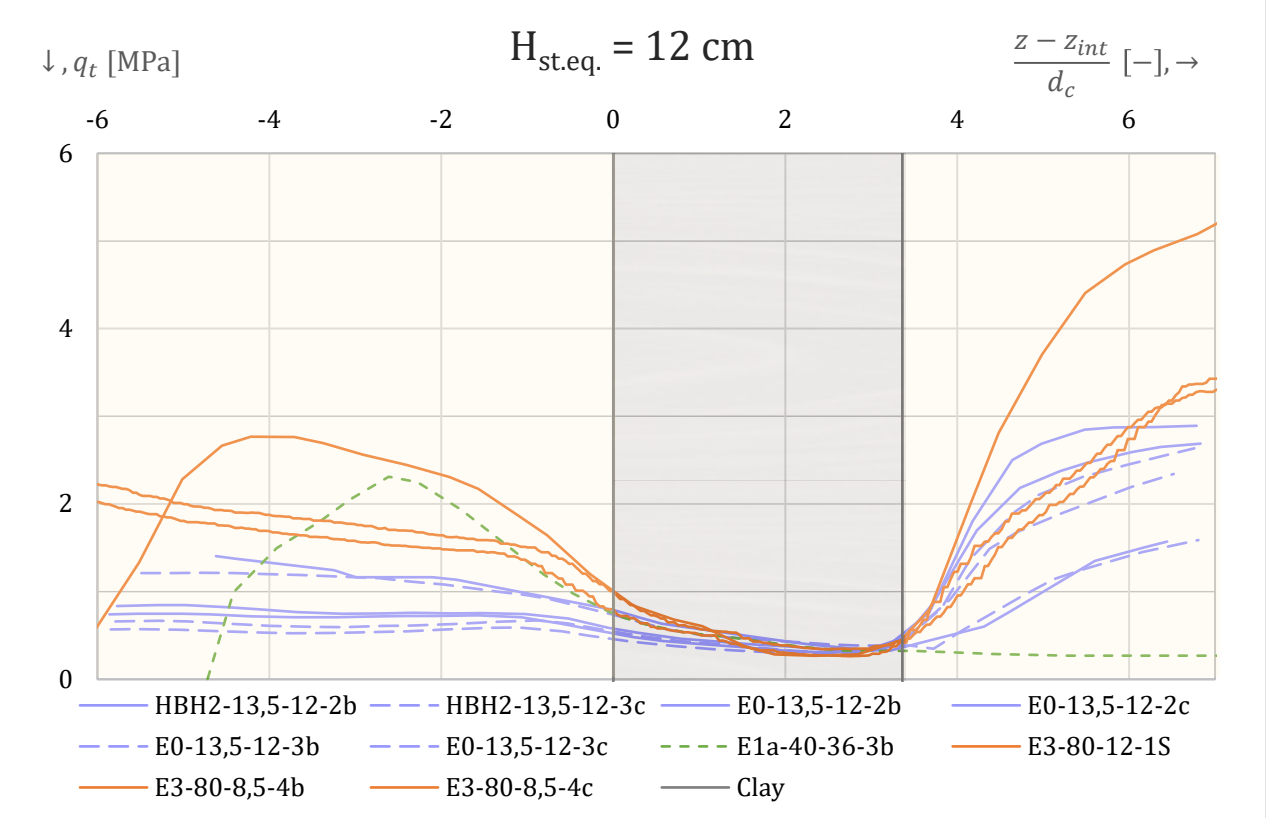

Figure 5.17. $H_{st}.eq. = 12\ cm$: Tip resistance profiles normalized with respect to cone diameter.

Note that both stress level and relative density is quite different between these measures, with D_r going from ca. 30 to 40% in experiment 0 (purple), and D_r going from ca. 40 to 60% in experiment 3 (orange). The imposed loads on top of the chamber samples are respectively 13,5 kPa and 80 kPa, however, these blocks are placed at the lowest level in the chamber. According to stress distributions worked out in ch. 5.3.3 the E0-units and the E3-units experience respectively ca. 16 and 64-65 kPa.

5.2 Supplementary laboratory results

In the following pages, most of the results from the supplementary laboratory tests will be presented. The presented data will mainly be focused on the last experiment with natural clay.

5.2.1 Tests on natural clay

The natural clay was utilized in the last experiment, E3. Most of the measurements was done during the excavation, and thereby, most results are from the moment with most accumulated disturbance. The measured soil properties will first be presented alongside data from the Flotten site report (L'Heureux et al. 2019). These data are followed by a compilation of soil properties associated the different sounded specimens given alongside the tip resistance profiles. Almost every specimen has been tested, and the centre specimens in the lower (α) and middle (β) level have been cut in two, horizontally, i.e., they were tested twice. Most water content samples are from during the excavation, as the cylinder specimens were kept intact under preparation, and little excess clay was available. Three plots will be shown for the measured water content, the first two consist only of measurements from the experiment: The first is associated reference depth at Flotten, the second is reference depth in the chamber. The third shows specimen results with values from the Flotten-site report as reference. The water content measured: in the preliminary test is denoted w_0; from sample build-in is denoted w_1; and from the excavation denoted w_2. In addition, there were samples taken from the clay blocks' tops and bottoms. These latter, and w_0 was not part of the chamber sample, but supplementary tests, hence placed in bottom of chamber graph.

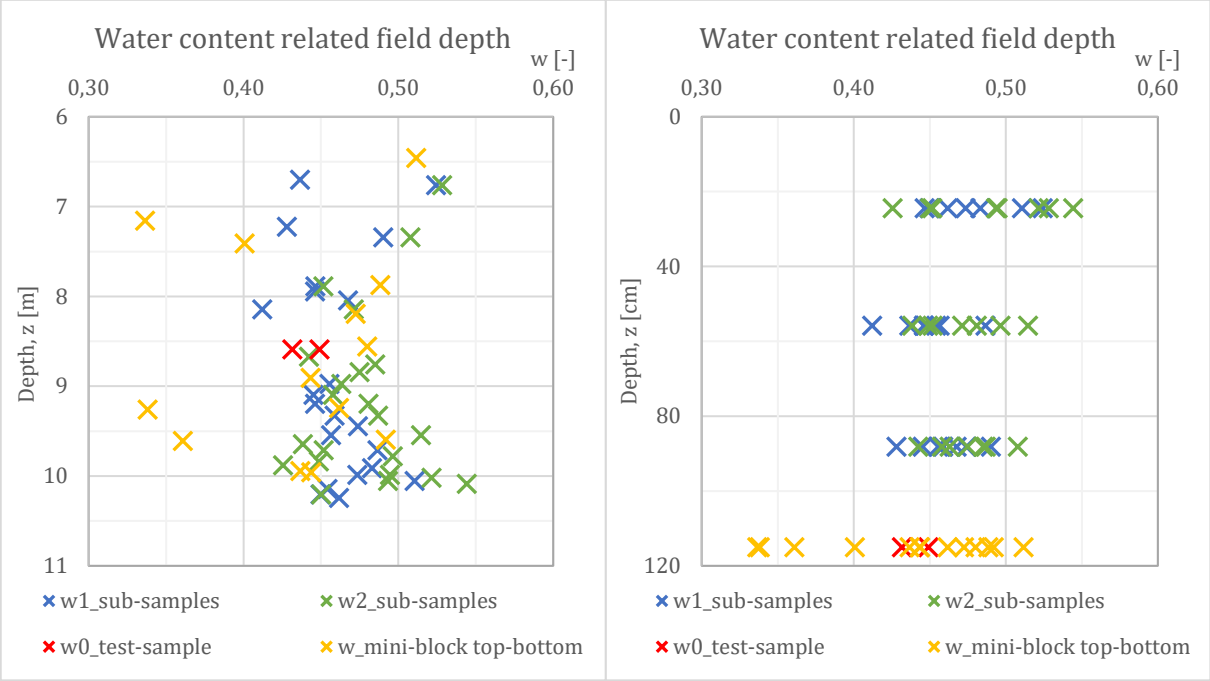

Figure 5.18. Water content with reference depth at Flotten (left) and in the chamber (right).

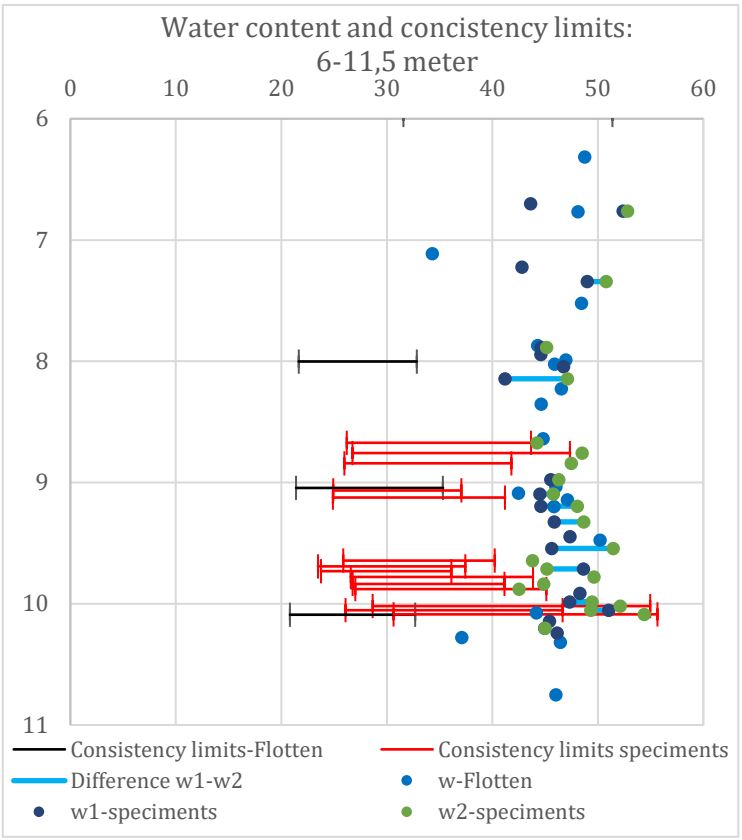

Figure 5.19. Measured water content and consistency limits for all specimens, with reference to values from the Flotten site report.

For the plasticity index, the nearest values with depths at Flotten are shown as reference, including the regression line for field layer profile. For the liquidity index, different Flotten-measurements are shown.

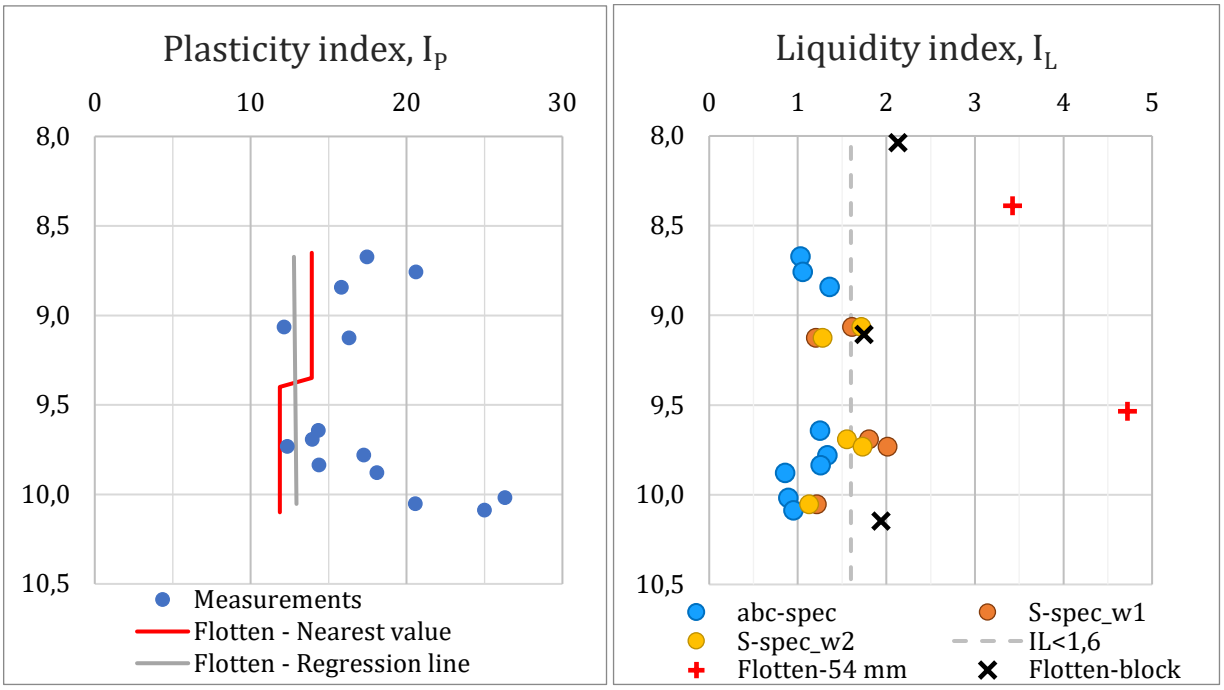

Figure 5.20. Plasticity index and liquidity index for specimens with reference to extraction depth at Flotten.

Further, other test results will be presented: Salitinity, liquid limit and shear strength measurements.

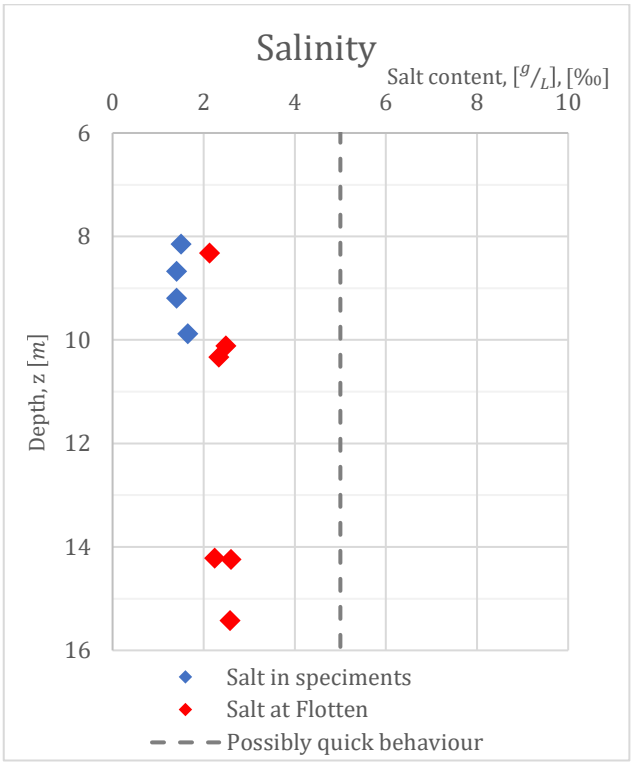

Figure 5.21. Measurements of salinity from the excavation, with reference values from Flotten.

For the liquid limit, the three-point method was used. As an excerpt, results from the lowest of three clay layers are presented below.

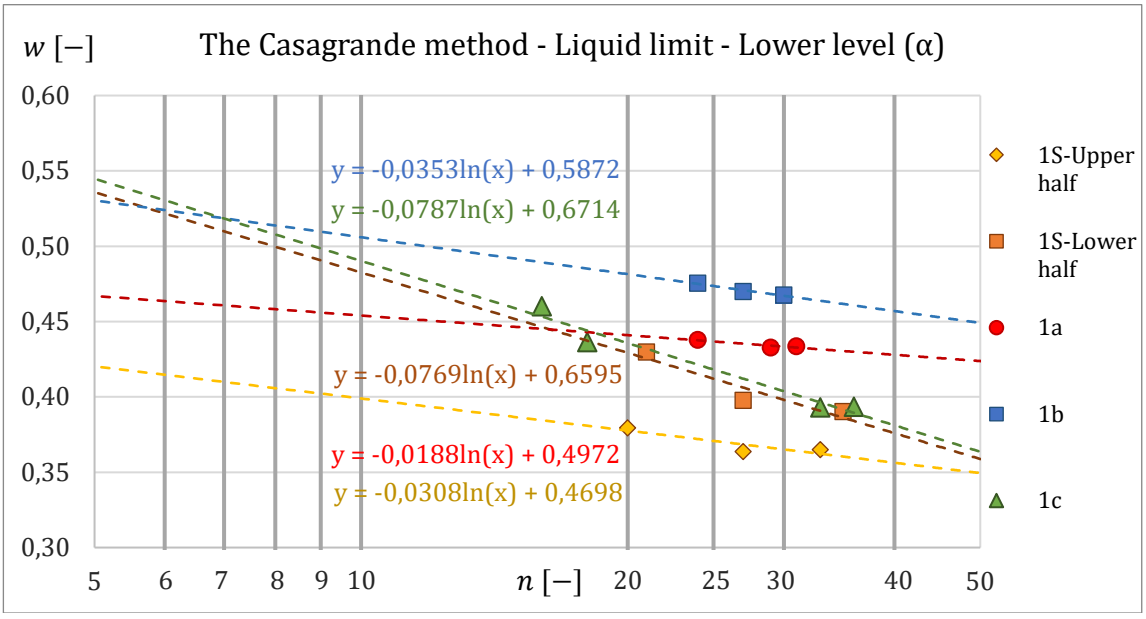

Figure 5.22. Determination of the liquid limit. Specimens from the lowest level (α).

S_u was measured with some of the most basic tests: uniaxial compression test and falling cone.

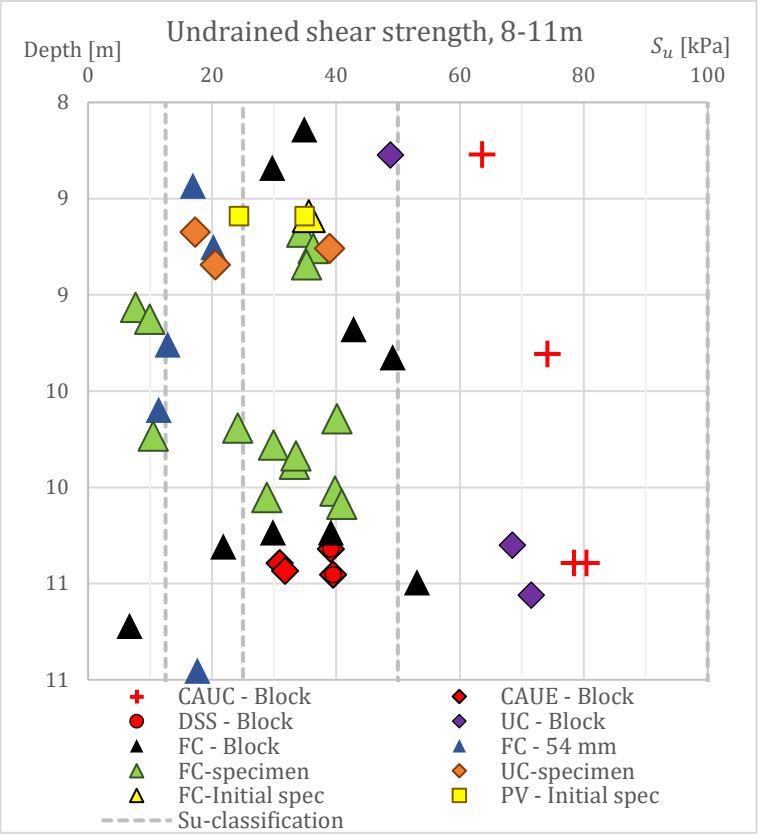

Figure 5.23. Different undrained shear strength measurements, with values from Flotten as reference.

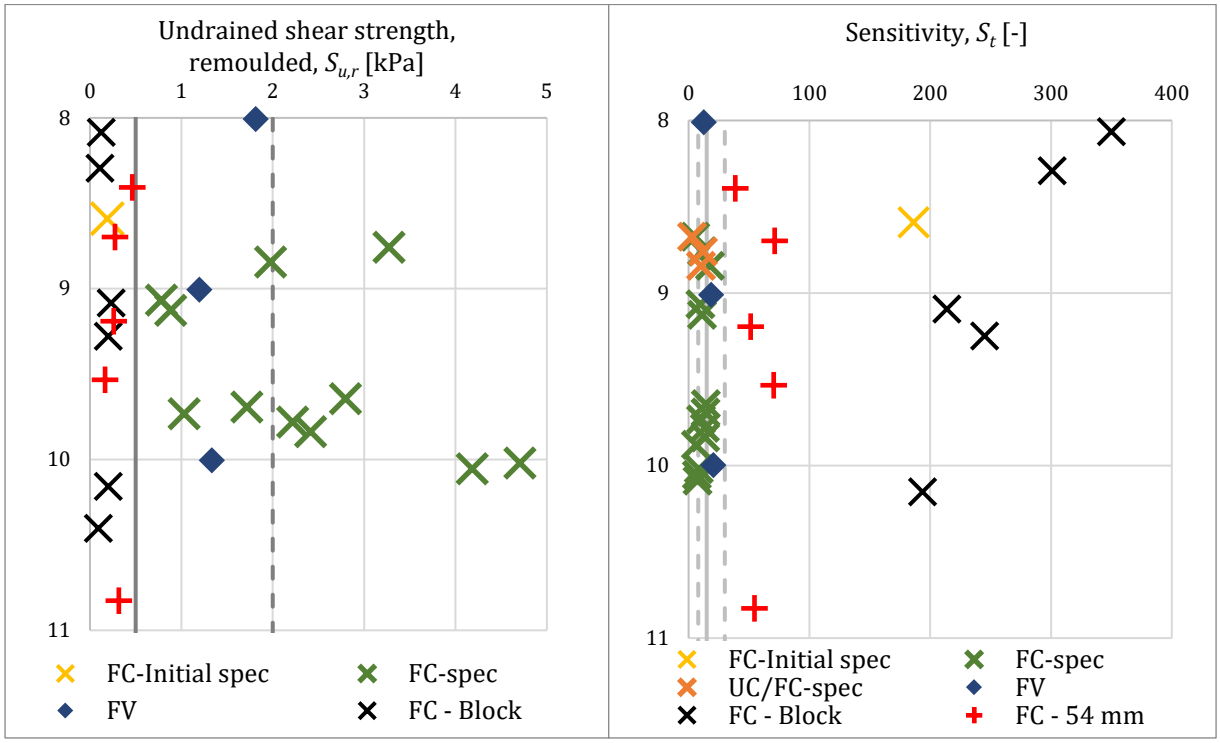

Figure 5.24. Remoulded undrained shear strength (left) and associated sensitivities (right).

In the sensitivity plot, the uniaxial compression test results are also included, by dividing their measured S_u on the remoulded shear strengths determined by falling cone tests.

5.2.1.1 Sounding 1S

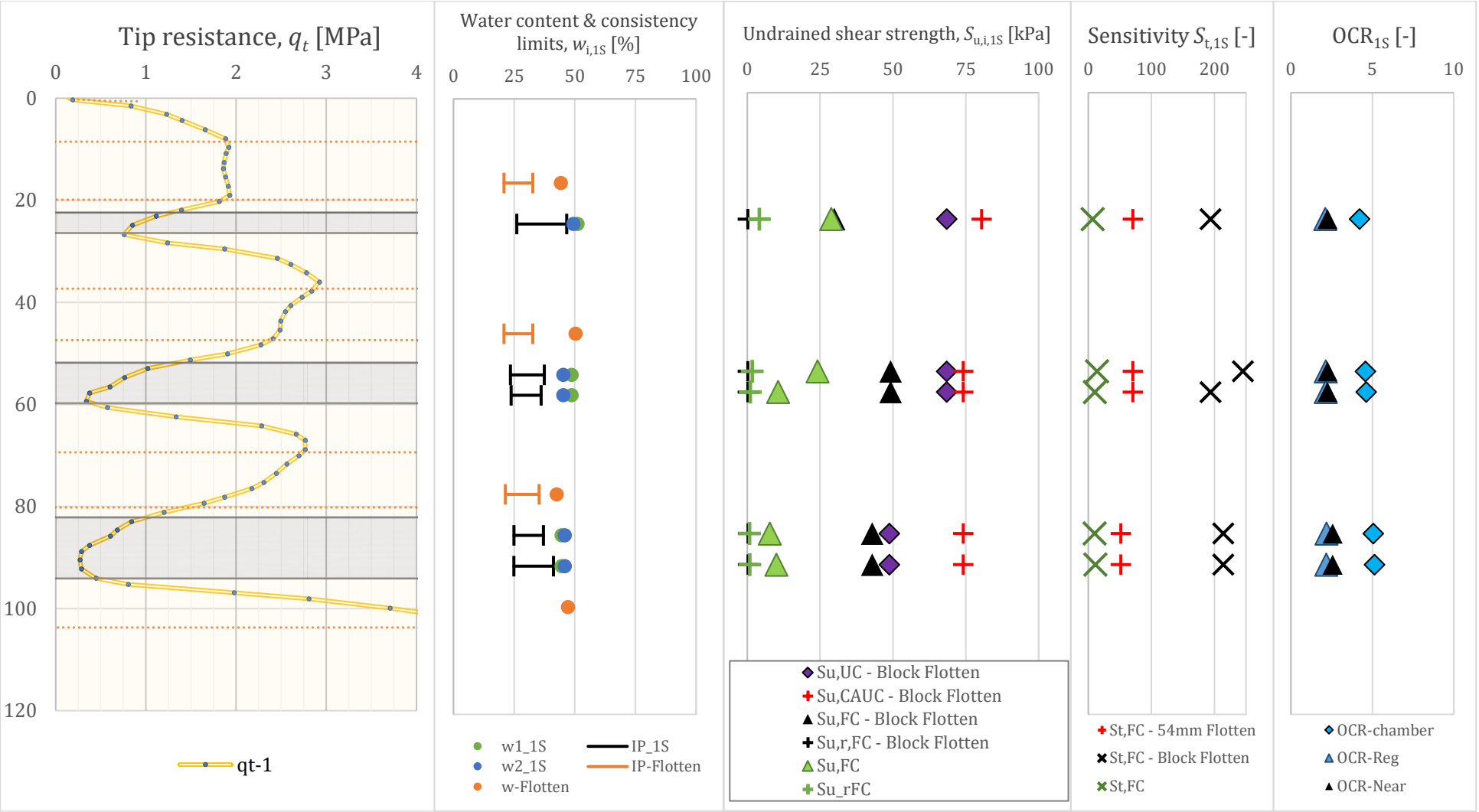

Figure 5.25. Sounding 1S, with associated soil properties: extracted from the Flotten site report; and determined in subsequent laboratory tests.

Note: Sometimes, values from Flotten will be duplications of each other, as the field reference values may be nearest to several specimens.
The top of each sand layer, which were directly vibrated during sample construction, are marked as orange dotted lines in the q_t-profile.

5.2.1.2 Sounding 3a

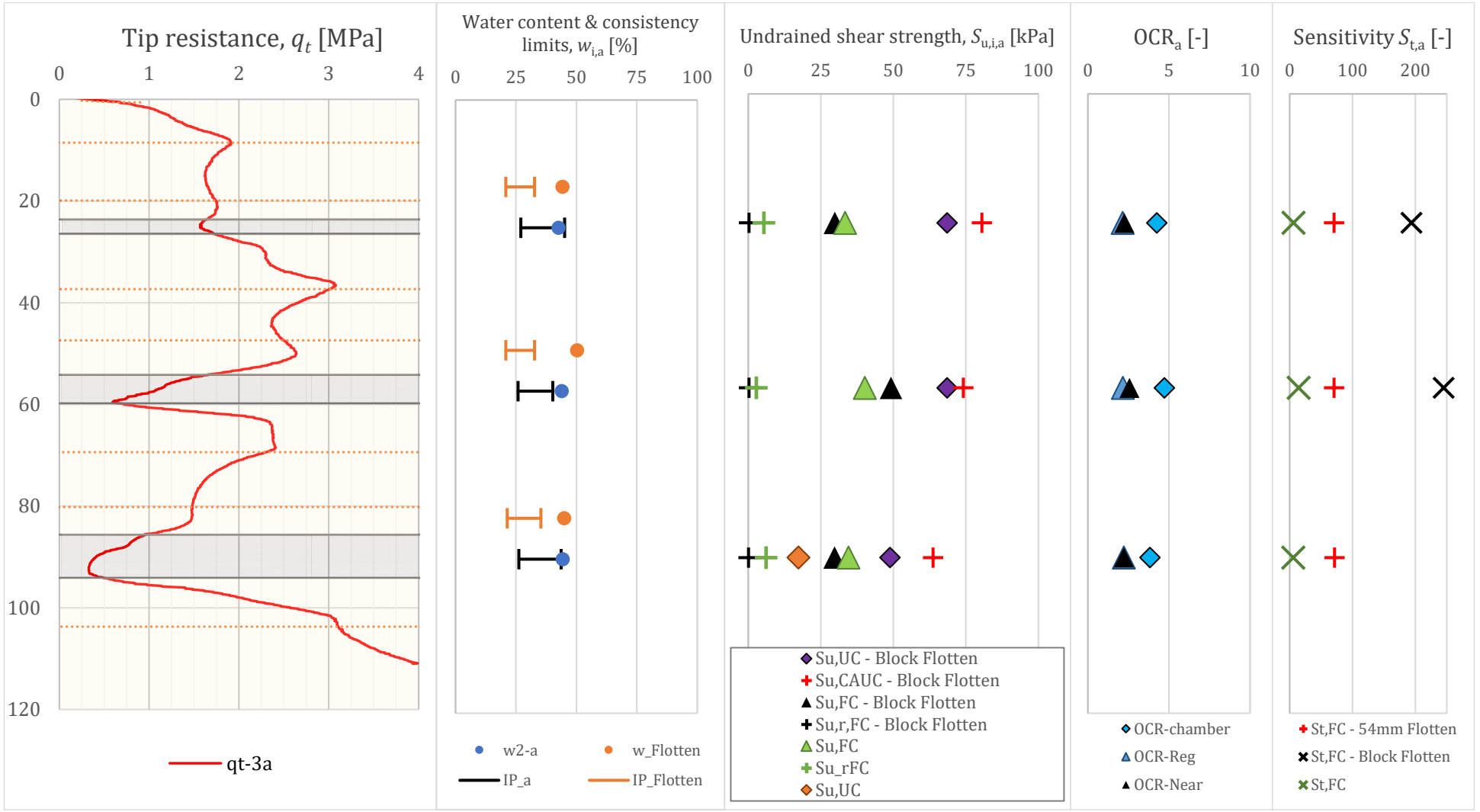

Figure 5.26. Sounding 3a, with associated soil properties: extracted from the Flotten site report; and determined in subsequent laboratory tests.

Note that this sounding was in the periphery of the specimen. Furthermore, the data from 4a, was unfortunately not treated.

5.2.1.3 Sounding 3b and 4b

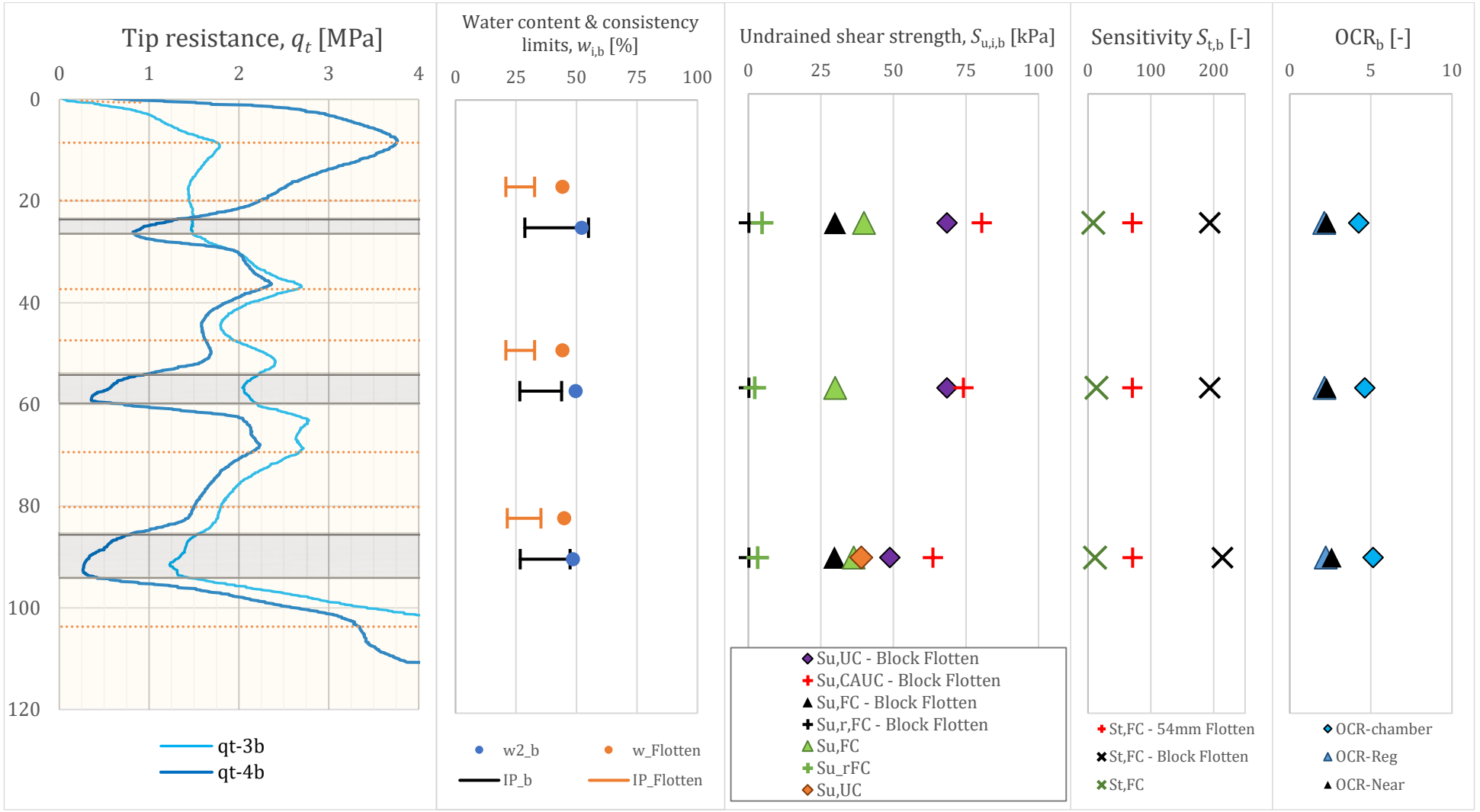

Figure 5.27. Soundings in sub-sample b, with associated soil properties: extracted from the Flotten site report; and determined in subsequent laboratory tests.

Note that the secondary sounding is higher in the top. This is due to the second build-in of zone BC above the upper clay layer.

5.2.1.4 Sounding 3c and 4c

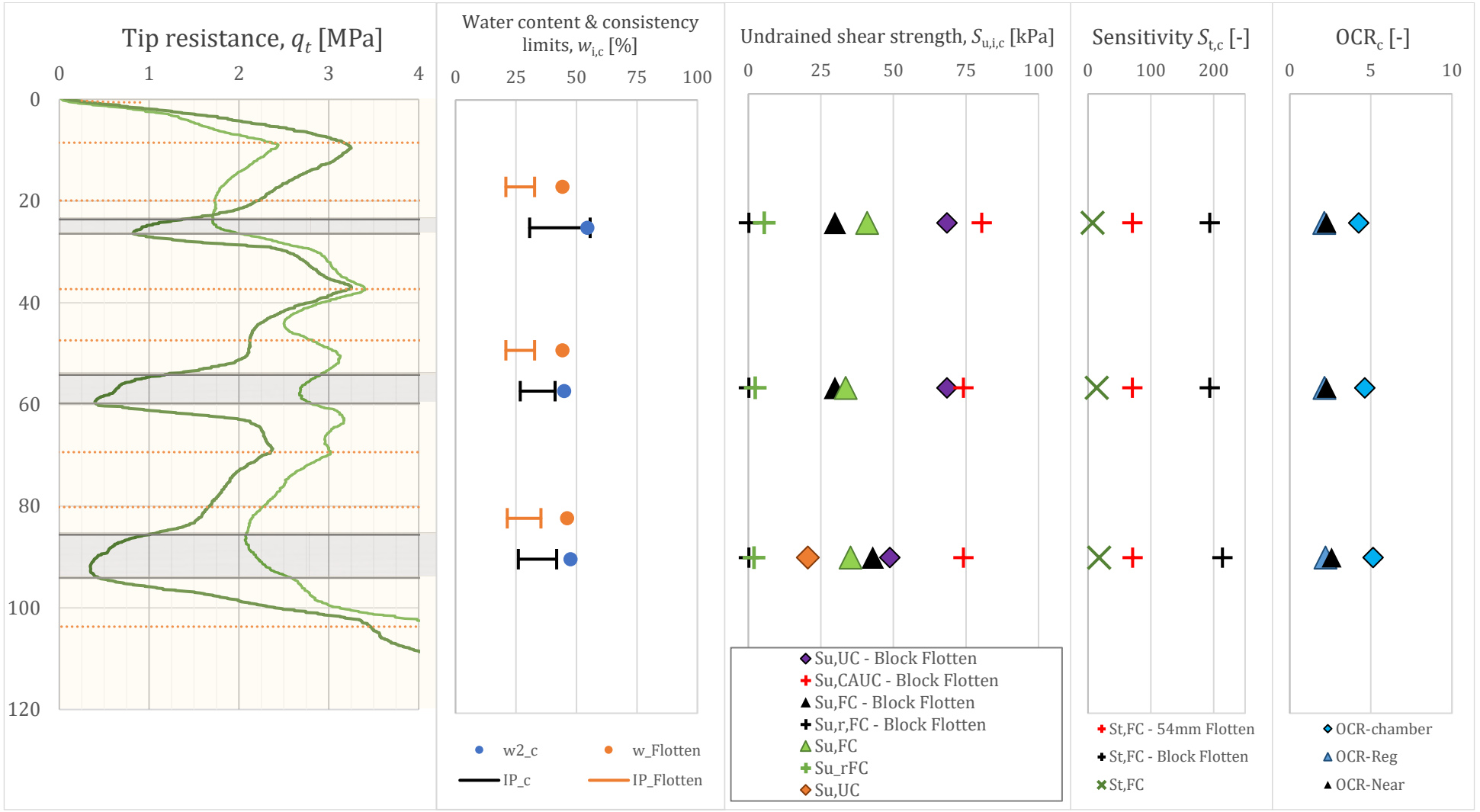

Figure 5.28. Soundings in sub-sample c, with associated soil properties: extracted from the Flotten site report; and determined in subsequent laboratory tests.

5.2.2 Density tests

In this sub-chapter, the results from the density samples are shown, with the parameters: the relative density and the porosity (shown with "predetermined boundaries", from Hammer's (2020) work following instructions from DEGEBO). The height of the density sample cylinders is marked in the charts with relative density.

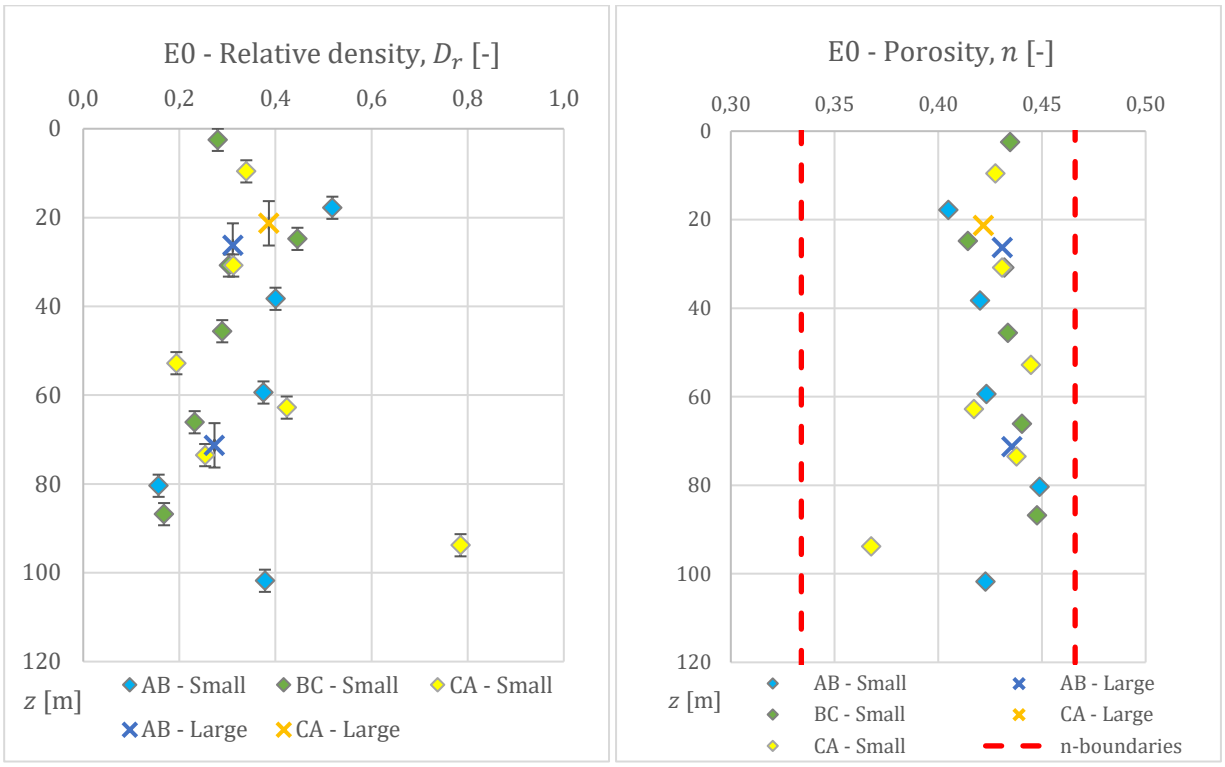

Figure 5.29. Experiment 0: Relative density and porosity.

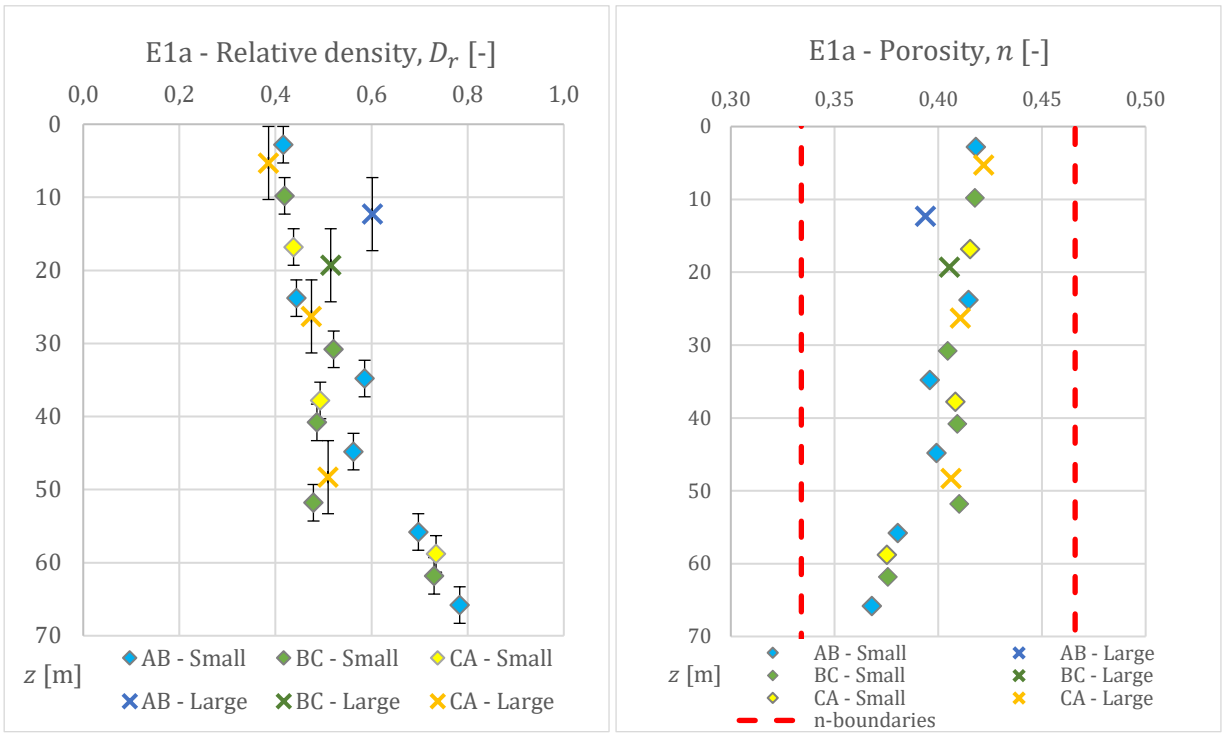

Figure 5.30. Experiment 1a: Relative density and porosity.

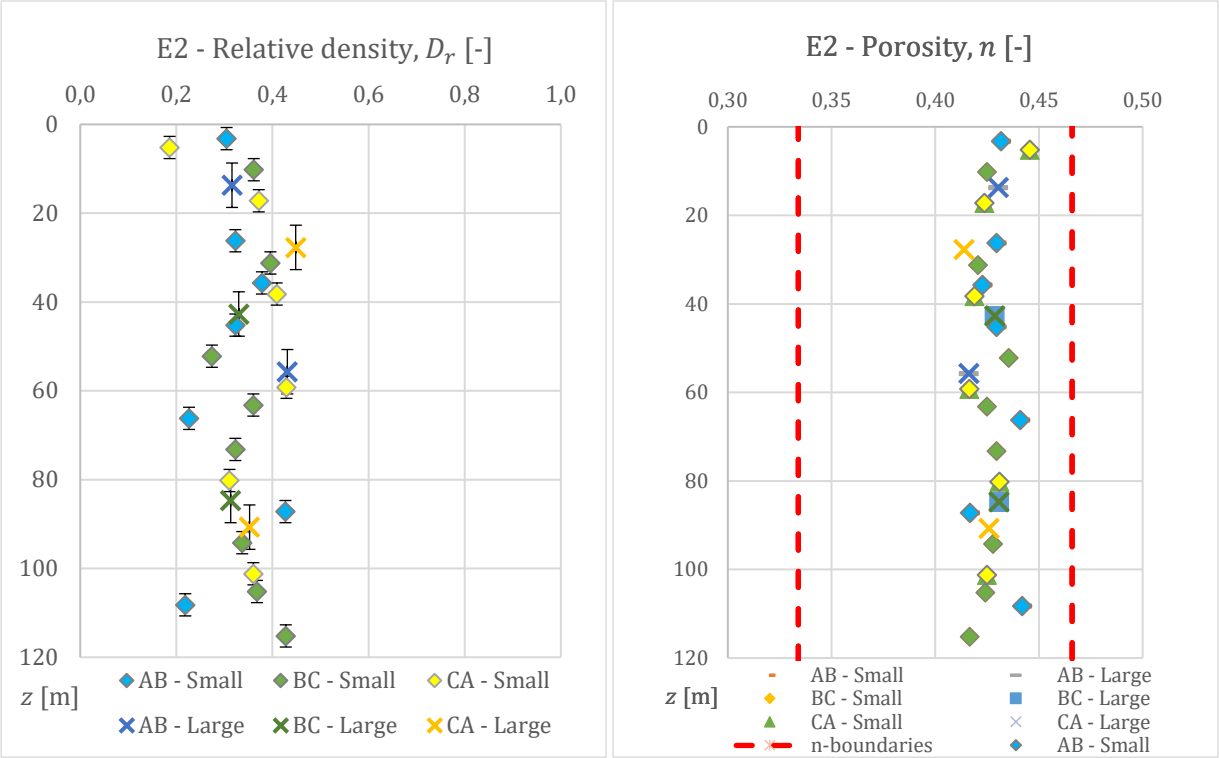

Figure 5.31. Experiment 2: Relative density and porosity.

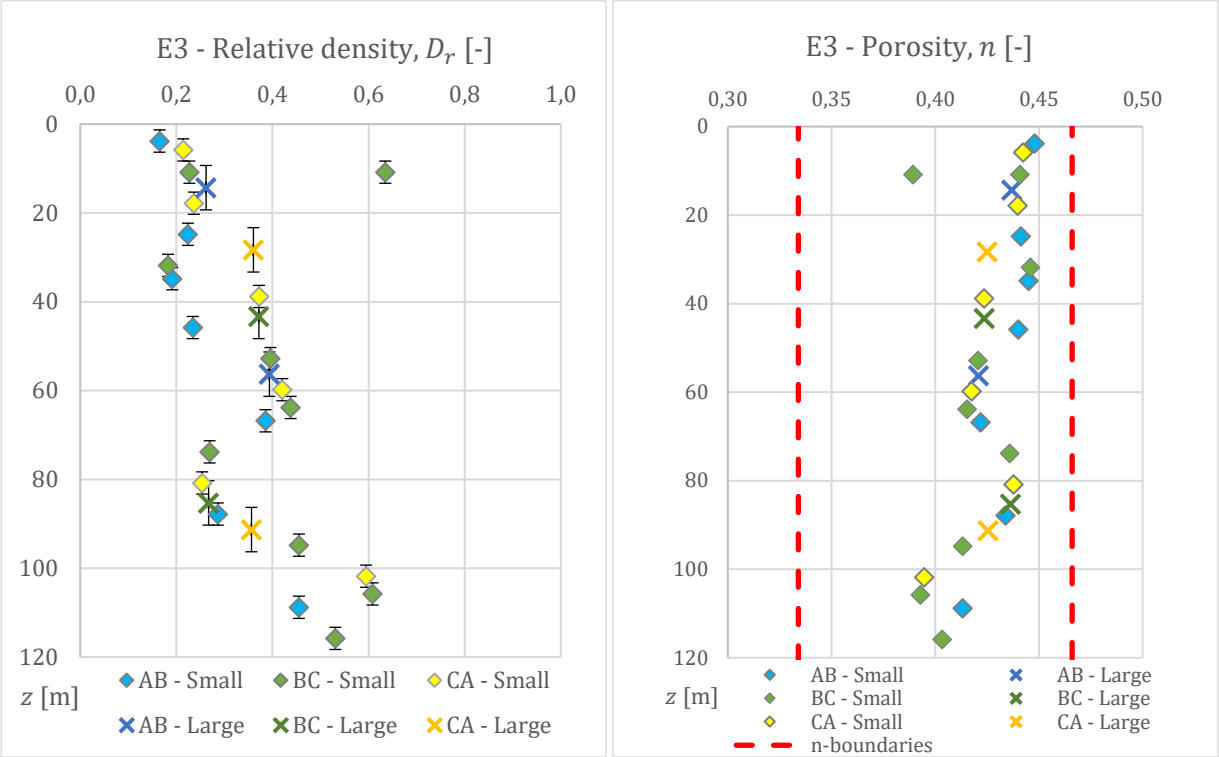

Figure 5.32. Experiment 3: Relative density and porosity.

In the last experiment, there was an excavation of zone BC above the upper clay layer, intermediate soundings 3a-c and 4a-4c, with a subsequent build-in. Thereby there are two density sample results for the same depth and zone in the graph. The latest build-in was more improvisatory, giving a larger D_r. This is also reflected in the soundings.

5.2.3 Tests on pottery clay

The determined soil properties of the pottery clay are mainly presented in ch. 4.2.2.3. These are based on tests either prior to, or after, a chamber sample build-in and excavation. The lab tests taken closest to unpacking of the clay blocks are prioritized in that table. The clay is very homogeneous for all blocks, and typically yield roughly the same results for every test. Much of the deviations are associated the test accuracies and the performed lab practice. The simpler the lab test, the less deviance was experienced, e.g., for water content samples.

The sample standard deviation of the measured water content is 7 ‰, with min and max respectively 22,8 % and 25,8 %, including all measurements, i.e., from both before and after a build-in. The tests with the most scattered data will be presented in the plots down below: The liquid limit, in *Figure 5.33* and the undrained shear strength found by the falling cone test in *Figure 5.34.*

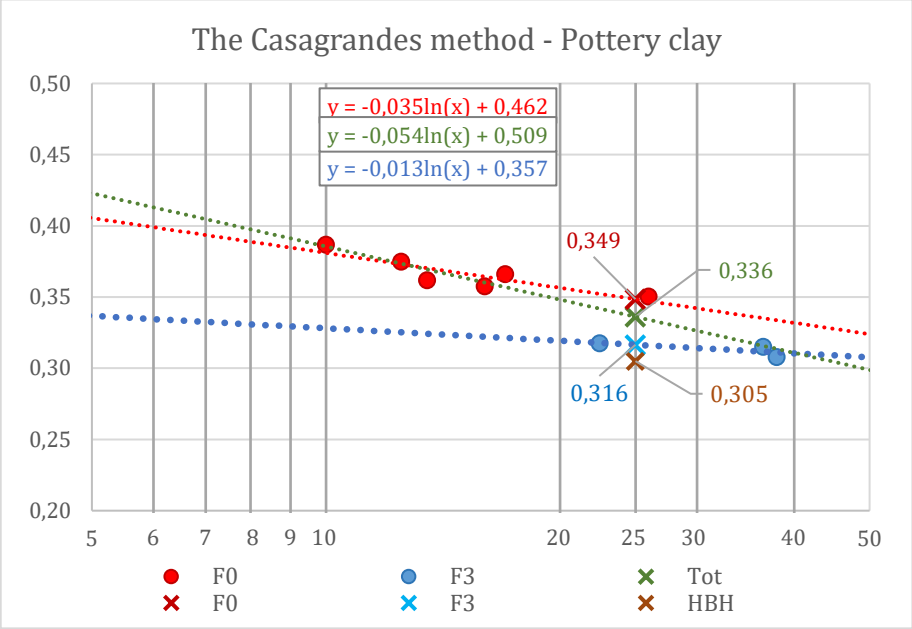

Figure 5.33. Determination of the pottery clay's liquid limit.

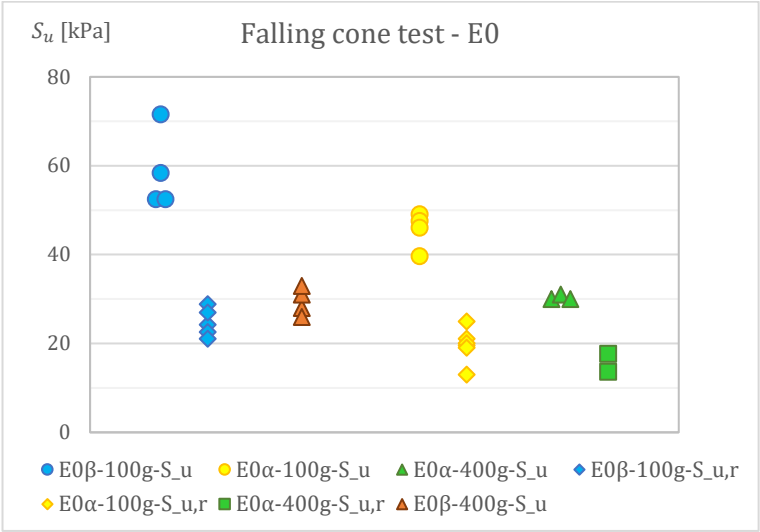

Figure 5.34. Measured undrained shear strength based on falling cone test.

5.3 Pressure cells

In this chapter the pressure measurements and the associated derived chamber stress distributions are presented. Due to sensitivity drift, all of the earth pressure cell data in this chapter are corrected with respect to starting- and ending points. If readings are missing for longer periods, it is assumed that the last logged values in advance of a gap are correct. The next readings are then corrected accordingly, with the change of water level taken into account. These compensations are either linear: from start to end; or constants for the start-up, and potential re-start-ups after time gaps. The readings could be altered to compensate for obvious undershooting, e.g., effective stresses below 0 (suction), yet this kind of interpretation is not well founded on any measurements, and is therefore typically avoided. However, to obtain horizontal stresses that are possible to use further in the stress assessment, this has been compensated in experiment 2 and 3. This has been visualized in the second chart in ch. 5.3.2.

The reliability of the pore pressure sensor has been very good throughout the experiments, and its readings should thereby be considered as correct. The sensor was positioned a bit over the chamber bottom and a bit underneath the sensors. All effective stress measurements have accordingly been adjusted for these height differences.

5.3.1 Sensitivity drift

The pressure cells were left in the chamber for some days to see the effect of sensitivity drift, see *Figure 5.35*. It is evident that the cells behave differently, both with respect to white noise and fluctuations over time. The plot also includes linear correction of readings, seen as thinner, darker curves. As can be seen in the figure below, readings will be inaccurate to some extent, regardless of corrections, but the magnitude of deviance is generally reduced by the corrections.

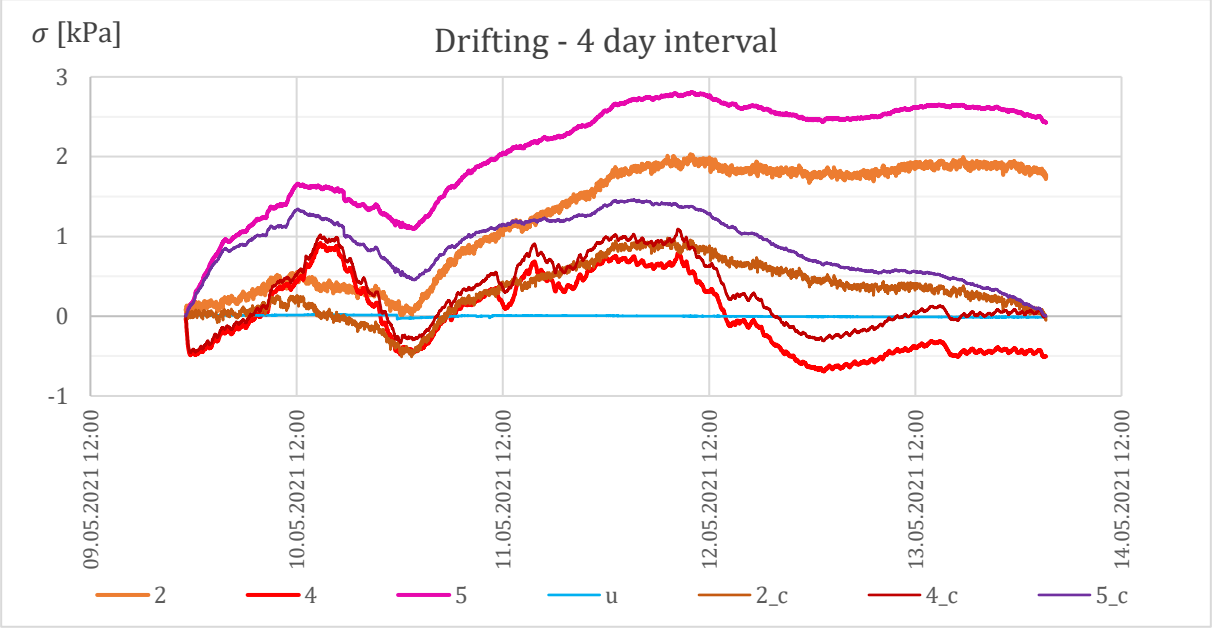

Figure 5.35. Sensitivity drift over 4 days, with no imposed load on the cell. The plot includes linearly corrected data which ends up at zero stress level.

5.3.2 Timelapse of sample construction

Only an excerpt of the time lapses of pressure readings are shown. The data have first been averaged as to remove white noise and unreliable extremal readings. This has been meticulously done as to not misrepresent the actual data (not exaggerated wide intervals, and no averaging over transitions of datasets which are far apart time-wise). Furthermore, as the datasets can be tens of thousands of rows, or even more for the most prolonged experiments, the data sets have been compressed by retrieving data at fixed time intervals. These time intervals were moreover shorter for more critical stages, such as loading and unloading. The averaging prevented that fluctuations caused by white noise or unreliable extremal readings were captured by the retrieving function which made the compressed data set. After both these treatments, the data was corrected as previously explained.

The deviations due to drifting became increasingly apparent for each experiment as they proceeded further. Thereby, the data from the start is regarded as the most reliable. In experiment 1a, *Figure 5.36*, the readings of the 1st and the 2nd cell descended below 0 kPa in the excavation phase, regardless of corrections. Another characteristic that has not yet been described is the typical inertia associated each building cycle (peaks followed by descents), as is visible in the graph. The 2nd pressure cell in experiment 1a showed a substantial difference in behaviour as compared to the other cells and was therefore replaced afterwards.

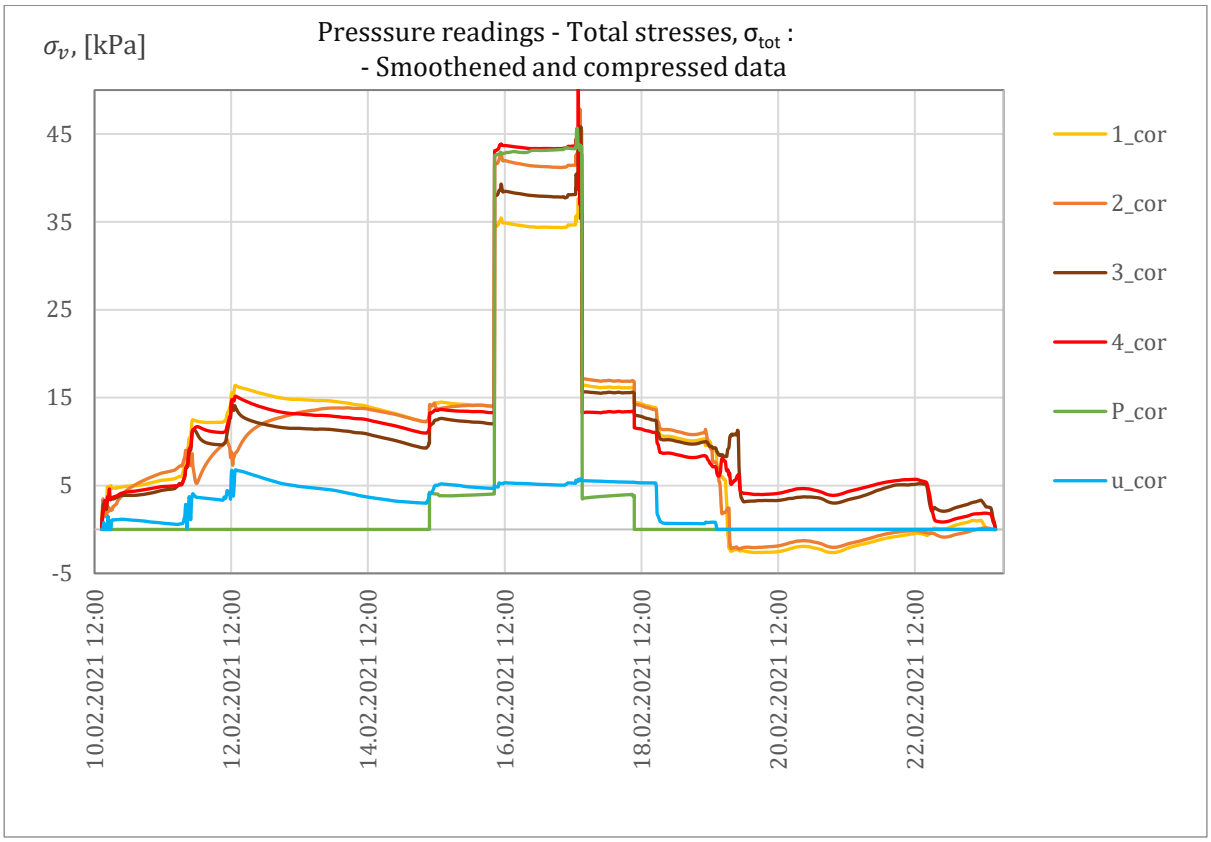

Figure 5.36. Timelapse of readings during E1a.

Gaps in the data were not untypical. The causes were many: sometimes logging was interrupted by forced computer updates, other times, the program was altered or crashed (generally due to erroneous file paths). In addition, some operations required the equipment to be disconnected, where the subsequent reconnection of the equipment may have been forgotten (uncertain). Regardless of causes, the logging was naturally not started again until the interruptions were detected, and could consequently leave behind up to 2 days of data missing.

In experiment 2, which is shown in *Figure 5.37*, the 5th cell descended a lot after build-in was commenced. The readings descended well below the water pressure (at cell five's level) and started first to ascend again halfway into the excavation phase. The stress path of cell 5 is expected to be more similar the proposed correction denoted as "5_manipulated" in the chart. This latter data set was used for the stress distribution assessment in the next chapter.

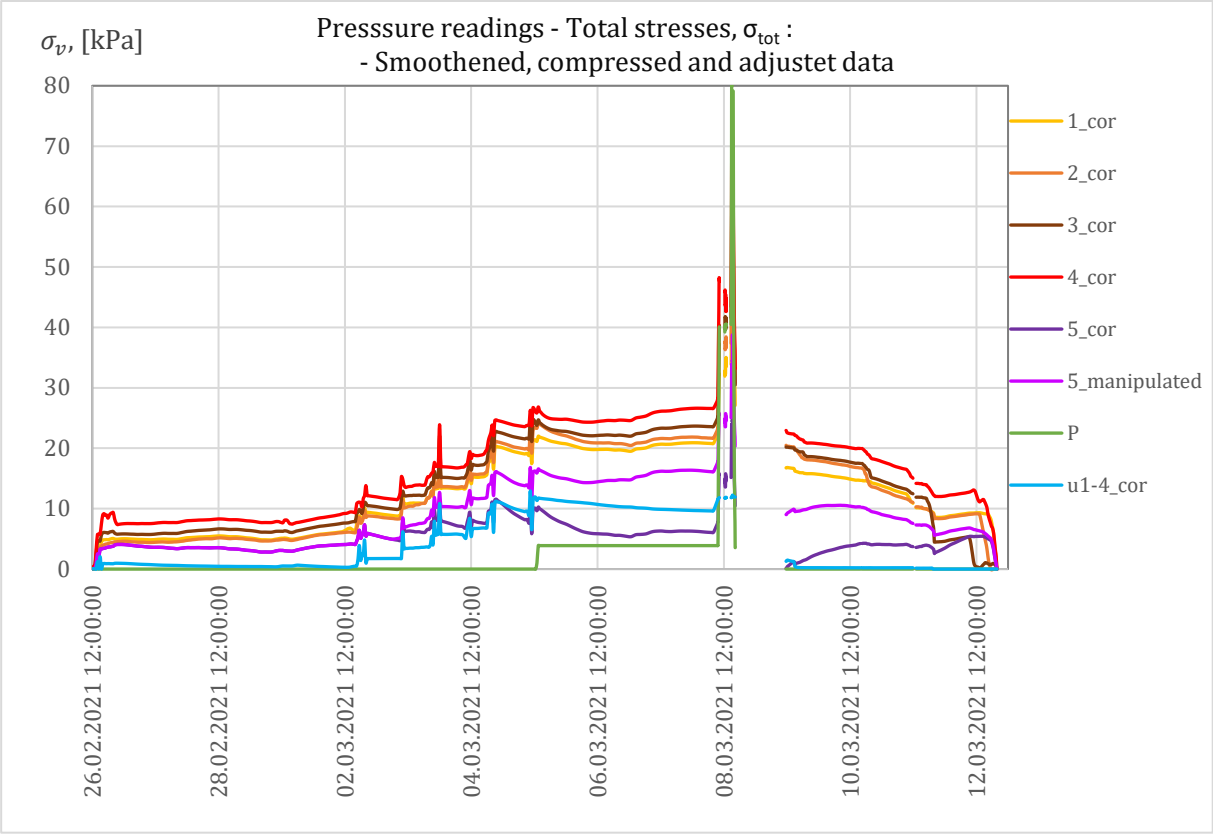

Figure 5.37. Timelapse of readings during E2.

5.3.3 Chamber stress distribution: The silo effect

In the assessment of stresses in the test chamber K' and δ' are assumed to be constant along the complete vertical depth in the silo. I.e., the ratio between average vertical effective stresses and horizontal effective stresses working on the wall is constant through the whole sample. The second element tells that the mobilized friction along the wall is constant with depth. The constants K' and δ' have been determined by incrementally changing them to approach a specified σ_v' and σ_h'. This was done using the "excel solver" and setting upper and lower limits for σ_v' and σ_h'. These stresses were moreover based on the interpreted stresses from the cell readings. For experiment 0 and 1a, K' and δ' could not be uniquely determined due to too few in-put arguments, however, l', which is a function of K' and δ' was possible to determine. Thereby, as no unique combination of the two existed, the graphs for the horizontal stresses are merely approximations, and may look quite different.

All of the vertical cell readings (cell 1-4) were averaged to determine $\overline{\sigma_v'}$, quite accordingly to the assumption in the differential slides method. The notations in the graphs are as follows: σ_v' and σ_v respectively means vertical effective stress and vertical total stress at a certain depth. The imposed normal stress on top of the sample is denoted q. The graphs show stresses accumulated by both self-weight and the overburden load: $\sigma_v' + q$ and $\sigma_v + q$. I.e., no plots designated only distribution of overburden load or self-weight is shown, and no curves of the stress-distribution without q are shown either. To illustrate how the arching effect reduces the stresses in the sample, corresponding plots without influence of the silo effect will be included too. These will be dashed. A last plot that is included is the vertical effective stress curve for a completely dry chamber ($u_0 = 0$). In this curve, the constant l' remains unchanged. More info on the silo effect is written in ch. 2.4.1. The formulas that were used to make the graphs accounts for the water table.

5.3.3.1 Experiment 0

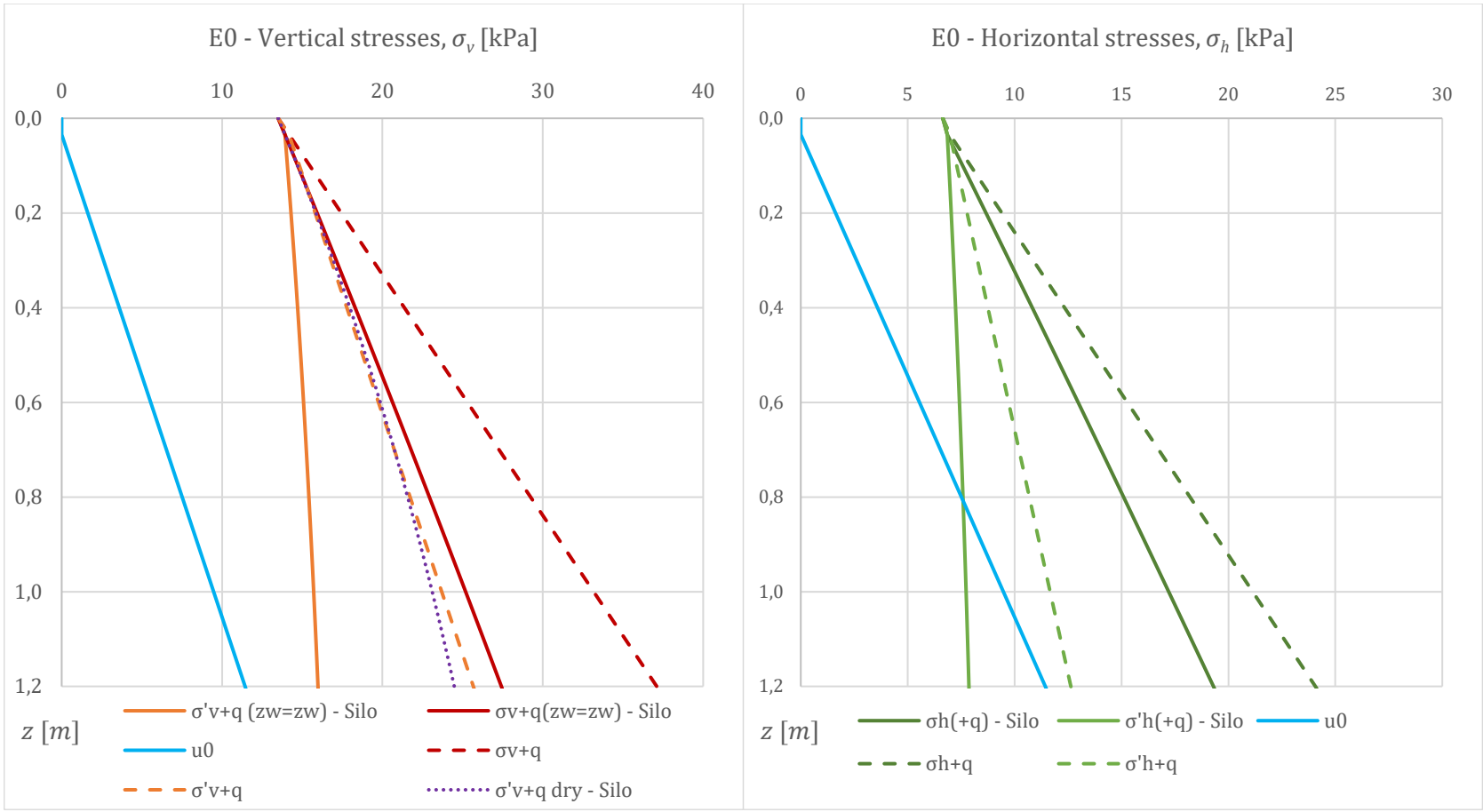

Figure 5.38. The interpreted stress distributions during soundings in experiment 0.

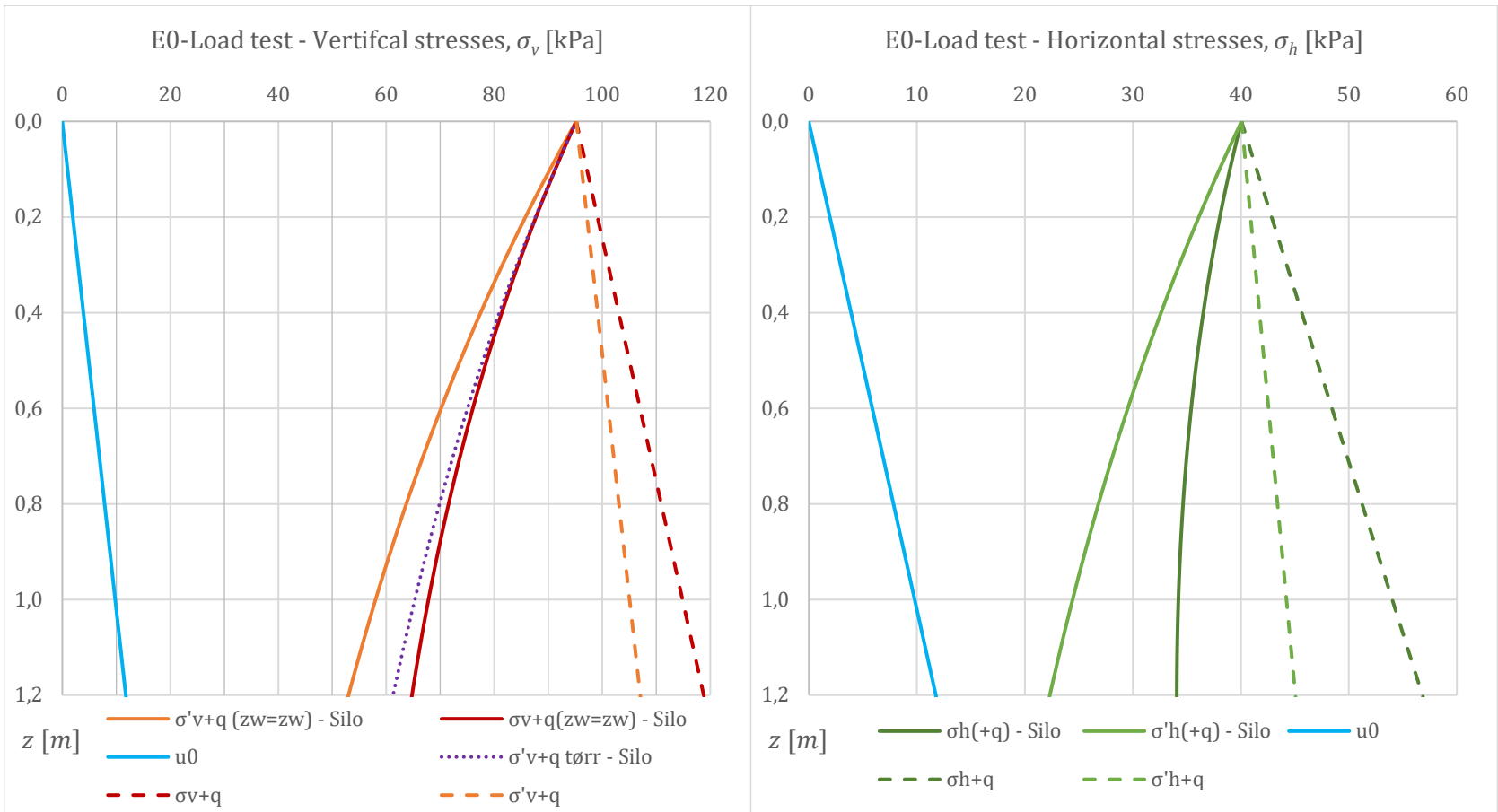

Figure 5.39. The interpreted stress distribution from the load test succeeding the soundings in experiment 0.

Note that in this experiment, no horizontal stress was measured, and thereby, the graphs on the right hand side are merely approximations. The vertical stress curves should anyhow be correct according to the differential slides method, only relying on the product of $l'(K', \delta')$. I.e., upper, and lower bounds are known, and the l' have been found accordingly. The graphs on the right hand side will for specific l's have many possible appearances, as too few boundary conditions are known to determine K' and δ'.

During the soundings in experiment 0, l' is approximated to have been 1,86.
During the load test succeeding the soundings in experiment 0, l' is approximated to have been 1,59.

5.3.3.2 Experiment 1a

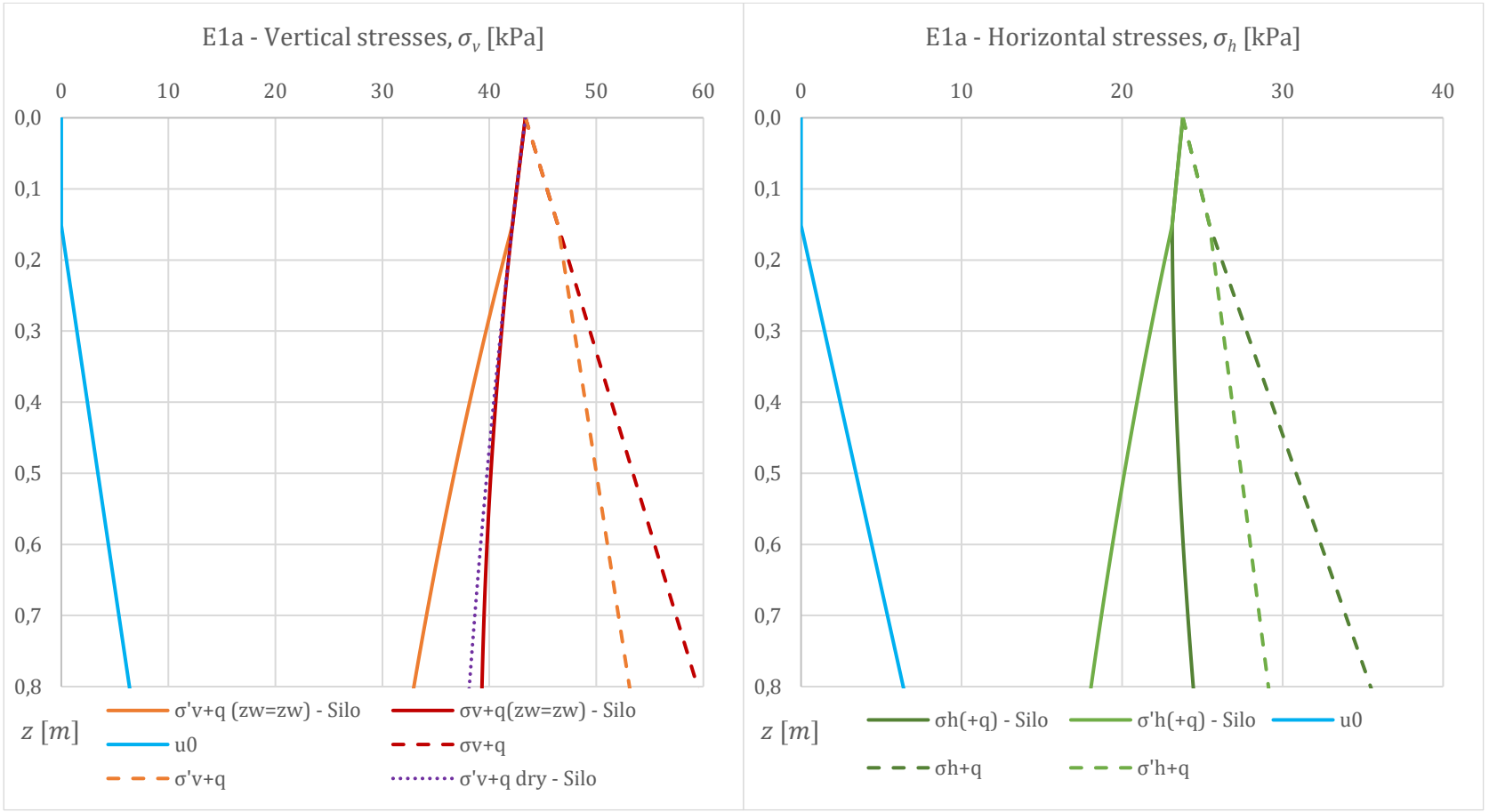

Figure 5.40. The interpreted stress distributions in E1a.

Note that this experiment was conducted only in the base chamber, hence the reduced depth. No horizontal stresses were measured in this experiment either, thereby, the graph on the right hand side remain only an approximation. The pore pressure sensor reading from this load stage was according to the graphs above. The clay block was placed at ca. 17-53 cm depth.

In this experiment l' is approximated to be 1,52.

5.3.3.3 Experiment 2

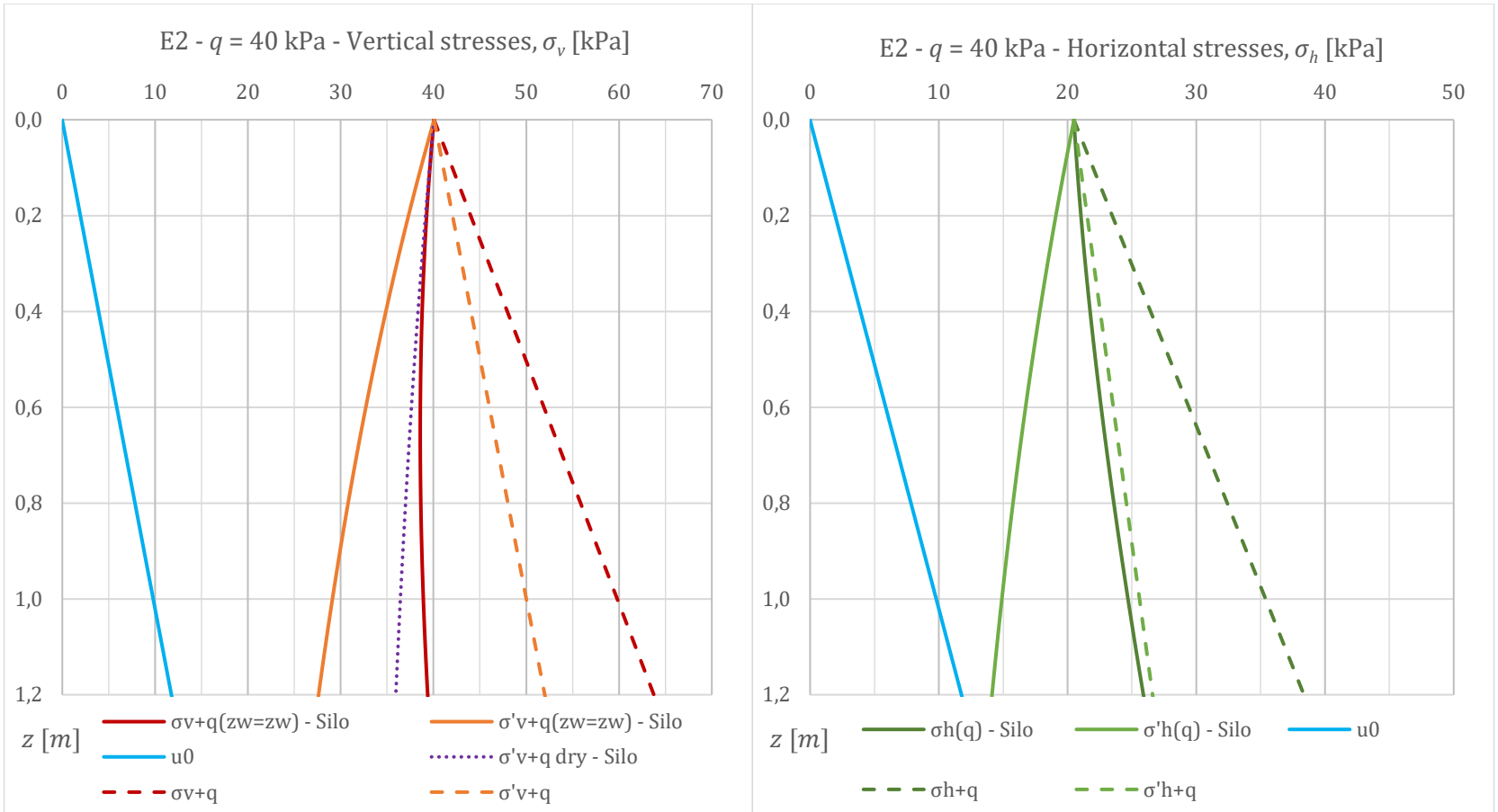

Figure 5.41. The interpreted stress distributions during the soundings of E2 with 40 kPa overburden load.

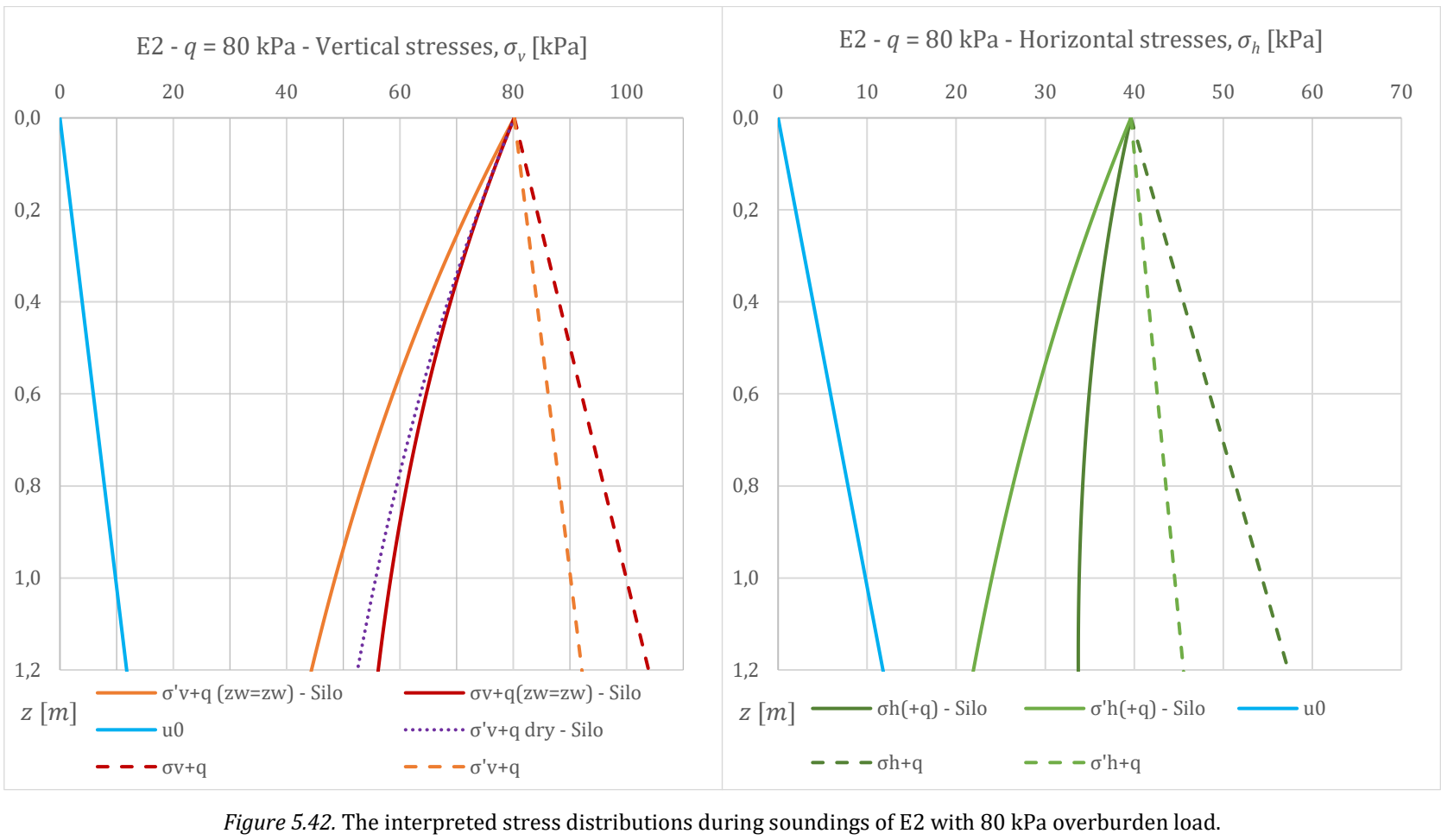

Figure 5.42. The interpreted stress distributions during soundings of E2 with 80 kPa overburden load.

In this experiment the horizontal stress was measured. The readings' reliability is however unfortunately not too good due to drifting, and some corrections have therefore been made. Thereby, the horizontal stress still remains an approximation, but with rather higher associated confidence.

The approximations of l', K' and δ' for the 40 kPa imposed load in experiment 2, are respectively 1,63, 0,548 and 19,6°.
The approximations of l', K' and δ' for the 80 kPa imposed load in experiment 2, are respectively 1,51, 0,494 and 21,8°.

5.3.3.4 Experiment 3

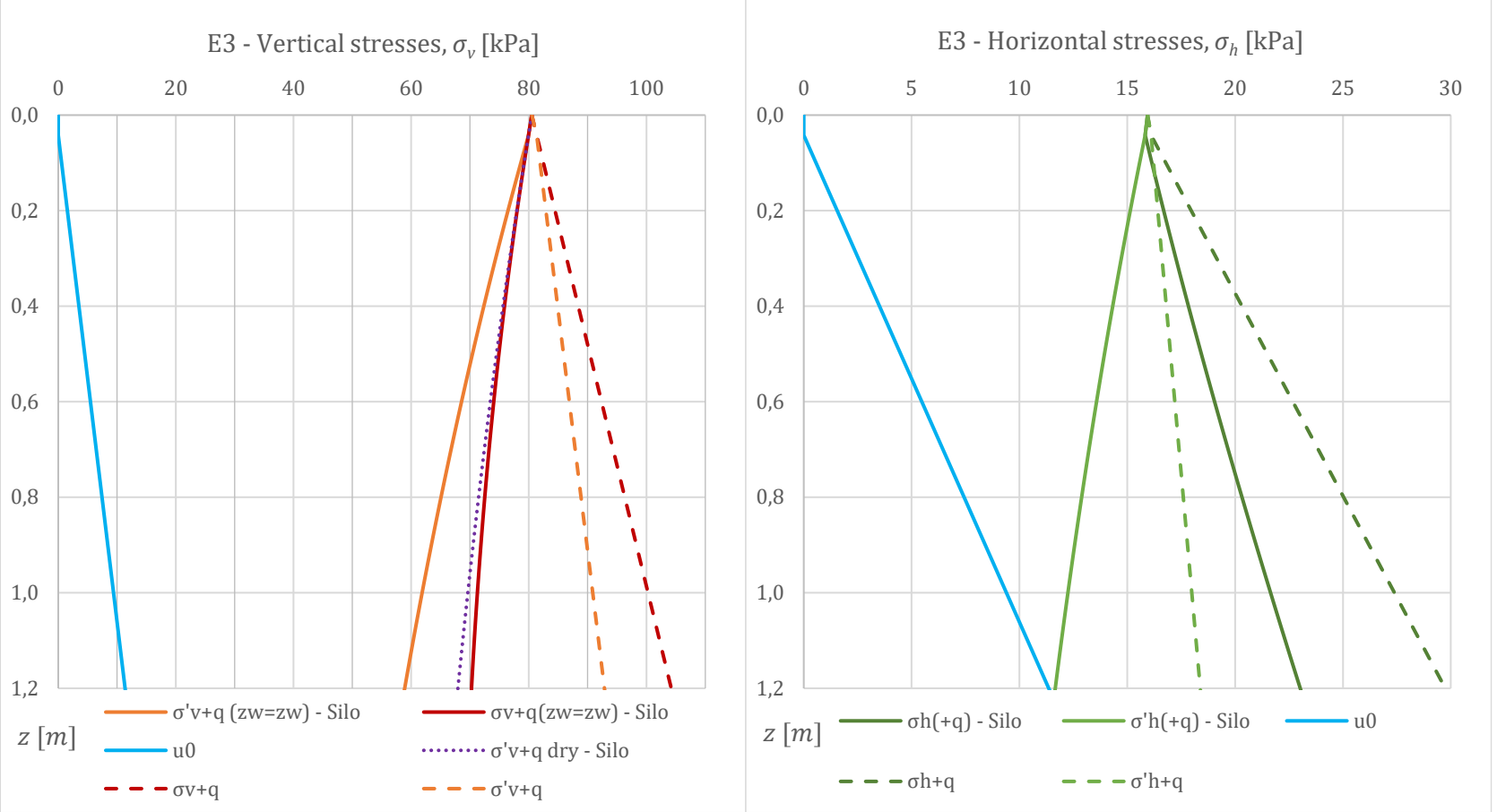

Figure 5.43. Interpreted stress distributions in E3.

In this experiment the horizontal stress was measured. Also in this experiment the readings' reliability were unfortunately not too good due to drifting. Some corrections have therefore been made. The horizontal stress still remains an approximation, but with higher associated confidence than without measurements.

The approximations of l', K' and δ' for the 80 kPa imposed load in experiment 2, are respectively 2,44, 0,198 and 31,6°.

5.3.4 Stress paths

As the pressure cells are less reliable over large time spans, thereby giving readings from certain time instances less reliable, another approach to get the decay length, l' is possible: By plotting the measured stresses in the cells versus the imposed load on top of the sample as shown in *Figure 5.44*. This plot gives information about how much stresses are absorbed by the walls, and how much go through the sample.

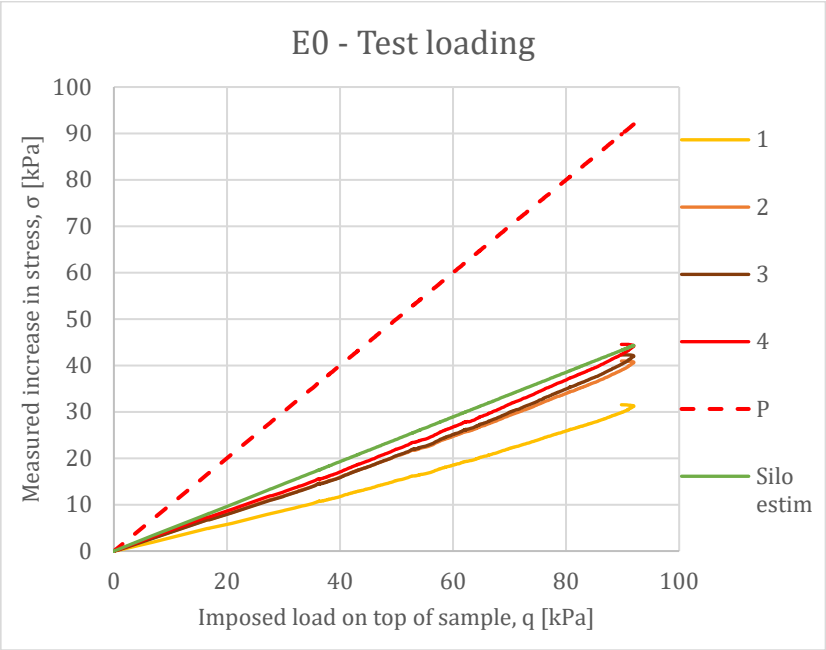

Figure 5.44. Load imposed on chamber sample, with associated stress paths at the cells.

An estimate of the increased stress based on q and l' only, is shown besides the readings of cell 1-4, marked in green. The estimate is based on the formula {2.47} given in ch. 2.4.1., and for q only, is repeated under in eq. {5.1}. To check the conformity between a loading sequence (as above) and the data used in the silo stress distributions (based on "absolute" values at specific instances in time lapses), the constant of $l' = 1{,}59$ was used. The "wedge" at the end of the stress path for the cells are related the previously described inertia in the cells.

$$\Delta\sigma_v = \Delta\sigma'_v = q \cdot e^{-\frac{z}{l}} \qquad \{5.1\}$$

Further, some of the stress paths are presented for the measured cell pressures versus the theoretical field values where no arching occurs. These graphs include data points from each build-in interval retrieved from the time instances where the written build-in log states that sand layers were finished. Furthermore, some datapoints have been added from the load imposing procedures. The first graph will be on total stress basis, while the rest are on effective stress basis.

In the graphs of experiment 0, the readings after 30 kPa on the x-axis is from the loading test.

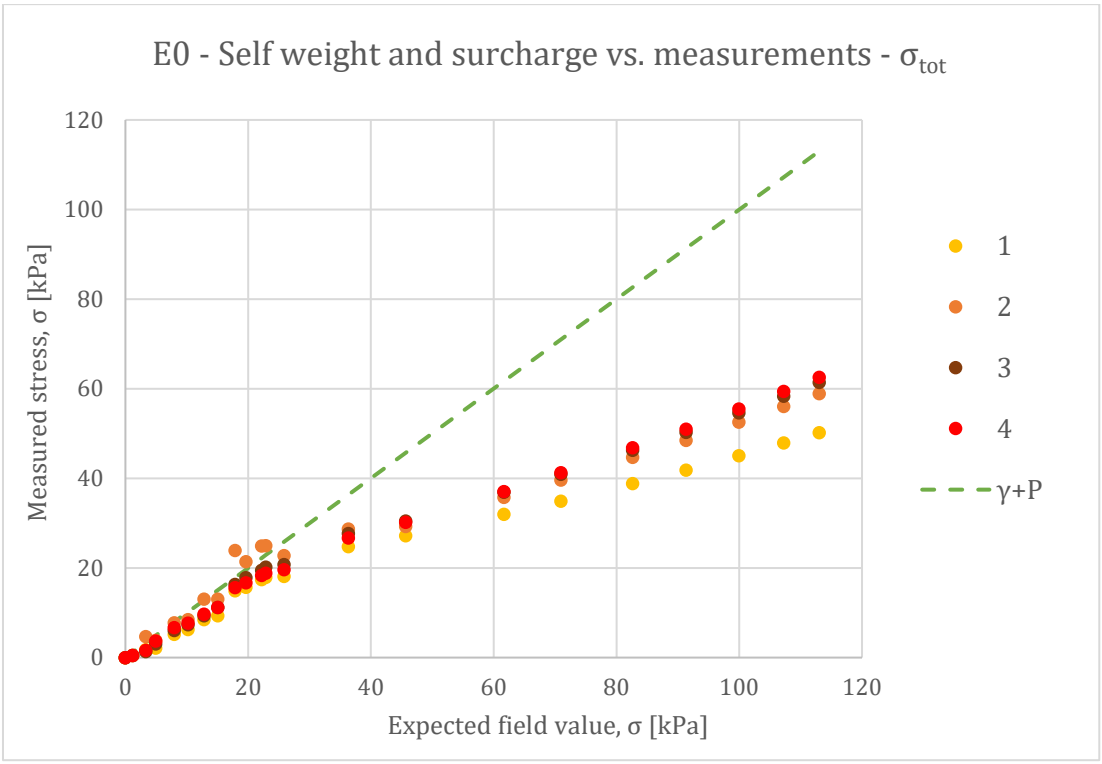

Figure 5.45. Imposed load and self-weight without arching, versus the cell readings.

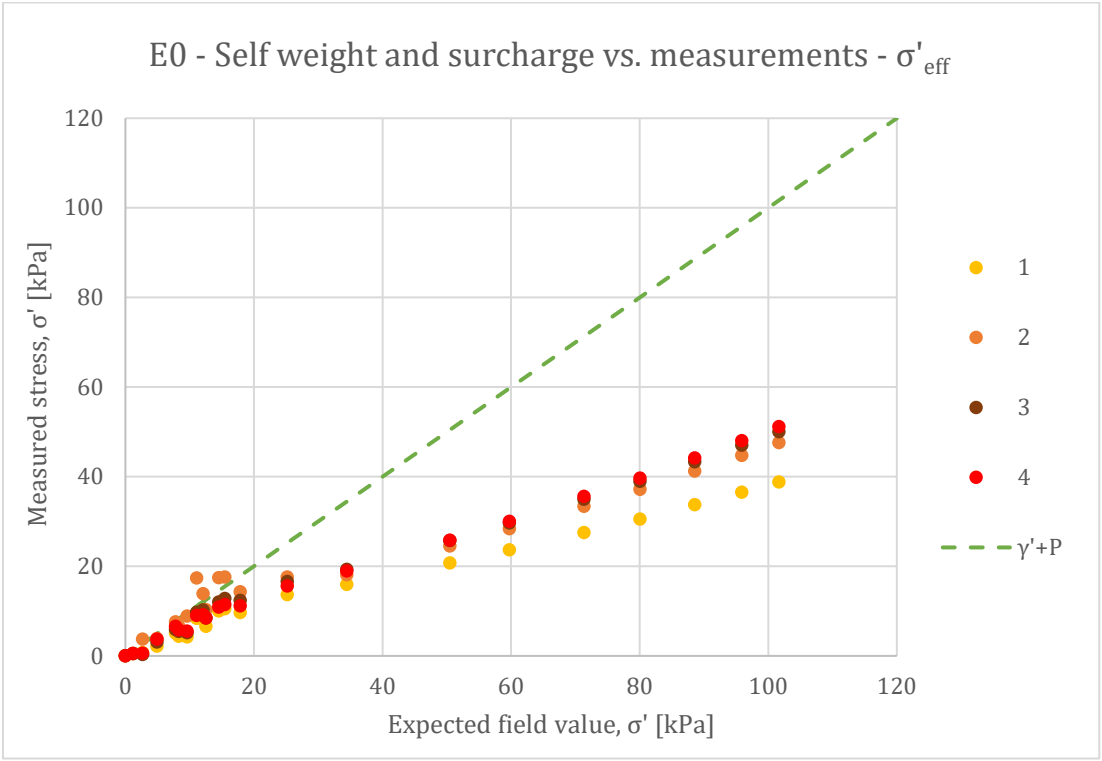

Figure 5.46. Imposed load and self-weight without arching, versus the cell readings, on effective stress basis.

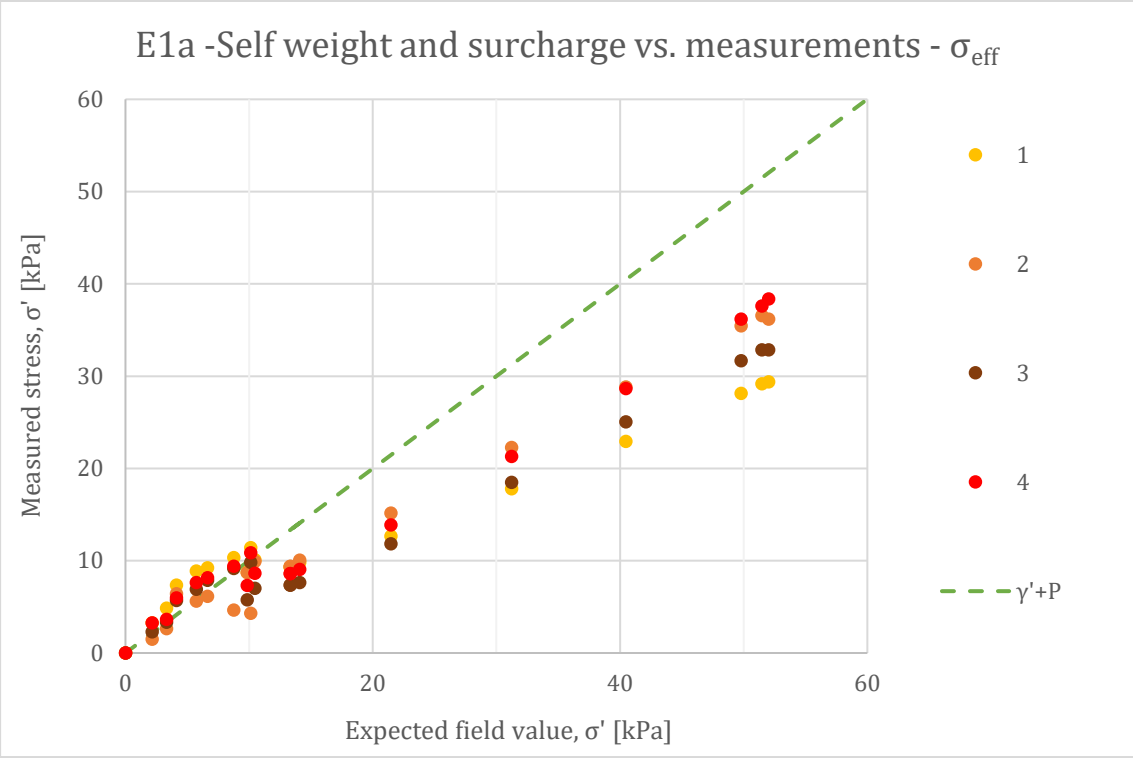

Figure 5.47. Imposed load and self-weight without arching, versus the cell readings, on effective stress basis.

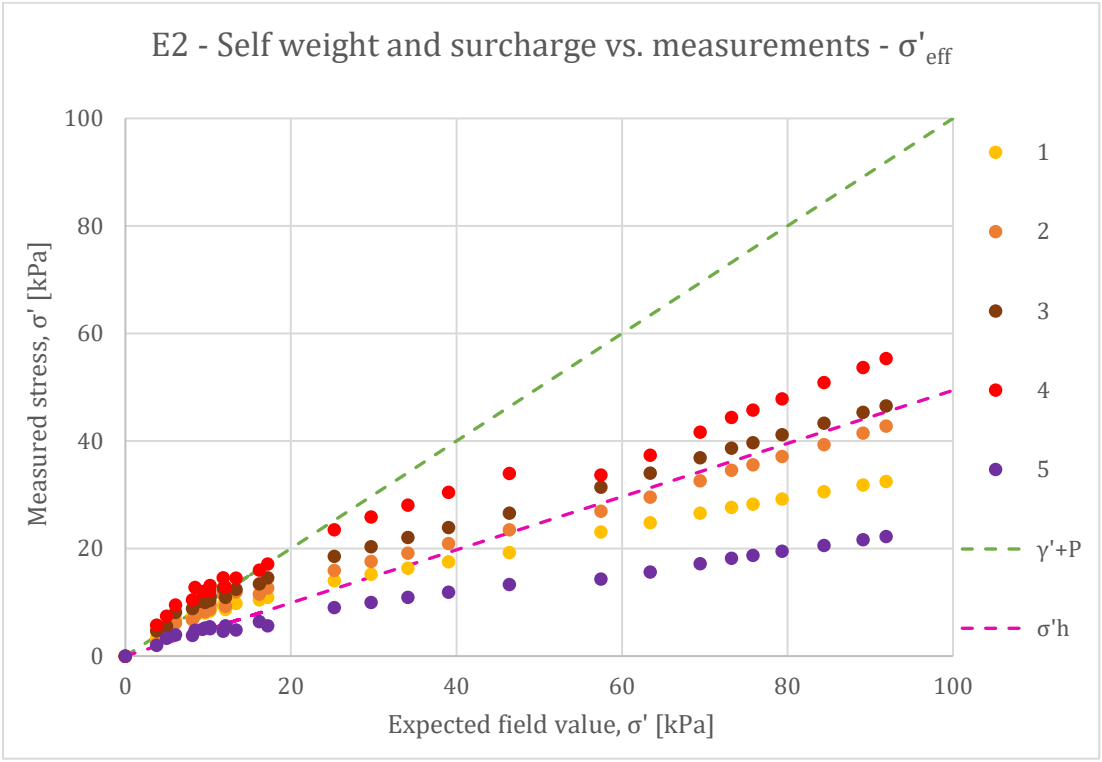

Figure 5.48. Imposed load and self-weight without arching, versus the cell readings, including horizontal measurement and associated field value (based on equal K' as estimated in silo).

Cell 5 is in *Figure 5.48* in addition to corrections, manipulated as to yield assumed results, and should therefore not be considered true. Yet, its actual readings from below 0 kPa are not reliable either.

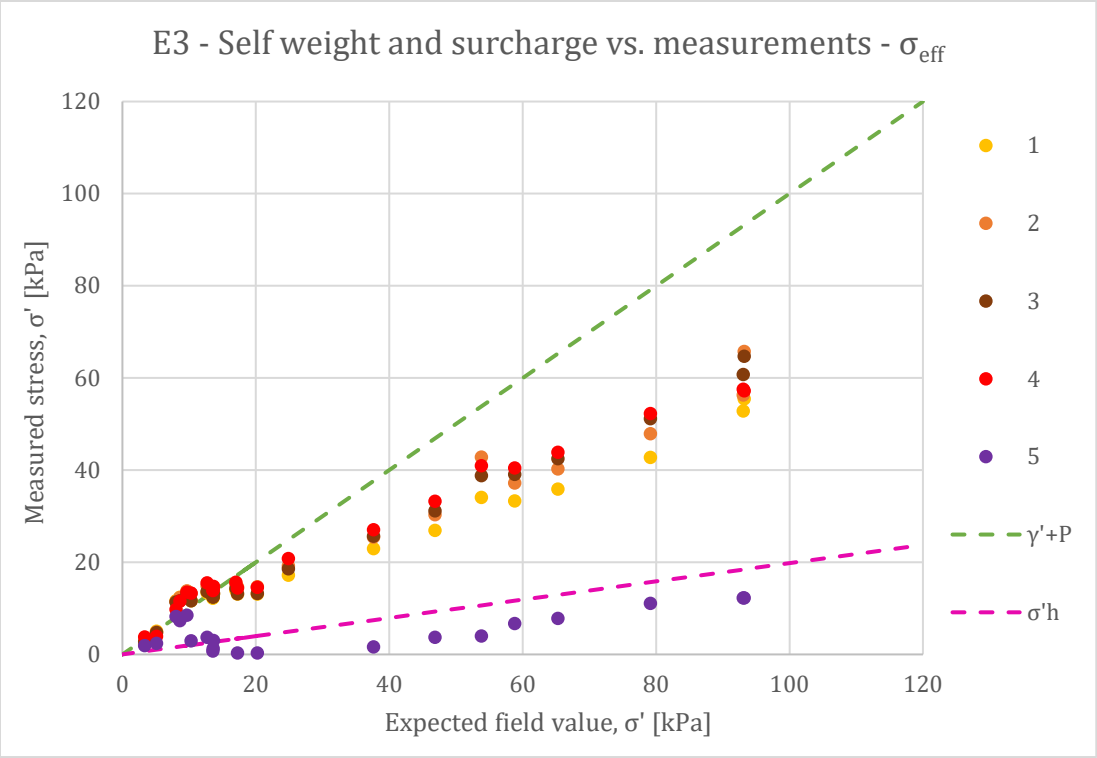

Figure 5.49. Imposed load and self-weight without arching, versus the cell readings, including horizontal measurement and associated field value (based on equal K' as estimated in silo).

In *Figure 5.49*, the readings of cell 5 are not manipulated, and thereby some of its readings remain below 0 kPa. These are cut out of the graph above.

6 Discussion

This chapter is divided in three. First the methodology is discussed to some degree and how it affects results. This includes a brief review of the latest experiment where quick clay was utilized. Then the pressure cell readings are considered with respect to reliability and the stress state, as affected by the silo effect. And lastly, the research topic of the thesis is regarded, i.e., an evaluation of the soundings and the typic characteristics of the thin layering effect is given.

6.1 Sample construction

6.1.1 Alterations of the chamber

6.1.1.1 Treatment of the chamber wall

As previously mentioned, the treatment of the chamber wall entailed some hitches. It turned out that the choice of treatment substances was rather poor. The product description was carefully read, as none of those involved had experience with spackle and water. Yet, despite no information about the spackle's reactive response to water, it turned out behave accordingly. The spackle was applied in good faith, but after the experiment 1a, it was evident that it did not withstand water very well. To make the matters even worse, the surface was only treated from just underneath the pressure cells (ca. 20 cm on the walls), whereupon the epoxy did not enclose the spackle completely. Thus, the water could enter into the spackle upon sample construction. Even if the treatment were done for the complete chamber, enclosing it with epoxy, scratching off epoxy from the walls would nonetheless occur during sample building, leaving an entrance for water anyhow.

The result was that some parts of the spackle/epoxy surface was loosening from the wall, and it started rupturing due to the epoxy cover's contraction towards the centre of the chamber. The quick fix was to put duct tape on the cracks, seen on the right in *Figure 6.1*. Furthermore, as a preventive measure to counteract new arbitrary ruptures, new fissures were cut vertically and taped, which was probably more efficient long-term, while it also assured that flakes would not peel off as shown on the left in *Figure 6.1*.

Figure 6.1. After experiment 1a. Left: Rupture of the epoxy cover. Right: First round of taping. Notice the dashed line drawn with permanent marker. They circumscribe the area that bulges from the wall.

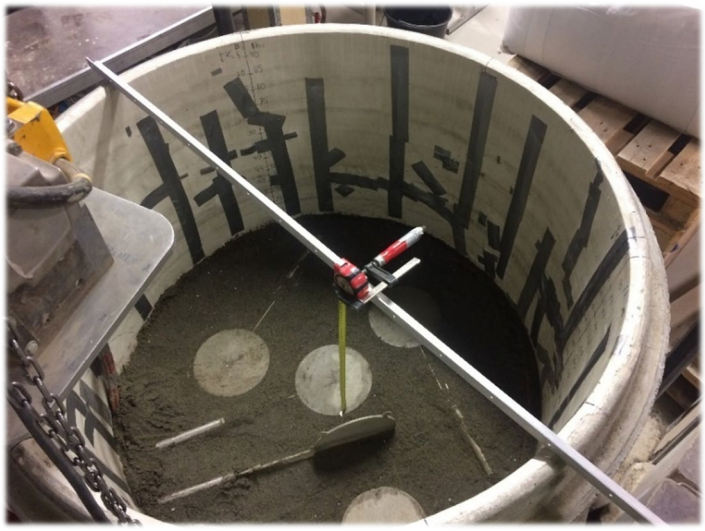

Figure 6.2. The walls intermediate experiment 2 and 3.

Despite the abundant taping, the wall surface remained quite smooth as the tape itself was smooth. No specific recommendations are provided as what to do with the walls further. The walls may provide adequate reduction of silo effects, or they may become worse with time. If it is decided to treat the interior surface again, any use of spackle is obviously discouraged and instead a more hydrophobe substance is recommended.

6.1.1.2 Possible improvements to chamber

To ease the installation and deinstallation of the chamber extension, a hole could be drilled in the side of the chamber and the cables threaded through it. The hole would then require proper sealing to prevent leakage of water. During the experiments, some clay layers have coincidentally been planned at the same height as the transition between the chamber base and extension. This have required either build-in after installation of the extension (working depth within chamber is a bit challenging), or alternatively, the clay must be properly protected. I.e., protected from the cables (and the DAQ-box if this is put in together), and from the possibility of the rubber gasket acting as a slingshot upon accidentally slipping it. It should be noted that a solution involving boring a hole through the wall is rather permanent, meaning that the cells will be only reserved this project. This implies that others at the institute that might need one cannot get it, or a rather demanding disassemble and associated mending is required upon allocation of cells.

6.1.2 Chamber sample sand

This sub-chapter review the results from the density tests in ch. 5.2.2 with respect to the described sand build-in procedures in ch. 4.2.3.2, and does in addition give a brief review of the NGI-99-assessment method.

6.1.2.1 Chamber sample sand dependence on build-in/construction

It is natural that the build-in procedures alter the properties of the sand layers. Depending on the different phases of sand layer construction, the sand may form a quite homogeneous structure, or it may have large local differences in compaction. This does both apply in the vertical and the horizontal direction. Regarding the homogeneity throughout horizontal cross-sections, the first phase of build-in, is regarded as most critical. I.e., the procedure of filling new sand into the chamber.

By utilizing the metal sieve in experiment 0, it was possible to distribute the sand evenly over the entire area, with an equal fall energy for all of the inserted sand. This did likely provide almost uniform horizontal layers of sand. For the subsequent experiments, the filling phase was renewed in the pursuit of higher yielded tip resistance, and sand was simply shovelled directly into the chamber from the sandbags. This is expected to have given large differences in fall energy, with the sand distributed unevenly with every shovel. Thereby the associated compaction probably became quite heterogeneous in the horizontal direction. However, there was general awareness regarding this during build-in, and this effect was thereby counteracted with high efforts.

Regarding the vertical homogeneity, many factors have been identified as influential:

1) First is the sand filling phase with its inherent different degree of compaction;
    a. The fall impact of the different methods was quite large, where the method of direct insertion is presumed to have compacted the sand a lot prior to subsequent compaction phases.
    b. The sand moisture during build-in decided how the sand would structure, which involve many complex implications, such as e.g., apparent cohesion.
        i. In the first experiment, 0, two sandbags were brought to the laboratory in the initiation of the build-in, where the sand used to fill the intermediate sand layer ended up being quite dry.
2) Secondly were the durations of each vibration phase which had to be timed correctly to achieve undercompaction;
    a. due to the requirement of using different sand layer thicknesses in build-in of clay samples, the planning of undercompaction became substantially rougher.
    b. This could furthermore not be adjusted for when the plate vibrator was used directly on the sample.

3) thirdly, the looser the sand is built-in, the more susceptible it becomes to compaction upon impacts, making looser layers more prone to becoming inhomogeneous as compared to dense layers.
    a. This is evident by comparing e.g., the D_r-plots of experiment 0 and 1a, respectively see *Figure 5.29* and *Figure 5.30*. The denser the chamber sample, typically the more conformity is seen between the density samples taken from different zones at ca. the same level.
4) the saturation level during vibration is assumed to have a large impact on how much the sand is compacted.
    a. If the water level is just close to the surface, the water pressure build-up momentarily, reducing the effective stresses in the sand, enabling suspension of smaller fraction and possibly even sand. At the same time, water is pushed out of the medium, leaving lesser porosity in the sample.
        i. The valves 2,3,4 in *Figure 4.35* were open during this phase, i.e., the water could flow freely in and out of the chamber.
        ii. Sometimes, at the end of a vibration phase, the water would come up on the sides of the wooden plate. This was tried counteracted in every build-in, by letting the water level sink sufficiently before vibration, yet it often seemed to remain more water in the sample as compared to what was read of the pore pressure sensor. I.e., the sand was very saturated, yet there was not particularly high water pressure.

The last phase regarding build-in was raising and subsequent lowering of water level between filling and vibration. This phase was executed equally every time, and is not regarded as being particularly important.

A last element of the build-in is the resulting lateral earth pressure coefficient. It is reasonable to state that during compaction of each sand layer, the horizontal stresses increased as the sand was compressed vertically, yet confined sideways. During the vibration phase, the sand closest to the surface was most overconsolidated, and upon vertical relief, kept much of its horizontal stresses. The concrete assessment of K' is given in ch. 6.2.1.2.1.

6.1.2.2 Assessment of sample density

Looking at the results in ch. 5.2.2, a general trend of increasing relative density with depth is seen. The largest increase was seen in experiment 1a, where the D_r increased with ca. 30-40 % over a 70 cm height. It has both the both largest compaction level, and the most increase of compaction with depth. This was expected due to vibration procedure, and show the importance of performing under compaction. In experiment 3, some general "upper limit" trend of D_r may be seen, stretching from ca. 20 % in the top to 60 % in the bottom, there are two deviations from this trend, which are probably caused by the large layer thicknesses surrounding the thicker clay layers (8-12 cm) in this experiment. In experiment 2, D_r remained very homogeneous throughout the whole sample, with ca. 30-40 % D_r. And lastly,

in experiment 0, the sample had an opposite trend with increasing density with height, yet the data scatter was higher for this test. In the first experiment, one of the sandbags was very dry, and may explain why the q_t- profiles in the intermediate sand layer were so low.

In the plotted D_r-profile from experiment 3, see *Figure 5.7*, the top surface of each built-in sand layer is marked with orange dots. Due to the Geomil-probe's high reading frequency, it is possible to see that the CPTU-soundings do indeed reflect the soil's properties in a very detailed manner. However, readings during the current experiments have naturally been obscured by the clay layers and the horizontal boundary conditions, being the chamber walls and the proximity to previous sounded holes. Considering that the influence zone in sand is extending ca. 20 d_c from the probe, this is to be expected. To counteract the effect of lowered yielded tip resistance in the CPTU-D_r-assesment, the constant k_{2,D_r} was altered to reach results resembling the density sample results. Mostly, a k_{2,D_r} of ca. 11, yielded profiles which trended with the sample results. For the samples with 80 kPa in overburden stress, the original expression with $k_{2,D_r} = 22$ seemed to fit for the first 30-40 cm, but as the stress typically decreased a lot with depth, the measured tip resistance in the sand decreased substantially with depth. To compensate for this in e.g., sounding 2c in experiment 2, k_{2,D_r} was linearly decreasing from 22 in the top to 11 in the bottom.

6.1.2.2.1 A mishappening

In the last experiment, there was a misfortune, where the units of a, b and c were placed with their perimeters at their supposed centres. This misfortune decreased the value of the soundings 3a-3c adversely. Luckily, it was detected at an early stage during excavations, enabling a solution which fortunately turned out to give useful results. This involved cutting new holes in the disc, with new holes 8 cm from the 3-tier holes. Moreover, the sand had to be filled back into zone BC above the upper clay layer.

It was expected that the original sample was very compact, due to the build-in and the following 80 kPa load on top. The new layer was therefore tampered well, actually, too well, and the D_r became ca. 60%, well over the previous 20%. Thereby, there are two density sample results for this same zone and depth in the graphs. This latest build-in was more improvisatory of nature and explains why the q_t was higher for soundings 4b and 4c, despite their proximate position to the previous soundings in 3b and 3c.

6.1.2.3 Conclusive words

As a conclusion regarding the sand construction, the last build-in procedure, 3, showed that one can more efficiently make relatively homogeneous sand layers, but undercompaction remains a challenge. If this is to be compensated for in future experiments, by compacting the upper layers relatively more than the lower ones, then one must keep some things in mind: If the undercompaction is done by only increasing the density as the sample is built in the height, then the compaction may become dangerously high for the equipment. I.e., the thrust resistance can exceed the capacity of the actuator with respect to buckling. The pressure cell attached to the actuator should however act as a safety net.

6.1.3 Build-in of clay

The build-in of clay was generally a demanding and time-consuming operation. This was done thoroughly as to get the precise dimension for each specimen and as to not disturb the samples.

6.1.3.1 Assumptions regarding the unit construction

The samples that were to be used in units had to be completely flat at surfaces meeting other clay specimens in order to achieve unity. Then, combining the specimens into one unit required a lot of effort, but they seemed to be acting as one. E.g., in the latest experiment, when the lowest centre block was to be cut out for further laboratory testing, it started rupturing in the top and through another specimen besides. When the block was cut out, it acted as a cantilever beam as the centre specimens had to be cut horizontally with the thread saw. This gave tensions in the top and following rupture. This happened twice, and the ruptures went far into the other specimens as well, indicating that the unit indeed acted as one, as the neighbouring specimens acted with tension on the centre specimen. Another example is from the preliminary test on the quick clay, where it was checked whether it was possible to unify two specimens. This worked better than expected, and the results is illustrated in *Figure 6.4*. Another important factor during unifying was to not exaggerate the clamping, as this would initiate failure in the blocks.

Figure 6.3. Left: Two specimens ruptured a bit. Right: Centre specimen ruptured twice.

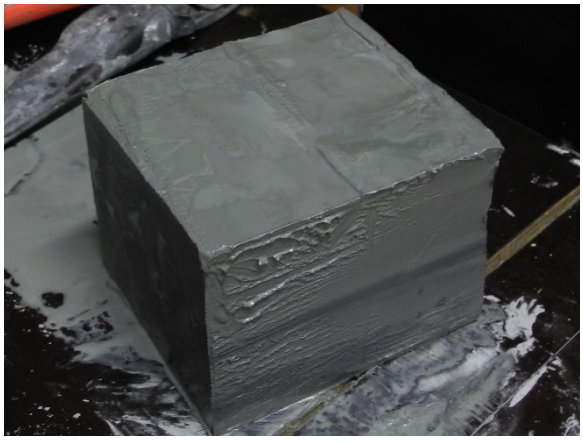

Figure 6.4. Preliminary test of unifying two specimens.

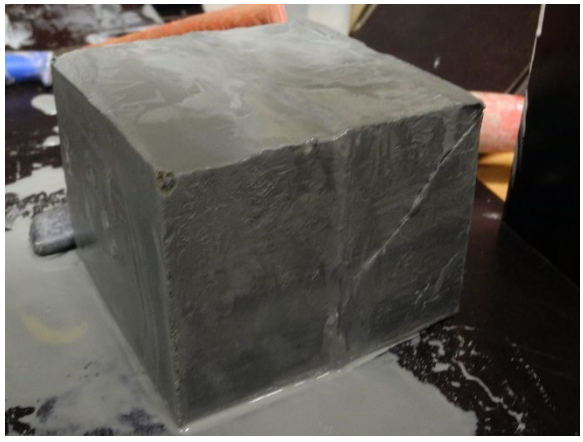

Figure 6.5. Imposed failure through unit.

The methodology involves some implications, as if there are any hollows or cavities between the layers, this may influence q_t to some lesser extent. This may not be of great magnitude, but for vertical stacked units, such as sub-sample 3b in experiment 3, the closing of gaps was essential. And even thought this was counteracted with high efforts, the pore pressure in this sounding reduced in the first interface between two clay specimens, indicating that there was a small hollow in-between them. This hollow allowed excess pore pressure to disperse, and thereby lowered the measurement of B_q.

Even though some of the units had imperfections, they all acted as one unit, and it is assumed that q_t was not altered by the construction of such blocks, neither for the quick clay nor for the pottery clay.

Furthermore, the relative sizes of the units had regularly minimal horizontal distances to the sand higher than 3 d_c. I.e., it was previously mentioned that soundings in clay are influenced at a distance of 2-3d_c. For the standard probe this is equal to 7,1-10,7 cm, while it is 5-7,6 cm for the mini-probe. The layers were not built larger than necessary considering that it demanded a lot of workload and clay, and it was observed that the units were sufficient by looking at rotation of the vertical sides of each unit. If any unit had rotated on one of its sides, it would indicate the horizontal spread of the unit was not large enough.

6.1.3.2 The pottery clay

There were conducted some tests on the pottery clay at some different stages, where clay the tested clay had experiences different degree of disturbance, i.e., some were tested prior to build-in, and some were done in posterity. The test showed that the pottery clay was very robust and only had slight changes for relative harsh treatment (being subjected to build-in with charging and discharging of water, vibration by a vibration plate, and sounding through the unit). Of course, it was tried to make samples for further supplementary lab tests from the zones least effected. As can be seen in *Figure 5.33*, the liquid limit was quite similar for two tests done in the current experiments, and the one done by Hammer. It can thereby be called quite robust.

Regarding the shear strength, the falling cone test on the pottery clay was giving quite a span of different values, mostly because two different cones were used, respectively 400 and 100 grams. These were not calibrated for the pottery clay but rather for local natural clays. It should be noted however, that there was little conformity between measurements of the 400 and 100 gram cone on the quick clay either. For the quick clay it was shown that the calibration sheets of the 10 gram, 60 gram and 100 gram cones were good.

6.1.3.3 The natural clay

It was previous to experiment 3 examined if whether quick clay specimens would survive build-in by the latest build-in procedures or not. These tests gave encouraging results. A pocket vane was used to check the block prior to and after a build-in of a cylindrical specimen equal to that of sub-samples a, b, and c. This proved to be successful with $S_{u,\mathrm{PV}}$ of 35 and 24,4

kPa respectively prior to and after build-in and following excavation. The deviance is thought to be mostly caused by methodology accuracy. The specimen was further tested with the falling cone test and showed averages of $S_{u,\mathrm{FC}} = 35{,}7$ and $S_{u,r,\mathrm{FC}} = 0{,}191$ giving a sensitivity of 186. With these data, it was decided to commence the last experiment. This was however done after easter unfortunately, leaving the mini-blocks in storage for another 1,5 weeks.

The sample construction elapsed in at a bit slower pace as compared to the previous ones. This was due to the extra care upon handling the quick clay samples, which were actually easier to cut as compared to the pottery clay and the natural low- to medium sensitive clay which was used in some triangles in some centre units. The experiment as a whole involved a much larger workload as compared to the previous experiments, due to the comprehensive supplementary laboratory works, and the nature of handling specimens in lab with intention of least disturbance.

6.1.4 Sample representativeness

In the Flotten site-report, all clay samples were tested in standardized laboratory procedures, and have thereby only been subjected to sampling methods, storage time and lastly specific preparation for their specific test, before actual testing. Necessarily, the clay specimens utilized in the last chamber experiment was exposed to several more sources of disturbance, and furthermore sources which may have greater magnitudes. Moreover, the utilized specimens could have been exposed to many sources of disturbance for a longer period of time, during build-in, sounding, the intermediate unplanned halt in progress, the second round of soundings and lastly, excavation.

General sample deterioration was experienced for most of the samples, with associated uncertainty upon when the most change in properties occurred. The unfortunate lowering of water level intermediate the sounding rounds, and during the excavation, respectively spanning 3,5 hours and 5-6 hours, also obscures the assessment. As the laboratory technically also was a workshop or a storage room, the room temperature spanned around 18-21°C, and the air was very dry (as is typical for storage rooms). This made the specimens visibly change as from when they were first retrieved out of the chamber, until they were finally tested in e.g., the falling cone test. In retrospect, it could have been possible to retrieve specimens and bring them to another lab in order to maintain the specimens' water content.

As a conclusion for further works, it can be said that is especially important to keep the quick clay moist, which due to its structure and high water content, tends to dry out and chemically deteriorate when exposed to the air. This can also be linked with Le Châtelier's principle: when the quick clay is no longer imposed to fully saturated boundary conditions (previous equilibrium state), the position of chemical equilibrium is moved. In addition, as mentioned in (L'Heureux & Kim et al. NIFS, 2014, p. 27), when a sample first is exposed to air, there may initiate some chemical reactions within the pore water, with oxidation reactions ultimately deteriorating samples to become some other material, as compared to the quick clay sample that was once extracted.

For future assessment of disturbance, the mentioned methodology by L'Heureux & Kim et al. (NIFS, 2014) of checking pore water pH upon sampling, possibly again during storage time and once again after tests have been conducted, could give valuable data regarding how intact the specimens remain.

6.1.4.1 Comparison of field data and experimental data

In this chapter, the supplementary results are reviewed rather briefly, as to assess to which degree the samples were disturbed. There are some different measurements that can be used for comparison basis. E.g., the S_u might be a good reference, as S_u deteriorate as a sample is subjected to e.g., chemical reactions or physical impacts. It should also be kept in mind that S_u results depend on the test procedures, as S_u is not uniquely defined. This is evident upon looking at the Flotten site report results shown in *Figure 3.6* in ch. 3.3.1.

It was observed that the clay layers at the top of the chamber had altered the most, not "sweating" upon getting cut, and upon remoulding in advance of falling cone tests it did neither approached the quick clay's characteristic soup-consistence. The water level was quickly raised again after this was realised, leaving the upper layers exposed to non-saturated conditions for up to 5-6 hours. As test were conducted further down into the chamber sample, the specimens started resembling quick clay again. In the very bottom layer, $S_{u,r}$ was measured as low as 0,78, but there was visibly very little difference between this test and that conducted on quick clay earlier on. The resulting sensitivities shown in *Figure 5.24* were quite low, but was mostly low due to the disturbance of the samples prior to testing S_u both for the falling cone test and the uniaxial compression test. I.e., with a low S_u it is difficult to obtain a high sensitivity, even for remoulded samples which have little resistance. Other parameters that were tested are the consistency limits. These showed a general trend of increased liquidity limit and plasticity limit, and with a substantial associated increase in the plasticity index, as seen respectively in *Figure 5.19* and *Figure 5.20*. The consequence of these increases was that the liquidity index was decreased, and by looking at eq. {3.4}, it is could be expected that the $S_{u,r}$ would increase, something which it namely did, see *Figure 5.24*. The "undisturbed" S_u had decreased since the preliminary test, see *Figure 5.23*, something which is linked with the handling and the rough history of build-in. A last parameter that was checked was the salinity which was smaller as compared to the results from the Flotten site report. An assumption is that the cycle of charging and discharging water has given some flow of minerals, and in addition due to the intermediate time periods of exposition to air during, e.g., sample construction, there have also been some changes in the pore water chemistry. In addition to the general trends, it should be acknowledged that soil in nature is not strictly homogeneous, and samples do thereby also have some natural variabilities.

As to conclude this sub-chapter: The lowest quick clay units showed in every sense very equal behaviour to regular quick clay, but had went through a lot, not only prior to excavation, but also especially during the supplementary tests due to a very dry and relatively hot environment. It is thereby not reflected well that in the results that the samples probably remained a bit quick, at least very sensitive and brittle. For the upper level however, there is associated more uncertainty, yet these units had also quite a sensitive behaviour.

6.1.4.2 Quality of soundings from experiment 3

The mishappening can be seen illustrated in the methodology chapter, with planned and actual arrangements of the clay layers, respectively *Figure 4.31* and *Figure 4.32*. The specimens the bottom chamber (lowest and middle level) in sector 3a-α and 3a-β were not penetrated in the centre and the perimeter. Instead, the penetrations were shifted relative away from the original chamber wall, see Figure 6.6. This stem from the clay arranging procedure, where clay units were placed with reference to the chamber walls, with basis on the intersection between the outer steel frame. It was evident that the chamber wall in the last experiment was quite deformed, caused by the unfortunate spackle- and epoxy solution. The fact that the wall surface contracted unequal in different direction was not perceived during construction of the last chamber sample. This first became evident during the excavations. The interior wall was however only shifted in section 3a (~1,8cm), while the soundings went exactly through the perimeter on all b- and c sub-samples, meaning they were not shifted at all. For the upper clay layer in section a, the wall was not shifted, as the chamber extension had not experienced much deterioration due to the improper choice of treatment substance, see *Figure 6.7*.

Figure 6.6. Cylinder at the lowest level in sector a. The penetration of sounding 3a was completely confined by clay. The unit in section a was shifted relatively away from the original chamber wall. The disc at top remained fixed due to the artificial load framework fixed position.

The soundings of 4b and 4c was quite equal to 3b and 3c in the sand, looking at the profiles below 30 cm depth. As usual, the secondary soundings were partially influenced by the earlier soundings in the proximity, giving reductions of q_t in the sand equal to ca. 0,25 to 0,5 MPa, only considering the intervals that were not influenced by the clay layers. Obviously, in the clay layers, the soundings 3b and 3c pierced the perimeters, giving a tip resistance most influenced by the sand. Thereby, the value of these soundings is close to zero, except that the middle parties of the sand layers are possible to compare with the other soundings.

Comparing the first soundings through the lowest and middle layer in 3a, with 4b and 4c, shows that $q_{t,3a}$ was approximately equal or larger than both $q_{t,4b}$ and $q_{t,4c}$, meanwhile f_s was approximately equal for all three soundings $f_{s,3a} \approx f_{s,4b} \approx f_{s,4c}$. The measured water pressure

was generally larger in soundings 4b and 4c. 3a can surprisingly be considered as quite valid for the lowest layer, reaching a lower tip resistance than for instance $q_{t,min,4c} = 344$ kPa $> q_{t,min,3a} = 328$ kPa. For the middle level however, the data are more misrepresenting with both lower tip resistance and lower measured pore pressure.

Figure 6.7. Left: Upper clay layer of sector a, sounding 3a went through the very perimeter. Right: Middle clay layer of sector a, sounding 3a went somewhat inside the perimeter.

6.2 The silo effect

6.2.1 Earth pressure readings

6.2.1.1 Accuracy of readings

Before the results are discussed, it is of importance to explain the behaviour of the pressure cells as this was not optimal with respect to reliability. An explanation will therefore be given on fluctuations in measurements, with rather brief theory. This latter could have been in the theory part, but due to its brevity, and to easier go through the steps of explanation it was combined with the discussion.

All kind of measuring devices have inherent inaccuracy characteristic, i.e., measurement instruments, regardless of being mechanical, analogues and to a lesser extent, digital measurement devices, are all prone to drift of measurements. This can either be experienced as zero-drift, sensitivity-drift, or a combination of both, as defined by Morris & Langari (2012). The general drift is experienced as a change in ambient conditions, e.g., change of temperature, pressure, and furthermore, for analogue instruments the energy supply will also alter the magnitude of the measurements.

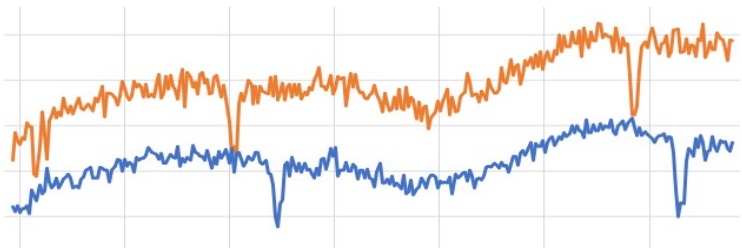

Figure 6.8. Pressure cell 1 and 4 with "white noise". Dips were equal to ca. 1 kPa in this case.

In addition, the different measurements will typically possess some white noise, this was evident for e.g., the pressure cells, which fluctuated a lot. After the last update of the logging program, it was possible to log several readings each second. The measurements were then typically pulsating, with a large dip every 15 seconds. It may be linked with the power supply, but the dip was not simultaneously for the different cells, see *Figure 6.8*, which contradicts this assertion. The program averaged the readings if the time interval was stretched out, meaning that white noise was eliminated. However, this give some implications regarding accuracy, but this is regarded as neglectable for the research purpose.

6.2.1.1.1 Deviations and drifting

Large fluctuations (not white noise) and drifting were experienced for the cells, as see in e.g., *Figure 5.35*, with some inertia for each building interval that is not well understood, but possibly linked with temperature of the added groundwater. The experienced inertia is very disadvantageous if the data do not converge before a next step is taken in the building procedure. To get better readings for single deviating cells, it is always possible to replace it with a better one, but it is not expected that are exist any available in-house- or affordable cells that may change the current trend of the readings.

Others that have experienced drifting in their experiments are Li et al. (2012). They filled a silo with dry sand, but experienced large deviances going from one day to the other as well. They could tell: "More work is required to investigate if this was only due to temperature variation… …over the night". Likewise, it was attempted to control and log the temperature in the latest experiments, by the use of a digital thermometer in the water container which the groundwater was added from. However, the measurements proved to be not too transferable to the pressure cell readings, and consequently most of this work was discarded for the thesis. Most likely this was partly due to the position of the thermometer's sensor probe, which necessarily was in the water container to add correctly tempered water, instead of placing it besides the pressure cells, to explain their ambient temperature condition. It was read in the instruction manual (Geokon, 2019, p. 20) that it is possible to measure the temperature on the cells by the integrated thermistors. It is then required to connect a digital ohmmeter for each cell. As this may improve the pressure readings, this is recommended for further experiments, even though it requires more labour, considering correcting procedures.

All water filled into the chamber should ideally have room temperature, as to not influence any measurement devices in the chamber (if they are temperature-sensitive). If other sources of drift are discovered these should also be counter-acted.

6.2.1.2 Pressure readings from sample construction

The methodology used in the data-treatment, has made sure that white noise is cancelled out and unreliable extremal values, moreover, the start and end points have been 0. Yet, due to the sensitivity drift of the cells, there is some associated inaccuracy related the readings. This is mainly seen for the 5th cell which is vertical. This cell descended below zero in both total and effective stress the last two experiments, 2 and 3. There is generally less reliability for measurements of horizontal stresses as explained by Lindgård & Ofstad (2017), yet this identified issue cannot be said to determine the measured horizontal stresses in these experiments as the stresses descended below 0 kPa. Thereby the only effect that can be pointed out is the device's accuracy. This may be linked to this specific cell, or in worst case all the cells are quite inaccurate.

The measurements of the other cells must be said to be better, especially after experiment 1a, when cell 2 was discarded. As can be seen in *Figure 5.36*, this cell was changed due to a different behaviour as compared to the other cells, and secondly, due to the large deviance after during the excavation. To assess the readings of ch. 5.3, it is first referred to the arrangement of the pressure cells, seen in *Figure 4.23*. By looking at *Figure 5.37*, cell 4 in the middle has the highest stress level; cell 2 and 3 with equal distances from the centre have approximately equal values, below cell 4; and lastly cell 1 is lowest as expected. The fifth cell was as mentioned not reliable with negative effective pressures, even upon correcting for start/end. The courses of the different readings were unfortunately a bit uncertain, and consequently all the processed data based on the cell readings have become a bit approximate.

6.2.1.2.1 Before and after epoxy

To assess the effect of treatment of the interior wall, different average vertical stresses are presented with a high reference level of imposed stresses, that was common in all tests (including load test in E0). As a reference for experiment 1a, the stress levels of 42,4 kPa and 43,4 were used. The data from experiment 1a may not be regarded as valid for comparison, but rather as of interest regarding stress state in a lower sample, therefore this is still added in the assessment. The imposed load, q, and the estimated average effective stress in the bottom of the chamber, $\overline{\sigma_v'}$ are presented in the table beneath.

Table 6.1. Table with reference level of imposed stresses, with associated average vertical effective stresses. Units are given in kPa.

Experiment	q	$\overline{\sigma_v'}$	q	$\overline{\sigma_v'}$	D_r [%]
0	42,4	34,1	43,4	34,2	32
2	42,6	27,7	43,6	28,0	35,2
3	42,4	32,3	43,4	32,6	35,8
Small chamber sample – 1a	42,5	29,5	43,5	30,0	50,9

As may be deduced from looking at *Table 6.1*, there are large deviations caused by the pressure cells characteristics, which result in rather illogical corelations between the data. The lowest sample with largest height to depth-ratio is according to the data second worst in sustaining imposed stress through the sample, and this is while chamber wall treatment is not regarded. The data from experiment 0 is furthest away from initiation of sample construction time-wise, and should thereby be regarded as least reliable among the data above. If the data were more correct and possibly consistent showing trends, it would allow to analyse the effect of wall treatment and maybe also looking at effects such as compaction. The latter is presumed to alter not only the density and thereby the weight of the sample, but also the soil structure (direction of stresses) and the overconsolidation, influencing σ_h'.

6.2.1.3 Pressure readings from imposed load

In ch. 5.3.4 the decay length was calculated by only evaluating the loading of a chamber sample. This provided results conforming well with those found in the stress distribution graphs. These latter were based on σ_v' and σ_h' based on the pressure cell loggings which as previously told were not as reliable as hoped for. This might be a coincident, or it might show that cell 1-4 in fact were quite accurate, at least for higher stress levels. Unfortunately, no time was left for checking for every chamber sample.

Considering the graphs showing "*pressure cell readings* versus *expected field values of self-weight and surcharge*", *Figure 5.48* must be said to be the best graph (experiment 2), as the time span of this experiment was the smallest. Moreover, it may be seen that this graph is smoother than the others and in a larger degree show some trends. At the left hand side of the graph, i.e., when each sand layer and clay was built into the chamber, the readings exceed the estimated expected field value. This is probably due to the mentioned inertia for readings, as the readings were retrieved from the points in time where each layer was finished. It was at exactly this moment in time, the inertia-tops were at their peaks. Further on with build-in, the different cells showed more or less linear trends.

6.2.2 Comments on assumptions

There were as mentioned some assumptions for the estimations done in ch. 5.3. The assumption of $l'(K', \delta')$ remaining constant with depth, was a pragmatic solution used in the estimation of stress level in a silo, and is in fact a bit inaccurate at a detailed level. The formulas behind the estimations were presented in ch. 2.4.1. Situations with fully saturated bulk solids in silos are a bit complicated, as will be explained here: The interaction between the fill and the wall is altered by adjusting water level, as can be deduced by looking at an arbitrary increase of water pressure. The effective stresses are reduced, $\Delta\sigma_i' < 0$, while deviatoric stresses, q, are kept at the same level. This means K' is reduced, τ stays the same and the mobilized interface friction angle is increased. Despite such effects, estimation of the stress distribution in a "uniform" sample that are either completely saturated or completely dry, based on experimental measurements, using one specific $l'(\delta', K')$ for the complete depth, should be regarded as quite representative.

It is expected that K' would vary with depth due to the samples' inhomogeneity. Different build-in methods gave different levels of compaction, and with different degree of uniformity. Especially for the top of each sand layer, it is expected that sand was more compacted or consolidated, making the sand stiffer sideways, all of which made a higher K'. Moreover, the estimations are based on an equal interaction between the wall and the sand for the whole interior surface.

6.2.3 Future works

As for future experiments, it is recommended to keep the logging on at all times, as to not have gaps in the data. Then the sensitivity drifting can be tracked. During the build-ins the valve nr. 1 was almost always closed and the water container either lifted or lowered as to regulate the water level in the chamber. This was done in order to get continuous readings, also on an effective stress basis. For future experiments, the pressure cells could be studied further, with maybe some dedicated quick build-in tests as to assess the stress state and the cell readings with more reliable data.

6.3 Soundings

6.3.1 Tip resistance and normalized q_t-profile

6.3.1.1 A review of measurements

As the tip resistance has been identified as the most prominent CPTU-parameter for standard probes upon assessing CPTU-profiles in search for thin layers of clay, this chapter is quite detailed and separated in several parts. These present different aspects of both the analytical and the empirical approach. But first a more general review of the results will be mentioned:

Sounding 3b in experiment 1a is shown in every normalized q_t-graph as to have a comparison basis of the characteristic tip resistance of the pottery clay. Something that becomes apparent for this sub-sample is that the critical depth is never reached before the probe senses the clay unit which laid ca. 17 cm below the surface. This is evident when looking at the other q_t-profiles with imposed load of 40 kPa on the top (green graphs). Thus, the sensing depth of this sample cannot be considered as of the best quality, and consequently maybe giving a lower developing depth in the same unit. The result is however valuable, as the characteristic tip resistance can be assessed, being ca. 250 kPa.

For the other soundings, the critical depth is typically from 10 to 20 cm, for respectively heavy loaded and lightly loaded chamber samples. It might not be as clear, but by looking at *Figure 5.9*, it is seen that sounding 3a, 3b, 3c and 1S reaches a change of curvature respectively after 4 and 6-7 cm, followed by a second change of curvature upon reaching the top of a built-in sand layer. It is difficult to assess the critical depth for these ones, but the first 5 cm may be suggested. As for soundings 4b and 4c, these were going through a much denser layer due to the compaction upon rebuilding this zone. And in accordance with the info in ch. 2.3.3, the critical depth is much higher in dense sands, explaining why 4b and 4c seem to have larger z_c than the standard probe sounding S1.

There was a general trend of increasing q_t close to the bottom of the sample. This is linked with the interaction of the probe with the rigid boundaries the pressure cells make up. An exception is experiment 2, which had a very homogeneous sand and moreover was loaded with 40-80 kPa on top, it is not well understood why these did not increase at the bottom.

6.3.1.2 Averaging effects: An analytical-empirical approach

Upon transitions in sediments, CPTU-readings do not correctly reflect the material properties of neither the above- nor underlying material for some distance. As previously mentioned in ch. 2.3.4.3, the scaling effect entails smoothening, or "averaging" of the q_t-profile, giving an intermediate value of q_t. This intermediate value depends on the transition progression through an interface, and the influence of each material. As this smoothening only account for the geometry of the cone and the strata, it can be regarded as an *analytical averaging effect*. For infinite readings, the q_t-profile would be continuous, and its curvature would be restrained by solely analytical effects such as the scale factor, the materials' characteristic tip resistances and the intermediate layer thickness.

Besides this analytical averaging effect, there are other factors which cause averaging effects on all of the parameter profiles: Namely the reading frequency associated the probe's electronics, and the subsequent data-treatment itself. Firstly, it can be understood that lower reading frequencies give less data points, and thus the q_t-profile becomes less accurate. The lower the frequency gets, the more rarely extremal points are hit. Consequently, if the interval between data points is extended, the more probable it becomes that the readings are cutting the magnitude of the extremal points. I.e., soundings in weaker interbedded layers are susceptible for overshooting the magnitude of the analytical q_t-curve, vice versa for stronger layers. This is labelled as *the frequency averaging effect*. Secondary, the data treatment itself can lead to further inaccuracy, if one base the derived CPTU-parameters (B_q, Q_t, R_{ft},...) on only one associated parameter depth, e.g., z_{q_t}. In this methodology, the other parameters u_2 and f_s are interpolated to get the value at depth z_{q_t}. This implies that extremal in-puts from f_s and u_2 in these functions are technically an interpolation of the measured extremal reading and some other reading. This is denoted as *the interpolation averaging effect*.

To illustrate the different averaging effects, an arbitrary q_t-profile is illustrated for a thin clay layer in sand, see *Figure 6.9*. The blue and the red line represent respectively the analytical q_t-profile of a 10 cm² probe and a 5 cm² probe. As a reference, $q_{t,clay}^{char}$ and $q_{t,sand}^{char}$ have been added in the background as to reflect the materials' actual properties. The imagined readings of the standard probe are marked with yellow circles with solid black lines in-between. To illustrate the interpolation averaging effect, black crosses have been added in-between the imagined readings. This latter effect would only apply if one calculated derived CPTU-parameters on the basis of either z_{f_s} or z_{u_2}. For the CPTU-derivations made in this thesis, z_{q_t} have been used as basis, meaning that extremal u_2 and f_s readings are not used directly in the CPTU-derivations.

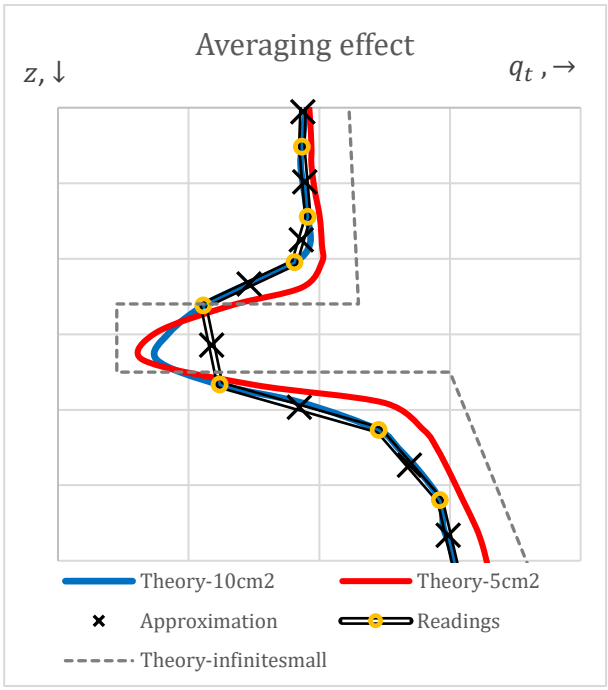

Figure 6.9. Averaging effect from 1) scale factor, 2) reading frequency, and 3) interpolation.

6.3.1.3 Stress levels influence on q_t

It is evident that for higher imposed stresses, the q_t measured in the sand increase. The same effect is seen for increased relative density. Meanwhile, the trend in the clay is that q_t is quite constant regardless of stress level. It is however not possible to assess this last assumption based on the thin layers, as these are too affected by the high q_t in the sand. By looking at q_t in the thicker layers, which are not as much affected by the surrounding sand's resistance, it is seen that q_t is very uniform. A hitch about this statement is that the thicker units have regularly been place at the bottom of the chamber, where the stresses have been quite equal for the different imposed stress levels due to the silo effect. So, inserted thicker clay layers in the top of the sample may show some deviance of reached q_t based on the stress level. But as previously stated, this is expected to be negligible different. Looking at sounding 1a, shows that the q_t reaches a rather constant level after some point, meanwhile the stress level through this sample is ca. $\sigma_v' \approx 42$ kPa to 37 kPa going from the top of the unit to the bottom. To summarize, the sand's yielded tip resistance is very dependent on the stress level, meanwhile the clay is practically independent, this latter may also be seen in *Figure E.1* in Appendix E, where the q_t is increasing very little for 3 meters of penetration.

6.3.2 Normalized q_t-profiles for different layer thicknesses

Upon assessing the normalized graphs, it is important to note that the q_t-profiles that are dashed are secondary soundings. I.e., these soundings have been conducted in the proximity of a previous sounding. The graphs are shown with "standard probe-equivalent clay layers thicknesses", denoted $H_{st.eq.}$, i.e., the height of the mini-probe specimens was normalized so that in normalized graphs, the layer thickness would be equal to those tested with the standard probe.

If one look at the four solid purple graphs in *Figure 5.15* with $H_{st.eq.} = 4$ cm, there are two soundings which reach a lower q_t in the sand after the clay layer piercing, meanwhile two are reaching a relatively higher q_t. These pairs are respectively from experiment 0 and from the latest experiment by Hammer. Even though they have quite different q_t in the sand prior to, and after the clay, they still show quite equal developing depth in the sand after penetration, and while the similarity in advance of the clay layer is rougher. An assumption that was proposed, may explaining a flaw of the testing, was that the quick approach towards $q_{t,sand}^{char}$ after a layer piercing could be linked with the more compacted zone on the top of each sand layer. The effect remained unknown, and it was assumed that the developing depths would be different for each setting if all the sand were always homogeneous. This could be checked when the mini-probe arrived, as will be explained.

To conclude this chapter: it has been verified that the q_t-profile at transitions is relying on the cone diameter, with results of the two different probes showing similar trends when their q_t-profiles are normalized with respect to d_c.

6.3.2.1 Comparison of standard probe and mini-probe soundings

Due to the relative size of the cone, the measured tip resistance approached the $q_{t,clay}^{char}$ during a shorter penetration length as compared to the standard cone. I.e., for a given distance in cm, the mini-cone would approach $q_{t,clay}^{char}$ faster than the standard cone. This is due to the extent of the failure zone surrounding the cone during penetration. When the penetration depth is normalized with respect to the cone diameter, the penetration through the normalized clay layers becomes very equal for the 5cm^2 and 10cm^2 probes. The sensing depth in the sand above the clay, and the developing depth underneath the clay is practically equal in the graphs shown for $H_{st.eq} = 4\text{cm}$ and the $H_{st.eq} = 8\text{cm}$. This is visible if one looks at e.g., the 4 cm graph, *Figure 5.15*: the developing depth in the sand after penetration reaches a curved top after ca. 1,4 d_c after the last interface. This is respectively equal to 3,5 cm and 4,9 cm for the standard probe and the mini-probe.

Further ahead and further prior to the clay layer, it is visible that the graphs deviate between the probes-sizes, but mostly due to the "shifting" or scaling. I.e., 2,6 d_c after the interface, the standard probe reaches a new top (i.e., distance to interface equal to 9,4 cm). Meanwhile, the top is reached after 3,9-4,3 d_c after the last interface, for the mini-probe, equal to 9,7-11 cm. This shows that the developing depth in the sand is equal when normalized, but for penetration in the rest of the sand, the probes reflect the compaction. This latest part is most visible in the non-normalized plots, see. ch. 5.1.1.4.

This finding disproves that it is the vibration and the localized compaction of the top of the next sand layer which decide when the developing depth in the sand is reached. This means that the earlier findings of a ca. equal developing depth after the last clay interface, regardless of stress level for every sounding, is true. This is an important implication, as it confirms a trend which technically was uncertain, yet was very easy to assume as it was visible. There were none way to prove it on the basis of the data prior to the arrival and testing with the mini-probe.

The soundings of 3b-4b and 3c-4c had ca. 3,2 d_c centre-distance, or 8 cm. By looking at ch. 5.2.1.3 and 5.2.1.4 it is evident that the proximate position to a previous sounded hole affects the results of a new sounding. It is not visible in the top due to the reconstructed sand however, but after ca. 40 cm one can start to evaluate this effect. It is important that one evaluates this far from the clay layers, as the soundings 3b and 3c went through the perimeter of the cylinder and the soundings 3c-4c and 3b-4b, and do thereby not reflect each other near clay layers. With this in mind, one can see that the tip resistance in the sand is ca. 0,5-0,75 MPa less in the sand.

In addition, it was found in the literature review (see ch. 2.3.4.3), that the grain size should not affect the results as $A_C = 5\text{cm}^2 \gg 1{,}5\text{cm}^2$.

6.3.2.2 Future refinement of presented normalized graphs

To refine the normalized q_t-profile assessment for each layer thickness, the graphs could rather show the different profiles with colour gradients according to stress level in regarded clay unit, and not based on the stress level imposed on the top of the sample. Moreover, if it is possible to visualize the D_r for the different soundings without making the plot too untidy, this would also aid any such assessment.

6.3.3 Side friction

In the presentation of f_s-results, it has been chosen to superimpose the associated readings not to middle point of the sleeve, but rather at the very front, where the friction sleeve makes it first encounter with the clay. By following that procedure, the extremal values of f_s occur at the same depth as the extremal values of u_2 and q_t. The component's relatively large size should be kept in mind upon assessing f_s, as it has an "averaging" or smoothening effect on the results.

A phenomenon which is not well understood, is why the f_s is reaching such high levels in the clay layers. The values of f_s in the sand is low with values ranging from ca. 5-15 kPa in medium dense sand, and 10-20 kPa in the dense sample (experiment 1a). Upon piercing the intermediate clay layers in the chamber sample, the side friction reaches level of 15-35 kPa. For comparison, the side friction in the clay at Flotten is ca. 7-8 kPa. Due to lack of experience with CPTU-interpretation, and no CPTU-data on the relevant type of soil stratigraphy were available, it is not known well how f_s regularly behaves in field soundings as opposed to the chamber soundings. A coarse CPTU-profile was found in the article of L'Heureux et al. (2010) which was conducted in a relevant soil-profile, see *Figure 6.10*, which showed that f_s was substantially lower for such weak thin interbedded layers.

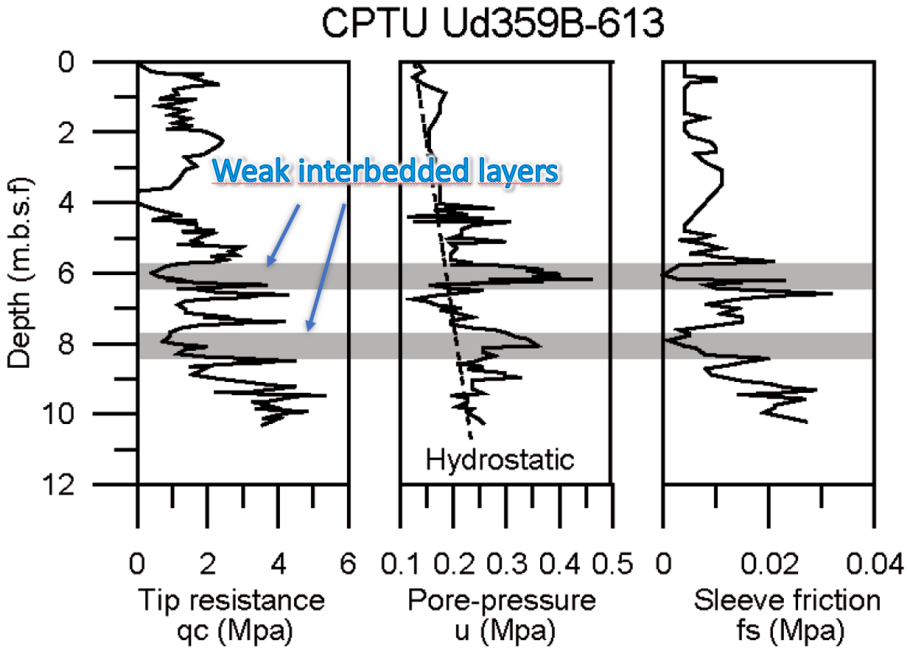

Figure 6.10. A CPTU-profile in deposits with weak interbedded clay layers.

At the moment, the apparent deviance from the field experience and the CPTU-results from the chamber experiments is not well understood. Some effects that may affect the results is that some of the samples have large overconsolidation ratios. Some information on OCR is given below:

The lowest stress state in a layer of pottery clay was experienced in experiment 0, giving the highest OCR-value for the pottery clay: $OCR = p_c'/\sigma_v'$ =100kPa/14,7kPa≈6,8; meanwhile the lowest OCR-value was ca. 1,4 in experiment 2. For the quick clay, p_c' at Flotten laid at ca. 258 to 292 kPa in the extraction depth interval, giving OCR ≈3,8 to 4,2 (if disturbance is disregarded).

An observation is that f_s seems to reach higher values for greater stress states, this is particularly visible in the f_s-profiles from experiment 2, ch. 5.1.1.3, where soundings 2a,2b and 3c had $q_{load} = 40$kPa, and 2c,3b and 3c had $q_{load} = 80$kPa. The peak value of f_s was in the upper clay layer in sounding 2c, experiment 2, with 35 kPa. This clay unit had only an OCR of 1,4, so it is a bit uncertain whether OCR really is a factor of influence.

Otherwise, the unit are not covering the entire cross-section, which may or may not have an impact. The high values may also be linked with the sand, and the interaction between the sand and the clay upon pushing sand into the clay during penetration, i.e., some sand is trapped in an intermediate position between the clay and the probe at top of the sample. However, if any cause is identified, it is not evident why the field soundings are so different from those obtained in the experiments.

A last possible reason, which was mentioned as the most probable in the project thesis was that the sand yielded artificially low f_s due to the low stress level in the sand. This may be true, but this do not explain the very high f_s in the clay as opposed to the field experience.

It is advised that future participants of the research program are provided CPTU-data from survey projects which have been conducted in areas with soil stratigraphy equal to what this very research program revolves around. Otherwise, the participants are recommended to actively request such data from the institute or possibly from some company or external institute, such as e.g., NGI. This can provide more information on the lack of conformity between experimental results and field results of f_s.

6.3.4 Pore pressure

The pore pressure readings are a good reference when trying to detect layers of undrained material, surrounded by more permeable mediums. The difficulty regarding detecting thin layers of clay in sand is much relying on two things, firstly the sampling rate and secondly on the clay layer thickness.

The first is evident in most of the graphs for the standard probe, where typically, only two readings were made in layers of 4 cm. For layers of 2 cm, it occurred that there was no measurement made at all inside the clay unit. And certainly, whenever measurements were done inside the clay, there were little to no pore pressure build-up. The effect of reading frequency became even more apparent upon conducting experiment 3, as two probes with

different reading frequencies were utilized. It is seen that the soundings 4b and 4c had ca. 10 measurements inside the clay layer of ca. 2,8 cm, meanwhile sounding S1 had only 2 in the 4 cm layer due to bad timing, otherwise it could have had 4. The adverse effect of conducting soundings with too low sampling frequency is that frequency averaging or smoothening of the u_2-curve will occur, as described for q_t in ch. 6.3.1.2.

For the second assertion, it is evident for the thinnest clay layers that there is no or little pore pressure build-up. This is explained by the penetration deformation of the clay layer, where sand is pushed downwards into the clay, and further pushed sideways. The amount of sand in front of the cone will decrease as the probe is pushed further and ultimately, there will be only clay surrounding the probe and the pore pressure filter. From this point on, the pore pressure will build-up. As seen in *Figure 6.11*, for sufficiently small intermediate clay layers, the penetration deformation may cause the clay to not surround, or only barely surround the pore filter at any instance. In addition, the effect of reading frequency would give a very low probability of making any measurement of any pore pressure build-up. An alternative, that would increase the value of the pore pressure readings would be to use a probe with a sensor at filter location u_1, which naturally would be surrounded by more clay as the probe penetrates a thin layer.

Another observation regarding pore pressure, is that after the penetration of a layer, the u_2 drops below the hydrostatic line, i.e., the excess pore pressure becomes negative. As the probe pierces the last interface, the trapped water with its high pressure is released creating a relative suction. This may not be very visible in the data from experiment 3, but is apparent in the u_2-plots of the other experiments.

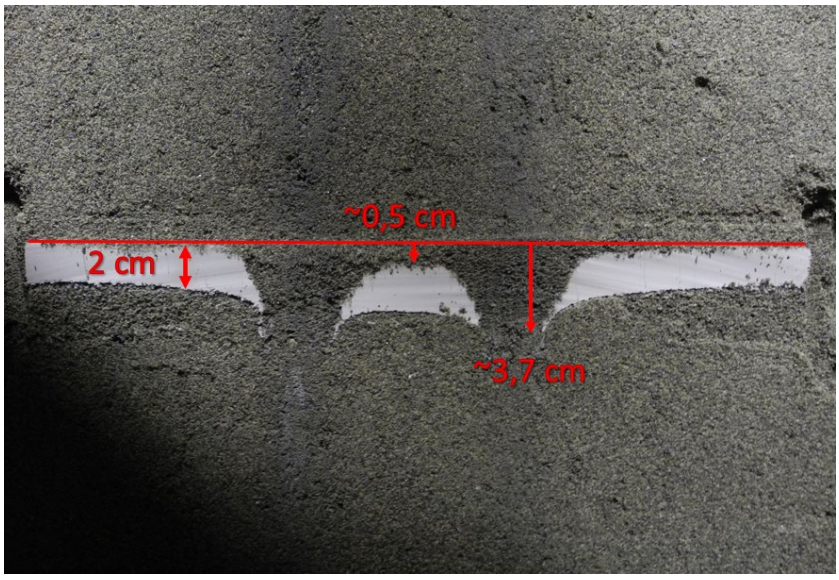

Figure 6.11. Deformation in 2 cm clay layer, little to no clay surrounds the probe at any instance.

The maximum measurement of u_2 was done in the largest clay unit, sounding 3b in experiment 1a, with a total of 110 kPa. It is believed that this could have become even higher, if the interface between the specimens was completely shut and no cavity or hollow existed. The trend was that as a sounding went through a layer, the pore pressure built up gradually. A strange observation was that the pore pressure build-up in some of the thicker quick clay

layers was equal to u_2 in some of the thinner layers, see *Figure 5.9*. This was not as expected, and is maybe linked to instances of intermediate siltier layers within the clay units. An example of such a specimen is seen in *Figure 6.12*. This was however not entirely unexpected, considering that the utilized specimens was of natural material, thereby entailing natural variations.

Figure 6.12. Most likely an intermediate siltier layer in a mini-block consisting mainly of quick clay.

The rather low u_2-reading in sounding 1a is assumed to be caused by insufficient or improper saturation prior to sounding.

6.3.5 Derived CPTU-parameters

The D_r-profiles obtained by using an adjusted NGI-99 method were discussed in ch. 6.1.2.2, as it seemed more fitting upon discussion of sand compaction and the results from the density samples.

6.3.5.1 Shear strength assessment

Among the three cone factors, Karlsrud et al. (1997) implied that $N_{\Delta u}$ had the best conformity between CPTU-readings and measured S_u, and consequently should be weighted the most upon evaluation of S_u based on the cone factors. As can be understood from the relations presented by Karlsrud et al. (1997), to find S_u, the cone factor must be known, and to find the cone factor, S_u must be known. This self-reference requires either calibration for every site, or relying on the approximate empirical relations given by Karlsrud et al. (1997).

The different cone factors were calculated for each clay layer based on interpolations of I_P and *OCR* for both the pottery clay and the quick clay. This was made on basis of previously determined $p'_{c,pottery\ clay}$ by Hammmer (2020), the field report (L'heureux et al. 2019), and the estimated stress distribution in the chamber.

The results are shown in ch. 5.1.1, and shows some general trends:

- $S_{u,\Delta u}$ was typically very low, around 0-5 kPa, explained by the low measurements of B_q, again explained by the low pore pressure build-up experienced in the thin clay layers.
    - However, it approached the predetermined S_u of 27,5 kPa of the pottery clay for sounding E1a-3b, see *Figure 5.3*. This took more than 12 cm of penetration, and due to the pore pressure loss, it was not verifiable whether if the true S_u would be reached.
- It was evident that $S_{u,ke}$ and $S_{u,kt}$ was overestimating the layer strength for the thin layers, and as the layers approached greater thicknesses, the estimated S_us became more and more accurate.
    - They both had extremities reaching quite near the true S_u for 8 cm thick layers
    - For 12 cm layers, they typically reached the S_u.
    - For the 36 cm unit, 1a-3b, the S_u was reached at ca. 10-13 cm.

For comparison, some soundings from the Flotten-site were downloaded and treated with regards to CPTU-parameters. In these CPTU-profiles the B_q was about 1-1,2, which can be told to be characteristic for the quick clay. Karlsrud et al. (1997) stated that $N_{\Delta u}$ was the most reliable of the cone factors in determining the shear strength of a soil. This suggestion do not fit well for the thin layering effect, for layers of ($H < 12$cm), due to the low measured B_q-values. The other cone factors seem to coincide better, based on the CPTU-results in the thin layers. However, by looking at the graphs of Flotten-soundings, the N_{ke} did not perform as well and S_u thereby fluctuated a lot. A brief summarize of the Flotten results are given in the tables on the next page.

Table 6.2. Summarize of CPTU-results for depth 8-10,5 meters, part 1:

Parameter	q_t	f_s	u_2	Δu_2	q_n
Depth [m]\Unit	[MPa]	[kPa]	[kPa]	[kPa]	[MPa]
8	0,70	8	700	650	0,65
10,5	0,90	8	825	800	0,7

Table 6.3. Summarize of CPTU-results for depth 8-10,5 meters, part 2:

Parameter	Q_t	R_{fn}	B_q	$S_{u,\Delta u_2}$	$S_{u,ke}$	$S_{u,kt}$
Depth [m]\Unit	[-]	[%]	[-]	[kPa]	[kPa]	[kPa]
8	5	1,0	1,0-1,2	110	20-50	65
10,5	4,5	1,0	1,0-12	120	25-55	75

As to underline previous mentioned information: Upon assessing thin layers of clay in sand, it is highly important the CPTU-assessment is done meticulously. I.e., u_2 should be assessed at the same depth as q_t. If this is not done, the B_q-values will become even lower than those presented in the graphs in ch. 5.1.1.

A last note in this chapter is that Lunne et al. (1997) could tell that a recognized approximation of remoulded shear strength $S_{u,r}$ was f_s. This would be true for a low sensitive clay, yet for the soundings gathered from Flotten, it seems that f_s was manyfold larger than the $S_{u,r}$ for the quick clay, so this approximation do not work at all sites and for all conditions.

6.3.5.2 THE NTH-method

Regarding the soundings data points placed in the NTH-chart, from sounding S1, see *Figure 5.12*, the N_m value was reaching some values asymptotically, around ca. 2. This falls within the spectre of the soft clay in

Table 2.3. However, due to a low B_q, the interpreted friction angle become very small, $\approx 16° \ll 29\text{-}32°$ which were interpreted in the Flotten site report. It is of course natural that the results deviate, considering that the parameters upon transitions don't reflect neither the upper nor lower layer. For the evaluation of N_m attraction was set to 10 kPa, while β was set to 0°.

The same attraction and plastification angle were used in the assessment of the CPTU-results from Flotten, shown in *Figure E.3* in Appendix E. There B_q was approximately 1-1,2, and N_m was thereby estimated to be ca. 4,8, giving a friction angle of $\tan(\phi') = 0{,}85$ or $\phi' = 40{,}4°$. This must be told to be very high, especially compared to the $29 - 32°$ suggested in the site report. This is probably due to the high estimated N_m, which moreover is caused by the low predetermined attraction. It was stated in the report by Senneset & Janbu (1985) that the apparent attraction obtained by CPTU-test is typically much larger than those typically found in laboratory testing. If they based their N_m-charts on attractions obtained by CPTU-assessment only, then this may describe the deviance. By inserting an attraction of 200 kPa (as mentioned in their text), N_m for the same profile would become 2, giving $\phi = \tan^{-1}(0{,}6) = 30{,}96°$. This would conform very much with the interpretations in the site report (L'Heuerux et al. 2019).

6.3.6 Classificiation charts

Only a few classification charts were included, as to illustrate how CPTU-readings behave for layer transitions. Moreover, the charts are only of sounding 4b from experiment 3 which went through quick clay. This sounding was chosen as one could expect that the characteristic B_q-value is ca. 1-1,2 for this clay, as can be seen in the B_q-plot for the quick clay interval at Flotten in *Figure E.2* in Appendix E. As is clearly visible in all the classification charts, the soundings are approaching slowly towards their characterized classification zone.

For the Robertson diagrams, sector 1 is defined as “sensitive, fine-grained” and should embody quick clay. Sector 5 and 6 should respectively embody “sand mixtures; silty sands to sandy silts” and “sands; clean sands to silty sands”. For soundings affected by nearby layers these extremities are never maintained, and for soundings experiencing the thing layering effect, i.e., where the influence length is never surpassed, the intermediates layer’s associated extremity is never reached.

In the Q_t-F_r diagram, *Figure 5.11*, the penetrations of the thin layers are following scythe alike paths/patterns. This is explained by the logarithmic scale of the diagram. It is however a bit strange that the f_s-value becomes so large, as explained in ch. 6.3.3. As can be seen in sounding 3b in experiment 1a, f_s is reduced after some piercing distance through the clay, and it is therefore expected a much lower value of f_s. Anyhow, the effect of a large f_s relative to q_t makes the data path in the diagram go toward 2 instead of 1. However, if one looks at the Q_t-B_q diagram, the data path for each clay layer piercing is shown as approaching zone 1, through zones 3 and 4. As the pore-pressure never build up, the typical B_q of 1-1,2 is never reached, as reflected in the chart. This is also apparent in the NTH-classification chart, see Figure 5.12, where the trend is similar with an undershooting B_q. Yet, in this chart, the low q_t of very soft clays is reached, meanwhile the B_q moves the data out of defined borders.

With all of this information, it is apparent that the classification charts do not sort the data in a well manner for transitions. This is expected as they only regard measurements at certain depth or time instances. In order to create a chart that would manage transitions well, the relative change of each parameter would also have to be assessed.

6.3.7 Reading frequency

An advantage of using the mini-probe equipment by Geomil, was the increased reading frequency as opposed to the standard probe. This attribute should not be linked with the size but rather the electronics within. Anyhow, the tip resistance curves of the treated mini-probe readings are discrete as is reflected in the jagged behaviour. Because of the very high reading frequency, these curves became more or less continuous. This implies that one can with a better accuracy correlate the thin layering effect empirically with potential analytical approaches. As was explained in ch. 6.3.1.2 this higher reading frequency would ease the detection of thin weak interbedded layers as the probability of measuring the analytical extremal value is increased.

6.4 Regarding documentation

In order to build high quality chamber samples, it has been of outmost importance to first become acquainted with construction of chamber samples, and to further document all constructions and excavations with photos and regularly logging. As experience was gained, the sample procedures could be adjusted accordingly, in an incremental fashion as new experiments were conducted. In posterity, the documentation has been very helpful, as whenever a memory has been unclear, or some explanation is sought, much have been found in previous documentation. However, the abundant documentation has also made it easy to fumble, regarding things to explain and retell, so keeping a focus one task at the time has been essential. A hope was to show more pictures of the project, but this seemed perhaps too excessive for the master, as the level of detail would either fluctuate through the written thesis, or a higher degree of detail would be necessary for the entire master. All documentation and pictures have been structured and left as a copy at the university, in order for later participants to gain insight in what has been done.

7 Conclusion

The results show that the piezocone penetrometer is an excellent tool with a repeatable methodology that provides results which reflect homogeneous soil's properties. However, it has been made clear that for transitions between layers, the measured tip resistance becomes an intermediate value of the characteristic tip resistance of the lower layer and the characteristic tip resistance of the upper layer. This implies that it can be difficult to determine soil stratigraphy and the layers' physical properties for deposits of thin interbedded layers of clay in sand. Regarding this issue, the results indicate that 8-12 cm thick clay layers can be identified using the conventional CPTU-tool normally used in practice. The tip resistance in the thin layers does not reach the material's characteristic tip resistance since the failure mechanism around the tip will involve both materials. In practice this implies that the shear strength of thin layers is overestimated, and consequently should be corrected for. Moreover, the measured pore pressure build-up starts after some distance in the clay, and does not reach the characteristic level of clays. Thus, regular classification charts cannot be used for detecting thin weak layers, as they only regard measurements at specific depths or time instances. It is apparent that during transitions, the relative changes of the measured parameters must be considered.

This study suggests that tip resistance is the most prominent parameter in detection of thin clay layers in sand, while pore pressure readings provide a good support for the findings. Three elements have been identified to influence the thin layering effect the most, these are: the cone geometry; the intermediate layer's thickness; and lastly, the contrast in soil strength, or more specifically, the contrast in the materials' yield of characteristic tip resistance. The use of a mini-probe (5 cm^2) has reinforced previous assumptions regarding the scaling effect and supports the reliability of the previously obtained CPTU-results (see ch. 6.3.2). In addition, this equipment has illustrated the effect of reading frequency.

The experiment on natural quick clay proved that it is possible to build easily disturbed quick clay specimens cut from field block samples into the chamber. However, some moderate deterioration of certain properties was experienced. This confirms that sensitive clays, such as quick clay, require considerable awareness, precision, and careful execution when thin layers are built from clay sampled by a mini-block sampler at depths in the field.

The 4 different chamber samples that have been tested provide an abundant amount of data, creating a good foundation for further work in the research program. The tests have been executed thoroughly, with accompanying supplementary laboratory tests to provide more information on the testing conditions, this may ease interpretation work in the future, and make it more reliable.

Regarding the stress state in the chamber, the data foundation is a bit inaccurate due to sensitivity drifting. This makes the estimations a bit imprecise, but they are regarded as adequate for the purpose of this research.

8 Future work and recommendations

8.1 Documentation of laboratory work and results

The laboratory work has been quite comprehensive and executed thoroughly in the aim of valuable results for further research. The data and information gathered throughout this master's thesis is too excessive to fit into this paper. A large selection of this data and information will therefore be left as a copy in systematized folders, available for future participants of the program that may want to delve deeper into the matter if they find anything missing, or if they are generally curious. The data includes literature, procedures, photographs of the different procedures, logging templates, raw files of sounding results and pressure cell readings, and processed tables and figures in Microsoft Excel, etc. The most important and useful information has been refined in specific documents and their titles will be presented below. The quality of these documents will hopefully make them very useful for future participants. The highlighted documents are:

Procedures:

Building procedures and logging templates

Sounding procedures and logging templates

Excavation procedures and logging templates

Results:

Compilation of sounding results, with all performed parametrizations, and documents on the associated stress state for each experiment.

Compilation of supplementary laboratory results

In posterity the comprehensive documentation has been very helpful, as whenever a memory was unclear, or some explanation was sought, many answers have been found in previous documentation in the form of photographs or logs. It is therefore highly recommended for future participants to document their work thoroughly as well.

8.2 Propositions and further work

8.2.1 Further data treatment of obtained results

As previously told, the data assessment regarding the thin layering effect is not very in-depth, and further processing of the data is possible in the pursuit of more new knowledge about the phenomenon. A compilation of sounding results is transferred to the project, so the data will be available for assessment regarding both thin layering correction and calibration of the reversed spatial filtering method presented by Hammer (2020).

8.2.2 Refinement of laboratory facilities

8.2.2.1 Possible improvements to the chamber

The improvements elaborated in ch. 6.1 are relevant, but may not be necessary. Another idea that may improve future experiments is inspired by the set-up explained by Houlsby & Hitchman (1988). They inserted flexible rubber membranes both along the interior wall and at the chamber base, which were used to apply normal stresses by the means of water pressure. Such improvements would enable determination of stresses along sample boundaries. However, the set-up was never illustrated in their article, and it is thereby unknown whether such a solution would require extensive alterations of the current chamber, or if the solution would be rather simplistic. If this is feasible, the chamber can be defined as a true calibration chamber, according to most definitions found on the internet, e.g., from ISMGEO's website. In the meantime, the chamber could rather be defined as a semi-calibration chamber, as the vertical boundary can be adjusted with respect to σ_v.

8.2.2.2 Possible improvement of devices

It is of high interest to get more reliable pressure cell reading. In the instruction manual of the earth pressure cells (Geokon, 2019, p. 20) it is stated that they are equipped with integrated thermistors, which allow for logging of temperature. This would require a digital ohmmeter for each cell, which may either already be available at the campus, or possibly it could be invested in a couple of new ones, if they are affordable. In the same manual it is stated that the readings can be corrected for the temperature changes. The subject requires more study, but might yield better results for the research program in the long run. If other sources of the drifting are identified, these should naturally be counteracted as far as practically possible. Elsehow, it could also be an alternative to replace the cells with better ones, if this exists.

Another suggestion in the pursuit of enhanced detection of thin clay layers, is to introduce a new CPTU-probe with a pore pressure sensor located at the cone, u_1, to the future experiments. This may be available at NTNU in the near future.

8.3 Future experiments

8.3.1 Further assessment of stress distribution

To assess the normal stresses acting on the wall, either the proposed calibration chamber advancement may be utilized, or possibly, an experiment similar to that explained in the field and laboratory compendium, p. 321 (NTNU Geoteknikk, IBM, 2017) could be of interest. This experiment is based on measuring lateral stress by waterfilled pressure cells with rubber membranes mounted on the wall, see *Figure 2.38*. A hitch regarding the latter is that the cells must be concave to fit along the wall.

Furthermore, experiments focusing solely on describing the silo-effect in the chamber can be conducted. This could involve e.g., placing the pressure cells at different positions in the chamber, with respect to both height and distance to centre. This could be included with a regular experiment, where one section is not sounded, as the pressure cells may obstruct the paths or affect the soundings.

It could also be interesting to conduct a fast build-in, with succeeding load application, as to assess the stress level with more reliable pressure cell data.

In the article by Li et al. (2012) the interface friction angle was measured by some preliminary lab test. This test may also be conducted for the chamber wall, but it is uncertain whether there is such equipment available at NTNU.

8.3.2 Layer set-up

New experiments can be conducted in order to gain data on other combinations of stress states and layer thicknesses. This would enable further development of e.g., charts for the thin layering correction, K_H, (an initial chart made by Hammer is presented in *Figure 2.34*). Moreover, it will give a better foundation for calibration of the spatial filtering method, also presented by Hammer (2020, appendix B). To specify regarding the first proposition: In order to get a larger contrast of $q_{t,i}^{char}$ between the sand and the clay for the thicker clay layers, the thickest clay layers can be placed at upper level in some experiments.

8.3.3 Sand sample construction

It is evident that the construction of sand samples is a complex matter as seen in e.g., the lengthy list of influences on the sand's density in ch. 6.1.2. Unfortunately, reviewing every detail of the procedures and the practices would be rather excessive for the thesis. Instead, it is proposed that future participants of the research program get acquainted with the sample build-in, based on the given information, and the supplementary written procedures. In addition to this, some supplementary experiences may be transferred orally. The desired density was obtained with the sand preparation procedure 3, which is thus recommended in future build-ins. However, refinement is still possible, regarding homogeneity and under-compaction. An important notice to keep in mind during the build-in of the sand, is the max capacity of the actuator, as to prevent buckling.

8.3.4 Use of natural clay

Considering the quick clay's susceptibility of deterioration upon exposure, the practice of watering and covering the specimens should have been emphasized even more in the laboratory work. In this regard, the lowering of the ground water during the excavations should have been held to a bare minimum. The failure, or neglection to keep the environment surrounding the quick clay specimens wet at all times, is regarded as the most likely reason for alterations of the clay's properties. To assess the changes of soil properties during an experiment, more tests could have been conducted prior to the chamber-build-in. Furthermore, this assessment could have been improved by following the mentioned methodology by L'Heureux & Kim et al. (NIFS, 2019) with pH-measurements at different time instances.

8.3.5 Comparison with field data

For future participants of the research program, it is recommended to request CPTU-data from survey projects which have been conducted in areas with soil stratigraphy equal to what this very research program revolves around as it would allow for the opportunity to cross reference the results from the chamber soundings with that type of soil stratigraphy in its natural habitat. This could provide better insight and understanding into why f_s is so high in the chamber experiments as opposed to the field soundings.

8.3.6 Proposed advancements in the distant future

The large-scale model testing facility developed at NTNU provides a good opportunity to test a range of different chamber sample arrangements, beyond the current scope of the research program, which is namely looking at thin layers of clay in sand. By this, it is meant that once it has been acquired enough data for the research topic of thin clay layers in sand, it is possible to utilize the facility for testing other materials and other sample layouts. A change of scope for the sample production may be a rather smooth transition. Considering that soil stratigraphy in historic estuaries typically contain all soil separates, testing many different combinations of materials being sand-silt-clay interbedded each other, may help improve future CPTU-assessment both regarding identification of the layering of materials, but also in determination of their associated soil properties. This last statement is based upon the apparent uniqueness of specific soil type's influence on the curvature of the q_t-profile. That is, as an addition to the already mentioned effects of: the contrast in characteristic tip resistance; and the ratio of the layer thickness and the cone size. These parameters are rather deciding the extremal values obtained, but it is evident by looking at e.g., the figures *Figure 2.28* and *Figure 2.29* in ch. 2.3.4.2 - Tip resistance profiles, that the q_t-curvature is more complex than practically regarded in current thin layering assessments.

8.4 Recommendations for CPTU application in the industry

8.4.1 New procedures in prone areas

According to the CPTU-results, some specific recommendations can be suggested for the industry regarding investigations in areas susceptible for thin layers of clay in sand deposits, i.e., for locations under marine limits, which moreover can be narrowed down to areas with soil stratigraphy consisting of larger fractions. The penetration rate can with great benefits be reduced to 1,5 cm/s to increase the data point density by ca. 33 %. This implies that the rate effects in silts first should be investigated, as this material acts partly undrained under penetration, depending mainly on the grain size distribution, see ch. 2.2.1.2. The effect on the CPTU-parameters must then probably be taken into consideration in the CPTU assessment.

For a 30 meter deep sounding, the reduced penetration rate would imply increasing operation time from 25 minutes to 33,3 minutes. The 8 minutes of prolonged operation time is of high value, while the increased cost is not substantial. Karlsrud et al. (1997) stated that the length of sounded meters a day ranges around ca. 80-100 meters for a one-manned advanced multi-purpose rig. This implies that ca. 67-83 minutes of effective penetration is conducted in a day's work, which by a decrease in speed, would require 89-111 minutes, i.e., an increase of 16-28 minutes work for each day with surveys in such areas. Considering that setting up the rig and that other associated activities have to be performed regardless of the speed used during the soundings, this would be a feasible way of increasing chances of detecting thin layers of clay in sand. If such thin layers are detected, an increased data point density would moreover provide a better foundation for determining the soil's properties. I.e., there is a higher probability that the extremal point determined by the cone's geometry (analytical q_t-profile for the specific cone) is measured.

8.4.2 Further development of the CPTU-equipment

The effect of reading frequency was apparent for the 5 cm^2 probe as compared to the 10 cm^2 probe. This is of course only depending on the electronics, and not the geometrical design. However, the probe size is a prerequisite to which electronics may be inserted. Thereby the reading frequency may be restrained by the size. However, in this thesis it was apparent that this is not a constraint for the 10 cm^2 probe, as this intuitively is larger than 5 cm^2 probe.

Refinements of equipment electronics with an increased reading frequency can provide significant improvements to the resolution of CPTU-profiles. The CPTU-assessment would then be more based on the theoretical or analytical limitations of the method, and not so much on the discrete nature of the data which is seen today for the standard equipment.

Reference list

Ahmadi, M.M., Robertson, P.K. (10.2005) Thin-layer effects on the CPT q_c measurement. *Canadian Geotechnical Journal*, 42(5):1302-1317. Available at:https://doi.org/10.1139/t05-036 [Accessed: 11.06.2021]

Amundsen, A.H., Thakur, V., Emdal, A. (2016) Sample disturbance in the block samples of plastic soft clays. *17th Nordic Geotechnical Meeting*. Reykjavik, 05.2016. Available at: https://www.researchgate.net/publication/303517274_Sample_disturbances_in_the_block_samples_of_low_plastic_soft_clays [Accessed: 16.05.2021]

Boulanger, R.W., DeJong, J.T. (2018) Inverse filtering procedure to correct cone penetration data for thin-layer and transition effects. *Proceedings of the 4th International Symposium on Cone Penetration Testing (CPT'18)*. The Netherlands, Delft, June 21.-22. 2018. Available at: https://faculty.engineering.ucdavis.edu/boulanger/wp-content/uploads/sites/71/2018/06/Boulanger-DeJong-Inversion-of-CPT-data-CPT18-2018.pdf [Accessed: 01.06.2021]

CEN - European committee for standardization (2004) *EN ISO 17892-12:2004 Geotechnical investigation and testing — Laboratory testing of soil — Part 12: Determination of Atterberg limits.*

CEN - European committee for standardization (2012) *EN ISO 22476-1:2012 Geotechnical investigation and testing: Field testing: Part 1: Electrical cone and piezocone penetration test*. p. 16 (digital p. 24)

CEN - European committee for standardization (2016) *EN ISO 19905-1:2016 Petroleum and natural gas industries – Site-specific assessment of mobile offshore units – Part 1: Jack-ups*.

CEN - European committee for standardization (2017) *ISO 14688-2:2017 Geotechnical investigation and testing - Identification and classification of soil - Part 1: Identification and description.*

Clausen C.J.F., Aas, P.M., Karlsrud, K. (2005) *Bearing capacity of driven piles in sand, the NGI-99 approach*. Oslo, Norway: Norwegian Geotechnical Institute (NGI). Available at: https://www.researchgate.net/publication/290599390_Bearing_capacity_of_driven_piles_in_sand_the_NGI_approach [Accessed: 30.05.2021]

Cone penetration test (2020) Available at: https://en.wikipedia.org/wiki/Cone_penetration_test [Accessed: 19.12.2020]

Dayal, U., Allen, J.H. (1975) The effect of penetration rate on the strength of remolded clay and sand samples. *Canadian Geotechnical Journal*, 12(3):336-348. Available at: https://doi.org/10.1139/t75-038 [Accessed: 31.05.2021]

De Beer, E.E. (1963) The Scale Effect in the Transposition of the Results of Deep-sounding Tests on the Ultimate Bearing Capacity of Piles and Caisson Foundations. *Géotechnique*, 13(1):39-75. Available at: https://www.icevirtuallibrary.com/doi/pdf/10.1680/geot.1963.13.1.39 [Accessed: 19.03.2021] [Accessed: 05.2021]

Doherty, J.P., Gourvenec, S., Gaone, F.M., Pineda, J.A., Kelly, R., O'Loughlin, C.D., Cassidy, M.J., Sloan, S.W. (2018) A novel web based application for storing, managing and sharing geotechnical data, illustrated using the national soft soil field testing facility in Ballina, Australia. *Computers and Geotechnics*, 93:3-8, ISSN 0266-352X. Available at: https://doi.org/10.1016/j.compgeo.2017.05.007 [Accessed: 24.06.2021]

Emdal, A., Gylland, A., Amundsen, H.A., Kåsin, K., Long, M. (2016) Mini-block sampler. *Canadian geotechnical journal*, 53(8):1235-1245. Available at: dx.doi.org/10.1139/cgj-2015-0628 [Accessed: 16.05.2021]

Geokon (2019) *Instruction manual: Model 3500 Series: Earth Pressure Cells*. Available at: https://www.geokon.com/3500-Series [Accessed: 22.02.2021]

Geomil Equipment B.V. (201Xa) *Saturation Process*. Available at: https://s3.eu-central-1.amazonaws.com/z3r2zxopa4uuqpw5a4ju/geomil/files/guidelines/12-004_rev_1_Saturation-process.pdf [Accessed: 15.04.2021]

Geomil Equipment B.V. (201Xb) *CPTest - Software Operation Instructions*. Moordrecht, The Netherlands: Geomil Equipment B.V. Available at: https://www.geomil.com/about-geomil/downloads/ [Accessed: 15.04.2021]

Geomil Equipment B.V. (201Xc) *GSN - Ethernet + Virtual COM Configuration: GSN - Geotechnical Snesor Network*. Moordrecht, The Netherlands: Geomil Equipment B.V. Available at: https://www.geomil.com/about-geomil/downloads/ [Accessed: 15.04.2021]

Geomil Equipment B.V. (201Xd) *GSN - Quick start guide: GME-700, GME-700 Connect, CPTest, GSN - Geotechnical Snesor Network*. Moordrecht, The Netherlands: Geomil Equipment B.V. Available at: https://www.geomil.com/about-geomil/downloads/ [Accessed: 15.04.2021]

Hammer, H.B. (2020) *Physical experiments on CPTU thin-layer effects of thin clay layers embedded in sand: With analysis and possible correction of cone resistance in layered profiles.* M.Eng. Master Thesis. Faculty of Civil Engineering, Norwegian University of Science and Technology (NTNU). Available at: https://ntnuopen.ntnu.no/ntnu-xmlui/handle/11250/2689484 [Accessed: 10.10.2020]

Houlsby, G.T., Hitchman, R. (1988) Calibration chamber tests of a cone penetrometer in sand. *Géotechnique.* 38(1):39-44. Available at: https://doi.org/10.1680/geot.1988.38.1.39 [Accessed: 17.05.2021]

Houlsby, G.T., Martin, C.M. (2003) Undrained bearing capacity factors for conical footings on clay. *Géotechnique.* 53(5):513-520. Available at: https://www.researchgate.net/publication/240371700_Undrained_bearing_capacity_factors_for_conical_footings_on_clay [Accessed: 31.05.2021]

Hvorslev, M.J. (1949) *Subsurface Exploration and Sampling of Soils for Civil Engineering Purposes*. Vicksburg, Mississippi: Waterways Experiment Station. Available at: https://babel.hathitrust.org/cgi/pt?id=mdp.39015002125634&view=1up&seq=222&skin=2021&size=125 [Accessed: 16.05.2021]

Ingenjörsfirman Geotech AB (2012) *Användermanual för CPT-log*. Sweden, Göteborg. Available at: https://static1.squarespace.com/static/565c5cc1e4b05079e4c0fcfb/t/587c984bbf629abac09d265f/1484560476906/6-SWE-CPT-LOG-v5.xx.pdf [Accessed: 16.01.2021]

Janssen, H.A. (1895) Versuche über getreidedruck in solozellen. *Zeiteschrift des Vereins deutscher Ingenieure*. 39(35):1045-1049. Available at: https://web.archive.org/web/20110303223406/http://www.phy.duke.edu/~msperl/Janssen/Janssen1895.pdf [Accessed: 25.05.2021]

Karlsrud, K., Lunne, T., Kort, D.A., Strandvik, S. (1997) *CPTU Correlations for Clays*. Norwegian Geotechnical Institute (NGI). Available at: https://www.researchgate.net/publication/285733117_CPTU_correlations_for_clays [Accessed: 20.06.2021]

L'Heureux, J. S., Hansen. L., Longva, O., Emdal, A., & Grande, L. O. (2010) A multidisciplinary study of submarine landslides at the Nidelva fjord delta, Central Norway, - Implications for the assessment of geohazards. *Norwegian Journal of Geology*, Vol 90:1-20. Trondheim, ISSN 029-196X. Available at: https://www.researchgate.net/publication/234101112_A_multidisciplinary_study_of_submarine_landslides_at_the_Nidelva_fjord_delta_Central_Norway_-_Implications_for_geohazard_assessment [Accessed: 30.06.2021]

L'Heureux, J.S., Longva, O., Steiner, A., Hansen, L., Vardy, M. E., Vanneste, M., Haflidason, H., Brendryen, J., Kvalstad, T.J., Forsberg, C.F., Chand, S., Kopf, A. (2012) Identification of Weak Layers and Their Role for the Stability of Slopes at Finneidfjord, northern Norway. In: Yamada, Y. et al. (eds.), Submarine mass movements and their consequences*. Advances in Natural and Technological Hazards Research*, vol. 31. Springer, Dordrecht (pp. 321-330). Available at: https://doi.org/10.1007/978-94-007-2162-3_29 [Accessed: 29.07.21]

L'Heureux, J.S., Kim, Y., (NGI) (2014) NIFS: *Report nr. 68/2014: Effect of storage time on sample quality.* Norway: Norges vassdrags- og energidirektorat i et samarbeid med Statens vegvesen og Jernbaneverket. Available at: http://publikasjoner.nve.no/rapport/2014/rapport2014_68.pdf [Accessed: 16.05.2021]

L'Hereux, J.S., Lindgård, A., Emdal, A. (2019) The Tiller-Flotten research site: Geotechnical characterization of a very sensitive clay deposit. NGI, NTNU. *AIMS Geosciences*, 5(4):831-867. Available at: https://ngi.brage.unit.no/ngi-xmlui/handle/11250/2630879 [Accessed: 25.03.2021]

Lefebvre, G., Poulin, C. (1979) A new method of sampling in sensitive clay. *Canadian Geotechnical Journal*, 16(1) pp. 226–233. Available from doi: 10.1139/t79-019. [Accessed:16.05.2021]

Lefebvre, G., Bozozuk, M., Philibert, A. Hornych (1991) Evaluating K_o in Champlain clays with hydraulic fracture tests. *Canadian Geotechnical Journal*, 28(3):365-377. Available at: https://www.researchgate.net/publication/237378704_Evaluating_Ko_in_Champlain_clays_with_hydraulic_fracture_tests [Accessed: 27.05.2021]

Levesque, Y., Saeidi, A., Rouleau, A. (2017) An earth pressure coefficient based on the geomechanical and geometric parameters of backfll in a mine stope. *International Journal of Geo-Engineering, 8(27)*. Available at: https://doi.org/10.1186/s40703-017-0065-8 [Accessed: 25.05.2021]

Li, L. Aubertin, J., Dubé, J.S. (2012) Pressure Measurement in A Silo Backfilled with A Cohesionless Soil, *World Congress on Advances in Civil, Environmental, and Materials Research (ACEM' 12)*. Seoul, Korea, August 26-30, 2012. Montreal: Department of Construction Engineering. Available at: https://www.semanticscholar.org/paper/Pressure-Measurement-in-A-Silo-Backfilled-with-A-*-Li-Aubertin/47a61eebb32b2315058c22ddae4d9ddb13e8f5ab#paper-header [Accessed: 26.04.2021]

Li, L., Aubertin, J., Dubé, J. (2014) Stress Distribution in a Cohesionless Backfill Poured in a Silo. *The Open Civil Engineering Journal*, 8(1):1-8. Available at: https://www.researchgate.net/publication/263926711_Stress_Distribution_in_a_Cohesionless_Backfill_Poured_in_a_Silo [Accessed: 30.05.2021]

Lindgård, A., Ofstad, S.C. (2017) *Field and laboratory investigations to evaluate the coefficient of earth pressure at rest*. M.Eng. Master Thesis. NTNU, Trondheim, Norway. Available at: https://ntnuopen.ntnu.no/ntnu-xmlui/handle/11250/2458795 [Accessed: 26.05.2021]

Longva O., Janbu N., Blikra L.H., Bøe R. (2003) The 1996 Finneidfjord Slide; Seafloor Failure and Slide Dynamics. In: Locat J., Mienert J., Boisvert L. (eds.), Submarine Mass Movements and Their Consequences. *Advances in Natural and Technological Hazards Research, vol 19*. Springer, Dordrecht. Available at: https://doi.org/10.1007/978-94-010-0093-2_58 [Accessed: 30.07.2021]

Lunne, T., Robertson, P.K., Powell, J.J.M. (1997) *Cone Penetration Testing in Geotechnical Practice.* UK, London, Blackie academic & professional.

Mayne, P.W. (2005a) Integrated Ground Behavior: In-Situ and Lab Tests. *Deformation Characteristics of Geomaterials*, Vol 2. Lyon, France: Taylor & Francis, London, United Kingdom, pp. 155-177. Chapter available at: https://www.researchgate.net/publication/286002220_Integrated_ground_behavior_In-situ_and_lab_tests [Accessed: 02.06.2021]

Mayne, P.W. (2007) *NCHRP Synthesis 368: Cone Penetration Testing: A synthesis of Highway Practice.* Washington, D.C: Transportation Research Board, National Academies of Sciences, pp. 51, 58. Available at: https://www.geoengineer.org/storage/publication/24048/publication_file/7872/568ed98382174-Mayne_2007___NCHRP_368___Cone_Penetration_Testing.pdf [Accessed: 29.05.2021]

Meca, J.B. (2004) *Rate effects of rapid loading in clay soils*. Ph.D. Thesis. University of Sheffield, England. Available at: https://etheses.whiterose.ac.uk/15053/1/414638.pdf?fbclid=IwAR2cq0ejbq2hX7EvgnQ-kal4NfMDdCmHZd7zbaGhzj131uTQ2nGrch5BktU [Accessed: 31.05.2021]

Meisina, C., Öztürk Kardoğan, P. S., Bonì, R., Stacul, S., Castaldini, D., Fontana, D., Lugli, S., Bordoni, M., Lo Presti, D. (02.2021) Development and Use of a Minicone for Liquefaction Risk Evaluation in Layered Soil Deposits. *Journal of Geotechnical and Geoenvironmental Engineering*. 147(2). Available at: https://doi.org/10.1061/(ASCE)GT.1943-5606.0002457 [Accessed: 08.04.2021]

Mo, P.-Q., Marshall, A. M., & Yu, H.-S. (2017) Layered effects on soil displacement around a penetrometer. *Soils and Foundations*, 57(4):669-678.

Morris. A.S., Langari, R. (2012) Instrument Types and Performance Characteristics. *Measurement and Instrumentation, Theory and Application*. Butterworth-Heinemann. Available at: https://www.sciencedirect.com/science/article/pii/B9780123819604000024 [Accessed: 03.06.2021]

Nordal, S. NTNU geoteknikk, IBM (2020) Compendium. *TBA4116: Geotechnical engineering, Advanced course.*

Norwegian Geotechnical Society (Norsk Geoteknisk Forening – NGF) (2011) *Veiledning for symboler og definisjoner i geoteknikk: Identifisering og klassifisering i jord*. Oslo, Norway: NGF. Available at: http://ngf.no/?page_id=67 [Accessed: 24.06.2021]

Nottingham, L.C. (1975) *Use of Quasi-Static Friction Cone Penetrometer Data to Predict Load Capacity of Displacement Piles.* Ph.D. Thesis. Department of Civil Engineering, University of Florida. Available at: http://ufdcimages.uflib.ufl.edu/UF/00/09/83/18/00001/useofquasistatic00nott.pdf [Accessed: 29.06.2021]

NTNU Geoteknikk, IBM. Emdal, A., Eiksund, G., Grande, L., Grimstad, G., Nordal, S., (2016) Compendium. *TBA4105: Geotechnics calculation methods*. Trondheim.

NTNU Geoteknikk, IBM. Sandven, R., Senneset, K., Emdal, A., Nordal, S., Janbu, N., Grande, L., Amundsen, H.A. (2017) Compendium. *TBA4110: Geotechnics, Field and Laboratory Investigations.* Trondheim.

NTNU Geoteknikk, IBM (2018) Compendium. *TBA4100: Geotechnical Engineering and Engineering Geology*. Trondheim.

Parker (2019) *ETH Electro Cylinder, Parker High Force Electro Thrust Cylinder*. Product catalouge. Available at: https://www.parker.com/Literature/Electromechanical%20Europe/Literature/192_550017_ETH_Catalog.pdf [Accessed: 10.02.2021]

Robertson, P.K. (1990) Soil classification using the cone penetration test. *Canadian Geotechnical Journal*, 27(1):151-158. Available at: https://www.cpt-robertson.com/publications/ [Accessed: 29.05.2021]

Robertson, P.K., Fear, C.E. (1995) Liquefaction of sands and its evaluation. *Proceedings of 1st Int. Conference on Earthquake Geotechnical Engineering.* Tokyo, 1995. Rotterdam: Balkema, pp. 1253-1289. Available at: https://www.cpt-robertson.com/PublicationsPDF/Rob%20%26%20Fear%2C%201ICEGE%2C%20Tokyo%201995.pdf [Accessed: 11.06.2021]

Robertson & Wride (1998) Evaluating cyclic liquefaction potential using the cone penetration test. *Canadian Geotechnical Journal*, 35(3):442-459. Available at: https://www.researchgate.net/publication/254226691_Evaluating_cyclic_liquefaction_potential_using_the_cone_penetration_test [accessed 10.05.2021]

Robertson, P.K. (2016) Cone penetration test (CPT)-based soil behaviour type (SBT) classification system — an update*. Canadian Geotechnical Journal*, 53(12):1-18. Available at: https://doi.org/10.1139/cgj-2016-0044 [Accessed: 10.05.2021]

Rognlien, P. (2017*) Sherbrooke Block Sampler - Time Effect in Ordinary Sherbrooke Block Sampler contra Mini-block Sampler*. M.Eng. Master Thesis. NTNU, Trondheim, Norway. Available at: https://ntnuopen.ntnu.no/ntnu-xmlui/handle/11250/2561549?show=full [Accessed: 16.05.2021]

Sandven, R., Montafia, A., Gylland, A. (Multiconsult), Kåsin, K., Pfaffhuber, A.A. (NGI), Long, M. (UCD) (2015) *NIFS: Report nr. 126-2015: – Detection of quick clay – final report: Guideline Detection of brittle materials summary report with recommendations.* Norway, Trondheim: Statens vegvesen, Jernbaneverket and NVE. Available at: http://ngf.no/wp-content/uploads/2015/02/NIFS-NGF-Detection-of-brittle-materials-summary-report-with-recommendations.pdf [Accessed 10.06.2021]

Schulze, D. (2017a) Stresses in silos part 1: Bulk solid properties – Stresses in the vertical section. *Bulk solids handling*, 37(2):42-49. Available at: https://news.bulk-online.com/bulk-solids-handling-archive/stresses-in-silos-part-1-bulk-solid-properties-stresses-in-the-vertical-section.html [Accessed: 20.05.2021]

Schulze, D. (2017b) Stresses in silos part 2: Stresses in hoppers – Disturbances to the stress distribution. *Bulk solids handling*, 37(3). Available at: https://news.bulk-online.com/bulk-solids-handling-archive/stresses-in-silos-part-2-stresses-in-hoppers-disturbances-to-the-stress-distribution.html [Accessed: 20.05.2021]

Senneset, K. and Janbu, N. (1985) Shear strength parameters obtained from static cone penetration tests. In: *Strength Testing of Marine Sediments.* Laboratory and In-Situ Measurements, ed. R. Chaney and K. Demars. West Conshohocken, PA*:* ASTM STP 883, Philadelphia, 1985, pp. 41-54. Available at: https://doi.org/10.1520/STP36328S [Accessed: 30.05.2021]

Senneset, K., Sandven, R. and Janbu, N. (1989) Evaluation of soil parameters from piezocone tests. *Transportation Reasearch Record,* 1235, National Research Council, Washington D.C., 24-37. Available at: http://onlinepubs.trb.org/Onlinepubs/trr/1989/1235/1235-003.pdf [Accessed: 18.05.2021]

Solberg, I.L., Geological Survey of Norway (NGU) (2019) *Geotechincal methods*. Available at: https://www.ngu.no/en/topic/geotechnical-methods [Accessed: 06.12.2020]

Standard Norge (1988) *NS 8015:1988 Geoteknisk prøving – Laboratoriemetoder – bestemmelser av udrenert skjærstyrke ved konusprøving*. [Accessed: 10.06.2021]

Standard Norge (2017) *NS_EN ISO 17892-6:2017: Geotekniske feit- og laboratorie-undersøkelser. Laboratorieprøving av jord. Del 6: Konusårøving*. [Accessed: 10.06.2021]

Sun, S., Zhao, J., Zhang, C. (2018) Calculation of Silo Wall Pressure considering the Intermediate Stress Effect. *Advances in Civil Engineering, vol 2018*. Available at: https://doi.org/10.1155/2018/3673515 [Accessed: 19.05.2021]

Tehrani, F.S., Arshad, M. I., Prezzi, M., Salgado, R. (2017) Physical modeling of cone penetration in layered sand. *Journal of Geotechnical and Geoenvironmental Engineering,* 144(1). Available at: https://doi.org/10.1061/(ASCE)GT.1943-5606.0001809 [Accessed 10.06.2021]

Terzaghi, K. (1943) *Theoretical Soil Mechanics*. New York: John Wiley & Sons, Inc. Available at: https://onlinelibrary.wiley.com/doi/book/10.1002/9780470172766 [Accessed: 19.05.2021]

Tien, H.J. (1996) *A literature study of the arching effect*. Thesis (M.S.). Massachusetts Institute of Technology. Available at: https://dspace.mit.edu/handle/1721.1/39056 [Accessed: 19.05.2021]

Vesić, A.S., Jones, J.A. (1977) *NCHRP Synthesis of Highway Practice 42: Design of Pile Foundations*. Transportation Research Board, National Research Council, Washington, D.C., pp. 65. Available at: http://onlinepubs.trb.org/Onlinepubs/nchrp/nchrp_syn_42.pdf [Accessed 01.06.2021]

Vreugdenhil, R., Davis, R., Berrill, J. (1994) Interpretation of cone penetration resutls in multilayered soils. *International journal for numerical and analytical methods in geomechanis*. 18:589-599. Available at: https://doi.org/10.1002/nag.1610180902 [Accessed: 09.06.2021]

Wang, Y. (2019) *Centrifuge Modelling and Numerical Analysis of Penetrometers in Uniform and Layered Clays*. Ph.D. Thesis. The University of Western Australia.

Widisinghe, S., Sivakugan, N. (2012) Vertical Stresses within Granular Materials in Silos. *Proceedings of the 11th Australia New Zealand Conference on Geomechanics*. Melbourne, 15-18 July 2012. pp. 590-595. Available at: https://researchonline.jcu.edu.au/23806/1/Sankha_ANZ2012.pdf [Accessed: 24.05.2021]

Yang, P., Li, L., Aubertin, M. (2018) Theoretical and numerical analysis of earth pressure coefficient along the centerline of vertical openings with granular fills. *Applied sciences*, 8(10):1721. Available at: https://doi.org/10.3390/app8101721 [Accessed: 21.05.2021]

Zhao, C.F., Fei, Y., Zhao, C., Jia, S.H. (2018) Analysis of Expanded Radius and Internal Expanding Pressure for Undrained Cylindrical Cavity Expansion*. International journal of geomechanics,* 18(2). Available at: https://ascelibrary.org/doi/abs/10.1061/%28ASCE%29GM.1943-5622.0001058 [Accessed: 2021]

Figure list

Table list

Appendices

Appendix A Deduction - Method of differential slices

An illustration with an infinitesimal vertical increment, with thickness dz, is shown below as background to the deduction of $\overline{\sigma_v'}(z)$. In the figure, g is the gravitational acceleration, and φ_x is the wall-soil interface friction angle, denoted δ' in this thesis.

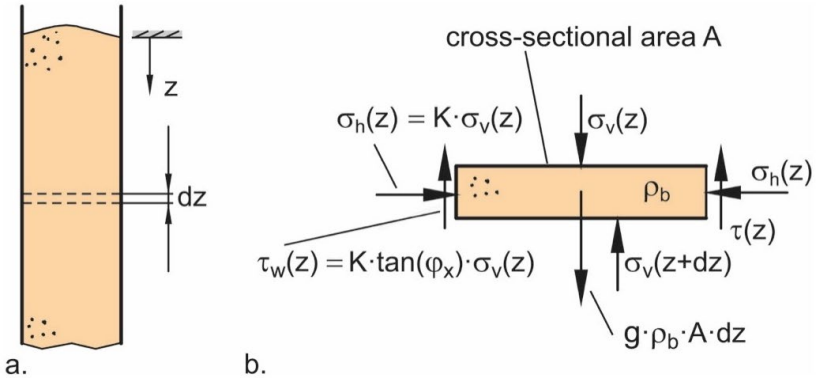

Figure A.1. Incremental slice element (b.) of cylinder (a.), with associated forces acting on slice notated. *Schulze (2017a)* Fig. 6: a) Slice element of height dz in the vertical section; b) Stresses on the boundaries of the slice element.

From the elements presented in *Figure 2.35* an equation for the sum of vertical forces, $\sum F_z$, can be deduced, {A.1}. U is here the perimeter of the silo, i.e., $\pi \cdot D_c$.

$$\sum F_z = 0 = A \cdot \left(\sigma_v'(z) - \sigma_v'(z+dz)\right) + g \cdot \rho_b' \cdot A \cdot dz - \tau_w \cdot U \cdot dz \qquad \{A.1\}$$

$\overline{\sigma_v'}(z)$ will for the following equations be simplified to σ_v', to improve the visual impression of the deduction. The term $\sigma_v'(z) - \sigma_v'(z+dz)$ can be substituted by $d\sigma_v'$ and the term $\rho_b' \cdot g$ by γ', this gives eq. {A.2}. Here τ_w has been substituted by $K'\sigma_v' \tan(\delta')$ in order to be able to solve the differential eq. {A.3}.

$$A \cdot d\sigma_v' + \gamma' \cdot A \cdot dz - K'\sigma_v' \tan(\delta') \cdot U \cdot dz = 0 \qquad \{A.2\}$$

$$\int_0^z dz = \int_q^{\sigma_v'} \frac{d\sigma_v'}{\left(\gamma' - K'\sigma_v' \tan(\delta') \cdot \frac{U}{A}\right)} \qquad \{A.3\}$$

By substituting the variable σ_v' with the term λ, we get expression {A.4}, with the relation reformulated in eq. {A.5}.

$$\lambda = \gamma' - K'\sigma_v' \tan(\delta') \cdot \frac{U}{A} \qquad \{A.4\}$$

$$\sigma_v' = \frac{\gamma' - \lambda}{K' tan(\delta') \cdot \frac{U}{A}} \qquad \{A.5\}$$

The differential of the integral is substituted by eq. {A.7} using the relation in eq. {A.6}. A step further, the new integrand shown on the right hand of eq. {A.8}.

$$\frac{d\lambda}{d\sigma_v} = \left(-K' \tan(\delta') \cdot \frac{U}{A}\right) \qquad \{A.6\} \qquad d\sigma_v' = \frac{d\lambda}{-K' \tan(\delta') \cdot \frac{U}{A}} \qquad \{A.7\}$$

$$\frac{1}{\left(\gamma' - \frac{\gamma' - \lambda}{\cancel{K' tan(\delta') \cdot \frac{U}{A}}} \cdot \cancel{K' tan(\delta') \cdot \frac{U}{A}}\right)} \cdot \frac{d\lambda}{\left(-K' \tan(\delta') \cdot \frac{U}{A}\right)} \Rightarrow \frac{1}{\lambda} \cdot \frac{-d\lambda}{K' \tan(\delta') \cdot \frac{U}{A}} \qquad \{A.8\}$$

With the new integrand the last step is substituting former boundary conditions with $\lambda_1(\sigma_v')$ and $\lambda_0(q)$. Considering the right hand side of eq. {A.3}, the integral is solved in steps {A.9} and {A.10}, giving us the complete eq. {A.11}.

$$\frac{-A}{K' \tan(\delta')\, U} \cdot \int_{\gamma' - \frac{K' q \tan(\delta') U}{A}}^{\gamma' - \frac{K' \sigma_v' \tan(\delta') U}{A}} \frac{d\lambda}{\lambda} \qquad \{A.9\} \qquad \frac{-A}{K' \tan(\delta')\, U} \cdot [\ln(\lambda)]_{\gamma' - \frac{K' q \tan(\delta') U}{A}}^{\gamma' - \frac{K' \sigma_v' \tan(\delta') U}{A}} \qquad \{A.10\}$$

$$[z]_0^z = z = \frac{-A}{K' \tan(\delta')\, U} \cdot \left[\ln\left(\gamma' - \frac{K' \sigma_v' \tan(\delta')\, U}{A}\right) - \ln\left(\gamma' - \frac{K' q\, tan(\delta')\, U}{A}\right)\right] \qquad \{A.11\}$$

From fluid mechanics we have the *hydraulic diameter*, D_h, which represent the ratio of the cross-section area and the perimeter (Schulze, 2017a). It is expressed by eq. {A.12} and for a cylindrical cross-section it is equal to the diameter. By also introducing the term *decay length*, l', (Duran, 2001, as cited by Hammer, 2020) the equations above can be simplified to the one in eq. {A.14}.

$$D_h = \frac{4 \cdot A}{U} = D_c \qquad \{A.12\} \qquad \boldsymbol{l' = \frac{D_h}{4 \cdot K' \cdot \tan(\delta')} = \frac{\cancel{4} \cdot A}{\cancel{4} \cdot K' \cdot \tan(\delta') \cdot U}} \qquad \{A.13\}$$

$$-\frac{z}{l'} = \left[\ln\left(\gamma' - \frac{\sigma_v'}{l'}\right) - \ln\left(\gamma' - \frac{q}{l'}\right)\right] \qquad \{A.14\}$$

Finally, by solving the last equations {A.14} and {A.15} we get the formula {A.16}.

$$-\frac{z}{l'} = \ln\left(\left(\gamma' - \frac{\sigma_v'}{l'}\right) / \left(\gamma' - \frac{q}{l'}\right)\right) \Rightarrow e^{-\frac{z}{l'}} = \frac{\left(\gamma' - \frac{\sigma_v'}{l'}\right)}{\left(\gamma' - \frac{q}{l'}\right)} \qquad \{A.15\}$$

$$\overline{\boldsymbol{\sigma_v'}}(\boldsymbol{z}) = \boldsymbol{\sigma_v' = q e^{-\frac{z}{l'}} + \gamma' l' \left(1 - e^{-\frac{z}{l'}}\right)} = \gamma' l' + e^{-\frac{z}{l'}}(q - \gamma' l') \qquad \{A.16\}$$

For the case where $q = 0$, the equation becomes:

$$\overline{\boldsymbol{\sigma_v'}}(\boldsymbol{z}) = \boldsymbol{\gamma' l' \left(1 - e^{-\frac{z}{l'}}\right)} \qquad \{A.17\}$$

It should be emphasized that all solutions presented are based on some assumptions as e.g., the δ', γ' and K' are all constant with depth. The vertical stress in every slice is an average over the whole cross-section area, giving us a $\overline{\sigma_v'}$ (see ch. 2.4.1.5). The horizontal force that is accounted for, through K', is working along the wall, meaning that the horizontal stress elsewhere in the fill material does not necessarily have the same proportionally with σ_v', this can be imagined by looking at *Figure 2.35*. The estimation of K' is discussed in ch. 2.4.1.4.

A.1 Terzaghi's arching theory

In Terzaghi's analysis of the arching effect (Terzaghi, 1943, ch. V), the focus was laid on arching effects experienced in the field and not specifically for silos. He developed a similar equation to that of eq. {A.1}, with the difference being a *plane strain*-condition over a width $2 \cdot B$, where $\tau_w \cdot U \cdot dz$ was substituted by $2 \cdot (c + \tau) \cdot dz$, and A substituted by $2 \cdot B$. This gave the eq. {A.18}. He conducted a trap door experiment to back up his theory in 1936 (Terzaghi, 1936, as cited by Tien, H.-J. 1996), see *Figure A.2* and *Figure A.3*.

$$2 \cdot B \cdot d\sigma_v + \gamma \cdot 2 \cdot B \cdot dz - 2 \cdot (c - \tau) \cdot dz = 0 \qquad \{A.18\}$$

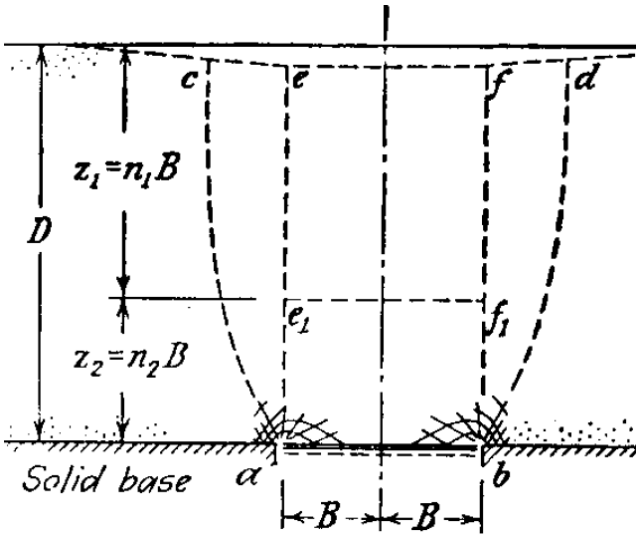

Figure A.2. Vertical lowering of a base with width 2B under cohesionless sand, inducing yield zones "following arching geometry" / "governed by arching". Terzaghi, K. *(1943) Figure 17. Failure in cohesionless sand preceded by arching.*

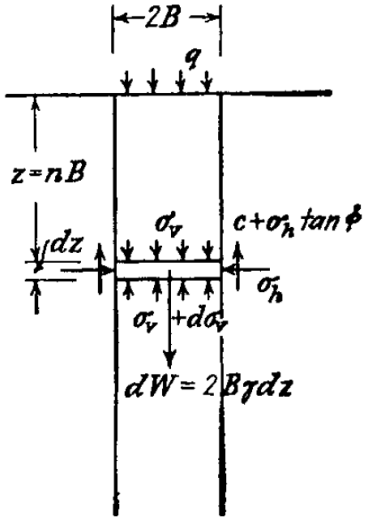

Figure A.3. Incremental slice of a lowered in-plane rectangle, with associated notation. *Terzaghi, K.* (1943) Figure 18: Diagram illustrating assumptions on which computation of pressure in sand between two vertical surfaces of sliding is based.

Appendix B Additional sample arrangements

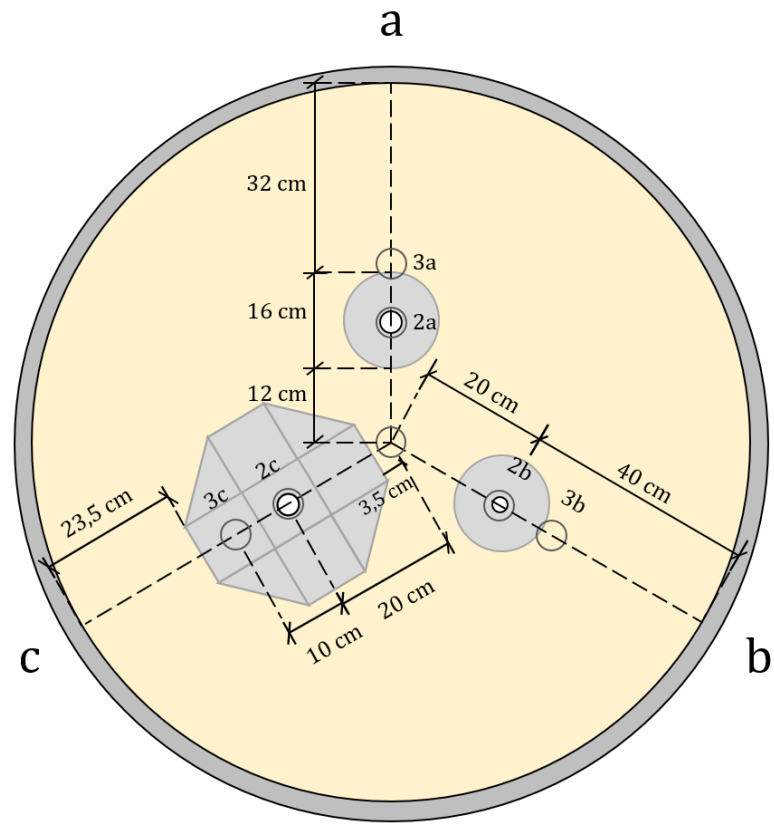

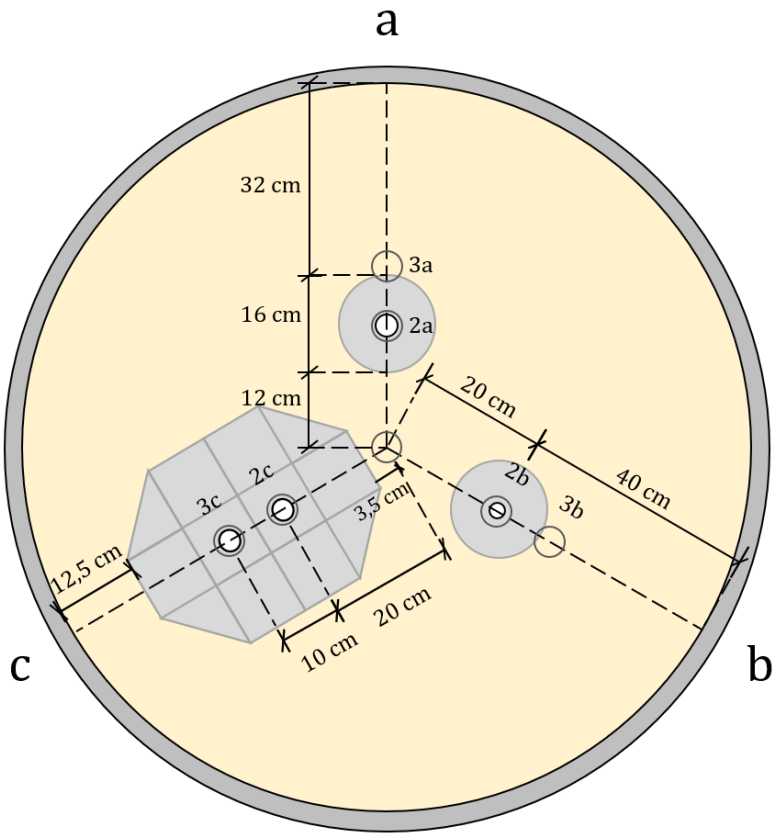

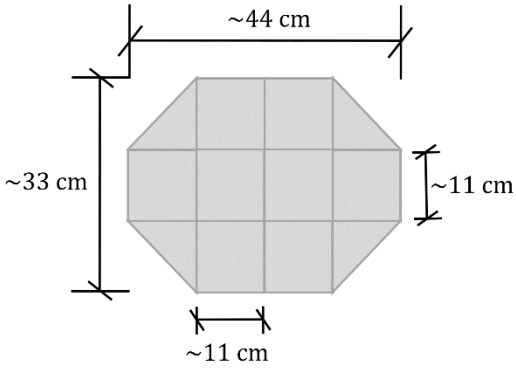

*Figure B.*1. Other evaluated sample arrangements for the natural quick clay samples:

Appendix C Depth profile and specimen set-up

Table C.1. Depth profile:

Mini-block:		Specimen	Level	Block-position
I-II	6,7-6,78	1	2, β	S-6
II-I	7,185-7,225	2	3, γ	S-6
	7,225-7,345	3	1, α	S-6
	7,345-7,465	4	1, α	S-7
III-I	7,865-7,905	5	3, γ	S-7
	7,905-7,985	6	2, β	S-2
	7,985-8,105	7	1, α	S-2
	8,105-8,185	8	2, β	S-7
IV-I	8.63-8,715	9	1, α	**a**
	8,715-8,8	10	1, α	**b**
	8,8-8,885	11	1, α	**c**
IV-II	8,915-9,035	12	1, α	S-3
	9,035-9,155	13	1, α	**S-1**
	9,155-9,235	14	2, β	S-3
IV-III	9,265-9,385	15	1, α	S-4
	9,385-9,505	16	1, α	S-5
	9,505-9,585	17	2, β	S-4
IV-IV	9,615-9,672	18	2, β	**a**
	9,672-9,752	19	2, β	**S-1**
	9,752-9,808	20	2, β	**b**
	9,808-9,865	21	2, β	**c**
	9,865-9,893	22	3, γ	**a**
	9,893-9,933	23	3, γ	S-2
IV-V	9,965-10,005	24	3, γ	S-3
	10,005-10,033	25	3, γ	**b**
	10,033-10,073	26	3, γ	**S-1**
	10,073-10,102	27	3, γ	**c**
	10,102-10,182	28	2, β	S-5
	10,182-10,222	29	3, γ	S-4
	10,222-10,262	30	3, γ	S-5

Appendix D List of equipment

Table D.1. List of lab facility equipment.

Earth pressure cells (5)	Pore pressure sensor	
Tension measurement device	Actuator	
Computers, 2+	Rack for actuator	
10 cm² CPTU-probe, acoustic with logger	Crane	
Input/output modules for transition pressure sensors and DAQ-box	Equipment related mini-probe (DAQ-box: GME-700, junction box, proximity switch etc)	
DAQ-boxes to pressure sensors and actuator	5 cm² CPTU-probe, cabled	
Artificial overburden load frame (complex, elaborated in ch. 0)	Probe saturation liquids (glycerol, antifreeze, and silicone oil)	
Chamber base	Valves (4)	Cutting stand for clay
Chamber extension	Hoses (water, air)	Wire saw
Chamber water in-/oulet	20-litre water container	Silicone lubricant
Chamber rubber gasket	Sedimentation basin (small crate)	Small plates for clay handling
Filter cloth	Shovel tray (2)	Small and large F-clamps
Scaffolds	Steel brackets (4)	Weight 0-4 kg & 0-200g
Small L-beam, 1,4 m	Circular metal sieve, $D = 1{,}15$ m	Plastic foil
Steel tape measure	Circular wooden plate, $D = 1{,}13$ m	Falling cone apparatus
Tailor tape measure	Plate vibrator	Casagrande device
Folding meterstick	Sample cylinders (H=5,10 cm, D=7,2 cm)	
	Hand hydraulic stacker	
	Pallet jack	

Appendix E CPTU-data from the reference site

A few soundings from the Flotten research site were downloaded from the open-content site DataMap and assessed by the same parametrizations as the data assessment from the current experiments. This was done as to provide some foundation for comparison of results. The position of each sounding is shown in *Figure 3.3*. Only an excerpt from the sampling depth at Flotten is shown, as this is the depth which reflects the material used in the latest experiment. Note that RCPTU-sounding TILC34 (Yellow in charts) has a general trend of deviating from the rest of the result.

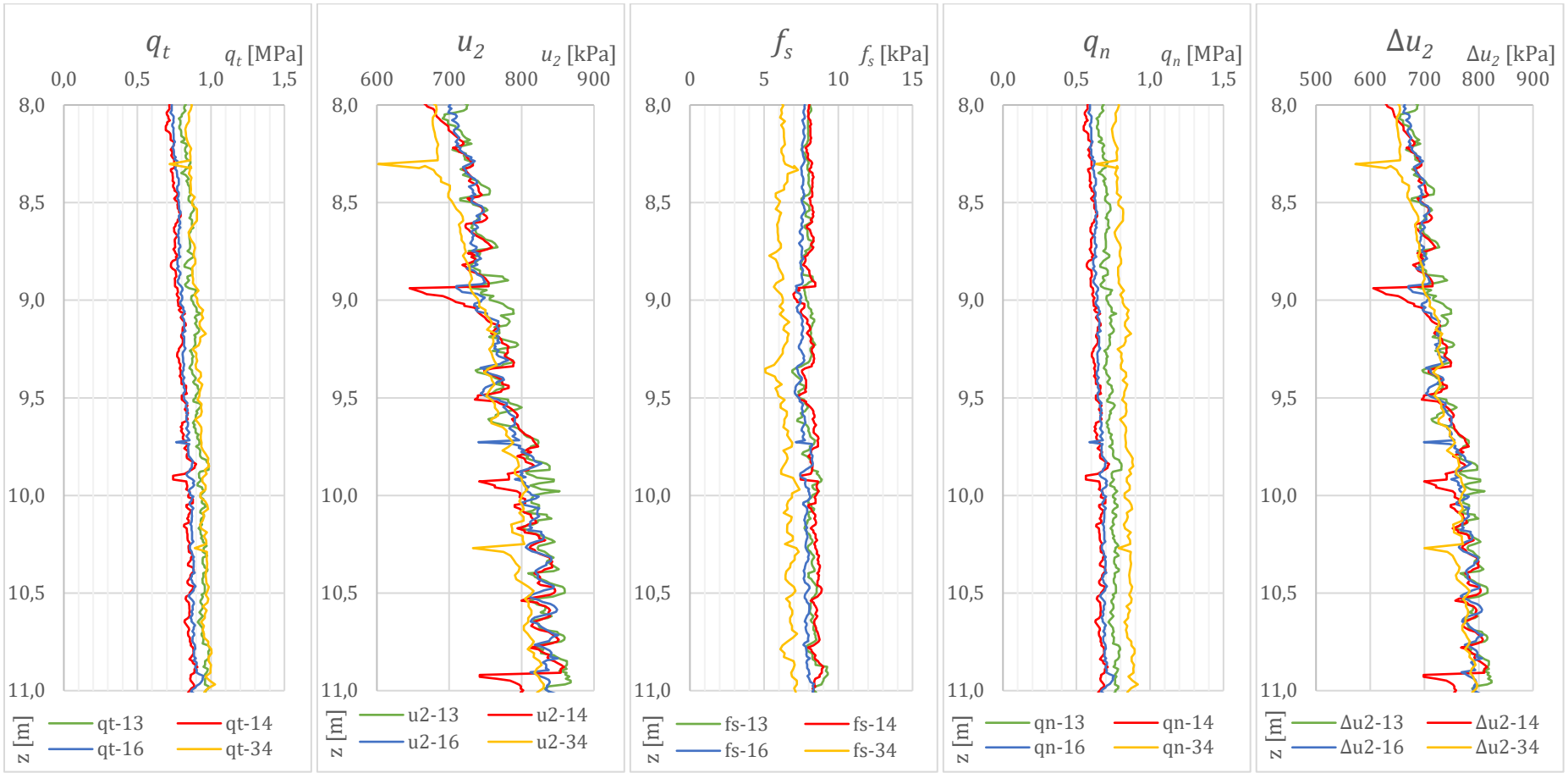

Figure E.1. Standard CPTU-parametrizations.

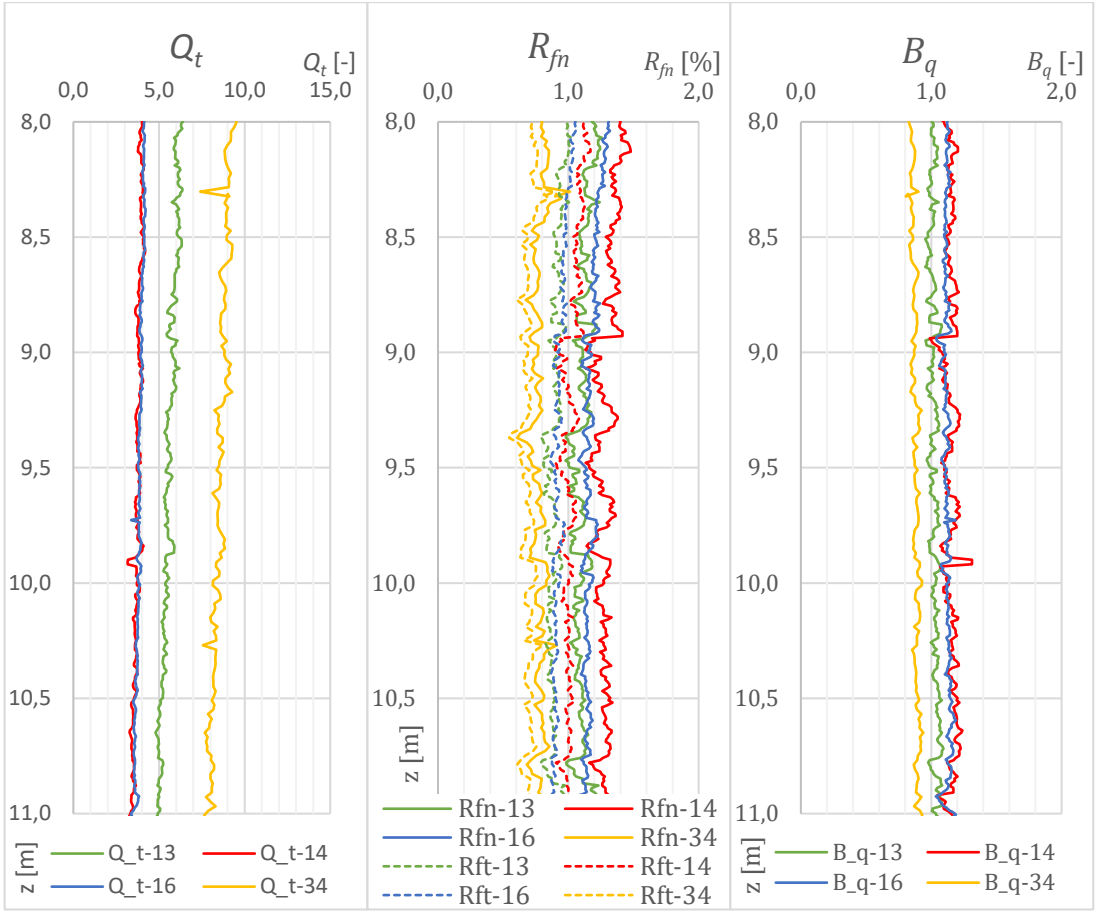

Figure E.2. Normalized parametrizations.

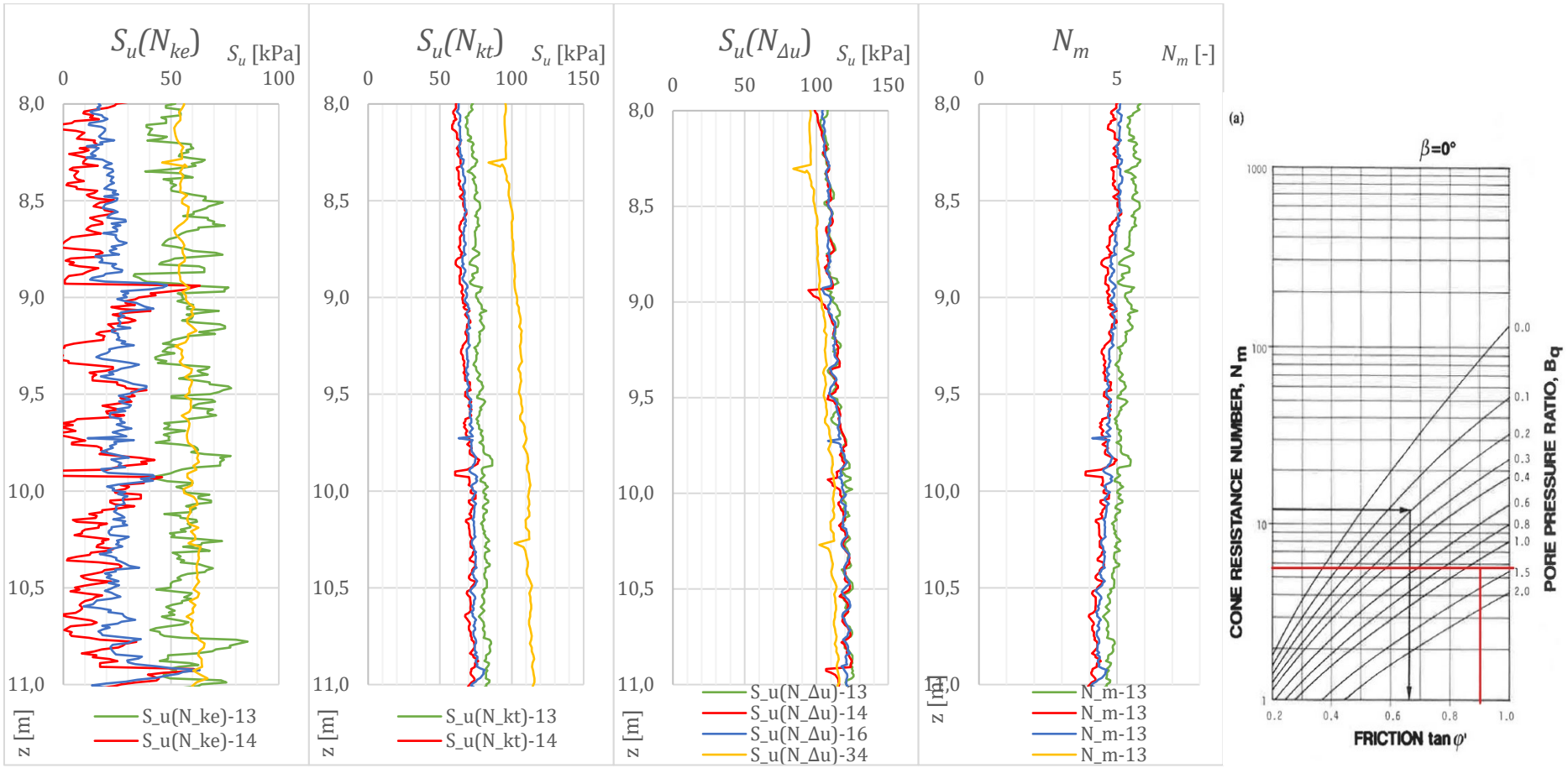

Figure E.3. S_u- values aqcuired by using different cone bearing factors. On the right hand side the tip resistance number and the associated chart is shown.

For comments on N_m, look in the discussion part, ch. .

Hallvard Skrede

CPTU detection of thin clay layers in sand - Results from calibration chamber testing

NTNU
Norwegian University of
Science and Technology